Etudes de bruit du fond dans le canal H→ZZ*→4l pour le Run 1 du LHC. Perspectives du mode bbH(→γγ) et études d'un système de détecteur pixel amélioré pour la mise à niveau de l'expérience ATLAS pour la phase HL-LHC

Evangelos Gkougkousis

HAL Id: tel-01307137

https://tel.archives-ouvertes.fr/tel-01307137

Submitted on 26 Apr 2016

THESE DE DOCTORAT
DE L'UNIVERSITE PARIS-SACLAY,
préparée à l'Université Paris-Sud

ÉCOLE DOCTORALE N° 756 - PHENIICS
Particules hadrons énergie et noyau: instrumentation, image, cosmos et simulation

Spécialité de doctorat : Physique des particules

Par

M. Gkougkousis Evangelos-Leonidas

Background studies on the H→ZZ→4l channel at LHC Run 1. Prospects of the bbH(→γγ) mode and studies for an improved pixel detector system for the ATLAS upgrade towards HL-LHC

Thèse présentée et soutenue à Orsay, le 4 février 2016 :

Composition du Jury :

M., STOCCHI, Achille	Laboratoire de l'Accélérateur Linéaire (UMR8607) - Université Paris Sud	Président
M., CONTARDO, Didier	Institut de Physique Nucléaire de Lyon	Examinateur
M., MOLL, Michael	Organisation européenne pour la Recherche nucléaire (CERN)	Rapporteur
M., NISATI, Aleandro	Istituto Nazionale di Fisica Nucleare Università degli Studi di Roma "La Sapienza"	Rapporteur
Mme., ICONOMIDOU - FAYARD, Lydia	Laboratoire de l'Accélérateur Linéaire (UMR8607) - Université Paris Sud	Directeur de thèse
M., LOUNIS, Abdenour	Laboratoire de l'Accélérateur Linéaire (UMR8607) - Université Paris Sud	Co-directeur de thèse

Titre : Etudes de bruit du fond dans le canal H→ZZ*→4l pour le Run 1 du LHC. Perspectives du mode bbH(→γγ) et études d'un système de détecteur pixel amélioré pour la mise à niveau de l'expérience ATLAS pour la phase HL-LHC

Mots clés : Higgs, Pixels, ATLAS, CERN, Haute Luminosité, Mise à niveau

Résumé : La première prise des données du LHC (2010 - 2012) a été marquée par la découverte du boson scalaire, dit boson de Higgs. Sa masse a été mesurée avec une précision de $< 0,2$ % en utilisant ses désintégrations en deux photons et celles en deux bosons Z donnant quatre leptons dans l'état final. Les couplages ont été estimés en combinant plusieurs états finaux, tandis que la précision sur leur mesure pourra bénéficier énormément de la grande statistique qui sera accumulée pendant les prochaines périodes de prise des données au LHC (Run 2, Phase II).

Le canal H→ZZ*→4 leptons, a un rapport d'embranchement réduit mais présente un faible bruit de fond, ce qui le rend attractif pour la détermination des propriétés du nouveau boson. Dans cette thèse, l'analyse conduite pour la mise en évidence de ce mode dans l'expérience ATLAS est détaillée, avec un poids particulier porté à la mesure et au contrôle du bruit de fond réductible en présence d'électrons.

Dans le cadre de la préparation de futures prises de données à très haute luminosité, pré-vues à partir de 2025, deux études sont menées:
- La première concerne l'observabilité du mode de production du boson de Higgs en association avec des quarks b. Une analyse multivariée, basée sur des données simulées, confirme un très faible signal dans le canal H→2 photons.
- La seconde concerne la conception et le développement d'un détecteur interne en silicium, adapté à l'environnement hostile, de haute irradiation et de taux d'occupation élevé, attendus pendant la Phase II du LHC. Des études concernant l'optimisation de la géométrie, l'amélioration de l'efficacité ainsi que la résistance à l'irradiation ont été menées. A travers des mesures SIMS et des simulations des procédés de fabrication, les profils de dopage et les caractéristiques électriques attendues pour des technologies innovantes sont explorés. Des prototypes ont été testés sous faisceau et soumis à des irradiations, afin d'évaluer les performances du détecteur et celles de son électronique associée.

Title: Background studies on the H→ZZ→4l channel at LHC Run 1. Prospects of the bbH(→γγ) mode and studies for an improved pixel detector system for the ATLAS upgrade towards HL-LHC

Keywords : Higgs, Pixels, ATLAS, CERN, High-Luminosity, Upgrade

Abstract: The discovery of a scalar boson, known as the Higgs boson, marked the first LHC data period (2010 - 2012). Using mainly di-photon and di-Z decays, with the latest leading to a four lepton final state, the mass of the boson was measured with a precision of < 0.2 %. Relevant couplings were estimated by combining several final states, while corresponding uncertainties would largely benefit from the increased statistics expected during coming LHC data periods (Run 2, Phase II).

The $H \rightarrow ZZ^* \rightarrow 4l$ channel, in spite of its suppressed brunching ratio, benefits from a weak background, making it a prime choice for the investigation of the new boson's properties. In this thesis, the analysis aimed to the observation of this mode with the ALTAS detector is presented, with a focus on the measurement and control of the reducible electron background.

In the context of preparation for future high luminosity data periods, foreseen from 2025 onwards, two distinct studies are conducted:

➢ The first concerns the observability potential of the Higgs associated production mode in conjunction with two b-quarks. A multivariate analysis based on simulated data confirms a very weak expected signal in the H→di-photon channel.

➢ The second revolves around the conception and development of an inner silicon detector capable of operating in the hostile environment of high radiation and increased occupancy, expected during LHC Phase II. Main studies were concentrated on improving radiation hardness, geometrical and detection efficiency. Through fabrication process simulation and SIMS measurements, doping profiles and electrical characteristics, expected for innovative technologies, are explored. Prototypes were designed and evaluated in test beams and irradiation experiments in order to assess their performances and that of associated read-out electronics.

Introduction

The Standard Model is a unified theory that governs fundamental interactions between elementary particles. It predicts the existence of the Higgs boson as a manifestation of the electroweak symmetry breaking. This long researched for scalar boson is the centerpiece of LHC research program and consists the epitome of Run 1 physics results. The announcement of the particle's discovery took place on the 4th of July 2012. This result is beyond doubt consolidated by the total recorded luminosity of 26.425 fb^{-1}, collected during the first two years of operation, while an intensive program is under way to further investigate the particle's properties, measure its couplings and observe rare production and decay modes. The program's 10-year horizon aims at a total of 3000 fb^{-1} integrated luminosity.

During my thesis, research activities extended to two different domains. The first involves data analysis on Higgs Physics related searches. In this context, two analyses are presented, with one part of my work devoted to the estimation of the reducible electron background in the H→ZZ$^{(*)}$→4l channel. Using Run 1 data, a more accurate result was obtained for final publications. The second analysis was conducted in the framework of the future HL-LHC project. The observability potential of one of the rarest production modes, that of Higgs associated production with two b quarks in its di-photon decay mode, was investigated.

The second half of my thesis is devoted to the development of a pixelated silicon tracker, capable of coping with the requirements of the future upgrade of the ATLAS inner detector, towards the high luminosity LHC phase. Using production process simulation, geometrical optimization and Secondary ion Mass Spectroscopy (SIMS) measurements, the active edge technology is evaluated. Electrical characterization of prototypes is presented, while through test beam experiments detection efficiency is assessed.

This document is structured in six chapters:

1. In the first chapter, the theoretical basis of the Higgs mechanism are detailed with a particular focus on the production and decay mechanisms. Current ATLAS and CMS results are presented, including couplings measurements and uncertainties.

2. The second chapter is devoted to the LHC machine, the ATLAS detector and its geometry as well as data acquisition and particle reconstruction. The detailed geometry of individual detector subsystems is presented, followed by a description of the trigger system. An introduction to main analysis objects used in the subsequent chapters is also given.

3. In the third chapter, the four lepton analysis is presented, including event selection, background estimation and final results. A long section is devoted to the reducible electron background estimation and in particular to the truth-reco unfolding method that constitutes my personal contribution.

4. The upgrade program for the High Luminosity LHC, its physics incentive and the considered detector scenarios are detailed in chapter four. Following the detailed timetable, the various options are presented as well as the corresponding improvements with respect to the already installed upgrades at the end of Run 1.

5. Chapter five presents my work on the observability potential of the bbH(→γγ) mode for the 3000fb^{-1} expected integrated luminosity at the end of LHC Phase II. Using simulated data and applying corrections for expected detector performances, a weak significance is observed through a multivariate approach analysis

6. The sixth and final chapter is entirely devoted to the development of a pixel detector capable of operating in the harsh radiation and occupancy conditions foreseen during Phase II of the LHC. My work is presented for the whole spectrum of the R&D activities, ranging from design, process simulation and SIMS measurements to evaluate production, electrical characterization of prototypes and irradiation testing. Different active edge geometries are compared. Finally, Low Gain Avalanche Diode sensors are presented, through simulations and SIMS measurements while the potential of a gallium implanted structure is particularly investigated.

Acknowledgements

The support of Themis, Alexandre, Baptiste, Pierros and Giannis especially during the last few intensive and very difficult months of the manuscript preparation was capital to the conclusion of this work. I address a great recognition for their encouragement and help, which remained undiminished thought the completion of the PhD.

Background studies on the H→ZZ→4l channel for LHC Run 1. Prospects of the bbH(→γγ) mode and studies for an improved pixel detector system for the ATLAS up-grade towards HL-LHC

Table of Contents

1 The Standard Model and the electroweak symmetry breaking mechanism

1.1 The Standard model

The Standard Model (SM) of particle physics was developed over the second half of the 20th century and took its present form during the 70s. It effectively describes most of the interactions between elementary particles and since several decades, numerous experiments have tested and certified its validity by verifying the predictions with an accuracy reaching 0.1 % in some cases [1].

The SM is a quantum field theory, based on gauge symmetry and expressed as a combination of $SU(3)_C \times SU(2)_L \times U(1)_Y$ groups [2]. The final product contains the symmetry group of strong interactions, $SU(3)_C$, as well as the one corresponding to electroweak interactions, $SU2_L \times U(1)_Y$. The group corresponding to electromagnetism, $U(1)_{em}$, is included as a subgroup of the $SU(2)_L \times U(1)_Y$ product, since electromagnetic and weak forces are unified thanks to the works of Glashow [3], Salam [5] and Weinberg [4].

Elementary particles are divided into two main categories according to their statistical properties, fermions and bosons. Fermions, (*Figure 1.1 left*) obeying Fermi - Dirac statistics are further distinguished into three families, whose members have similar properties but different masses. They are also classified into two categories, leptons and quarks. While leptons can exist in a free-state and exhibit full electrical load, quarks bare a fraction of electric charge in multiples of 1/3. They are subject to the strong interaction and are confined within states related to integer electric charge and to zero color. An antiparticle is associated with each fermion, with the same mass and statistic rules but opposite quantum numbers. Bosons (*Figure 1.1 right*) are integer spin particles obeying the Bose-Einstein statistics, allowing them to coexist in the same quantum state. Two types of bosons can be distinguished, with the first being spin s = 1 vector fields, convening elementary interactions. The second type of bosons, with spin s = 0, has a single member so far, the so-called Higgs boson, that is a scalar field responsible for the electroweak symmetry breaking.

FERMIONS matter constituents spin = 1/2, 3/2, 5/2, ...						BOSONS force carriers spin = 0, 1, 2, ...					
Leptons spin =1/2			**Quarks** spin =1/2			**Unified Electroweak** spin = 1			**Strong (color)** spin = 1		
Flavor	Mass GeV/c^2	Electric charge	Flavor	Approx. Mass GeV/c^2	Electric charge	Name	Mass GeV/c^2	Electric charge	Name	Mass GeV/c^2	Electric charge
ν_L lightest neutrino*	$(0-2) \times 10^{-9}$	0	u up	0.002	2/3	γ photon	0	0	g gluon	0	0
e electron	0.000511	−1	d down	0.005	−1/3						
ν_M middle neutrino*	$(0.009-2) \times 10^{-9}$	0	c charm	1.3	2/3	W$^-$	80.39	−1	**Higgs Boson** spin = 0		
μ muon	0.106	−1	s strange	0.1	−1/3	W$^+$ W bosons	80.39	+1	Name	Mass GeV/c^2	Electric charge
ν_H heaviest neutrino*	$(0.05-2) \times 10^{-9}$	0	t top	173	2/3	Z^0 Z boson	91.188	0	H Higgs	126	0
τ tau	1.777	−1	b bottom	4.2	−1/3						

Figure 1.1: *Standard Model particles and their properties. The fermions (left table) are the elementary constitutes of matter, while bosons (right table) act as mediators for all interactions.*

The standard model gauge sector is composed of:

- *Eight gluons*, corresponding to the $SU(3)_C$ gauge bosons, responsible for the strong interaction that binds quarks together. Because of the color confinement, gluons and quarks cannot exist as free particles. Gluons have zero mass and unitary spin.

- *The photon and the Z, $W^{\pm,0}$* correspond to the gauge bosons of the electroweak interaction. The weak interaction is responsible for fission and beta decay. Its intensity is significantly

weaker than that of other elementary forces, while the short distance action indicates that the mediator bosons $W^{\pm,0}$ and Z^0 are massive. The electromagnetic interaction, mediated by the photon, is responsible for magnetic and electric phenomena. The range of the electromagnetic force is infinite in the measure where the photon has a zero mass.

- *Higgs boson:* An additional - new type - boson, discovered in the summer of 2012, the Higgs boson is vital in understanding the spontaneous electroweak symmetry breaking. It has been at the epicenter of intense theoretical and experimental research for more than 50 years.

1.2   Gauge invariance in QED

To introduce gauge symmetries, the example of the quantum electrodynamics is often used. A spin ½ particle with mass m is described by the Dirac equation in its covariant form:

$$(i\gamma^\mu \partial_\mu - m)\Psi = 0 \qquad (1\text{-}1)$$

The corresponding Lagrangian can then be expressed in the following form:

$$L_e = \overline{\Psi}(i\gamma^\mu \partial_\mu - m) \quad (1\text{-}2)$$

which would consequently remain invariant under a phase transformation:

$$\Psi \to e^{i\alpha}\Psi \Leftrightarrow \qquad (1\text{-}3)$$
$$L_e = \overline{\Psi}(i\gamma^\mu \partial_\mu - m)\Psi \to L'_e = e^{-i\alpha}\overline{\Psi}(i\gamma^\mu \partial_\mu - m)e^{i\alpha}\Psi \Rightarrow \qquad (1\text{-}4)$$
$$L'_e = e^{-i\alpha}e^{i\alpha}\overline{\Psi}(i\gamma^\mu \partial_\mu - m)\Psi \Rightarrow \qquad (1\text{-}5)$$
$$L'_e = L_e \qquad (1\text{-}6)$$

On the contrary, if this phase transform is space dependent, then the Lagrangian invariance is lost:

$$\Psi \to e^{i\alpha(x)}\Psi \Leftrightarrow \qquad (1\text{-}7)$$
$$L'_e = e^{-i\alpha(x)}\overline{\Psi}(i\gamma^\mu \partial_\mu - m)e^{i\alpha(x)}\Psi \Rightarrow \qquad (1\text{-}8)$$
$$L''_e = L_e + e^{-i\alpha(x)}\overline{\Psi}(i\gamma^\mu(\partial_\mu e^{i\alpha(x)}))e^{i\alpha(x)}\Psi \qquad (1\text{-}9)$$

In order to preserve invariance, a covariant derivative introducing a gauge field A_μ is used, with respect to the following definition:

$$D_\mu = \partial_\mu - ieA_\mu \qquad (1\text{-}10)$$

where e represents the electron charge and is related to the coupling constant α of electromagnetic interaction by $\alpha = e^2/4\pi \sim 1/137$.

The purpose of this new definition is to absorb the second term of the Lagrangian in the *equation 1-9*. Under a space dependent phase transformation, individual elements can be expressed in the following form:

$$\Psi \to e^{i\alpha(x)}\Psi \qquad (1\text{-}11)$$
$$D_\mu \to e^{i\alpha(x)}D_\mu \qquad (1\text{-}12)$$
$$A_\mu \to A_\mu + \frac{1}{e}\partial_\mu a(x) \qquad (1\text{-}13)$$

Gauge invariance of the free electron Lagrangian is therefore impossible unless we accept the existence of a gauge field A_μ. This would have to be a zero mass field, since a mass term in the form of $m_\gamma \cdot 2 \cdot A_\mu \cdot A_\mu$ would render the Lagrangian non-invariant. By introducing the corresponding field coupling terms, in the form of $\Psi(x) \cdot A_\mu \Psi(x)$, one can observe that an interaction is mediated between free electrons. In reality, this field corresponds to the photon, mediator of electromagnetic interactions, with zero mass, while its coupling constant is identified as the elementary electromagnetic charge. The conclusive step left would be to describe the dynamics of this gauge field by introducing an additional term in the Lagrangian. We can define the electromagnetic tensor as:

$$F^{\mu\nu} = \partial^\mu A_\nu - \partial^\nu A_\mu \qquad (1\text{-}14)$$

Finally, by expanding all terms, while using the definition of the tensor above, the Lagrangian can be expressed as:

$$L = \overline{\Psi}\left(i\gamma^\mu \partial_\mu - m_e\right)\Psi + e\overline{\Psi}\gamma^\mu A_\mu \Psi - \frac{1}{4}F^{\mu\nu}F_{\mu\nu} \qquad (1\text{-}15)$$

1.3   Electroweak gauge invariance

In order to fully describe the electroweak interaction, three gauge fields are introduced. Two charged currents are needed ($W^\pm$), as well as a neutral one (W^0) to achieve unification with electromagnetic interaction. This constraint imposes a representation by the $SU_L(2)$ group, being the minimum unitary group with the normal three-dimensional representation. The quantum number associated with this group is the weak isospin I. For the electromagnetic part, a unique gauge field is sufficient, so the choice of $U(1)_Y$ group is natural. The associated quantum number is the hypercharge Y, a generalization of the electromagnetic charge.

In the context of the electroweak interaction $SU(2) \otimes U(1)$ group, lepton representations correspond to $SU(2)$ doublets:

$$\begin{pmatrix} \nu_e \\ e^- \end{pmatrix}, \begin{pmatrix} \nu_\mu \\ \mu^- \end{pmatrix}, \begin{pmatrix} \nu_\tau \\ \tau^- \end{pmatrix} \qquad (1\text{-}16)$$

One could further separate these doublets of their right and left helicity by writing the corresponding spinors:

$$L = \frac{1}{2}(1+\gamma_5)\begin{pmatrix} \nu_e \\ e^- \end{pmatrix} = \begin{pmatrix} \nu_e \\ e^- \end{pmatrix}_L, \quad R = \frac{1}{2}(1-\gamma_5)\begin{pmatrix} \nu_e \\ e^- \end{pmatrix} = \begin{pmatrix} \nu_e \\ e^- \end{pmatrix}_R \qquad (1\text{-}17)$$

The electroweak interaction doesn't preserve parity symmetry [6] resulting to the absence of right handed particles:

$$\begin{aligned}
L_1 &= \frac{1}{2}(1+\gamma_5)\begin{pmatrix} \nu_e \\ e^- \end{pmatrix} = \begin{pmatrix} \nu_e \\ e^- \end{pmatrix}_L, \quad e_{R_1} = \overline{e} \\
L_2 &= \frac{1}{2}(1+\gamma_5)\begin{pmatrix} \nu_\mu \\ \mu^- \end{pmatrix} = \begin{pmatrix} \nu_\mu \\ \mu^- \end{pmatrix}_L, \quad e_{R_2} = \overline{\mu} \\
L_2 &= \frac{1}{2}(1+\gamma_5)\begin{pmatrix} \nu_\tau \\ \tau^- \end{pmatrix} = \begin{pmatrix} \nu_\tau \\ \tau^- \end{pmatrix}_L, \quad e_{R_3} = \overline{\tau}
\end{aligned} \qquad (1\text{-}18)$$

In a similar fashion for quarks, there are no right-handed doublets and we can deduct that:

$$Q_1 = \begin{pmatrix} u \\ d \end{pmatrix}_L \quad , \quad u_{R_1} = u_R \text{ et } d_{R_1} = d_R$$

$$Q_2 = \begin{pmatrix} c \\ s \end{pmatrix}_L \quad , \quad c_{R_2} = c_R \text{ et } s_{R_2} = s_R \qquad (1\text{-}19)$$

$$Q_3 = \begin{pmatrix} t \\ b \end{pmatrix}_L \quad , \quad t_{R_3} = t_R \text{ et } b_{R_3} = b_R$$

In order to unify the weak interaction isospin with the electromagnetic charge, a new quantity, the hypercharge, has to be introduced:

$$Y = 2Q - 2I_3 \qquad (1\text{-}20)$$

where Q is the charge and I_3 the third component of the isotopic spin [7]. Using this definition, is possible to calculate hypercharge eigenvalues:

$$Y_{L_i} = -1 \; , \; Y_{e_{R_i}} = -2 \; , \; Y_{Q_i} = \tfrac{1}{3} \; , \; Y_{u_{R_i}} = \tfrac{4}{3} \; , \; Y_{d_{R_i}} = -\tfrac{2}{3} \qquad (1\text{-}21)$$

The corresponding gauge fields on the mediator bosons would be the B_μ for Y generators of $U(1)_Y$ group as well as the three $W_\mu^{1,2,3}$ fields of the $T^{1,2,3}$ generators corresponding to the SU(2) group. These generators are defined in the following way:

$$T^i = \tfrac{1}{2}\sigma^i \text{ with } \sigma^i \text{ the Pauli matrices} \qquad (1\text{-}22)$$

$$W_{\mu\nu}^i = \partial_\mu W_\nu^i - \partial_\nu W_\mu^i + g' g^{\mu\nu} W_\nu^j W_\mu^k B_{\mu\nu} = \partial_\mu B_\nu^i - \partial_\nu B_\mu^i \qquad (1\text{-}23)$$

where $g^{\mu\nu}$ denotes the anti-symmetric tensor.

In a similar manner as in the quantum electrodynamics case, in order to respect gauge invariance it is necessary to introduce a new covariant derivative in the Lagrangian that describes the electro-weak interaction. One can use:

$$D_\mu = \left(\partial_\mu - ig'' T_i W_\mu^i - ig' \frac{Y}{2} B_\mu \right) \qquad (1\text{-}24)$$

with g′ et g″ the two coupling coefficients corresponding to the fields B_μ et de $W_\mu^{1,2,3}$ respectively. By continuing this approach, the electroweak Lagrangian can be written in the form of:

$$\begin{aligned}
L_{EW} = &-\frac{1}{4} W_{\mu\nu}^a W_a^{\mu\nu} - \frac{1}{4} B_{\mu\nu}^a B_a^{\mu\nu} + \bar{L}_i i D_\mu \gamma^\mu L_i \\
&+ \overline{e_{R_i}} i D_\mu \gamma^\mu e_{R_i} + \overline{Q_i} i D_\mu \gamma^\mu Q_i + \overline{u_{R_i}} i D_\mu \gamma^\mu u_{R_i} \qquad (1\text{-}25) \\
&+ \overline{d_{R_i}} i D_\mu \gamma^\mu d_{R_i}
\end{aligned}$$

In this formula, the neutral bosons W_μ^3 and B_μ correspond to linear combinations of the photon and the weak Z boson [8], while charged bosons W^2, W^3 are equivalent to $W^\pm$ bosons [9]. The absence of any mass term for all fields and in particular for the W_μ^3 and B_μ components known to be massive because of their short action, has been a puzzling issue of the theory for years.

1.4   The BEH mechanism and electroweak symmetry breaking

The work of P. Higgs [10], F. Englert and R. Brout [11], G.S. Guralnik et al. [12] resulted in a model that explains the appearance of the weak force mediators masses through the spontaneous breaking of electroweak symmetry, while keeping photons and gluons massless.

1.4.1   The BEH mechanism

Particles can acquire mass through their interaction with the Higgs field. The mechanism attributes mass to the bosons by absorption of Nambu - Goldstone bosons, occurring from the spontaneous symmetry breaking. In its simplest expression, an additional field, the Higgs, is added to the gauge theory. The spontaneous breaking of the underlying local symmetry triggers the conversion of the field components to Goldstone bosons, interacting with the other fields of the theory in order to produce the mass terms of the gauge bosons. This mechanism leaves behind a scalar elementary particle (spin 0), known as the Higgs boson, while respecting the need of a massless photon.

To generate masses for the W and Z bosons while maintaining the $U(1)_{em}$ unchanged, one has to break the $SU(2)_L \times U(1)_Y$ symmetry. To do so, a neutral component of a scalar complex field doublet is introduced.

$$\Phi = \begin{pmatrix} \varphi^\dagger \\ \varphi^0 \end{pmatrix} \quad , \quad Y_\varphi = 1 \qquad (1\text{-}26)$$

This new field can be fully described by the following Lagrangian:

$$L_H = \left(D_\mu \Phi\right)^\dagger \left(D^\mu \Phi\right) - \mu^2 \Phi^\dagger \Phi - \lambda \left(\Phi^\dagger \Phi\right)^2 \qquad (1\text{-}27)$$

where D_μ the covariant derivative defined at the electroweak interaction and μ, λ are unknown constants. The kinetic term is already included in the expression $[(D_\mu \Phi^*)(D^\mu \Phi)]$ along with a potential term $[V=\mu^2 \Phi^*\Phi+\lambda(\Phi^*\Phi)^2]$, the most generic possible while respecting SU(2) invariance. By fixing one of the parameters assuming $\lambda > 0$, we can examine the behavior for different values of μ^2. If the latest is positive, then the potential nominal value would be zero. On the contrary, if μ^2 is considered negative, the potential will develop a non-zero vacuum expectation value (*Figure 1.2*).

The kinetic term of the Lagrangian also contains the mass factor of the boson associated with the Higgs field. This originates from the second neutral component of the field. Both components, the charged one and one of the neutrals, are Goldstone bosons, acting as the third component of longitudinal polarization of massive $W^\pm$ and Z bosons. The remaining neutral component is associated with the massive Higgs boson. Since the Higgs field is a scalar, the corresponding gauge boson has spin zero, no electric charge or color, while its wave function is symmetric.
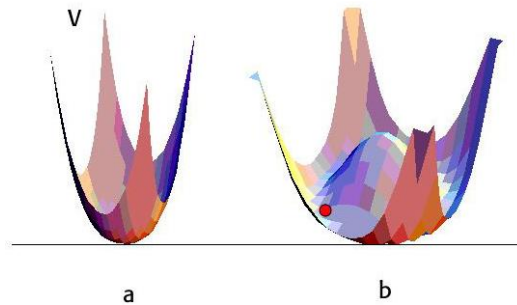
Figure 1.2: *Form of the* Higgs *potential in the complex plan for positive (a) or negative μ² (b) The small sphere indicates a possible choice for the direction of the potential vector.*

The vacuum expectation value can be computed from the potential by applying the operator to the wave function:

$$\langle \Phi_0 \rangle = \langle 0|\hat{\Phi}|0\rangle = \frac{1}{\sqrt{2}}\begin{pmatrix} 0 \\ \sqrt{\frac{-\mu^2}{\lambda}} \end{pmatrix} \qquad (1\text{-}28)$$

The $1/\sqrt{2}$ factor is imposed by the normalization requirement. The minimum expected value is calculated as the absolute value of $\sqrt{-\mu^2/\lambda}$, estimated from the Fermi constant to be ~ 246 GeV. This form of potential is more commonly known as "The Mexican Hat Potential", since its initial value, or vacuum value, is non-zero. There are infinite possibilities of passing to a stable minimum, which causes the symmetry breaking by leaving the initial value. Keeping in mind the demand to maintain U(1)$_{em}$ while breaking the SU(2)$_L$ × U(1)$_Y$ symmetry, from the infinite amount of algebraic solutions implied by *equation 1-28*, an appropriate suggestion for the wave fiction representation is the following:

$$\boldsymbol{\varphi} = \begin{pmatrix} \mathbf{0} \\ \frac{\mathbf{v}}{\sqrt{\mathbf{2}}} \end{pmatrix} \qquad (1\text{-}29)$$

Although an analytic solution for the Lagrangian (*equation 1-27*) would not be possible in its general form, one can approach the problem by an expansion at the minimum potential value [13]. Since the appearance of the Goldstone bosons is intrinsic on the theoretical side, it is convenient to use a parameterization that would eliminate the corresponding terms:

$$\boldsymbol{\varphi} \to \boldsymbol{\varphi}' = \frac{e^{\frac{i\sigma a(x)}{v}}}{\sqrt{\mathbf{2}}}\begin{pmatrix} \mathbf{0} \\ \boldsymbol{v} + \boldsymbol{h(x)} \end{pmatrix} \qquad (1\text{-}30)$$

Expanding the Lagrangian at the minimum potential value using *equation 1-30* we can derive at the fourth order term approximation:

$$\begin{aligned}
\mathbf{L} = &\frac{\mathbf{1}}{\mathbf{2}}\boldsymbol{\partial_\mu h \partial^\mu h} - \frac{\mathbf{1}}{\mathbf{2}}\boldsymbol{\lambda v^2 h^2} - \boldsymbol{\lambda v h^3} - \frac{\boldsymbol{\lambda}}{\mathbf{4}}\mathbf{h^4} + \\
&+ \frac{\mathbf{1}}{\mathbf{2}}\left[\frac{\mathbf{g'^2 v^3}}{\mathbf{4}}\mathbf{B_\mu B^\mu} - \frac{\mathbf{gg'v^2}}{\mathbf{2}}\mathbf{W_\mu^3 B^\mu} + \frac{\mathbf{g^2 v^2}}{\mathbf{4}}\mathbf{W_\mu W^\mu}\right] \\
&+ \frac{\mathbf{1}}{\mathbf{v}}\left[\frac{\mathbf{g'^2 v^2}}{\mathbf{4}}\mathbf{B_\mu B^\mu h} - \frac{\mathbf{gg'v^2}}{\mathbf{2}}\mathbf{W_\mu^3 B^\mu h} + \frac{\mathbf{g^2 v^2}}{\mathbf{4}}\mathbf{W_\mu W^\mu h}\right] \\
&+ \frac{\mathbf{1}}{\mathbf{v^2}}\left[\frac{\mathbf{g'^2 v^2}}{\mathbf{4}}\mathbf{B_\mu B^\mu h^2} - \frac{\mathbf{gg'v^2}}{\mathbf{2}}\mathbf{W_\mu^3 B^\mu h^2} + \frac{\mathbf{g^2 v^2}}{\mathbf{4}}\mathbf{W_\mu W^\mu h^2}\right] + \cdots
\end{aligned} \qquad (1\text{-}31)$$

- The first term of *equation 1-31* represents the Higgs field dynamics as well as the particles mass as a function of the potential vacuum expectation value, $m_H^2 = 2\lambda v^2$.

- Subsequent terms on the second line generate W$^\pm$, Z bosons masses. The B$_\mu$ and W$_\mu^3$ are mixed together in the first two terms, with one of them generating the QED photon field A$_\mu$ of zero mass. Z boson mass can appear by deagonalizing the mixing matrix with the help of the weak interaction angle θ_w according to the following definition:

$$\frac{1}{4}\begin{pmatrix} g^2 v^2 & -gg'^{v^2} \\ -g'gv^2 & g'^2 v^2 \end{pmatrix} = M^{-1}\begin{pmatrix} m_z^2 & 0 \\ 0 & 0 \end{pmatrix}M \ , \ M = \begin{pmatrix} \cos(\theta_w) & -\sin(\theta_w) \\ \sin(\theta_w) & \cos(\theta_w) \end{pmatrix} \ (1\text{-}32)$$

It can be deducted that $m_z^2 = (g^2 + g'^2)v^2/4$

- The W$^\pm$ is included in the third term of the second line within the multiplication factor:

$$\frac{g^2 v^2}{4}W_\mu W^\mu \to \frac{1}{2}vg\left|\frac{1}{\sqrt{2}}\left(W^{`1} \mp W^{`2}\right)\right| \to m_w = \frac{1}{2}vg \qquad (1\text{-}33)$$

- The two last lines of the Lagrangian describe the interaction of the Higgs boson with the W, Z and γ boson fields.

Although for the boson case the mass generation is straight-forward appearing in the Lagrangian, fermion masses are not explained. Adding a mass term to the theory in the form of $m(L\bar{L} + R\bar{R})$ would not be possible since this would violate the SU(2)$_L$ gauge invariance. Instead, one can introduce indirect interactions with the Higgs field via Yukawa couplings in the initial Lagrangian which for the electron case would take the form:

$$L_H = -\lambda_e(\bar{L}_l \varphi R_l + \overline{R_l}\varphi^\dagger L_l) \qquad \text{(1-34)}$$

By applying the spontaneous symmetry breaking $\varphi \to \varphi' = \frac{1}{\sqrt{2}}\begin{pmatrix} 0 \\ v + h(x) \end{pmatrix}$ in the same manner as for the bosons *equation 1-34* becomes:

$$L_H = -\frac{\lambda_e v}{\sqrt{2}}\overline{\psi}_l\psi_l - \frac{\lambda_e}{\sqrt{2}}\overline{\psi}_l\psi_l h \qquad \text{(1-35)}$$

In this form, the first term corresponds to the electron mass, while the second represents the Higgs coupling to the electron and hence proportional to the electro mass. By repeating the same process for each lepton all the masses can be generated, whereas a constant g is introduced in each case.

In the quark case, the process remains identical with the exception of the up-type particles where a rotation of the Higgs field has to be considered in the form of:

$$\varphi \to \varphi' = \frac{1}{\sqrt{2}}\begin{pmatrix} v + h(x) \\ 0 \end{pmatrix} \qquad \text{(1-36)}$$

In a nutshell, the Higgs mechanism introduces the mass for all the gauge bosons and fermions as described in *Table 1-1*. The unavoidable side-effect is the introduction of a new massive field associated with a corresponding scalar boson, the Higgs boson. The corresponding couplings are proportional to the generated masses and for all intents and purposes are described as λ_f for the fermions, λ_b for the bosons and λ for the Higgs self-coupling.

Boson masses	$m_b = \dfrac{\lambda_b v}{2}$
Fermion masses	$m_f = \dfrac{\lambda_f v}{\sqrt{2}}$
Higgs mass	$m_H = \sqrt{2\lambda v^2}$

Table 1-1: *Generated mass of the Standard Model particles and their corresponding formulas.*

1.4.2 The Higgs boson mass

The Higgs boson mass is a free parameter of the model and can be constrained indirectly by several higher order effects present in loops, resulting in tiny corrections in various precision measurements of the electroweak parameters. Thus, the fit of the most precise results obtained essentially from LEP experiment have been used for a long time to extract a most probable Higgs mass field's value [1].

The mass of the Higgs boson can be calculated from the following formula:

$$m_H = \sqrt{-2\mu^2} \qquad \text{(1-37)}$$

Since µ is related to λ with respect to the vacuum expectation value of the potential, $v = \sqrt{\mu^2/\lambda}$ and λ is not fixed, m_H remains unknown. Before the discovery, constraints have been imposed by considering the unitarity of the standard model, triviality and the vacuum stability.

Perturbative unitarity: While considering the case of W bosons elastic scattering, the corresponding cross-section increases with respect to scattering energy, violating the principle of unitarity around ~ 1 TeV. In order to restore balance to the theory, the Higgs mechanism introduces and additional interaction diagram through its coupling with the W boson. This interaction path restores equilibrium for the increasing contributions with respect to the energy value for certain values of the Higgs mass. The corresponding upper limit is:

$$m_H = \left(\frac{8\pi\sqrt{2}}{3G_F}\right) \approx 700 \; GeV/c^2 \qquad (1\text{-}38)$$

Triviality: Consideration of higher order relative corrections in Higgs self-coupling constant λ_H, introduces an energy dependence of this very constant ("running coupling constant"). This allows the extraction of a limit for the Higgs mass of around ~ 160 GeV [14], for a validity up to the 10^{16} GeV scale.

Vacuum stability: The argument of vacuum stability is based on the fact that the Higgs potential has to always be limited with respect to its minimal value. This means that the coupling constant $\lambda(Q)$ has to remain positive, introducing a lower limit on the Higgs mass. In fact, if λ becomes extremely small, top quark and weak boson loops start to appear due to their strong coupling with the Higgs field. As a result, λ could become negative and the vacuum would become unstable since no minimum value would exist [15]. The constraint of a positive coupling content $\lambda(Q^2)$ implies that $m_H > 70$ GeV/c^2 for a validity of the Standard Model up to the TeV scale. *Figure 1.3* presents imposed limits on the Higgs mass with respect to the validity scale of the Standard Model.
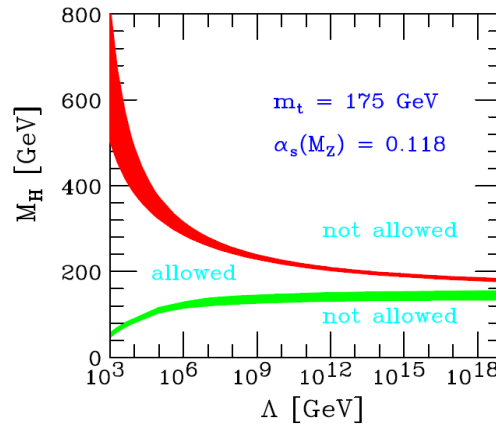
Figure 1.3: *Lower and higher limits of the Higgs mass with respect to the standard models validity scale (µ² < 0).*

1.5   Higgs production modes at hadronic colliders

Four main processes exist for the production of the Higgs boson in hadronic colliders:

- Gluon fusion (*Figure 1.5 a*)
- Vector boson fusion (VBF) (*Figure 1.5 b*)
- Associated production with W or Z bosons, also known as Higgsstrahlung (*Figure 1.5 c*)
- Associated production with a quark pair, mainly the $t\bar{t}$ (*Figure 1.5 d*)

At LHC energies *(Figure 1.4)*, the dominant Higgs production process is gluon fusion. Since the Higgs boson is not coupled with gluons, its production is carried out indirectly through quark loops and notably the top. This production mode is at least one order-of-magnitude larger than all other production processes because of the gluon component abundance in the colliding protons at the LHC energy range.
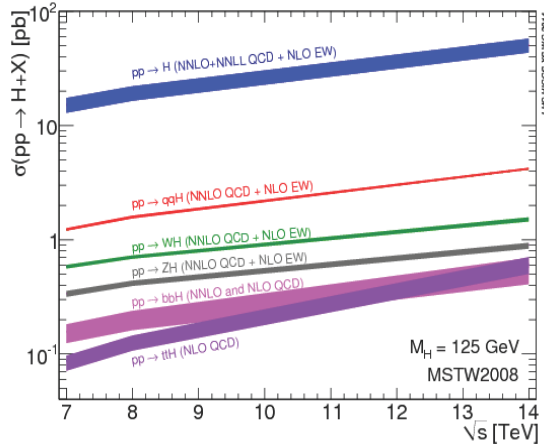
Figure 1.4 : Cross section of the various Higgs production modes as a function of the collision energy, *for 7 TeV < $\sqrt{s}$ < 14 TeV [16].*

The second most important mode is the vector boson fusion (VBF). This process demonstrates a particular topology. The quarks interact through a W or Z boson, indicating that this is an electroweak process and does not imply a color exchange between the initial and final quark states. The two final quarks generate forward jets in opposite hemispheres inside the detector, making a clear topology which allows for a very good signal-to-background separation.

A Higgs boson can also be produced in association with a W/Z boson. One of the initial quarks of the colliding protons can annihilate with an antiquark, producing in the final state a real Z or W in conjunction with a Higgs boson.

The last production mode comes from a heavy quark pair (top or bottom). Quite often, in proton collisions, a gluon or quark pair can annihilate generating a pair of heavy quarks. Those can fuse generating a Higgs boson in the processes. This phenomenon is quite rare, estimated at least 100 times less significant with respect to the gluon-gluon fusion mode.
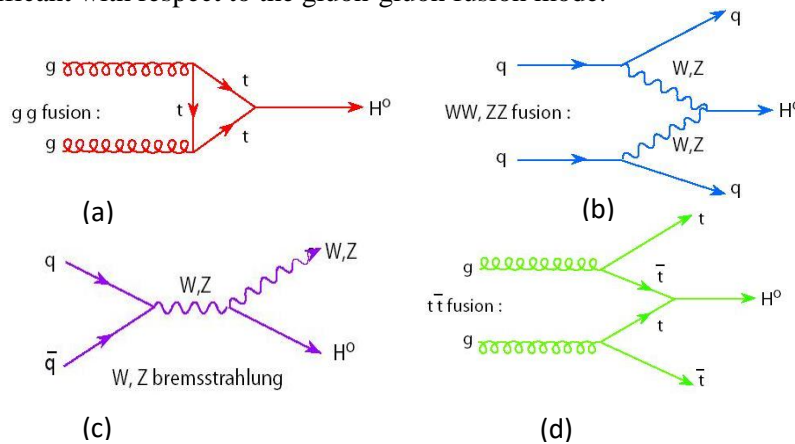
Figure 1.5: *Feynman diagrams for the main Higgs production modes. From top left to bottom right: gluon fusion process (a), vector boson fusion (b), quark-quark scattering (c) and quark gluon annihilation (d) also referred as Higgsstrahlung.*

The VBF and W/Z or top associated production modes are of different nature with respect to the gluon-gluon fusion process, in the sense that the final Higgs boson is produced in association with additional objects at the final state. This allows for a better signal to background separation although the sensitivity is generally reduced in low luminosity. All production modes are being considered in the Higgs boson studies. In LHC conditions, due to the proton-proton composition of the beam, qq scattering is favored and VBF is the second most important production mode after the dominant gluon-gluon fusion mode.
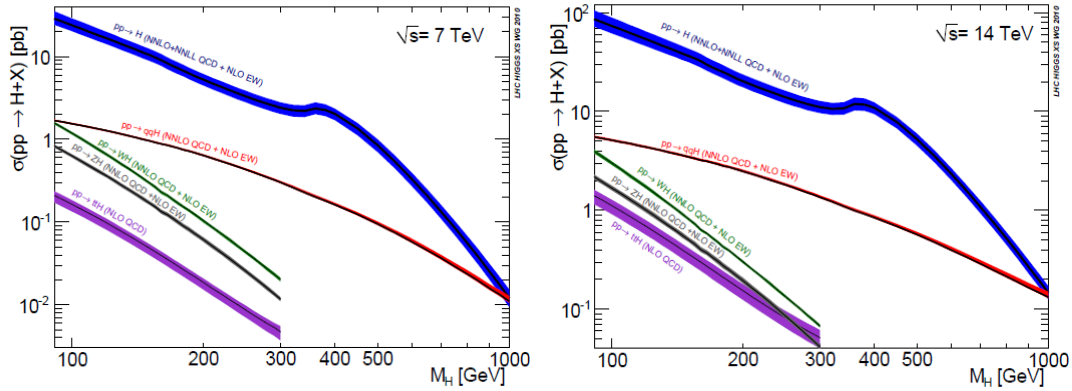
Figure 1.6: *The LHC SM Higgs production cross-section for the five most prominent modes at a $\sqrt{s} = 7\,TeV$ (left) and $\sqrt{s} = 14\,TeV$ (right) center of mass energy.*

Computation of the Higgs boson production cross-section in the various modes requires to take into account higher order corrections. Recently, Anastasiou et al. [17] achieved the long-waited NNNLO computation of the main production mode gg→H. This major accomplishment permits the understanding of gluon-gluon fusion cross-section within a ~ 3 % uncertainty. In this computation, an additional source of uncertainty comes from the Parton Density Functions (PDF) used, presently known within 2 – 3 % precision [18]. These two major breakthroughs have been achieved after the end of Run 1 of LHC.

1.6   Higgs decay channels

Higgs decay modes can be distinguished into three main categories:

➢ Prompt decays to a particle-antiparticle pair (quarks: $c\bar{c}, s\bar{s}, t\bar{t}, b\bar{b}$ and leptons: $\mu\bar{\mu}, \tau\bar{\tau}$)
➢ Decays though virtual loops (top, W)
➢ Decays to vector bosons WW* and ZZ*

Feynman diagrams for the different Higgs decay modes are illustrated in the following figure (*Figure 1.7*):
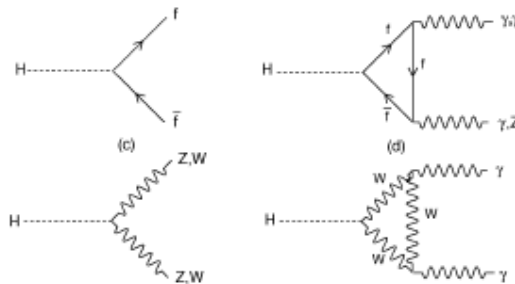
Figure 1.7: *Feynman diagrams of the main Higgs decay modes.*

As for the mass of the Higgs, the coupling constants for bosons and fermions are not fixed by the theory. The branching fractions of the various modes are shown relative to the mass of the boson (*Figure 1.8*). Higgs couples preferentially with the most massive particles, therefore, the most important branching ratios would be to the heaviest particles allowed by the Higgs mass value.

In the fermion case, the decay width can be expressed using the color factor N_c (N_c= 1 for leptons and N_c = 3 for quarks), the original fermion and Higgs particle masses as well as the minimum potential value. The color factor is introduced when final decay products carry color charge in order to ensure a colorless fermion - antifermion final state, since the Higgs field is colorless. As a result, decay width is formulated in the following way:

$$\Gamma(H \to f\bar{f}) = \frac{m_H}{8\pi}\left(\frac{m_f}{v}\right)^2 N_c \left(1 - \frac{4m_f^2}{m_H^2}\right)^{3/2} \qquad (1\text{-}39)$$

Except for the top case, where the approximation ($m_H \gg m_f$) is no longer valid, one can approximate the formulation by considering the fermion mass significantly smaller with respect to that of the Higgs. The last term of the width expression then becomes increasingly close to the unity and we can safely assume that the final resonance width or the fermion decay is proportional to the boson mass. Conversely, decays to top quarks would only come from a Higgs mass around twice that of the quark. For the fermion decays, one can notice that the widths are linear as a function of the Higgs mass.
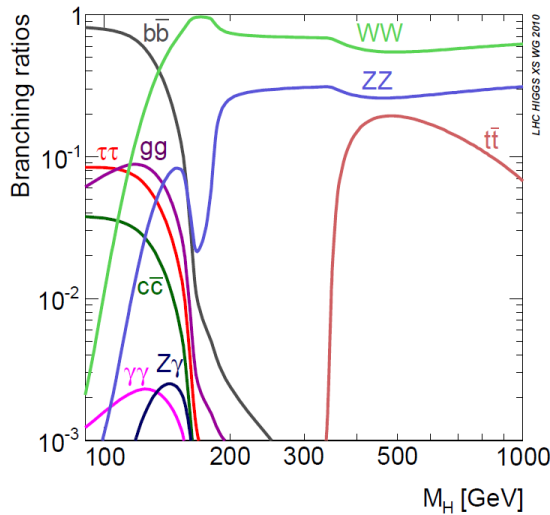
Figure 1.8: *Branching ratio for the different decay modes foreseen in tree-level SM [14].*
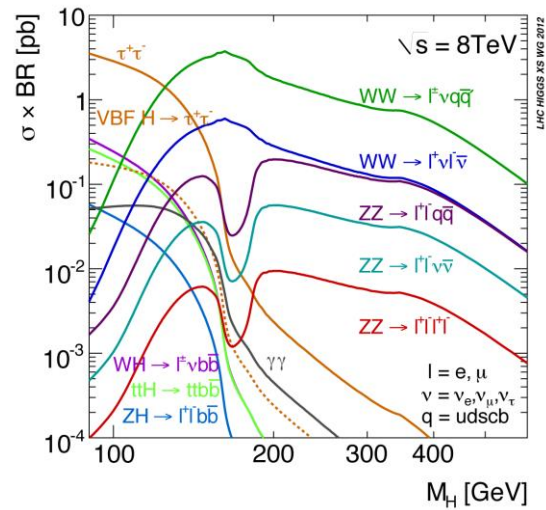
Figure 1.9 : *Variation of the natural Higgs width with respect to the particle mass.*

Considering bosonic decays, a slightly altered approach has to be considered for the massive electroweak ($W^\pm$ and Z) and massless photon and gluon cases. In the electroweak case, no color compensation factor has to be included since there is no possible mediation of color charged objects but the indistinguishable nature of the outgoing $W^\pm$ field for a neutral Higgs case impose the introduction of an additional factor of two at the WW decay width. Except for the additional mass change, calculations are identical, yielding widths described correspondingly by the representations:

$$\Gamma(H \to ZZ) = \frac{m_H}{32\pi}\left(\frac{m_H}{v^2}\right)^2 \left(1 - \frac{4m_Z^2}{m_H^2}\right)^{1/2}\left[1 - 4\left(\frac{m_Z^2}{m_H^2}\right) + 12\left(\frac{m_Z^2}{m_H^2}\right)^2\right] \qquad (1\text{-}40)$$

$$\Gamma(H \to WW) = \frac{m_H}{16\pi}\left(\frac{m_H}{v^2}\right)^2 \left(1 - \frac{4m_W^2}{m_H^2}\right)^{1/2}\left[1 - 4\left(\frac{m_W^2}{m_H^2}\right) + 12\left(\frac{m_W^2}{m_H^2}\right)^2\right] \qquad (1\text{-}41)$$

As previously stated, in the $m_H > m_{w,z}$ case, the second term of the width formulation increasingly tends towards unity, while $1/m_H$ dependence can be derived for the last term when approximated by a converging sequence. Overall, the width dependence would be proportional to $\sim m_H^3$, rendering the increase in the resonance width faster than in the fermions case.

From the previous width formulas (*equations 1-39, 1-40 and 1-41*) it can be concluded that Higgs decays preferably to the most massive particles allowed by its rest-mass value. This implies zero interaction with massless particles like gluons and photons at tree level. The di-photon final state is rare because of solely loop coupling with the photon. This decay is realized through top quark and W boson loops. Despite the small branching ratio, this mode remains very important with a very clear signal into two photons in the end state. It allows direct measurement of the mass boson.

In the width calculation, one can use the same approximations for all massless bosons, gluons and photons, with the caveat of including the color-factor in the photon case as well as the electric charge of the intermediate fermion (Q_f), while for gluons the δ^{AB} needs to be introduced to ensure that the intermediate fermionic pair is colorless. In more detail the corresponding width for the gluon decays is:

$$\Gamma(H \rightarrow gg) = \frac{a a_s{}^2 m_H^3}{2\pi^2 m_w^2 sin^2\theta_w}\left|\sum_q I(\frac{m_H^2}{m_q^2})^2\right| \qquad (1\text{-}42)$$

Where I is the form factor integral [19]. Concerning the photon case calculations, an additional complexity is imposed by the number of available interaction diagrams and the different possible topologies (26 in total for the W –loop case). Using the same approach as before one can approximate:

$$\Gamma(H \rightarrow \gamma\gamma) \approx \frac{a^3 m_H^3}{256\pi^2 m_w^2 sin^2\theta_w}\left|7 - \frac{16}{9} + \cdots\right|^2 \qquad (1\text{-}43)$$

Terms within *equation's 1-42* last factor correspond to W, top, etc. loop contributions respectively, while the most predominant one is the W contribution of the initial term. Given the proximity of the W mass value to that of the Higgs ($\approx 2/3$ of m_H) and its region in the mass scale, when appropriate approximations are applied to *equations 1-43 and 1-34*, it is derived that the dependence of the Higgs resonance width is proportional to m_H^2 in both the gluon and photon case, thus making it uniform for all bosonic decay modes.
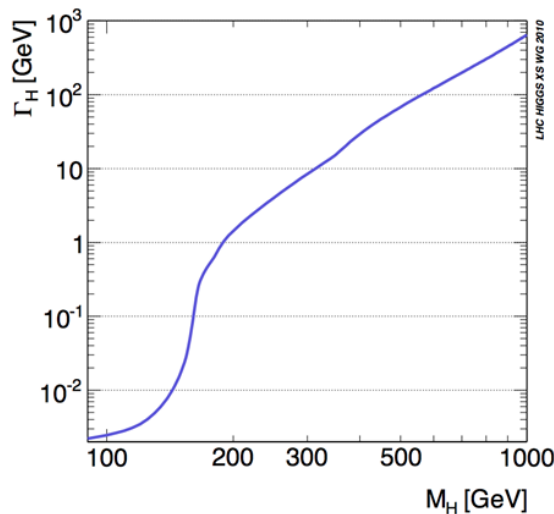
Figure 1.10: Variation of the total natural Higgs resonance width with respect to its mass.

The relative importance of a decay mode is qualified within the standard model by its branching ratio (*Figure 1.8*):

$$ßr_i = \frac{\Gamma_i}{\Gamma_{tot}} \qquad (1\text{-}44)$$

where Γ_i denotes the Higgs decay width to the ith channel. *Figure 1.10* presents the dependence of the total Higgs width on its mass, varying from 4.2 MeV at 125 GeV to 100 GeV at 500 GeV. The 125 GeV mass of the discovered boson allows for a narrow total width, far below any achievable detector resolution, making experimental performances the most dominant effect in any combined Higgs mass or decay width measurement.

1.7 Current Status of Higgs measurements

1.7.1 Mass measurement

The final result on the mass of the new boson was published by the ATLAS collaboration in July 2014, considering all available Run 1 data. Using a total integrated luminosity of 25 fb[-1], improved analysis approaches and better control of systematics, the H→γγ and the H→ZZ*→4l channels were combined to extract the most precise mass estimation. In the di-photon channel, 475.9 events are expected following the Standard Model prediction, while for the four lepton final state, this number is reduced to 26.5 events. By combining the corresponding measurements, the ATLAS measured mass value is estimated at:

$$m_H = 125.36\pm0.37(\text{stat})\pm0.18(\text{syst}) \text{ GeV} \qquad (1\text{-}45)$$

where the total uncertainty is dominated by the statistical term [20]. *Figure 1.11* presents the ratio of the profiled likelihood defined as:

$$\Lambda(m_H) = \frac{L(m_H, \hat{\mu}_{\gamma\gamma}(m_H), \hat{\mu}_{4l}(m_H), \hat{\theta}(m_H))}{L(m_H, \hat{\mu}_{\gamma\gamma}, \hat{\mu}_{4l}, \hat{\theta})} \qquad (1\text{-}46)$$

where m_H represents the probed Higgs mass and $\mu_{\gamma\gamma} - \mu_{4l}$ are the signal strengths for the di-photon and four lepton channels respectively, treated as nuisance parameters in the final fit [21]. The profiled likelihood variations in the two individual channels and the combination are profiled as a function of the m_H. The Higgs boson masses estimated with the di-photon and the four-lepton channels are compatible within 1.98 sigma ($\delta m_H = 1.47\pm0.72$ GeV).
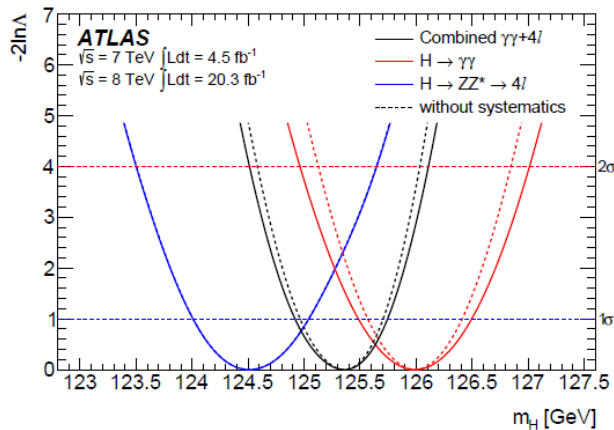
Figure 1.11: *Scans of the negative log likelihood with respect of the Higgs mass for ATLAS experiment in each channel and the total combination, in black. Dashed curves show the results accounted for statistical uncertainties.*

A corresponding combination was also published by the CMS experiment evaluating all available data on the di-photon and the four lepton channels. The two collaborations use diverse detector technologies and analogous analyses approaches. A similar combination campaign has been driven among the two collaborations to fully exploit the total LHC statistics [22]. Theoretical and model uncertainties, which are identical to both experiment, are considered to be completely correlated, while uncertainties connected to detector design, specifically the momentum scale and the resolution of objects, are unique to each experiment and are considered uncorrelated. Combining all available data, the mass of the Higgs boson at LHC is found to be:

$$m_H = 125.09 \pm 0.24 \text{ GeV}$$
$$= 125.09 \pm 0.21(\text{stat}) \pm 0.11(\text{system}) \text{ GeV} \qquad (1\text{-}47)$$

The impact of each uncertainty category can be assessed by fixing the corresponding nuisance parameters to their best fit values increased or decreased by 1 σ, while the rest are being profiled. In a breakdown it can be calculated:

$$m_H = 125.09 \pm 0.21 \text{ (stat.)} \pm 0.11 \text{ (scale)} \pm 0.02 \text{ (other)} \pm 0.01 \text{ (theory) GeV} \qquad (1\text{-}48)$$

Although both collaborations have improved the understanding of their detector and its performance since Run 1, it is clear that the scale uncertainties dominate the systematic term.

The mass evaluation of the individual channels (H→γγ and H→ZZ) have also been combined between the two experiments. *Figure 1.12* presents the summary of the individual and combined channels. Small tensions are observed between the ATLAS and CMS H→γγ and H→ZZ* masses at the level of less than 1.5 sigma. The final mass value is again limited by statistics, while the most important systematic uncertainty is related to the energy and momentum precision in both experiments.
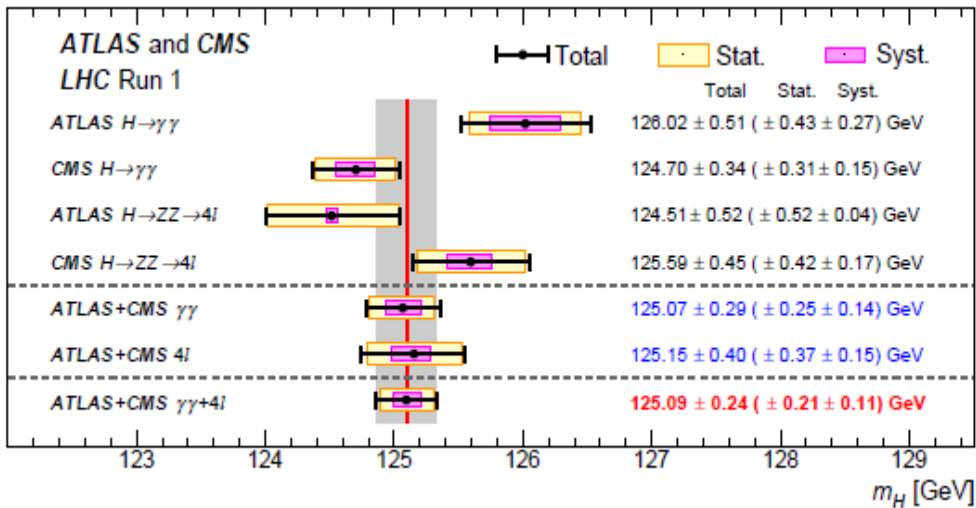
Figure 1.12: *Consistency between different results of the ATLAS and CMS collaborations in the two combined channels for Run 1 data.*

1.7.2   Couplings Estimation

Measurement or constraint of the Higgs production and decay modes has been performed by both ATLAS and CMS. Main production processes include gluon-gluon fusion, VBF component and associated production with mainly top quark. The studied decay channels concern bosonic final states (ZZ, WW, γγ) and fermionic ones (bb, ττ, μμ). In the following table significances and limits

for each treated mode are presented with corresponding uncertainties from both ATLAS and CMS collaborations (*Table 1-2*).

Channel	Signal Strength (μ)		Signal Significance (σ)	
	ATLAS	CMS	ATLAS	CMS
H→γγ	$1.15^{+0.27}_{-0.25}$	$1.12^{+0.25}_{-0.23}$	5.0	5.6
H→ZZ*→4l	$1.51^{+0.39}_{-0.34}$	$1.05^{+0.32}_{-0.27}$	6.6	7.0
H→WW	$1.23^{+0.23}_{-0.21}$	$0.91^{+0.24}_{-0.21}$	6.8	4.8
H→ττ	$1.41^{+0.40}_{-0.35}$	$0.89^{+0.31}_{-0.28}$	4.4	3.4
H→bb	$0.62^{+0.37}_{-0.36}$	$0.81^{+0.45}_{-0.42}$	1.7	2.0
H→μμ	$-0.7^{+3.6}_{-3.6}$	$0.8^{+3.5}_{-3.5}$		
ttH	$1.9^{+0.8}_{-0.7}$	$2.9^{+1.0}_{-0.9}$	2.7	3.6

Table 1-2: *Measured significances and signal strength for all Higgs primary decay* modes by both ATLAS and CMS collaborations.

In the hypothesis that the Higgs boson width (predicted to be 4 MeV for the SM) is sufficiently small for the narrow width approximation to be valid, production and decay processes can be decomposed and factorized. Using this factorization, a specific process i→H→f, where i denotes the initial state and f the final product, can be described by the product of the production mode cross-section multiplied by the branching ration of the final state in the following manner (*equation 1-49*):

$$\sigma_i \times BR_f = \sigma_i \times (\Gamma_f / \Gamma_H) \qquad (1\text{-}49)$$

where σ_i is the cross-section of the production process, BR_f the branching ratio of the final state, Γ_H the total natural width of the Higgs and Γ_f the Higgs decay width in the probed final state.

Combination of the coupling results from the two collaborations has been performed to increase the testing sensitivity of the SM predictions. Because measurement of the yield of a Higgs decay channel is not enough to determine the cross-section and the branching ratio independently, various methods have been developed in LHC to probe the compatibility of the results with SM expectations. To bypass the lack of full information, one of the parameterizations applied in the combination uses normalized yields of i→H→f to the gg→H→ZZ rate. This choice is driven by the fact that the corresponding cross-section presents the smallest overall uncertainty. Calculating ratios of cross-sections and branching ratios yields results independent from any theoretical uncertainties on absolute rates.

The observed number of H→ZZ*→4l events are expressed as the product of the gluon-gluon fusion Higgs production cross-section multiplied by the ZZ* channel branching ratio (*equation1-50*):

$$\sigma_{ZZ} = \sigma_{ggF}^H \times BR_{ZZ} \Rightarrow \sigma_{ggF}^H = \frac{\sigma_{ZZ}}{BR_{ZZ}} \qquad (1\text{-}50)$$

Using this definition, the cross-sections of all other processes can be expressed as yields with respect to the four lepton channel. For the di-photon case it would be (*equation 1-51*):

$$\sigma_{\gamma\gamma} = \frac{\sigma_{ZZ}}{BR_{ZZ}} \times BR_{\gamma\gamma} \Rightarrow \sigma_{\gamma\gamma} = \frac{BR_{\gamma\gamma}}{BR_{ZZ}} \times \sigma_{ZZ} \qquad (1\text{-}51)$$

In that way, one can evaluate all cross-sections as yields with respect to the ZZ production channel.

Figure 1.13 presents the per-experiment and the combined values of the cross-sections and of the branching ratios for various production and decay modes. Each ratio is normalized to the SM prediction such as, assuming model validity, all ratios would be unitary. All available Run 1 data (at 7 and 8 TeV) are included in the fit with the global compatibility hypothesis to SM (ratios ≈ 1)

having a p-value of 10^{-6}. In this figure, the most precise measurements are indeed in agreement with the SM within less than 2 sigma [23]. The largest deviations are due to the ttH channel (2.3 sigma deviation) and to the ZH (excess observed only in CMS data [25]). The smallest ratio is observed in the Br_{bb}/Br_{ZZ} case. For bb analyses, the proper associated production mode (ZH($\rightarrow$bb)) is studied, since it allows an increased rejection of the continuum b-quark QCD background through the use of the Z decay leptons. The cross-section in this case is expressed as (*equation 1-52*):

$$\sigma_{bb}^{ZH} = \sigma_{ZH}^{H} \times BR_{bb} \Rightarrow \sigma_{bb}^{ZH} = \sigma_{ZH}^{H} \times \frac{\sigma_{zz}}{BR_{ZZ}} \times \frac{BR_{bb}}{\sigma_{ggF}^{H}} \Rightarrow \sigma_{bb}^{ZH} = \sigma_{ZH}^{H} \times \frac{BR_{bb}}{BR_{ZZ}} \times \frac{\sigma_{zz}}{\sigma_{ggF}^{H}} \qquad (1\text{-}52)$$

The measured cross-section ratio σ_{ZH} / σ_{ZZ} is quite significant (close to 3) as shown in the same figure. As a result, the branching ratio of bb decay over the ZZ channel branching ratio is found to be reduced with respect to SM predictions, in order to keep the measured number of events to the observed rate. Search for the H$\rightarrow$bb decay by both collaborations yields signals with low significances [24, 25], of 1.7 and 2.0 sigma for ATLAS and CMS respectively.
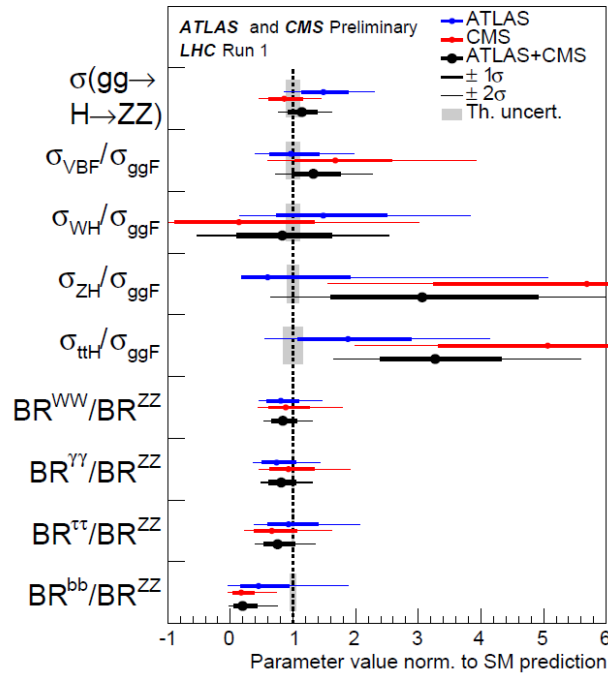
Figure 1.13: *Best fit values for cross-sections, ratios of cross-sections and branching ratios from ATLAS and CMS experiments data. The ATLAS and CMS combined values are shown in black.*

1.8   Conclusions

It is a triviality to emphasize the impressive harvest of results on the Higgs Boson research achieved by the LHC experiments using Run 1 data samples. This is however only the beginning of the Higgs era, since a lot of information concerning the properties of the new boson is still missing: not all not all production modes nor all decay channels have been identified. The jump in energy and in luminosity expected at Run 2 will allow to collect a gigantic amount of Higgs data, which will be utilized to enrich the available anthology of the boson properties.

During the next phases of the accelerator, the LHC collaboration will be able to examine to an unprecedented detail the nature of the Higgs mechanism and to probe the existence of new sectors of physics.

1.9   References

[1]   Particle Data Group, "REVIEW OF PARTICLE PHYSICS", Chinese Physics C Vol. 38, No. 9 (2014) 090001

[2]   M. Herrero, "The standard model", Departamento de Fisica Teorica Facultad de Ciencias, Universidad Autonoma de Madrid, 1998

[3]   S.L. Glashow, "Partial-Symetries of Weak Interactions", Nucl. Phys. 22, (1961) 579

[4]   S. Weinberg, "A Model of Leptons", Phys. Rev. Lett. 19, (1967) 1264

[5]   A. Salam, N. Svartholm, "Elementary Particle Physics: Relativistic Groups and Analyticity", Eighth Nobel Symposium, Stockholm: Almquvist and Wiksell. p. 367 (1968)

[6]   C.S. Wu, "Experimental Test Of Parity Conservation In Beta Decay", PhysRev 105-1413

[7]   K. Nishijima, "Charge Independence Theory of V Particles", Progr. Of Theor., Phys 13 (1955) 285

[8]   P. Bagnaia et al., "Evidence for $Z^0 \rightarrow$ e+ e- at the CERN anti-p p collider", Phys. Lett., B129:130–140, 1983.

[9]   G. Arnison, "Experimental observation of lepton pairs of invariant mass around 95 GeV/c^2 at the CERN SPS collider", Physics Letters B, 126(5):398–410, July 1983

[10] P. W. Higgs, "Broken Symmetries and the Masses of Gauge Bosons". Phys. Rev. Let. 13 (16): p. 508–509 (1964)

[11] F. Englert, R. Brout, "Broken Symmetry and the Mass of Gauge Vector Mesons". Phys. Rev. Let. 13 (9): p. 321–323 (1964)

[12] G.S. Guralnik, C.R. Hagen, T.W.B. Kibble, "Global Conservation Laws and Massless Particles", Phys. Rev. Lett. 13 (1964) 585

[13] J.H. Christenson et al., "Evidence for the 2π Decay of the K^0_2 Meson",Phys. Rev. Lett. 13, 138 (1964).

[14] G. Bhattacharyya, "A Pedagogical Review of Electroweak Symmetry Breaking Scenarios", Saha Institute of Nuclear Physics, India, SINP/TNP/2009/23, arXiv:0910.5095v1 [hep-ph]

[15] Schael et al. "Precision electroweak measurements on the Z resonance" In:Phys. Rept.427 (2006), pp. 257–454. DOI: 10.1016/j.physrep.2005.12.006.arXiv:hep- ex/0509008[hep-ex]

[16] LHC Higgs Cross Section Working Group, https://twiki.cern.ch/twiki/bin/view/LHCPhysics/CrossSections

[17] C. Anastasiou, C. Duhr, F. Dulat, F. Herzog, B. Mistlberger, "Higgs boson gluon-fusion production in N3LO QCD", CERN-PH-TH/2015-055, CP3-15-07, arXiv:1503.06056v1 [hep-ph], 20 Mar 2015

[18] S. Forte, "Parton Distributions for LHC Run 2", LAL Orsay (France), July 2015

[19] M. E. Peskin, D. V. Schroeder, "An Introduction to Quantum Field Theory", page 776. Westview Press, 1995

[20] The ATLAS Collaboration, "Measurement of the Higgs boson mass from the H→γγ and H→ZZ*→4l channels with the ATLAS detector using 25 fb^{-1} of pp collision data", arXiv:1406.3827v1 [hep-ex] 15 Jun 2014

[21] G. Cowan, K. Cranmer, E. Gross, O. Vitells, "Asymptotic formulae for likelihood-based tests of new physics", Eur.Phys.J. C71 1554 (2011), arXiv:1007.1727 [physics.data-an]

[22] The ATLAS and CMS Collaborations, "Combined Measurement of the Higgs Boson Mass in pp Collisions at √s=7 and 8 TeV with the ATLAS and CMS Experiments", Phys. Rev. Lett. 114 (2015) 191803, Mar 26, 2015

[23] The ATLAS and CMS Collaborations, "Measurements of the Higgs boson production and decay rates and constraints on its couplings from a combined ATLAS and CMS analysis of the LHC pp collision data at vs = 7 and 8 TeV", ATLAS-CONF-2015-044, 15 Sep 2015

[24] The ATLAS collaboration, "Search for the bb decay of the Standard Model Higgs boson in associated (W/Z)H production with the ATLAS detector", ArXiv ePrint: 1409.?6212

[25] CMS Collaboration, "Search for the standard model Higgs boson produced in association with a W or a Z boson and decaying to bottom quarks", Phys. Rev. D 89 (2014) 012003, arXiv:1310.3687 [hep-ex]

2 LHC and the ATLAS experiment

2.1 The Large Hadron Collider

The construction of a new accelerator was necessary in order to achieve energies up to several TeV. The LHC, whose design began in 1980, was placed at CERN in Geneva, within the preexisting LEP tunnel. The accelerator, designed to perform proton collisions at a center of mass energy of 14 TeV with an instantaneous luminosity of 10^{34} cm^{-2}s^{-1}, started its operation at 7 TeV in summer 2010. Although mainly proton-proton collisions are studied, ion beams are also provided (including Pb) with an energy of 2.8 ATEV and maximum instantaneous luminosity of 10^{27} cm^{-2}s^{-1}.

2.1.1 Structure

The large Hadron Collider is a hadron accelerator, consists of two concentric rings, installed at the pre-existing LEP tunnel. Composed of eight straight sections and an equal number of arcs, it is placed in a depth between 45 m and 175 m under the surface, in a geologically stable plane of 1.4 % incline. Two existing beam transport lines of 2.5 km long connect the LHC ring with the existing CERN accelerator complex. The initial tunnel geometry was conceived for LEP, where RF cavities were installed in the straight sections to compensate synchrotron radiation losses of the electron - positron beams, circulating in opposite directions. Since for the LHC the main constraint is imposed by the elevated proton mass requiring an increased magnetic field, in contrast the arcs have been extended to accommodate for the enlarged beam transport magnets. Experiments are placed in four of the tunnel straight sections. Since installation of two separate rings was impossible given the limited dimensions of the preexisting structure (3.7 m diameter), a single superconductive magnet was used with double boring [1].
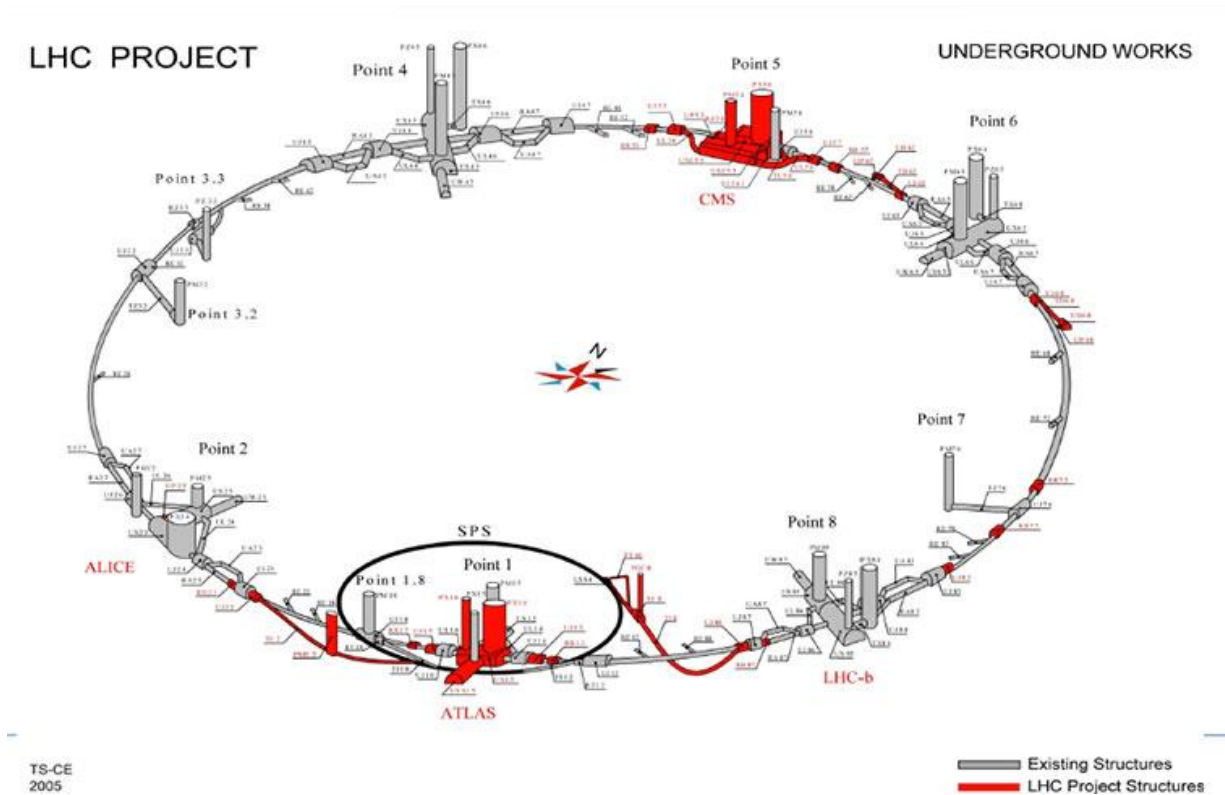
Figure 2.1: *Positioning of the four major experiments with respect to LHC ring geometry and structure of the accelerator ring.*

A total of 1232, 15 m long, dipole magnets are installed, capable of maintaining a maximum field of 8.33 T at a temperature of 1.9 K, to provide the necessary angular acceleration for transporting the proton beam within the ring circumference. Layout has been optimized to have the minimum possible number of transport magnets with the least possible interconnection points [2]. Focalization is assured by the 392, 5 – 7 m long, quadruple magnets, while higher order k-pole elements close to the interaction points further focalize the beam and limit its transverse dimensions to increase collision probability during bunch crossing. LHC arc sections, accounting for the majority of the rings perimeter, are each comprised of 23 elementary unit cells, corresponding to 106 cells for the entire ring. Each lattice unit cell follows the FODO geometry (a magnet structure consisting of alternating focusing and defocusing quadruple lenses interleaved with transport elements), composed of a horizontally focusing dipole, three beam transfer dipole magnets and a vertically focusing quadruplet followed by the last three beam transfer dipoles [3]. Small straight sections are interleaved between the cells for smooth coupling and geometry adaptation to the LEP tunnel. Finally, a dispersion suppressor is located at the intersection point between each straight section and an arc, yielding a total of 18 units across the entire ring. Except from adapting the LHC reference orbit to the LEP tunnel geometry, their main purpose is to cancel horizontal dispersions from the transition between the sections and to match the insertion optics to the periodic lattice of the arc [4].

The two independent beam pipes constitute two separate continuous vacuum systems, present over the entire length of the cryostat but segmented at the ends of each arc with a distance of 194 mm between them. Two distinct power circuits are implemented per arc, one for the focusing elements (quadruples) and one for the beam transfer optics. In that way, no coupling is imposed between the longitudinal and transverse plane. Cryogenics are segmented by arc, with only one system installed per section, used for both transfer lines.

The diagram in *Figure 2.1* shows the arrangement of the four LHC experiments with respect to the collision point of the accelerator. ATLAS and CMS are general purpose experiments, designed to search for the Higgs boson and new physics research. The LHCb experiment is designed to study the matter-antimatter asymmetry (CP violation) and rare physical processes in the B mesons decay. The aim of the ALICE experiment is to study the quark-gluon plasma during heavy-ion collisions, especially lead (Pb) nuclei.

2.1.2   Acceleration

The LHC ring is the last piece of the CERN accelerator complex (*Figure 2.2*). A number of injectors and boosters pre-accelerate and adjust beam parameters prior to injection at the main ring. An initial 350 mA proton beam is produced by a duoplasmatron source at the beginning of the LINAC 2 linear accelerator. The beam is accelerated to 120 MeV and reshaped to 30 nsec pulses of 180 mA output current before injected to the Proton-Synchrotron Booster (PSB) [5]. There, the protons are further accelerated to 1.4 GeV prior injection into the PS ring. Within the PS, the beam is shaped into 25 ns spaced bunches and reaches an energy of 26 GeV for Run 2 operations, while a 50 ns bunch spacing was maintained during Run1 [6]. Seventy-two bunches are provided at the output forming a so-called bunch - train every 3.6 s and are subsequently injected to the final pre-acceleration step before the LHC, the Super Proton Synchrotron ring. To correctly synchronize with the 200 MHz SPS acceleration cavity, bunches are reshaped to a 4nsec length while maintaining the original 25 ns spacing [7]. Before final injection to LHC ring, four trains of 72 bunches are grouped and accelerated to 450 GeV.

Once within the LHC tunnel, the beam is directed to one of the two beam pipes where it reaches the final target energy of 13 TeV (2015). Acceleration is performed at straight section 4, where 8 klystrons per beam are responsible for providing the required power.
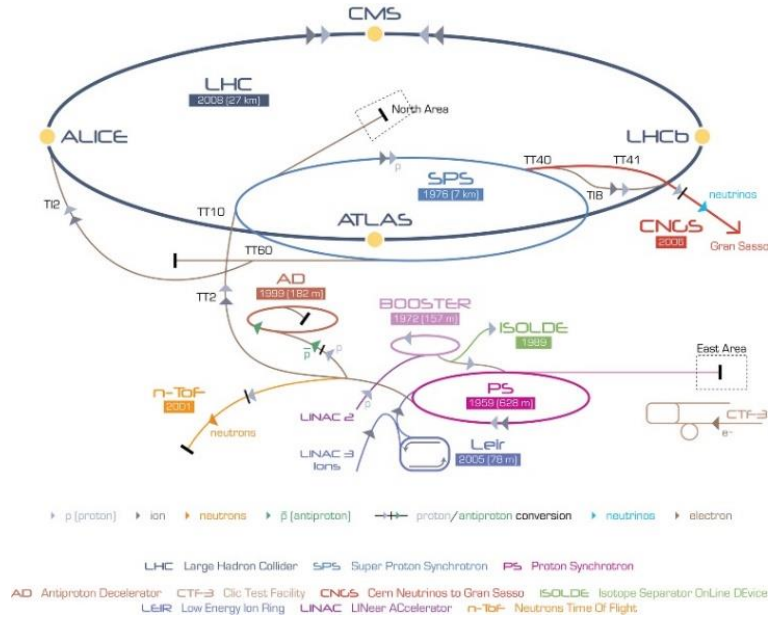
Figure 2.2: Complete CERN accelerator complex structure.

2.1.3   Luminosity

In accelerator design the most important factor to account for is the number of generated events per second in collisions. For the case of the Higgs, this would be equal to (*equation 2.1*):

$$N_{events} = L\sigma_H \qquad (2\text{-}1)$$

where σ_H is the total Higgs event cross-section and L is the luminosity of the machine which only depends on the beam parameters. This corresponds to the number of interactions produced per second per area, and for a Gaussian beam distribution can be expressed as (*equation 2.2*):

$$L = \frac{N_b^2 n_b f_{rev} \gamma}{4\pi\varepsilon_n \beta^*} F \qquad (2\text{-}2)$$

where N_b is the number of particles per bunch
  n_b the number of bunches in the tube
   γ the Lorentz factor
  ε_n the beam transverse emmitance
  β^* the β function on the interaction point
  F the luminosity reduction factor due to the beam crossing angle at the interaction point (285mrad) approximately estimated to be 0.9 for the LHC.

To increase event rate and to probe new physics, both high energy and high delivered luminosity are mandatory. For the two general purpose experiments of LHC, ATLAS and CMS, peak values of 10^{34} cm^{-2}sec^{-1} are recorded during current operations.

A more convenient estimation of the total number of expected events at a certain period of time can be achieved by calculating the time integral of the instantaneous luminosity. At the beginning of each run, a total of 1374 bunches are injected in LHC in trains of 72. As time elapses, the number of particles in the beam decreases due to collisions, dispersion effects, scattering and space

charge effects. The total beam lifetime is estimated to be around 14 h, while a refill operation (turn-around time) requires between 1.2 – 7 h. Given the exponential decrease of the number of particles, the total luminosity in a run can be calculated by integrating *equation 2.2* as (*equation 2.3*):

$$L_{int} = L_0 t_L \left(1 - e^{-t_{run}/t_L}\right) \qquad (2\text{-}3)$$

where t_L and t_{run} are the beam lifetime and run time respectively while L_0 is the initial injected luminosity. Beam lifetime is affected by different processes in the longitudinal and transverse plane. Collisions with residual in the beam tube gas, deliberate beam collisions at the interaction points and interactions with the electron cloud, created on the adjacent conductive beam pipe walls following packet movement, are the main causes for transverse instabilities. In the longitudinal direction, the Tuschek effect, consisting of coulomb scattering of particle within the same bunch and RF non-linarites reduce beam lifetime. Sudden beam losses have also been observed from fallouts within the vacuum tube, mostly conglomerates of particles, referred as UFO (unidentified Falling Objects) [8]. If the introduced perturbation in the beam cannot be recovered then a controlled dump is performed. Assuming stable operations for 200 days per year and 24 h per day, the total per year integrated luminosity can be estimated by *equation 2.4,* where the run time and the turnaround time (necessary period for the beam to restart and reach optimal conditions after the dump) are in the denominator:

$$L_{tot} = \frac{200\,(days) \times 24(hours)}{t_{run} + t_{turnaround}} L_{int} \qquad (2\text{-}4)$$

In practice, at the startup of LHC during 2010, only 45.0 pb^{-1} of integrated luminosity was collected while, the value for 2011 was 5.08 fb^{-1}. The bulk of the luminosity was recorded in 2012 with a value of 21.3 fb^{-1}, accounting for a total Run 1 integrated luminosity of 26.425 fb^{-1}, with 99 % of the data being used for physics analysis (*Figure 2.3*) [9]. During LHC Run 1, the collision energy was limited to 7 TeV for the first year (2011) and 8 TeV the following (2012), with a bunch spacing of 50 ns. This corresponds to twice the design values of 25 ns, foreseen for later runs.
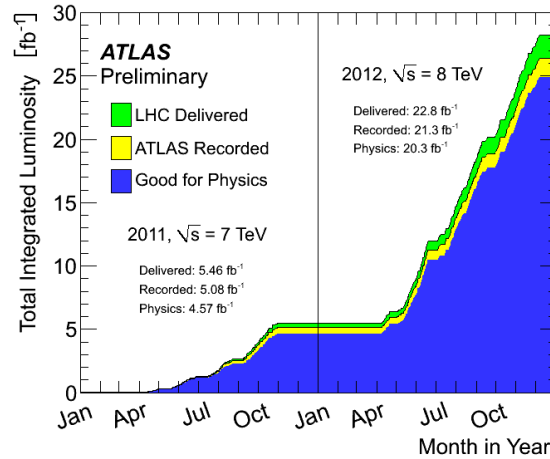
Figure 2.3: *Integrated delivered, measured and physics luminosity for the ATLAS detector during the two main years of LHC operation.*

2.1.4   Beam Crossing and Pile-Up

To obtain as many collisions as possible at the interaction points, the beams are squeezed to very small sizes. The beam squeezing parameter, known as β*, corresponds to a measure of the distance from the interaction point at which the beam has twice the size of that at the collision spot. The smaller the ß*, the stronger the squeezing and the more increased the interaction probability

becomes. β* at the ATLAS point was set at 1m at the beginning of Run 1, whereas latter values were largely improved, achieving a value of 0.6 m in 2012, extremely close to the design definition of 0.55 m. It has to be noted that, in contrast with the strong beam squeezing at the interaction points, an average value of 11 m is achieved at the arcs sections of the LHC [10]. Because of the repulsive coulomb forces from the space charge effect, the smaller the beam size at the interaction point, the faster the rise of the beta function (and thus the beam size) when fending off from it. In practice, the aperture of the beam line elements (e.g. focusing magnets) around the interaction point limits how small β* can be made.
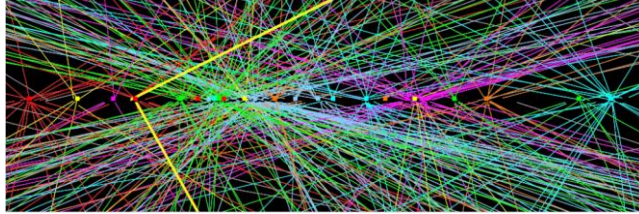
Figure 2.4: *An ATLAS Z→μμ event candidate with 22 reconstructed primary vertexes from LHC Run 1 at 7 TeV.*

Although a tighter beam at the interaction point and increased instantaneous luminosity favor physics data, they are also accompanied by an important downside; in general, more than one collision-per-bunch crossing can occur, making detector readout and event reconstruction complicated (*Figure 2.4*). When the readout of the detector includes information of more than one primary beam interaction, this is referred to as PileUp. These multiple interactions may either occur when several protons of the crossing bunches interact together (in-time) or when protons from crossing beams interact with remnants of previous collisions or even particles from preceding bunches (off-time).

The average number of interactions per crossing is defined as the μ value. The following figure (*Figure 2.5*) demonstrates the number of interactions during Run 1 where for the 7 TeV period a μ ≈ 7 was observed while for the 8 TeV, the average μ was ~ 25 with a maximum value of 70. In general, the expected number of per-event reconstructed primary vertexes is estimated to be 44 % of the μ value. Since up to ten colliding bunch pairs can contribute to a calorimetric signal because of its integration time (~ 600 ns long), challenging pile-up rejection techniques are applied.
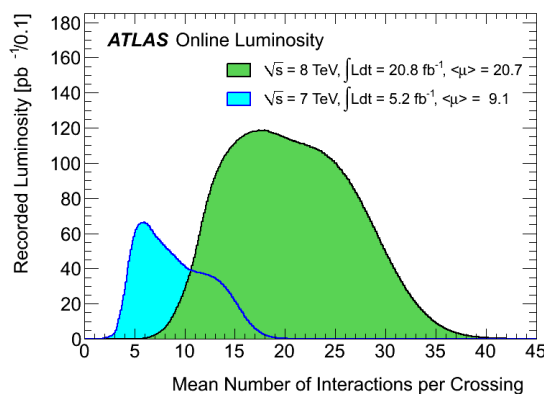
Figure 2.5: *Number of interactions per crossing during the 7 and 8TeV beams of Run 1.*

2.2   The ATLAS Detector

The ATLAS (A Toroidal LHC ApparatuS) detector is a general purpose experiment aiming at studying the Standard Model physics precisely. Specifically, this includes finding the Higgs boson,

exploring the electroweak symmetry breaking sector and searching for new physics. Constraints with respect to the design of the detector are imposed by the strong radiation and the high rate of expected events, especially during the second phase of the LHC. Devices and readout systems capable of copping with an elevated equivalent dose and provide stable operation are required, in addition to highly segmented detectors. The search for the Higgs boson was very demanding in terms of energy and momentum resolution and stability of the detector response.
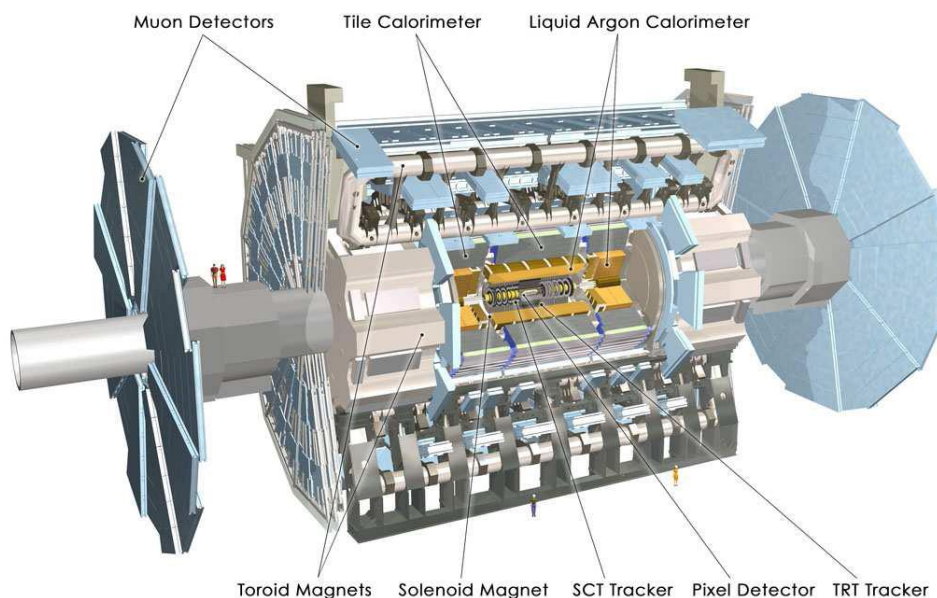
Figure 2.6: *General geometry of the ATLAS detector.*

The total assembly is a cylindrical geometry detector, 46 m in length and 22 m in height, having a total weight of 7000 tones. It is the largest experimental setup installed at CERN. *Figure 2.6* demonstrates the various subsystems of the experiment. The inner detector containing the pixel detector, the semiconductor tracker and the transition radiation tracker, is surrounded by a solenoid. The electromagnetic liquid argon calorimeter and hadron calorimeter are placed outside, followed by the muon spectrometer with a large toroid magnet [11].

2.2.1   Magnetic System

The ATLAS magnetic system is comprised of the central solenoid, providing the magnetic field for the inner detector, the barrel and end-cap toroid with no solid cores, responsible for the magnetic field at the muon chambers. The total size of the complete system is 26 m long by 20 m high and is the largest component of the ATLAS detector [12].

The central solenoid magnet consists of a single superconductive coil layer wrapped internally around a support cylinder. The 5.3 m long structure has an internal radius of 2.3 m and is hosted within the cryostat of the liquid argon calorimeter, at the inner side. The superconductive coil is organized in flat cables wrapped in a hardened aluminum alloy support and cooled to 4.5 K. The maximum magnetic field value is 2 T while it can peak to 2.6 T on the superconductor windings. Power requirements are satisfied by an independent 8kA supply unit while refrigeration is assured via a Dewars coupled to the refrigerator.

The barrel toroid magnet is situated after the calorimeters and is composed of eight superconductive coils equally distributed along the periphery of the inner cylindrical structure, running the entire length of the detector. The peak magnetic field is 3.9 T with an average value in the order of 0.5 -1 T. The inner system diameter is 9.4 m and the outer is 20.1 m, with a total length of 25.3 m.

Individual coils use a NbTi superconductor housed in aluminum casing to support the induced magnetic stress. An outer cryostat is then added which also serves as mechanical support of the complete coil. Finally, the eight coils are linked together via a final support structure around the detector center (*Figure 2.7*). Services to the individual coils are provided by a ring-shaped cryostat included in the final support structure, directly linked to the powering and refrigerating circuits.
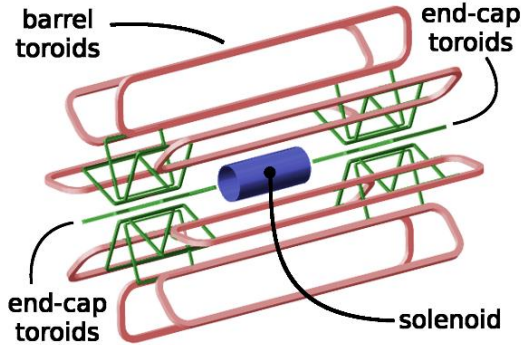
Figure 2.7: *Layout of the complete ATLAS magnetic system with all the support structures removed.*
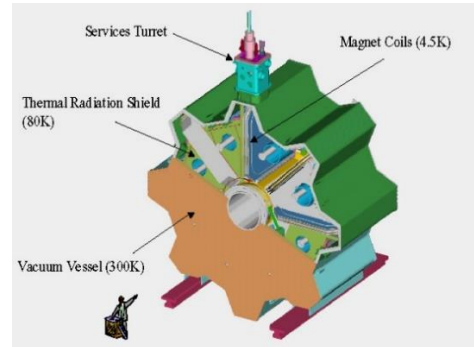
Figure 2.8: *Schematic view of the end-cap toroid assembly.*

The end-cap toroid is equally made of eight toroids placed at either end of the central barrel detector and rotated by an angle of 20.5 degrees along the z axis with respect to the central magnet assembly. The toroids are assembled radially and symmetrically with respect to the beam axis with an inner diameter of 1.65 m and an outer of 10.7 m. Total axial length of each of the two assemblies is 5 m and are placed inside each end of the central toroid. The magnetic field value is 4.1 T while the same NbTi superconductor is used as for the barrel system [13]. A common cryostat, reinforced with perpendicular rods to sustain the magnetic forces, is used for all height coils which serves as the vacuum vessel and thermal radiation shield (*Figure 2.8*). Services are provided through a turret at the highest point of the cryostat while powering in each side is independently assured by a serial circuit.

2.2.2   Inner Detector

The inner detector is the first element located immediately around the beam tube. It is a tracker designed to effectively reconstruct charge, particle momentum and direction with a fine resolution over a wide dynamic range. Good resolution vertex is also required to identify the primary and secondary vertex which appear for instance in the case of B mesons [14]. Housed in a 3.5 m long and 1.2 m radius cylinder, within the 2 T solenoid magnet, it is composed of three subsystems made with different and complementary targets. Each system is composed of a central portion (the barrel) and two end-cap regions (one on each side of the barrel), as shown in *Figure 2.9*.

2.2.2.1 *The Pixel detector*

The pixel detector provides an accurate measurement of charged particles near the interaction point providing an eta coverage of $|\eta| < 2.5$ with a transverse momentum (P_T) resolution of less than 30 % for a 500 GeV particle. A 90% track reconstruction efficiency is attained for particles with $P_T \sim 5$ GeV while, in the range of $P_T \sim 100$ Gev, a transverse momentum resolution ($\sigma[P_T]/P_T$) of 5% is achieved for charged particles reconstruction. The pixel detector not only provides an accurate position of primary vertex with a 110 μm resolution in the z direction (along the beam axis) and 12 μm in azimuth (rφ) [15] and is essential for jet flavor tagging and level 2 triggering (*Figure 2.10*).

Three pixel layers of cylindrical shape are installed in the central region ($|\eta| < 1.37$), radially symmetrical to the beam axis, at radii of 50.5, 88.5 and 122.5 mm respectively. The inner most pixel layer, called the b-physics layer, as well as the second layer extend up to z = 350.4 mm from the

center of the detector in both z-directions, while the third layer extends up to 414.2 mm. Three end-cap pixel disks are placed at each side at z-distances of 499 mm, 554 mm and 799 mm with respect to the detector center. All discs are identical with an inner radius of 115 mm and an outer of 212 mm [16]. Total length of the entire detector is 1.6 m, providing a three hit system for particles within $|\eta| < 2.5$.
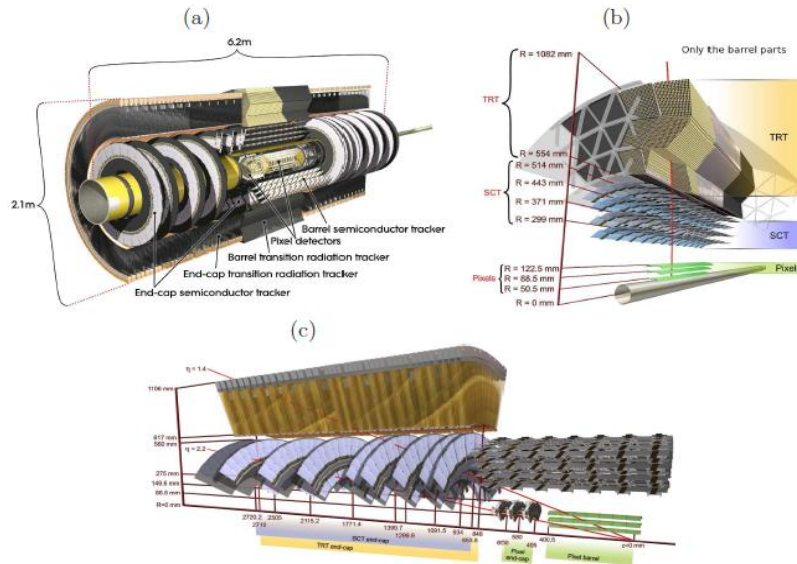
Figure 2.9 : *The ATLAS inner detector with its three distinct stations.*

The basic building unit of the pixel detector is a module. A module is comprised of 8 double pixel sensor matrixes directly coupled to 16 readout Front End chips (designated FE-I3). Pixel are defined as 50 μ × 400 μm rectangular shaped diodes, with the larger dimension oriented along the beam axis. The sensors were fabricated with the n$^+$ technology on an n-substrate, such as after irradiation, a type inversion will occur. The introduced defects are primarily of p-type, transforming the sensor for n-in-n to p-in-n, while the junction will be moved from the back-side to the front, keeping the matrix operational [17]. One sensor matrix consists of 18×160 individual pixels interconnected to the readout FE using individual bump bonds in a pixel level [15]. The entire assembly of the 8 double pixel matrixes with the 16 readout chips is then placed at a copper polyamide flex, equipped with a multiplexer and control chip. Connection to the FE integrated circuits is assured through wire bonds while a moral flex cable is attached at the center of the hybrid board providing services and high voltage (*Figure 2.11*).
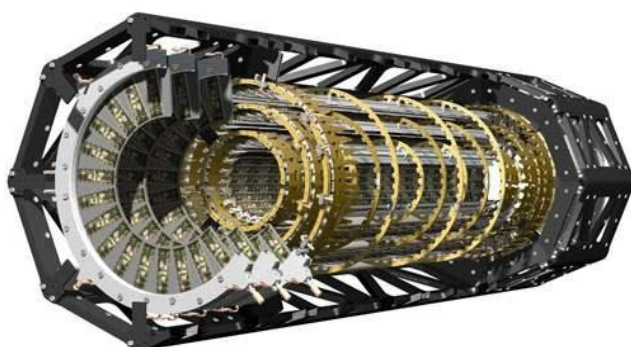
Figure 2.10: *Schematics of the ATLAS pixel detector with the central and end cap regions visible and support frames.*
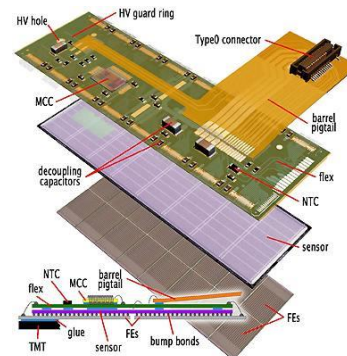
Figure 2.11: *ATLAS pixel module assembly. Pixel sensors are placed between the flex and the read-out chips connected to the flex board.*

All modules of the pixel detector are identical. In the barrel region, they are placed in an overlapping arrangement so that the dead regions at the edge of one module overlap with the active region of the next, using a slight inclination angle of 14 degrees. A turbofan arrangement is used for the end caps, maintaining the same inclination angle in a circular geometry. Approximately a total of 80 million pixels are used corresponding to 1744 modules of 10 cm^2 surface each and a total of 46,080 readout channels. End-cap disks account for 13 million pixels using 1,456 modules in the three disks of each side. The pixel detector covers a surface of 1.7 m^2 and is maintained at a constant temperature of -15 ^{0}C by evaporative C_3F_8 based bi-phase cooling, to reduce excessive leakage current caused by the irradiation, while 15 kW powering is provided [17].

2.2.2.2 The SemiConductor Tracker (SCT)

The ATLAS SemiConductor Tracker (SCT) is located after the pixel detector. It is composed of silicon strip sensors arranged in eight layers in the central region, which produce up to four specific points in 2-D space by charged particles. The end-cap assembly is composed of eighteen discs, with silicon strips extending radially at a distance varying from 80 to 280 cm from the interaction point (z = 0). Each module consists of two slightly inclined detectors at 40 mrad for measuring the z position. In total 4088 modules are used, representing a surface are of 63 m^2 for the SCT with approximately 6.3 million readout channels.

The strip tracker occupies the radial region extending from 30 to 52 cm around the beam pipe and extends to a total length of 2.7 m in each side of the central point along the z-axis, providing the same eta coverage as the pixel detector. The design requirements include a strip efficiency greater than 99 % and an occupancy of less than 5×10^{-4} per read out [18]. With a resolution of 580 μm in the z direction and 17 μm in the azimuthal (rφ) plane, it complements trajectory information provided by the inner pixel layers. An evaporative cooling system [19] of C_3F_8 is used with a normal operating point of -25 ºC, while temperatures at the silicon surface are in the order of -2 ºC.

2.2.2.3 The Transition Radiation Tracker (TRT)

The ATLAS Transition Radiation Tracker (TRT) is the final element of the inner detector and is placed after the SCT at a radial distance between 0.75 cm < r < 202 cm from the interaction point and a total length of 6.8 m [20]. Its goal is to provide continuous tracking up to high distances from the interaction point, enhancing particle identification through transition radiation effect and to offer fast information to the level 2 trigger system. It is a drift tube system consisting of 370 thousand cylindrical, 4mm diameter tubes that run along the entire length of the barrel region. It is also used to discriminate the electron from heavier charged particles, such as $\pi^{\pm}$. Each tube is made of kapton with an internal conductive coating, while a 30 μm diameter gold plated tungsten wire runs along the center of the structure. The outer region is kept in a negative high voltage active as a cathode and a mixture of 70 % xenon, 20 % methane and 10 % CO_2 is used as ionization gas. After the ionization of the gas by the passage of a charged particle, electrons are collected via the central wire at both ends of the tube providing timing information.

Tubes are interleaved with layers of radiators (polypropylene foils or fibers) [21]. The central portion consists of three layers of straw-tubes, 150 cm long, while the two end-caps are made of the eighteen wheels containing straw-tubes of lengths from 39 to 55 cm, radially oriented. TRT coverage allows trajectory reconstruction of up to |η| ~ 2.1, while a total of 351,000 readout channels are used.

2.2.3   Calorimeters

The role of a calorimeter in a generic particle physics detector is the energy measurement of the particles. Depending on their design, calorimeters can also provide information on the direction of the particles and can contribute on missing transverse energy measurement. Because of the high expected occupancy, fine segmentation and increased granularity are required in both the time and

spatial dimensions. Constraints are also imposed with respect to radiation hardness as well as pile-up robustness, especially in a high-frequency collision environment.

The ATLAS electromagnetic calorimeter (EM), located after the inner detector, is used to measure energy of photons and electrons in a wide dynamic range of energy (several MeV to 2 - 3 TeV). The hadron calorimeter, which follows the EM Calorimneter, measures the energy and direction of jets from quarks and gluons. Both calorimeters are separated in a central region covering $|\eta| < 1.5$, and two end-caps corresponding to the region of pseudorapidity ranging from $|\eta| > 1.5$ to $|\eta| < 3.2$. Finally, dedicated calorimeters are used in the forward $(3.1 \leq |\eta| \leq 4.9)$ regions to ensure complete calorimetric coverage up to $|\eta| < 5$ (*Figure 2.12*).
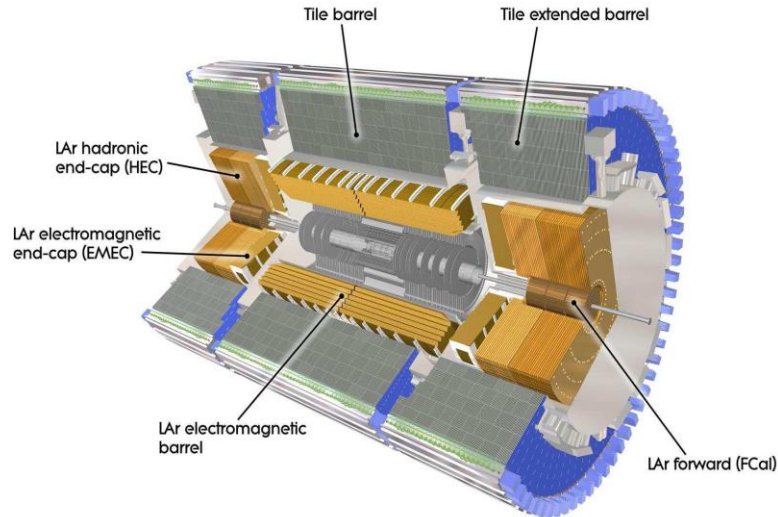
Figure 2.12: *Structure of the ATLAS calorimeter with the different calorimetric stations.*

2.2.3.1   *Liquid Argon Electromagnetic Calorimeter (LAr)*

The ATLAS electromagnetic calorimeter is a sampling calorimeter, consisting of alternating lead absorbers with liquid argon (LAr). An electrode is placed in the space between the two absorbers to collect the ionization signal. Absorbers are accordion shaped, following the detector radius to ensure hermiticity of the calorimeter. The detector consists of two parts, a central barrel region and two end-caps, using different cryostats to ensure a stable LAr temperature of 88.5 K. The barrel portion ($|\eta| < 1.37$) consists of two symmetrical pieces in the z-direction, having an inner radius $R_{in} = 1.15$ m and outer $R_{out} = 2.25$ m respectively. Each half-cylinder of the barrel portion consists of 16 azimuth modules (size $2\pi / 16$), containing 64 absorbers of 3.2 m in length (*Figure 2.13*). The end-caps are wheel-shaped, 63 cm thick assemblies, covering a rapidity area of $1.475 < |\eta| < 3.2$ with an inner and outer radii of $R_{in} = 30$ cm and $R_{out} = 2.1$ m respectively. Each wheel is in fact composed of an inner and an outer section, perpendicularly divided into $\eta = 2.5$ with a gap size, d, between the electrodes varying from d = 2.2 mm to d = 1.7 mm, respectively [22].

This two part architecture introduces a discontinuity at the calorimeter at $|\eta| = 1.5$, where the barrel meets the two end-caps. In the central region, particles having a high incident eta value are confronted with a higher material budget. In order to compensate this effect, thinner absorbers were used in $|\eta| > 0.8$ regions.

Particle identification is possible by studying shower characteristics, lateral dimensions and longitudinal dimensions and isolation. To allow for a precise particle identification, in the radial direction, the calorimeter is divided into four regions (*Figure 2.14*):

1. The pre-sampler, placed in front of the calorimetric volume, corrects for energy losses while traversing passive materials situated before the calorimeter, such as cryostats, or structural components. It is independent of other detector sections, covers a region up to $|\eta| < 1.8$ and has a coarse granularity.
2. The finely segmented first sampling region allows for the separation of close showers, as in the case of two photons originating from a π^0 decay. In this way, an efficient photon – π^0 separation is achieved.
3. The second layer has a much coarser segmentation and covers the biggest part of the calorimeter's radial volume. It is in this layer that electromagnetic particles deposit most of their energy.
4. The fourth layer allows to estimate the energy loss at the end of the electromagnetic shower.
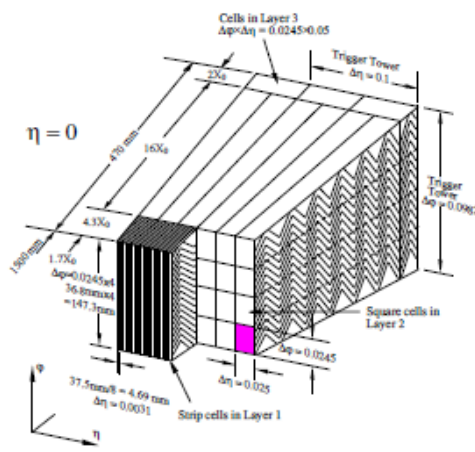
Figure 2.13: *Electromagnetic calorimeter module.*
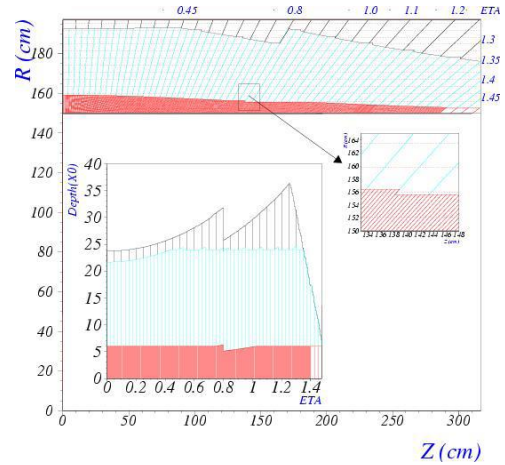
Figure 2.14: *Granularity and depth of the three sampling regions.*

Layer segmentation varies with respect to the η position of each cell as shown in (*Table 2-1*).

The Energy resolution of the calorimeter can be expressed as (*equation 2.5*):

$$\frac{\Delta E}{E} = \frac{\alpha}{\sqrt{E}} \oplus \frac{b}{E} \oplus c \qquad (2\text{-}5)$$

where **α** is the sampling or stochastic term, connected to the calorimeter structure. It originates from fluctuations of the physical processes involved in the charge generation of the deposited energy in the calorimeter and of the shower development. In the Liquid Argon Calorimeter of ATLAS, the sampling term is ~ 10% while, its dimensions are expressed in √GeV.

b is the energy independent noise term, taking into account electronic treatment noise as well as pile-up effects. It can be estimated at 0.3 GeV.

c represents the constant term taking into account the global non-uniformity of the detector as well as short distance inhomogeneity effects. It was measured at 0.007 and becomes the dominant term in high energy conditions (> 100 GeV).

An angular resolution of 50 - 60 mrad/√E (GeV) can be obtained by taking advantage of the high granularity of the different layers, while optimal time resolution in the electromagnetic calorimeter is in the order of 100 ps. In the end-cap region ($3.1 < |\eta| < 4$) the Forward Calorimeter is installed (FCal), consisting of cylindrical copper electrodes oriented in parallel with the beam axis, while a 250 μm spacing is implemented. Liquid argon is introduced within the electrode gaps which is subsequently ionized by conversion photons. Generated primary electrons drift towards the readout electrodes at the outer end of the cylinder where the signal is collected.

Calorimeter region	$|\eta|$ region			
	$0 < |\eta| < 1.8$	$1.8 < |\eta| < 2.0$	$2.0 < |\eta| < 2.5$	$2.5 < |\eta| < 3.2$
Pre-sampler	0.025×0.1			
1st Layer	0.0031×0.1	0.004×0.1	0.006×0.1	0.1×0.1
2nd Layer	0.025×0.025			0.1×0.1
3rd Layer	0.050×0.025			

Table 2-1: *$\eta \times \varphi$ granularity of the various compartments of the electromagnetic calorimeter.*

The current generated by a particle in the calorimeter is translated to energy following test beam studies and signal pulse calibrations. An initial adjustment of the energy scale was performed at the beginning of Run 1, based on test beam results. The final energy scale is set by investigating the position of the reconstructed Z mass peak using Z→e⁺e⁻ decays. During Run 1, a huge work has been driven to control the energy scale and the related systematics to an unprecedented level [23]. This work allowed the achievement of a calibration accurate to 0.05 % in most of the detector acceptance, rising to 0.2 % in regions with large amounts of passive material above 500 GeV (*Figure 2.15*). In parallel, the amount of material budget in the front region of the calorimeter was precisely defined and consequently detector simulation was updated. *Figure 2.15* presents the data-MC comparison of Z mass reconstructed in e+e- decays, after applying the calibration constants.
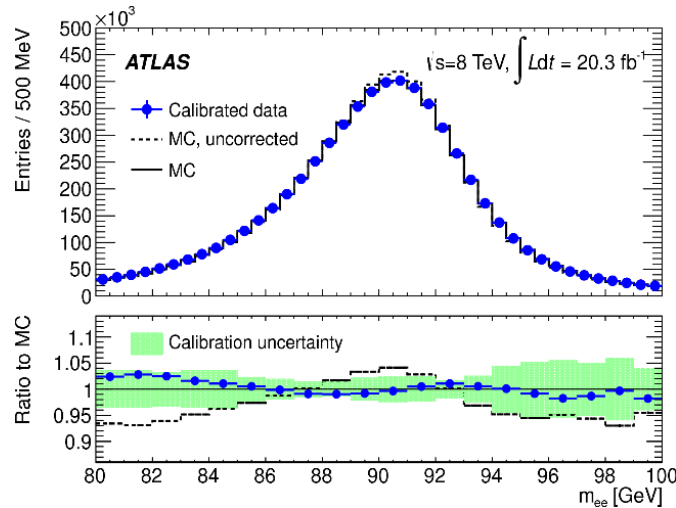
Figure 2.15: *Top: electron pair invariant mass distribution for Z→ ee decays in data and improved simulation. Energy scale corrections are applied to the data. The improved simulation is shown before and after energy resolution corrections, and is normalized to the number of events in data. Bottom: ratio of the data and uncorrected MC distributions to the corrected MC distribution with the calibration uncertainty band [22].*

2.2.3.2   *Tile hadronic Calorimeter*

The hadronic calorimeter (*Figure 2.16*) is situated outside and around the Liquid Argon Electromagnetic Calorimeter. The detector is divided into three distinct sections using different technologies. The barrel section, which covers the central part ($|\eta| < 1.6$) and consists of three interlocking cylindrical pieces, one covering the rapidity region of $|\eta| < 0.7$ and two on the extremities for the regions of $0.8 < |\eta| < 1.6$, uses an alternation of steel absorber with scintillating fibers. The Hadronic End Cap calorimeter (HEC), covering the regions of $0.5 < |\eta| < 3.2$, uses liquid argon alternating with cooper absorbers for increased radiation hardness. Finally, for the last section, the Forward Calorimeter (FCal) covering $3.1 < |\eta| < 4.9$, a similar technology as in the electromagnetic end-cap calorimeter is used with tungsten as the absorbing medium alternated with liquid argon [24]. The

hadronic calorimeter measures jet energy and is responsible for the identification of gluon and quark experimental signatures.

The barrel part is a sampling calorimeter composed of steel absorber interchanged with scintillating tile modules as an active medium. Scintillating photons are extracted at each extremity of the module using wavelength shifting optical fibers (*Figure 2.17*). Photomultiplier response time is in the order of 23.5 nsec, which allows precise identification of the collision from which the observed hadrons originate. Beam tests associating hadronic and electromagnetic calorimeter demonstrated that pion energy resolution can be parameterized by the same equation used for the electromagnetic energy resolution (*equation 2-5*), with a sampling term of (52.0±1.0) %, a noise term of 1.6 GeV±0.1 % and a constant term of about (3.0±0.1) %.

The end-cap region calorimeter (HEC) is a sampling liquid argon and copper calorimeter over the range of $1.5 < |\eta| < 3.2$. The HEC is comprised of an inner wheel made of 25 copper absorbers 25 mm thick, separated by a liquid argon gap of 8.5 mm, and an outer wheel, made up of 17 copper absorbers doubling the gap between them. The corresponding sampling term was identified by beam tests to be 56 % while the constant term is in the order of 2 %.

Small angle Calorimeters or Forward Calorimeters (FCALs) are relatively far from the interaction point (4.7 m) and cover a wide rapidity range $3.1 < |\eta| < 4.9$. They are composed of three different modules, commonly using liquid argon as active material while absorbers and electrode spacing differ for each module between tungsten and copper. Combined beam test of the hadronic and electromagnetic forward calorimeters determined the sampling term at (94.2±1.6) % and the constant part at (7.5±0.4) %.
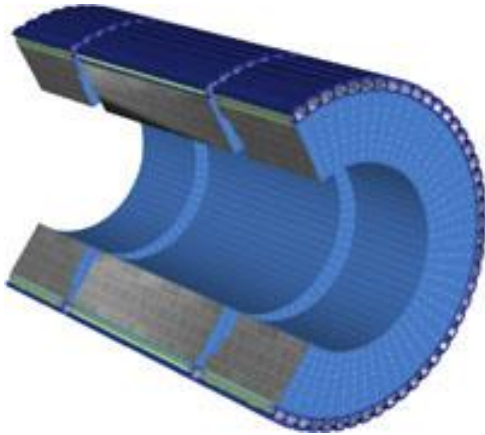
Figure 2.16: *Structure of the central region of the ATLAS hadronic calorimeter.*
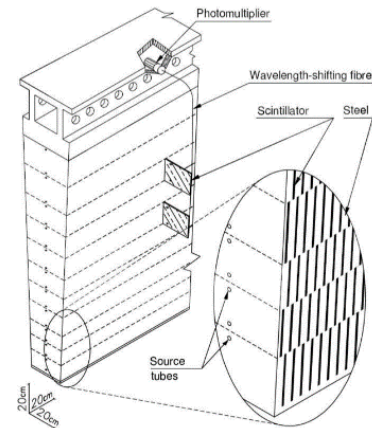
Figure 2.17: *Structure of a single tile module of the central region.*

2.2.4   Muon Spectrometer

The muon chambers (*Figure 2.18*) and the superconducting coils constitute the outer part of the ATLAS detector and contribute to its impressive size. The spectrometer was constructed with the aim of producing an accurate measurement of muon momentum in a wide dynamic range. Muon trajectories are curved while crossing the 2 T toroid magnetic field delivered by the outer coils while traversing the detectors. The system's geometry includes a cylinder at the central part and two end-caps for the forward regions while two types of chambers are used: precision chambers optimized for accurate position resolution and trigger chambers for fast event triggering.

Precision chambers are placed between the eight toroid magnet rings in the barrel and behind the two magnet end-caps. They allow a precise determination of muon momentum by measuring the

curvature of the corresponding track inside the magnetic field. In the central region, chambers are radially installed in two layers of inner radius r = 5.75 m and 10 m with respect to the beam axis while, two wheels are used for the end caps, placed at 7 m and 22 m from the interaction point in each side. Each muon chamber is divided into two areas with overlapping lateral extensions used for relative alignment of adjacent sectors and dead space minimization. In order to account for the large rate variation with respect to η position, two kinds of detectors are used. Monitored Drift Tubes are used in the central region, where low rates are expected, orientated orthogonally to the magnetic lines. At the forward region, $2.0 < |\eta| < 2.7$, Cathode Strip Chambers (CSC) are installed, which are multi-wire proportional chambers with segmented cathodes, allowing position determination.
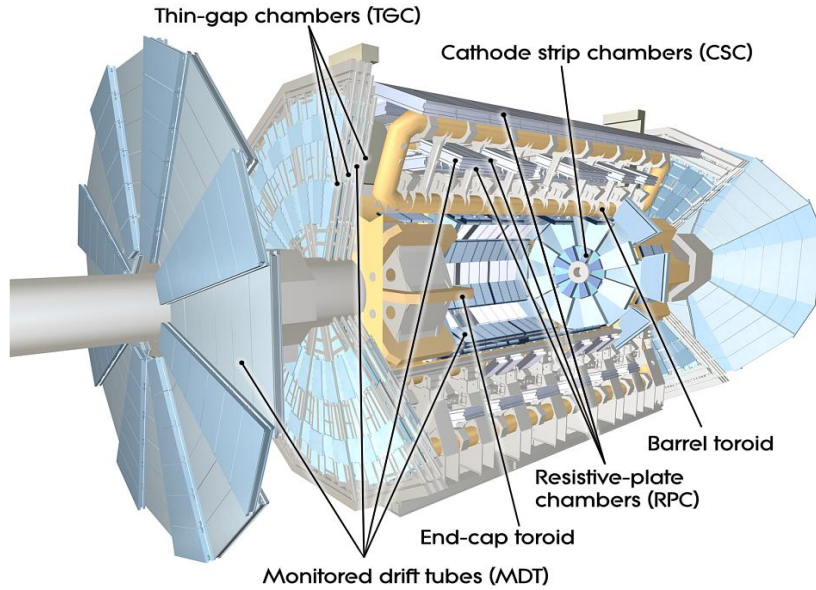
Figure 2.18: Structure of the ATLAS muon spectrometer.

For $|\eta| < 1.4$, trajectory deviation is achieved by the central toroid, in the $1.6 < |\eta| < 2.7$ region, the end-cap toroids provide the required magnetic field while, for the intermediate region of $1.4 < |\eta| < 1.6$, combination of the two fields create a more complex geometry. Triggering chambers have to be capable of discriminating rapidly on muon transverse momentum, measure non-curved quantities in conjunction with Muon Drift Tube (MDT) detector information and be resistive with respect to the random flux of neutrons and photons in the cavern. In the high pseudorapidity region $1.05 < |\eta| < 2.4$ Thin Gap Chambers are used while for the central region Resistive Plate chambers have been installed.

Muon momentum resolution in the ATLAS detector heavily depends on the incoming particles' η, φ and transverse momentum [25]. When using information provided only from the muon spectrometer, the P_T dependence of the muon momentum resolution can be parameterized to a good approximation as the quadratic sum of three terms in the following way (*equation 2-6*):

$$\frac{\sigma_{SA(P_T)}}{P_T} = a_{MS}(\eta, \varphi) \oplus b_{MS}(\eta, \varphi) \cdot P_T \oplus \frac{c(\eta, \varphi)}{P_T} \qquad \text{(2-6)}$$

The first term parameterizes multiple scattering effects, whilst the second the Muon Spectrometer intrinsic momentum resolution. The final term corresponds to the effect of muon energy loss fluctuations in the calorimeters. This final contribution is small for the momentum range of interest and the corresponding term is fixed by MC simulation.

In order to evaluate high energy muon momentum resolution, a special dataset was used with no toroidal magnetic field in the muon spectrometer region. In that way, the low curvature of energetic tracks was emulated to estimate a $b_{MS}(\eta, \varphi)$ value of~ 0.2 TeV^{-1} in the barrel and the MDT end-cap region (excluding the transition region) and ~ 0.4 TeV^{-1} in the CSC end-cap region. The estimated accuracy was in the order of 10 %, while the special dataset allowed for an improved alignment of the muon chambers, leading to a final values of $b_{MS}(\eta, \varphi) \leq 0.2$ TeV^{-1} for all regions in 2011 [26].
.

The dimuon invariant mass resolution from $Z \rightarrow \mu^+\mu^-$ decays as a function of pseudorapidity intervals is presented in *Figure 2-19 middle*. Both muons are required to be within the same interval, while the resolution corresponds to the width of the Gaussian, which when convoluted with generator level dimuon invariant mass distribution, reproduces the invariant mass distribution observed in data. Due to the form of the toroidal magnetic field the resulting resolution of the di-muon mass is expected to be independent of the η of the decay muons. Exceptions are observed in the magnet transition region ($1.05 < |\eta| < 1.7$), where the field is highly non-uniform [25], as well as in the region $1.05 < |\eta| < 1.3$ where several chambers are not installed. This translates to a measurement relying in only two layers of chambers, explaining for the observed degradation.

Figure 2-19 middle also demonstrates that Muon Spectrometer derived dimuon invariant mass resolution is consistently worse in data than in simulation (typically between 30% and 50%, depending on η region). Two sources for this effect can be identified.

1. Asymmetry of the magnetic field: in the MC simulation, a perfectly aligned detector is assumed. In reality, the two end-cap toroid systems are not symmetric with respect to the plane orthogonal to the major axis of the ID, and situated at the center of the detector. This small asymmetry translates into an asymmetry of the magnetic field integrals, in particular in the transition regions.
2. Residual misalignment of the muon chambers: even after the MS alignment procedures are applied, residual misalignments remain, which limit the attainable momentum resolution.

An alternative for muon momentum measurement is the use of information provided by the inner detector. Contrary to the Muon Spectrometer case, the relative momentum resolution can be parameterized as the quadratic sum of two terms [27], one corresponding to multiple scattering effects and a secondary describing the intrinsic resolution of the detector (*equations 2-7 and 2-8*):

$$\frac{\sigma_{ID(P_T)}}{P_T} = a_{ID}(\eta) \oplus b_{ID}(\eta) \cdot P_T \quad \text{for } 0 < |\eta| < 2.0 \qquad \textbf{(2-7)}$$

$$\frac{\sigma_{ID(P_T)}}{P_T} = a_{ID}(\eta) \oplus \frac{b_{ID}(\eta) \cdot P_T}{\tan^2(\theta)} \quad \text{for } 0 < |\eta| < 2. \qquad \textbf{(2-8)}$$

Intrinsic resolution effects are mainly due to the imperfect knowledge of the magnetic field in the Inner Detector as well as due to misalignment and resolution of individual detector components. For the region of $|\eta| > 2.0$, the best parameterization of the second term is given by $b_{ID}(\eta) \cdot P_T/\tan^2(\theta)$, while measurements of the material distribution in the Inner Detector contain $a_{ID}(\eta)$ parameter to values that agree with MC simulation to within 5% in the barrel and 10% in the end-caps. [28, 29].

The Inner Detector dimuon invariant mass resolution (*Figure 2.19 left*) is best in the barrel, where it is about 2 GeV, is better than 3 GeV for $|\eta| < 2.0$ and degrades to about 6 GeV for $2.0 < |\eta| < 2.5$. The degradation of the mass resolution with increasing $|\eta|$ is primarily caused by a lower field integral per track in that region. The fact that the di-muon invariant mass resolution measured in experimental data is worse than predicted (typically by about 30 %), is attributed to residual in thermal misalignments of the ID.

A third option is the combination of both Inner Detector and Muon Spectrometer information for a more accurate measurement. The resulting di-muon invariant mass resolution obtained profits from the complementary momentum measurements of the ID and MS. An invariant mass resolution between 1.4 GeV and 2.5 GeV is achieved, with little η dependence (*Figure 2.19 right*).
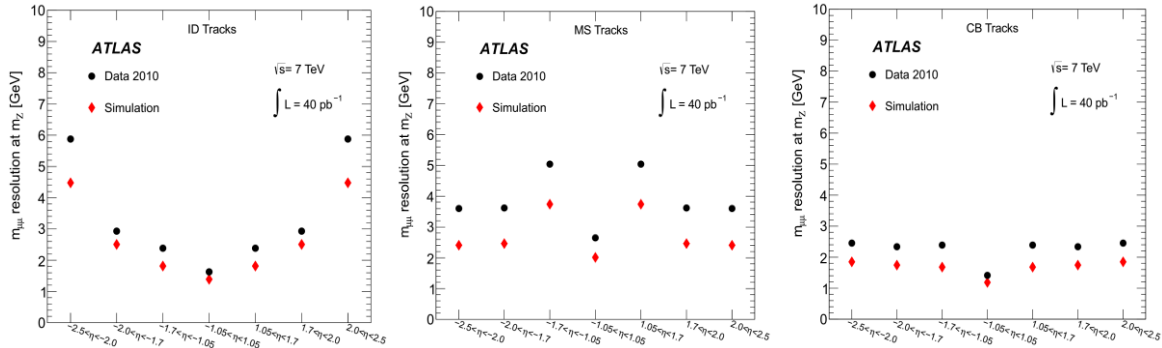
Figure 2.19: *Dimuon invariant mass ($m_{\mu\mu}$) resolutions for Z → μ⁺μ⁻ decays in the data and in the MC as a function of η region with both decay muons in the same η region, using information from inner detector only (left hand), Muon Spectrometer only (center) and combining both (right). Simulations assumes a perfect t alignment of the ATLAS detector.*

2.3   Event Trigger and reconstruction

In normal LHC conditions, a 40 MHz collision rate is maintained with 25 nsec spacing, accounting for 10^9 events per second. Only a very small fraction of occurring events are of interest in the rare physics searches and in studies of properties of existing particles. Given the total amount of available channels (10^8 for the inner detector, 10^5 for the calorimeters and 10^6 for the muon chambers) it is practically impossible to extract all available data from the detector at a 25 nsec rate. Signal propagations around the detector alone would require several microseconds and an efficient reduction scheme is necessary. The trigger system is in charge of reducing the produced data rate to manageable quantities while maintaining events with interesting information for physics analysis. Once an event has been stored, information from different detector subsystems are combined to form a complete picture, a snapshot of the event. The energy, trajectory and momentum of each particle is calculated and traced back to its vertex of origin. Off-line reconstruction algorithms use events saved after satisfying trigger requirements to provide useful physical quantities and identify particles that can be used from the various physics analyses.

2.3.1   Event Triggering

The ATLAS trigger system is a three stage implementation, using custom electronics to select events (snapshots of the detector) for final recording at a rate of approximately 300 Hz [30]. The first stage, Level 1 (L1) trigger, reduces the 40 MHz initial rate to less than 75 kHz. Signals from subsections of the calorimeter and the muon chambers are primarily used while event information is stored in pipelines pending the L1 trigger decision. When an event is accepted by L1, data on the detector are transferred to dedicated read-out buffers and are made available to the High Level Trigger processing farms for further analysis. The Layer 2 (L2) trigger is based on fast custom algorithms which focuses on processing partial event data within a Region of Interest (RoI) provided by the initial L1 decision. L2 achieves a final rate of 3 kHz with 40 ms/events processing time. The final trigger stage is mostly based on off-line algorithms using advanced calibrations to reconstruct data with an increased precision with respect to L2. The final output rate is ~ 200 Hz with a 4 s/event processing time.

The Level 1 trigger decision is formed by the Central Trigger Processor (CTP), receiving data from the calorimetric regions referred to as trigger towers, the muon chambers and several other subsystems like the forward detectors, the fast Cherenkov detectors and scintillators. A total of 160 inputs are considered by the CTP which forms 256 distinct trigger decisions. After an individual pre-scaling of each of the obtained results, if one is accepted, a single bit is issued and distributed across all detector systems. Meanwhile, a dead time is introduced by the CTP by vetoing subsequent triggers, for overflow protection of the event buffer, until the data are cleared and transferred to the Level 2 processing farms. For most of the events a simple dead time of 125 nsec was set following a Level 1 trigger while a most complex dead time allowing 8 triggers in 80 μsec: This amount is adjusted using rate calculations prior to any triggering while individual electronic systems may also send busy flags to the CTP [31].
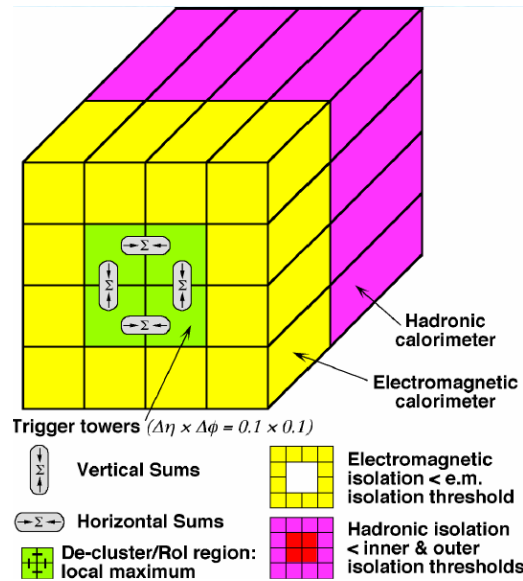
Figure 2.20: *A calorimetric trigger tower with the region of interest in the electromagnetic and hadronic part.*

Calorimetric towers (*Figure 2.20*) are analog sums of specific calorimeter cells in a $\Delta\eta \times \Delta\varphi = 0.1 \times 0.1$ region which are subsequently digitized and sent to the CTP [32]. The algorithms are looking for a specific set of energy deposit clusters which are higher than the set threshold. For electron and photon triggering, electromagnetic clusters are formed by the L1 trigger by summing trigger towers in a 2×2 region at the electromagnetic calorimeter (equivalent to $\Delta\eta \times \Delta\varphi = 0.2 \times 0.2$). The clusters' transverse energy (E_T) is calculated and compared to a programmable threshold while additional requirements are applied for lateral and longitudinal isolation. In a similar manner, tower clusters are constructed, combining information from the electromagnetic and hadronic sections in a 2×2 region. These can use a 4x4, 6x6 or 8x8 window in the $|\eta| < 3.2$, while for the forward part more options are available. In order to remove fake signals and to optimize noise rejection, trigger towers are calibrated to 1.2 GeV minimum E_T threshold, while timing has been synchronized to the global LHC clock with a 2 ns precision.

The High Level Trigger (HLT) corresponds to layer two and three of the trigger system and is composed of farms of commodity processors running specialized algorithms at 2.4 Ghz. Upon a favorable trigger one decision, data are transferred to dedicated detector readout buffers pending the Level 2 outcome. Level 2 algorithms only transfer data from the buffers corresponding to the detector elements within the region of interest provided by Level 1 trigger [33]. Only 2 – 6 % of the event data are used at a level two decision. The L2 provides a sufficient event rejection to reduce the rate to 3 kHz at 40 ms/event processing time. Upon a positive L2 decision, the event builder, assembles data from all readout buffers and provides them to the final trigger level. This will further reduce the

rate to 200 Hz with an average processing time of 0.4 s/event and an event size of 1.2 Mb. Final output rate is limited by the storing speed of off-line commuter resources.

2.3.2   Electron - Photon reconstruction and identification

Analog calorimetric signals from individual cells are initially digitized and preprocessed to calculate deposited energy, while noise and PileUp filtering is applied. Computed energies are subsequently corrected for localized defects and forwarded to the reconstruction algorithm. The initial step of the reconstruction is the formation of cell clusters using the sliding window algorithm. For both electromagnetic and combined objects (objects including information on the hadronic and electromagnetic calorimeter), the calorimeter surface in the $\eta \times \varphi$ space is divided into elementary cells of $\Delta\eta \times \Delta\varphi$ dimensions [34]. While φ boundaries are the same for combined and electromagnetic objects and include the entire detector, $|\eta|$ coverage is limited to 2.5 for EM objects and extended up to 5 for combined. Inside a single element, the energy of all longitudinal calorimetric cells is summed to what is defined as the tower energy. In case a cell is considered in more than one of the elementary $\Delta\eta \times \Delta\varphi$ regions, its energy is divided with respect to the cell area that covers each element.

Once the towers have been defined, a window of fixed dimensions containing five elementary cells in each direction, is seeded across the entire $\eta \times \varphi$ grid. If the transverse energy of the towers within the window exceeds a certain threshold or a local maximum is observed, an initial cluster is formed. To calculate the position of this pre-cluster, the energy barycenter of the $\eta \times \varphi$ cells enclosed within a smaller window (3×3 cells in each direction) around the maxima is calculated. This smaller window used for position determination makes the procedure less sensitive to noise fluctuations. Once the initial position has been defined, cells are assigned to this pre-cluster by considering all elements within the window dimensions in the different layers of the calorimeter. Since layer segmentation is different in each layer, the central position is recalculated for the strips layer, the presampler and the back of the calorimeter [35]. The total size of the cluster is optimized in order to include enough cells to account for the entire energy of the particle while reducing the number of noise. Electrons in the barrel have a longitudinally more extensive expansion with respect to photons.
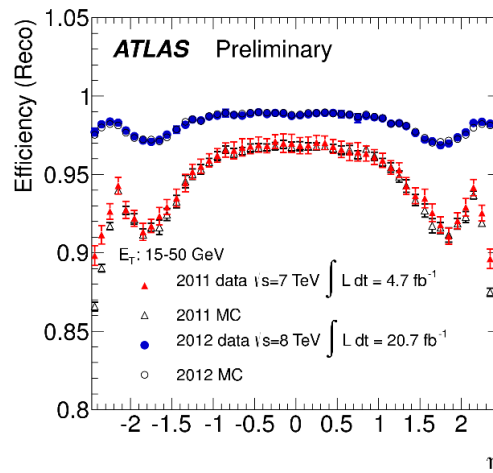
Figure 2.21: *Measured reconstruction efficiencies as a function of η for 15 GeV < E_T < 50 GeV for the 2011 (triangles) and the 2012 (circles) datasets.*

Electron candidates are reconstructed by combining information from the calorimetric clusters and the inner detector [36]. A suitable object is required to have a track with PT>0.5GeV in the inner detector, situated within a $\Delta\eta \times \Delta\varphi$ window of 0.05×0.10 with respect to the center of the corresponding cluster [37]. Selected candidates are subsequently submitted to an identification process to ensure uniform efficiency and rejection of background electrons from photon conversions and fake

QCD jets. For $|\eta| > 2.5$, where no tracker is implemented, a different identification process is used. The introduction of the Gaussian filter Sum algorithm in 2012, widening the area used to seek the track of the electrons, accounts for deflections due to multiple scattering and Bremsstrahlung which can significantly alter the curvature of the track within the magnetic field in the case of high radiative losses. Combined with an improved track pairing algorithm, this allowed for a significant increase of electron reconstruction efficiency with respect to 2011, especially at low E_T (*Figure 2.21*). After reconstruction, the resulting collection of electron candidates is highly polluted by jets. A series of identification criteria, based on shower dimensions in the calorimeter and track quality, are applied, offering various levels of electron efficiency and background rejection. In 2012 a likelihood method has been also used in parallel with cut-based criteria. The following figures present obtained efficiencies for the various identifications of the cut based (*Figure 2.22*) and two likelihood (*Figure 2.23*) menus with respect to electron E_T.
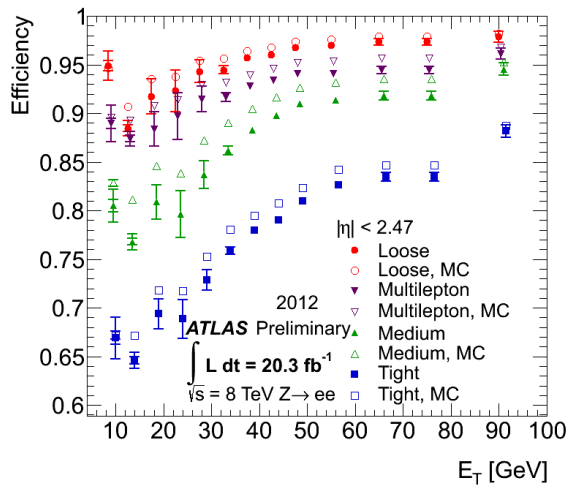
Figure 2.22: *Measured identification efficiencies as a function of E_T integrated over the full pseudorapidity range for various cut based electron identification menus. Empty markers represent MC data while data are plotted as solid points.*
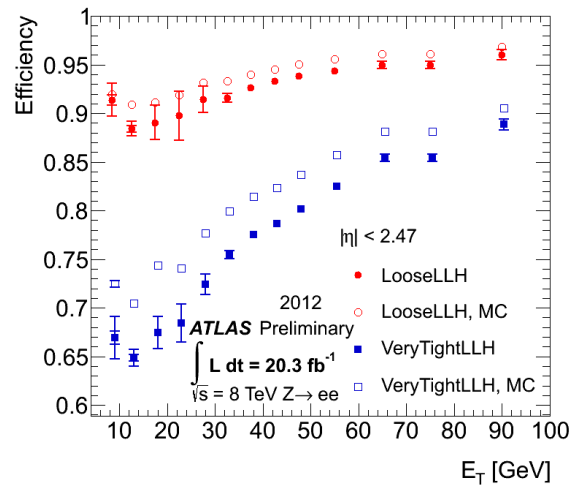
Figure 2.23: *Measured identification efficiencies as a function of E_T integrated over the full pseudorapidity range for various likelihood based menus. Empty markers represent MC data while actual data are plotted as solid points.*

Photon candidates are reconstructed from the final clusters if there is no matching inner detector track to the cluster barycenter or if a matching electron track from photon conversion is found. At a momentum region over 1 GeV, photon conversion is possible by interaction with detector material. The process yield can be considered independent of the original photon energy. Because of the asymmetric differential cross-section with respect to the energy ratios of the photon vs. electron and photon vs. proton, one of the two products in some fraction of the conversions will be produced with extremely low energy. If this is lower than the ATLAS electron reconstruction threshold, then the converted photon will be seen to have only one track (single conversion) [38]. The effect becomes important at low energies, as the proportion of conversion asymmetric enough to cause the loss of one product increases with decrease of the photon energy. Photon correction for conversion effects is necessary for high mass di-photon analyses searches, such as the Higgs and graviton channels. High identification efficiency on conversion electron candidates can be achieved if the conversion radius is greater than 800 mm while single conversion can also be accounted for by considering single tracks at the TRT without any pixel hits. The photon reconstruction efficiency for unconverted photons is at 60 % at the $E_T < 20$ GeV range and quickly increases to the optimal 96% after the 40 GeV transverse energy value (*Figure 2.24*) in all η regions. For converted photons (*Figure 2.25*),

reconstruction efficiency is reduced by 10 % at the lower E_T channels because of the single conversion effects, but reaches a higher value with respect to unconverted photons at increased energy since both converted electrons have high enough energies to be reconstructed.

A fraction of converted photons are also reconstructed as electrons. Approximately 2.1 % of electrons with $E_T > 20$ GeV are reconstructed as photons while 10.1 % of the reconstructed ones are ambiguous and are also considered as photons [39].
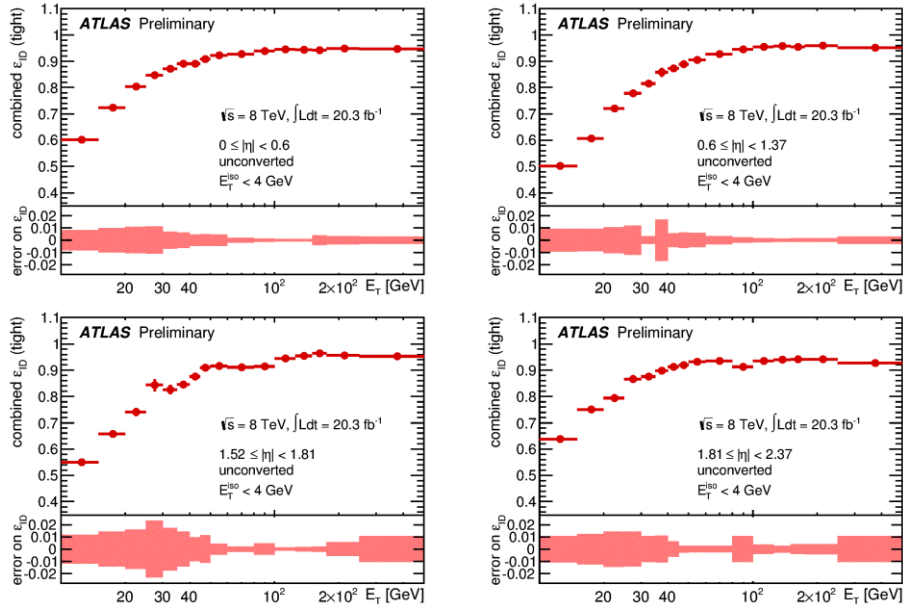
Figure 2.24: *Combination of the data-driven measurements of ε_{ID} for unconverted photons in the transverse energy range 10 GeV < E_T < 500 GeV. The ε_{ID} curves are shown in four different η regions. The error bars show the statistical and systematic uncertainties from the combination of the measurements in the overlapping E_T regions.*
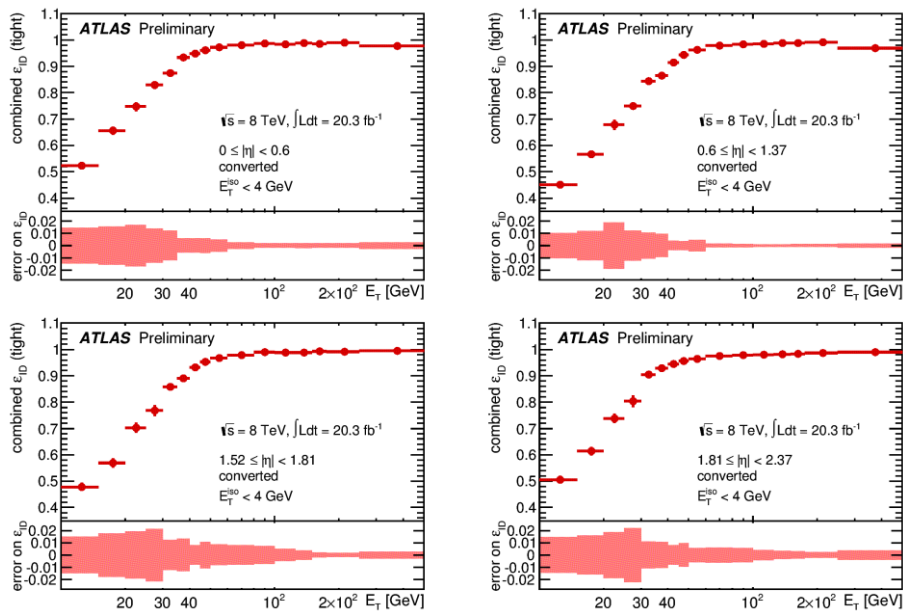
Figure 2.25: *Combination of the data-driven measurements of ε_{ID} for converted photons in the transverse energy range 10 GeV < E_T < 500 GeV. The ε_{ID} curves are shown in four different η regions. The error bars*

show the statistical and systematic uncertainties from the combination of the measurements in the overlapping E_T regions.

2.3.3   Muon reconstruction and identification

Muon candidates are reconstructed by associating an inner detector track with one built by the muon spectrometer. Four different types of muons are available to analyses:

1. Stand-Alone (SA) muons, reconstructed exclusively from tracks recorded by the muon spectrometer. Final particle parameters are obtained by track extrapolation to the interaction point taking into account diffusion effects and energy losses in the intermediate material.
2. Segment-Tagged (ST) muons, where a track from the inner detector can be associated to a partial track at the muon spectrometer. Track parameters in this case are provided exclusively by the inner detector.
3. ComBined (CB) muons require a complete track in the muon spectrometer extrapolated to a full trace of the inner detector. Vertex and directional information are acquired from the tracker. Combined muons provide the most accurate information.
4. Calo-Tagged (CT) muons, are reconstructed by matching an inner detector track with an energy deposit in the calorimeter corresponding to a minimum ionizing particle. Calo-Tagged muons are used in the region of $|\eta| < 0.1$ where the magnetic spectrometer is not instrumented. The identification algorithm is optimized for muon with $P_T > 15$ GeV

While CB reconstruction ensures highest purity of identified muons, the other three are often used to maximize the acceptance [40]. A high reconstruction efficiency of > 97 % is achieved for all muon types while, a slight decrease is observed in the central region $|\eta| < 0.1$, where only the CaloTag reconstruction is available, achieving a yield of ~ 95 % (*Figure 2.26*).
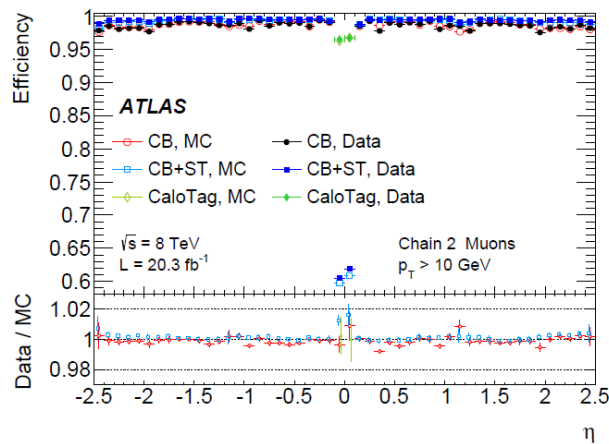
Figure 2.26: *Muon reconstruction efficiency as a function of η, measured using Z→µµ events for different muon reconstruction types. CaloTagged muons are only included in the region |η| < 0.1, where they are used in physics analyses. The error bars shown for the efficiencies represent the statistical uncertainty. The panel at the bottom shows the ratio between the measured and predicted efficiencies. The error bars show statistical and systematic uncertainties added in quadrature.*

2.3.4   Jet reconstruction and b-jet identification

In ATLAS the *AntiK$_T$* algorithm [41] is used to reconstruct jets within two different cone sizes, R = 0.4 and R = 0.6. The algorithm associates all objects around a proto-cluster, computing the distances d_{ij} (*equation 2-9*) between two particles or pseudo-jets i and j and the distance of the entry i from the beam (B), d_{iB} (*equation 2-10*):

$$d_{ij} = \min\left(p_{T_i}^2, p_{T_j}^2\right)\frac{\Delta_{ij}^2}{R^2} \qquad (2\text{-}9)$$

$$d_{iB} = \frac{1}{p_{T_i}^2} \qquad (2\text{-}10)$$

where $\Delta_{ij}^2 = (y_i - y_j)^2 + (\varphi_i - \varphi_j)^2$ while P_{Ti}, y_i and φ_i are respectively the transverse momentum, rapidity and azimuth of particle i. For each i, j particle pair, a comparison between d_{ij} and d_{iB} is performed. If d_{ij} is smaller, then i and j are combined to a single object whereas in the opposite case, i will be considered as a new jet. The algorithm proceeds in building up the energy of the jet symmetrically around the proto-cluster. In ATLAS, topo-clusters are used, measured in the calorimetric cells with energy beyond the noise level. The energy calibration of the jets is a heavy task because of the complex composition of the jet components. A first calibration is done taking into account each sub-particle nature (electromagnetic or hadronic). The final Jet Energy Scale (JES) is determined looking at the energetic balance of Z + jet or γ + jet events. The typical resolution for jet reconstruction in ATLAS is of ~ $10 - 15$ % for $P_T > 30$ GeV.

Bottom quark jets are interesting probes in several processes and in particular in Higgs and top physics. Identification of b-flavor jets can be accomplished by taking advantage of the long lifetime (1.5 ps) of b-hadrons, leading to a measurable flight length of a few mm before their decay. The latter will lead to a secondary vertex which can be identified by measuring the impact parameter (IP) of the originating tracks, which is their distance from the primary interaction vertex. Further identification can be achieved by taking into account the semileptonic decays of the original b-quarks which have a sizable transverse momentum. Tagging algorithms in ATLAS are divided into two main classes, the spatial tagger, exploiting position parameters like the IP, and soft-lepton taggers, using secondary vertices [42]. Most modern algorithms are based on a likelihood discriminant to separate jets by attributing a special weight, proportional to the probability of a jet being b-like, c-like or light. The performance of a b-tagging algorithm is defined by the efficiency in b-jet identification and the probability of mistakenly identifying a jet as a b quark originating from a charm quark or a light flavor (u, d, s) quark [43]. Latest studies with b-tagging working points used in 2012 analyses, show an efficiency of 70 % for b-jets keeping 20 % (0.7 %) of charm (light) jets.

2.4 Data Management and Efficiency

2.4.1 Data Management and Distribution

The operation of the detector produces a massive amount of data, impossible to centrally manage, store and analyze. Even after event selection and data reduction, corresponding physics information registered by CERN in the Run 1 period is in the order of 16 PB (petabytes) [44] with primary unprocessed (RAW) data accounting for 25 % of the total stored volume (*figure 2.27*). In optimal conditions, about 40 million beam crossings per second occur in the center of the detector at full luminosity. If all the data were to be saved, ~100 petabytes per second of raw data would have to be stored. Each event in the detector consists of about 25-MB of raw data (compressible to 1.5-2 MB). Using the trigger system, only events of physics interest are recorded for further processing. The first level trigger reduces the event rate from 40 million to about 100 thousand events per second (events/s). Further reduction is achieved by the second level trigger, to the more manageable rate of 2000 events/s. The final rate of 200 events/s is achieved through the Event Filter, constituting the third triggering level of the ATLAS experiment. Details on the various levels and the selection process are presented in previous sections (section 2.3.1).

The final less than 200 events/s selected by the Event Filter computing farms are stored for further processing and further off-line analysis. The sub-Farm output manager is responsible for collecting all files associated with an event and sending them as a single unit to the main storage

array. A set of five custom designed file servers with special file system collect data passed by the Event Filter and store them in form of data files while saving information to the handshake table (realized through Oracle data base management systems) notifying that data are ready to be processed. Events are then passed on to the CERN Advanced STORrage Manager (CASTOR), constituting the main available storage element. CASTOR allows storing of huge amounts of data transparently by seamlessly managing disk cache(s) and tape storage. ATLAS has several PB of disc cache storage in various pools and "unlimited" amount of tape storage. Castor pools are used to store both final and intermediate products during the ATLAS data processing.
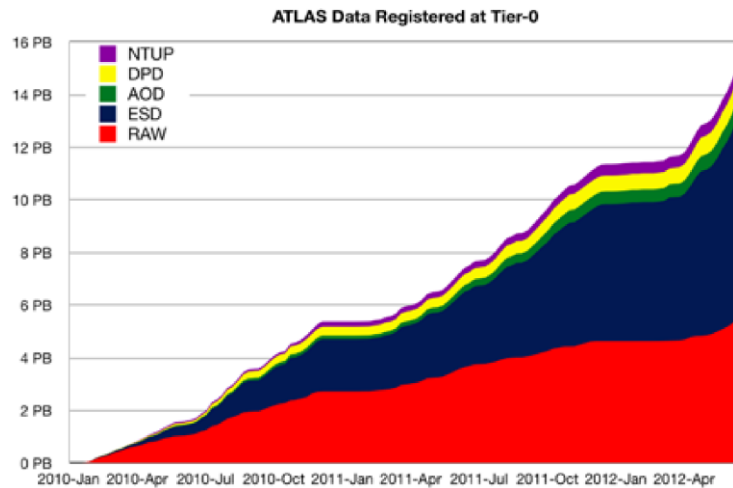
Figure 2.27: *Cumulative data volume registered in Tier-0 since 2010.*

Data processing and storage is organized in different layers within the ATLAS experiment. The first layer, called "Tier-0", corresponds to the CERN site, the only place where information is being produced. The task of the ATLAS Tier-0 system is to perform the prompt first pass processing on the express/calibration physics stream, 24-48 hours processing of full physics data stream with reasonable calibrations, and to register raw and reconstructed data to the Distributed Data Management System (DDM). From then on, data will be distributed to the second layer centers, "Tier-1", and beyond. ATLAS Tier-0 is composed of roughly 100 interconnected powerful computers housed in the CERN Computing Center. Tier-1 centers are very large computing centers for a whole country or region, each is connected to CERN by 10 GBit/s line. Tier-2s are medium local computing centers at institutes, they serve end users and support additional small Tier-3 centers.

Upon arrival of new RAW data to the Tier-0 storage pool, information is retrieved from the handshake table by the Tier-0 Management System (TOM). Based on the rate, amount and retrieved information of incoming data, TOM will define and monitor all tasks necessary to perform a prompt reconstruction and will make final datasets available to the ATLAS distributed data management system. Physics analysis can be carried out in the ATHENA framework [45], the main ATLAS user interface software, while jobs can be submitted to the computing grid, both developed at CERN. The LHC Computing Grid is a distribution network designed by CERN to handle the massive amounts of data produced by the LHC. It incorporates both private fiber optic cable links and existing high-speed portions of the public Internet. It is hierarchically structured to Tier-0, Tier-1 and Tier-2 centers and allows users to send their analysis jobs to places where data reside seamlessly [46].

Several levels of data organization exist with respect to the amount of information contained in the physically stored file. Raw Data contain all the information from the detector in compressed form. Each run and each stream produce one dataset (logically connected files). The Event Summary Data (ESD) are processed RAW data which still contain sufficient information to re-run parts of the reconstruction and are used preferentially to RAW data when possible. Analysis Object Data (AOD)

consist of a reduced size output of physics quantities from the reconstruction that should suffice for most kinds of analysis work. Independent tailor-made streams of AODs are foreseen for the different physics analysis with respect to their specific requirements. Finally, derived Physics Data (DPD) are subsets of ESDs which can either be used to study detector performance (Performance DPDs) or "Physics DPDs", useful for specific analysis.

By implementing a data distribution policy, redundancy is assured for all file types and between all levels of processing. For RAW data, one copy is always kept at CERN in tape storage, while files are also distributed to Tier-1 centers. A further Tier-2 copy can be made available for extended processing if needed. ESDs are initially kept on disks at CERN for preliminary analysis and are latter moved to tapes. Copies are randomly distributed to Tier-1 centers where they are mainly placed on disk storage, while one copy is sent at the Brookhaven National Laboratory. Finally, for AODs and DPDs, one copy always remains at CERN on tape, while a secondary copy is distributed in every Tier-1 to be stored mainly on disks. Tier-2 distribution is also possible for further storage and processing.

2.4.2   Data efficiency

During LHC operation, turn-on times of the high voltage power supplies for individual subsystems of the ATLAS detector (Pixels, SCT, Calorimeter and Muon Chambers) introduce delays in data taking. Furthermore, problems with a given sub-detector system or on-line data processing and storage also contribute to a detector down time. As a result, data taking efficiency in the ATLAS detector is affected since not all available data are recorded.
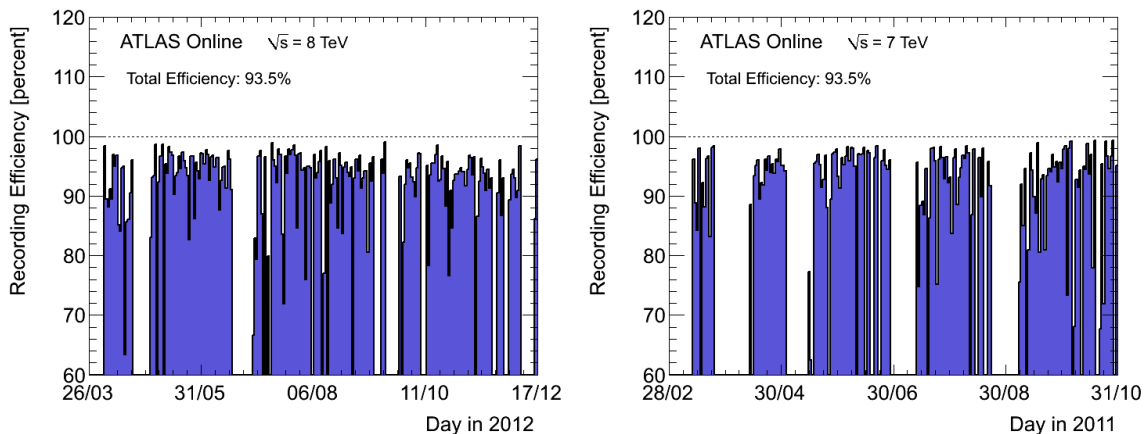
Figure 2.28: *Data recording efficiency for 2012 (left) and 2011 (right). Each bin represents a week. The empty bins are due to weeks in which no stable beams were delivered by the LHC.*

Data taking efficiency is defined as the ratio between ATLAS recorded luminosity with respect to that delivered by the LHC. The latter is measured as the luminosity delivered between the declaration of stable beams and the LHC request to turn the sensitive detectors off to allow a beam dump or beam studies. During the 2011 and 2012 periods, the overall efficiency remained in extremely high values, achieving a 93.5 % for both year (*Figure 2.28*). Each bin in the corresponding figure represents a week while, empty bins are due to weeks in which no stable beams were delivered by the LHC. The inefficiency accounts for the turn-on of the high voltage of the Pixel, SCT and some of the muon detectors and any inefficiencies due to dead-time or due to individual problems with a given sub-detector that prevent the ATLAS data taking to proceed.

2.5   References

[1]   The LHC Collaboration, LHC Design Report Volume I, "The LHC Main Ring, Layout and Performance", CERN, ab-div.web.cern.ch/ab-div/Publications/LHC-DesignReport.html

[2]   J. P. Koutchouk, W. Scandale and A. Verdier, "Optimization of the LHC Lattice and Chromaticity", Proc. of the IEEE Part. Acc. Conf., Washington DC, March 1987

[3]   Oliver Bruning, 10th LCH Machine Advisory Committee, "Progress Report on the LHC Optics", http://mgt-lhc-machine-advisory-committee.web.cern.ch/mgt-lhc-machine-advisory-committee/lhcmac10/ClosedSession/Bruning.pdf

[4]   A. Faus - Golfe, H. Grote, J - P Koutchouk, T. Risselada, A. Verdier, S. Weisz, "A more robust and flexible lattice for LHC", proceedings of PAC97, Vancouver, Canada

[5]   H. Ullrich, "Proposal for the upgrade of the Booster main magnet power supply", CERN PS/PO/Note 95-02(tech.), Geneva, 1995

[6]   F. Blas et al., "Conversion of the PS complex as LHC proton pre-injector", Proc. of PAC '97, Vancouver, 1997

[7]   R. Garoby, "Bunch Merging and Splitting Techniques in the Injectors for High Energy Hadron Colliders", CERN/PS 98-048(RF), Proc. of HEACC '98, Dubna, 1998.

[8]   Tobias Baer, "UFOs in the LHC", LHC Beam operation committee, June 2011

[9]   ATLAS Experiment, "Public Results, Luminosity public results", https://twiki.cern.ch/twiki/bin/view/AtlasPublic/LuminosityPublicResults#2010_pp_Collisions

[10]   H. Burkhardt et al., "Commissioning and Operation at $\beta^* = 1000$ m in the LHC", TUPWO050, Proceedings of IPAC2013, Shanghai, China

[11]   The ATLAS Collaboration, "ATLAS detector and physics performance : Technical Design Report", ATLAS-TDR-15; CERN-LHCC-99-015, Geneva: CERN, 1999

[12]   ATLAS Collaboration, "Magnet System Technical Design Report", ATLAS TDR 6, CRN/LHCC 97-18

[13]   "ATLAS Magnet System", http://atlas-cs.web.cern.ch/atlas-cs/

[14]   ATLAS Pixel Collaboration, "ATLAS Pixel Detector Technical Design Report", CERN/LHCC/98-13 (1998)

[15]   Fabian Hugging, "The ATLAS Pixel Detector", 5 Aug 2005, arXiv:physics/0412138v2, [physics.ins-det]

[16]   D. Bintinger, K. Einsweiler and M. Gilchriese, "Pixel Detector for Simulation for the ATLAS Technical Proposal", ATLAS Internal Note, INDET-NO-089, 1994

[17]   The ATLAS Collaboration, "ATLAS Facts sheet", http://www.atlas.ch/pdf/ATLAS_fact_sheets.pdf

[18]   E. Coniavitis, "ATLAS silicon microstrip detector operation and performance", Journal of Instrumentation, Volume 6, January 2011

[19]   D. Attree et al., "The evaporative cooling system for the ATLAS inner detector", 2008 JINST 3P07003

[20]   L. Jeanty, "The ATLAS Transition Radiation Tracker, NEPPSR, August 2007", http://physics.bu.edu/neppsr/2007/TALKS-2007/TRT_Jeanty.pdf

[21]   V. A. Mitsou, "The ATLAS Transition Radiaton Tracker", CERN - EP Division, arXiv:hep-ex/0311058v1, Nov 2003

[22]   The ATLAS Collaboration, "ATLAS calorimeter performance: Technical Design Report", CERN-LHCC-96-040, Geneva, 1996

[23]   ATLAS Collaboration, "Electron and photon energy calibration with the ATLAS detector using LHC Run 1 data", November 2014, http://arxiv.org/abs/1407.5063

[24]   The ATLAS Collaboration, "ATLAS tile calorimeter: Technical Design Report", ATLAS-TDR-3 - CERN-LHCC-96-042, Geneva, 1996

[25]   ATLAS Collaboration, "The ATLAS Experiment at the CERN Large Hadron Collider", JINST 3 (2008) S08003

[26]   The ATLAS Collaboration, "Muon reconstruction efficiency and momentum resolution of the ATLAS experiment in proton–proton collisions at $\sqrt{s} = 7$ TeV in 2010", arXiv:1404.4562v1, April 2014

[27] ATLAS Collaboration, "Expected Performance of the ATLAS Experiment - Detector, Trigger and Physics", arXiv:0901.0512

[28] ATLAS Collaboration, "Study of the Material Budget in the ATLAS Inner Detector with K_0^S decays in collision data at $\sqrt{s} = 900$ GeV", ATLAS-CONF-2010-019, 2010

[29] ATLAS Collaboration, "Mapping the material in the ATLAS Inner Detector using secondary hadronic interactions in 7 TeV collisions", ATLAS-CONF-2010-058, 2010

[30] The ATLAS Collaboration, "Performance of the ATLAS Trigger System in 2010", CERN-PH-EP-2011-0

[31] S. Rajagopalan, "The Performance of the ATLAS Trigger System in the LHC proton-proton Collisions", TIPP2011, doi: 10.1016/j.phpro.2012.02.503

[32] R. Achenbach et al., "The ATLAS Level-1 Calorimeter Trigger", JINST 3 (2008) P03001

[33] A. J. Lankford, "Overview of the ATLAS Trigger/DAQ system", May 2007, http://hep.ps.uci.edu/~wclhc07/ATLAS%20TDAQ.pdf

[34] W. Lampl et al., "Calorimeter Clustering Algorithms: Description and Performance", ATLAS note, April 2008

[35] ATLAS Collaboration, "Reconstruction of electrons in ATLAS", ATLAS CSC Note EG-1, http://www.physics.smu.edu/web/research/preprints/SMU-HEP-08-21.pdf

[36] Ron Madaras, "ATLAS Electron ID", May 2005, http://www-atlas.lbl.gov/physics/Ron_Atlas_EMID.pdf

[37] The ATLAS Collaboration, "Electron performance measurements with the ATLAS detector using the 2010 LHC proton-proton collision data", CERN-PH-EP-2011-117, arXiv:1110.3174v2 [hep-ex], March 2012

[38] The ATLAS Collaboration, "CSC Note – Photon Conversion in ATLAS", August 2008, http://www.physics.smu.edu/web/research/preprints/SMU-HEP-08-13.pdf

[39] The ATLAS Collaboration, "Readiness of the ATLAS Liquid Argon Calorimeter for LHC Collisions", arXiv:0912.2642 [physics.ins-det], December 2010

[40] Thomas Göpfer, "Tagging b-jets in ATLAS", http://www-library.desy.de/prep-arch/desy/proc/proc10-04/P74.pdf

[41] The ATLAS Collaboration, "Measurement of the muon reconstruction performance of the ATLAS detector using 2011 and 2012 LHC proton–proton collision data", CERN December 2014, arXiv:1407.3935v2 [hep-ex]

[42] Matteo Cacciari, Gavin P. Salam, Gregory Soyez, "The AntiK_T jet clustering algorithm", 2008, arXiv:0802.1189 [hep-ph]

[43] The ATLAS collaboration, "Commissioning of the ATLAS high-performance b-tagging algorithms in the 7 TeV collision data", ATLAS-CONF-2011-102, July 2011

[44] Ikuo Ueda, "The Present and Future Challenges of Distributed Computing in the ATLAS experiment", 36th International Conference on High Energy Physics, July 2012

[45] ATL A S Computing Group. "ATLAS Computing Technical Design Report", ATLAS TDR--017, CERN-LHCC-2005-022, 2005

[46] Tomáš Kubeš, "Data Processing in ATLAS", Symmetries and Spin, July 2009

3   Run 1 H→ZZ$^{(*)}$→4l studies

3.1   Introduction

In this chapter, the Run 1 analysis of the H→ZZ$^{(*)}$→4l channel is presented, with a special emphasis on the electron background estimation. In the pre-Higgs discovery era, the increased abundance of data at the initial phases of the LHC program led to an amplified demand for more intricate and robust analyses. While initial indications of the particles discovery were presented as early as 2011, it was not until the summer of 2012 that sufficient data were available for an announcement to be made. In addition, exploring and excluding any other possibility for all analysis channels was one of the most demanding and at the same time exciting tasks in the history of physics. Identifying the few interesting events leading to the certainty of an observation was one of the hardest data-mining endeavors undertaken by the scientific community. My personal contribution in the following chapter is the development and application of the so-called "Reco - Truth Unfolding" method for the reducible electron background estimation, this method was used as the baseline in 2011 analysis and as a systematic cross-check in 2012 data.

3.2   The H→ZZ$^{(*)}$→4l channel

The search for the Standard Model Higgs boson was one of the primary objectives of LHC Run 1 with the discovery announcement by the ATLAS and CMS collaborations being a pivotal moment in this campaign. Among its decay channels, the so called "golden channel" of H→ZZ$^{(*)}$→4l where "l" denotes an electron or muon, is the one offering the cleanest signature. It produces a very clear experimental signature of four isolated leptons in the final state with no missing transverse energy and low background. Good energy and momentum resolution allows an accurate measurement of the four lepton invariant mass in spite of the suppressed branching ratio (*Table 3-1*) [1]. In the four muon final state, experimental resolution on the mass measurement is in the order of 1.5 %, while in the four electron case, resolution is slightly degraded to 2 % for an m_H = 120 GeV.

√s	σ(gg→H) [pb]	σ(qq′→Hqq′) [pb]	σ($q\bar{q}$→WH) [pb]	σ($q\bar{q}$→ZH) [pb]	σ($q\bar{q}$/gg→$t\bar{t}$H/$b\bar{b}$H) [pb]	B(H→ZZ*→4l) [10^{-3}]
7 TeV	15.1±1.6	1.22±0.03	0.58±0.02	0.34±0.01	0.24±0.04	0.125±0.005
8 Tev	19.3±2.0	1.58±0.04	0.70±0.02	0.42±0.02	0.33±0.05	0.125±0.005

Table 3-1: *Production cross-sections and branching ratios on the four lepton channel for the dominant production modes [1].*

Final states can be categorized with respect to their lepton flavor in four distinct categories:

$$H→ZZ^{(*)}→e^+e^-e^+e^- \text{ (4e)} \qquad H→ZZ^{(*)}→e^+e^-\mu^+\mu^- \text{ (2e2μ)}$$
$$H→ZZ^{(*)}→\mu^+\mu^-\mu^+\mu^- \text{ (4μ)} \qquad H→ZZ^{(*)}→\mu^+\mu^-e^+e^- \text{ (2μ2e)}$$

For the Higgs boson discovered at a mass of 125 GeV, one or both of the intermediate Z bosons have to be virtual. As a convention, the first lepton pair is always considered to be the one whose combined mass is compatible, or is the closest to the invariant mass of a Z boson.

The main backgrounds affecting the analysis final state can be divided in two categories: an irreducible contribution, producing the same final state as the signal, and a reducible component, mainly due to object misidentification.

A. _The irreducible background_ constitutes the primary contribution. It originates from Electroweak ZZ(*) production in proton-proton collisions, through the diagrams shown in _Figure 3.1_ [2]. Four distinct states are possible:
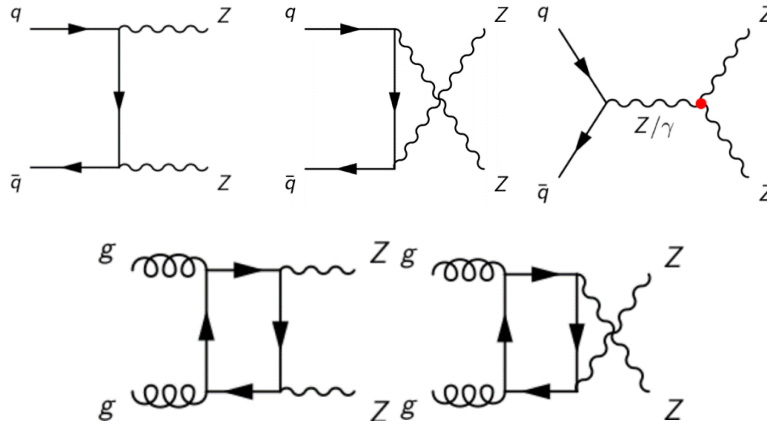
Figure 3.1: _Leading order Feynman diagrams for ZZ production through the qbar(q) and gg initial state at hadron colliders. The s-channel diagram, (last one on the top row), contains the ZZZ and ZZγ neutral TGC vertices which do not exist in the SM._

$$Z(*)Z(*) \qquad \gamma(*)Z(*)$$
$$Z(*)\gamma(*) \qquad \gamma(*)\gamma(*)$$

Although this process is very similar to the expected signal generating four isolated leptons at the final state, the invariant mass distribution is continuous, presenting a peak at the di-Z mass (180 GeV) where two "on-shell" Z bosons become possible. A slow decrease follows up to 500 GeV, where electroweak production fades out. This background is estimated exclusively thought Monte Carlo production extrapolated to data luminosity.

B. _As reducible background_ one can consider any process accounting for a true or fake four lepton final state with or without the intermediation of a true Z boson. In that context, the following main categories can be identified:

1. ZQQ→4l: A Z true boson, accompanied by a heavy quark-antiquark pair following semileptonic decays paths. The four lepton final state arises from the two true leptons of the Z decay and two non-isolated true leptons from each one of the quarks. Processes like $gg \rightarrow Zb\bar{b} \rightarrow 2lb\bar{b}$ are typical examples and their suppression heavily depends on lepton isolation criteria.

2. $gg, qq \rightarrow t\bar{t}$: These processes may produce quark-antiquark pairs accompanied by W bosons. The four lepton final state is then produced by the two leptons originating from each one of the W decays and the other two from quark semileptonic processes. This can primarily be achieved through a b-quark via the following process (_equation 3.1_):

$$t \rightarrow \begin{matrix} b \rightarrow l + v_l \\ W^+ \rightarrow l + v_l{'} \end{matrix} \qquad \bar{t} \rightarrow \begin{matrix} \bar{b} \rightarrow l + v_l \\ W^- \rightarrow l + v_l \end{matrix} \qquad (3\text{-}1)$$

In this final state we can find four leptons and missing transverse energy, a state very similar to the researched Higgs experimental signature.

3. Z inclusive: A Z vector boson produced via quark-antiquark scattering in association with jets and/or hadrons in the final state. This can be manifested in the form of $q\bar{q} \rightarrow$

$Z + X + Y$, where X and Y may be jets faking electrons. Suppression of this background depends on the identification efficiency and hadron rejection capability.

Reducible backgrounds become important at the low mass region (less than 180 GeV), where QCD processes can produce misidentified jets faking electrons of preferably low transverse momenta. The $t\bar{t}$ background can be considered small, with a quite flattened spectrum enhanced at small 4l invariant masses.

3.3   Data & Monte Carlo samples

3.3.1   Considered data

Data registered by the ATLAS detector have to satisfy good working conditions for all subsystems. Samples with identified issues in one or more detector stations are subsequently disregarded in any analysis. A total of 4.6 fb^{-1} and 20.7 fb^{-1} integrated luminosity, at 7 and 8 TeV respectively, were considered after quality filtering from 2011 and 2012 data runs.

3.3.2   Monte Carlo production

ATLAS material and detector simulations are performed via the GEANT package [3, 4]. Signal and background processes are simulated and subsequently interfaced to the reconstruction and digitization algorithm (ATHENA).

All available Higgs production processes are considered in this analysis. H →ZZ$^{(*)}$→ 4ℓ production is simulated via POWHEG, which can separately treat gluon-gluon fusion and vector boson fusion production modes up to NLO [6 - 9]. Higgs transverse momentum in the gluon-gluon case is refined to include NNLO QCD corrections and soft gluon resummations up to NNLL order [10, 11]. POWHEG is interfaced to PYTHIA for hadronization [12, 13] and to PHOTOS for QED radiative corrections at the final state [14, 15], while τ-lepton decays are generated by TAULA [16, 17]. Higgs associated production with a W, Z or top quarks is simulated by PYTHIA.

Higgs production cross-sections in the gluon-gluon fusion, the vector boson fusion, the W/Z associated production and the top associated contribution are calculated in next to leading order (LNLO) and next to next to leading order (NNLO) including NLO electroweak radiative corrections in all modes. Cross-sections for the gluon fusion process have been calculated to NLO and NNLO [18 - 20] while QCD soft-gluon resummations were calculated in the NNLL approximation [21]. Electroweak (EW) radiative corrections at NLO are also applied [22, 23]. For the VBF production process, full QCD and EW corrections up to NLO and approximate NNLO QCD corrections are used [24 - 26]. The cross-sections for associated WH-ZH production processes are computed at NLO and at NNLO in QCD, taking into account of NLO EW radiative corrections. Associated Higgs boson production cross-section with $t\bar{t}$ pairs is calculated at NLO [27]. The entire information and references are contained in [28]. The branching ratio to the four lepton channel has been estimated using PROFECY4F [29], including QCD and electroweak NLO corrections while taking into account identical final state fermion interferences and heavy Higgs boson corrections.

The irreducible background is simulated using POWHEG-BOX [30] and gg2ZZ [31] for the quark-antiquark and gluon fusion parts respectively. M$_{zz}$ spectrum cross-section is calculated in NLO with an estimated uncertainties of 5 % [32] from the QCD scale, corresponding to 4 % for the quark and 8 % gluon initiated processes respectively [33, 34]. Z + jets processes are simulated by ALPGEN, which is interfaced to PYTHIA for showering and hadronization. The process is divided in the Z + light jets, mainly taking into account c and b quarks in the massless approximation, and the Z + b part, where b mass is included in the computation [35]. To avoid double counting of

produced b-pairs, a separation of $\Delta R = \sqrt{\Delta \Phi^2 + \Delta \eta^2} > 0.4$ is applied on the final jets whereas, in the opposite case, parton shower $b\bar{b}$ pairs are used.

3.4   Event Selection

3.4.1   Trigger Application

Leptons from a ZZ* Higgs boson decay cover a wide range of transverse energies, from a few GeV in the case of virtual Zs, to tens of GeVs for "on-shell" Z production. Corresponding triggers for H→ 4ℓ events can either use single or double lepton criteria in order to increase the detection efficiency. Single lepton triggers apply a strict selection on the quality of the candidate and a high threshold on transverse energy. This threshold evolved during data taking to cope with the increase of the data rate from instantaneous luminosity evolution (*Table 3-2*). The trigger point for the electrons and isolated muons is at 24 GeV while isolation cuts have been added. These cuts are applied at level 3 trigger (Event Filter) and require the sum of the P_T of all tracks in a cone $\Delta R < 0.2$ surrounding the lepton to be less than 10 % of its corresponding P_T. In addition, an asymmetric P_T threshold is required for the double muon trigger at 18 GeV and 8 GeV for the first and the second muon respectively.

Mode	Single lepton	Di-lepton
4e	e24vhi medium1	2e12Tvh medium1
4μ	mu24i tight 2mu13	mu18 mu8 EFFS
2e2μ	e24vhi medium1, mu24i tight	2e12Tvh medium1, 2mu13, mu18 mu8 EFFS e12Tvh medium1 mu10, e24vhi loose1 mu8

Table 3-2: *Trigger threshold summary for 2012 data.*

In single Higgs production simulation, the trigger efficiency (by gluon-gluon fusion processes at $m_H \approx 130$ GeV) is estimated at 97.6 % for the four-muon final state, at 97.3 % for the mixed flavor case and at 99.7 % for the electronic final state. Trigger efficiencies are measured using data driven techniques, while any observed inconsistences with Monte Carlo estimations are corrected via scale factor application.

3.4.2   Lepton Selection

After reconstruction (see section 2.3.2), a series of criteria are applied to identify electron candidates, improving the signal over background ratio. Two main changes were introduced in 2012 with respect to 2011 conditions. To begin with, bremsstrahlung recovery was implemented during electron reconstruction, allowing for a 2 - 8 % gain, especially at low transverse momenta. Furthermore, a MultiVariant discriminant was constructed for electron identification, based on likelihood maximization. In this way, several different properties of the track and the cluster are simultaneously considered, combined and compared to probability density functions. In *Figure 3.2*, the improvement on the background rejection using likelihood with respect to the previously used cut-based identification is presented versus pseudorapidity and E$_T$. For the same signal efficiency, likelihood electron identification achieves a ~ 50 % increase in background rejection.

CB and ST muons are used in the barrel region for |η| < 2.5 with additional imposed criteria on the inner detector tracks. These mainly include a minimum required number of hits in the pixel and SCT detectors, as well as for the ratio of TRT outliers versus all TRT hits not to exceed a certain fraction. Detector conditions are taken into consideration by removing any tracks traversing dead regions. To increase the muon acceptance, StandAlone muons are added in the region 2.5 < |η| < 2.7, not covered by the inner detector, while additional cuts are imposed to ensure track quality. CB

muons are used in the central barrel region |η| < 0.1 For both electrons and muons, the impact parameter with respect to the main vertex must satisfy the condition $|d_0| < 0.2$ mm, whereas if an associated track in the inner detector is found, the closest point of that track in the z coordinate with respect to the primary vertex vertical plane must satisfy $|z_0| < 1.0$ mm.
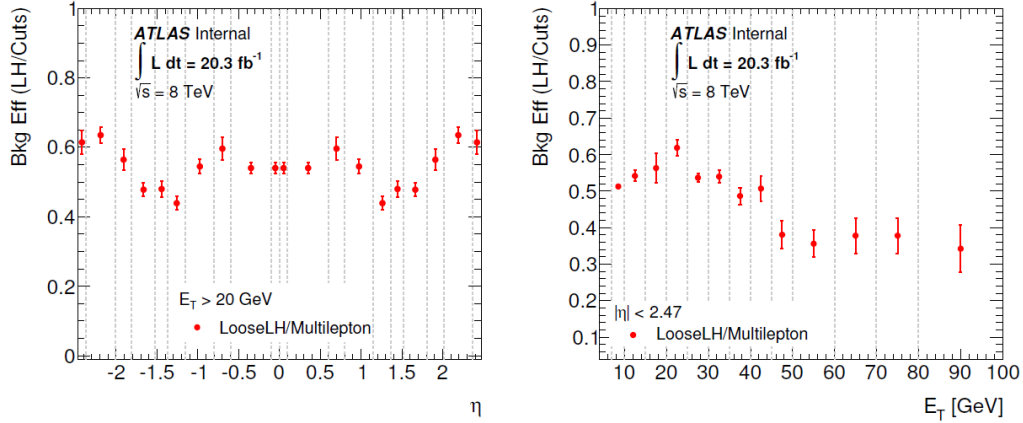
Figure 3.2: *Ratio of background efficiencies for the likelihood/cut-based menus vs. η (left) and vs. E$_T$ (right). Represented data correspond to light jets. A 40-50 % background reduction is observed by using the LooseLH menu (multivariate criteria) instead of the 2011 used Multilepton selection (cut-based). The working point of the LooseLH menu is fixed to yield identical efficiency with respect to the Multilepton selection for true electrons.*

3.4.3   Quadruplet Selection

Event selection criteria take into account lepton quality, kinematic cuts, as well as lepton isolation and impact parameter criteria. Quadruplet formation is performed by selecting two same flavor, opposite sign lepton pairs per event. For muons, a minimum P_T threshold at 6 GeV is imposed while acceptance is limited to |η| < 2.7. In the electron case, a transverse energy threshold at 7 GeV is applied with a pseudorapidity acceptance limited at the barrel calorimetric volume (|η| < 2.47). Isolation requirement between same flavor type leptons is set at ΔR > 0.1 with the requirement increasing to ΔR > 0.2 for different flavor. The lepton pair with a combined mass closest to that of the Z is considered as the leading one (m$_{12}$), whereas the other two leptons constitute the sub-leading pair (m$_{34}$). While for the leading pair an invariant mass cut is applied at 50 GeV < m$_{12}$ < 106 GeV, for the sub-leading pair, a minimum threshold is imposed (m$_{th}$) with respect to the quadruplet invariant mass (*Table 3-3*) In particular, to increase acceptance, minimum sub-leading threshold mass value is defined at 12.0 GeV while intermediate values are calculated with linear extrapolation. In any case, the maximum sub-leading invariant mass is retained at 115 GeV.

Threshold mass				
m$_{4\ell}$ (GeV)	< 140	140	190	> 190
m$_{seuil}$(GeV)	12.0	12.0	50	50

Table 3-3: *Threshold mass with respect to quadruplet invariant mass.*

The imposed requirement for track isolation demands that the sum of all tracks (ΣP$_T$) within a cone of ΔR < 0.2 for any selected lepton should not exceed 15 % of the particles P$_T$. Although this requirement is applied to both electrons and muons, tracks considered in this operation vary with respect to lepton flavor:

- *For muons:* Tracks with at least four hits in the pixel and SCT detectors and P$_T$ > 1GeV are considered in the sum.
- *For electrons:* Tracks with at least nine hits at the pixel and SCT detectors including one hit on the b-layer, and minimum P$_T$ of 0.4 GeV are considered.

An equivalent calorimetric isolation is also defined for leptons. For muons, the sum of the energy deposited into all calorimeter cells within $\Delta R < 0.2$ around the muon cluster should not exceed 30 % of the total muon transverse momentum. Central cells accounting for any muon energy deposition in the calorimeter are excluded from this sum. For electrons, calorimetric isolation requires that the sum of the energy deposited in the TopoClusers surrounding the particle should not exceed 20 % on its transverse momentum, while the cluster of the electron is excluded from the sum. This reduced threshold in the electron case, allows for a better PileUp rejection in the calorimeter, while muons are less affected because of the reduced amount of energy that they deposit. In calorimetric isolation calculations, contributions from other leptons within the quadruplet are not taken into account. Finally, an impact parameter significance cut is applied, defined as the ratio of d_0/σ_{d0}, at 3.5 for the muons and 6.5 for the electrons. The more relaxed cut in the electron case is introduced to account for radiative energy losses though Bremsstrahlung. A detailed summary of all applied cuts is presented in *Table 3-4*.

Object Pre-selection		
Electrons	LooseLH electrons with $E_T > 7$ GeV and $|\eta| < 2.47$	
Muons	No more than one CaloTagged or StandAlone muon per quadruplet	
	Combined or Segmented Tag muons	$P_T > 6$ GeV
		$|\eta| < 2.7$
	CaloTagged Muons	$P_T > 15$ GeV
		$|\eta| < 0.1$
	StandAlone muons	$P_T > 6$ GeV
		$2.5 < |\eta| < 2.7$
		$\Delta R > 0.2$ with respect to the closest SegmentedTagged muon
Event Selection		
Kinematic Selection	At least one quadruplet with two pairs of opposite sign same flavor leptons	
	P_T threshold of the three primary leptons : 20, 15 et 10 GeV	
	50 GeV $< m_{12} < 106$ GeV	
	$m_{threshold} < m_{34} < 115$ GeV	
	Remove quadruplet if an alternative pair yields $m_{\ell\ell} < 5$ GeV	
	$\Delta R(\ell,\ell') > 0.10$ (0.20) for same (different) flavor leptons	
Isolation	Lepton track isolation ($\Delta R = 0.20$) : $\Sigma P_T / P_T < 0.15$	
	Electron calorimetric isolation ($\Delta R = 0.20$) : $\Sigma E_T / E_T < 0.20$	
	Muon calorimetric isolation ($\Delta R = 0.20$) : $\Sigma E_T / E_T < 0.30$	
	StandAlone muon calorimetric isolation ($\Delta R = 0.20$) : $\Sigma E_T / E_T < 0.15$	
Impact parameter significance	electrons : $d_0/\sigma_{d0} < 6.5$	
	muons : $d_0/\sigma_{d0} < 3.5$	

Table 3-4: *Summary of event selection. The masses of the two lepton pairs are* referred to as m_{12} and m_{34} respectively, while values of the $m_{threshold}$ are presented in the previous table.

A final correction to the four-lepton mass is applied, accounting for QED radiative Z decays, leading to energy loss via photon production at the final state (Final State Radiation - FSR). A dedicated method has been developed to identify FSR photons in the calorimeter and incorporate them to the four lepton measurement, in both collinear and non-collinear geometries [36]. While collinear photons (defined as photons with $\Delta R_{cluster,\mu} \leq 0.15$) can only be associated with muons, since their effect on electron measurement has already been taken into account in the calorimetric shower, non-

collinear photons (defined as photons with $\Delta R_{cluster,\mu} > 0.15$) can be associated either with muons or electrons.

At most one FSR photon is used per event since the probability of a double FSR production with significant energy is negligible. Priority is given to collinear photons, required to have $E_T > 1.5$ GeV and a fraction of the total energy deposited in the front sampling layer of the calorimeter greater than 0.1. If more than one collinear photon are found, only the one with the highest E_T is kept. Collinear FSR selection recovers 70 % of the FSR photons within the selected fiducial region with a purity of about 85 %, while misidentified FSR photons originate from PileUp and muon ionization. Non-collinear photons must have $E_T > 10$ GeV, be isolated (E_T below 4 GeV within a cone of size $\Delta R = 0.4$, excluding the photon itself), and satisfy strict ("tight") identification criteria [37]. As in the collinear photon case, only the highest-E_T non-collinear photon is retained, and only if no collinear photon is found. The non-collinear FSR selection has an efficiency of approximately 60 % and a purity greater than 95 % within the detector fiducial region.

Photon FSR correction is only applied to the leading di-lepton if corresponding invariant mass is between 66 GeV $< m_{ll} < 89$ GeV and $m_{ll\gamma} < 100$ GeV. If the collinear-photon search fails then the non-collinear FSR photon is added, provided it satisfies $m_{ll} < 81$ GeV and $m_{ll\gamma} < 100$ GeV. The expected fraction of collinear (non-collinear) corrected events is 4 % (1 %). For the 7 TeV data, the combined signal reconstruction and selection efficiency at $m_H = 125$ GeV is 39 % for the 4μ channel, 25 % for the 2e2μ/2μ2e channels and 17 % for the 4e channel. The improvements in the electron reconstruction and identification for the 8 TeV data lead to increases in these efficiencies by 10 % - 15 % for the electronic channels, bringing their efficiencies to 27 % for the 2e2μ/2μ2e and 20 % for the 4e cases respectively. In *Figure 3.3* the invariant mass distributions of Z→μ$^+$μ$^-$ candidate events, where a collinear FSR photon is found, are shown before and after addition of the FSR photon for both data and simulation. Good agreement between data and simulation is observed.
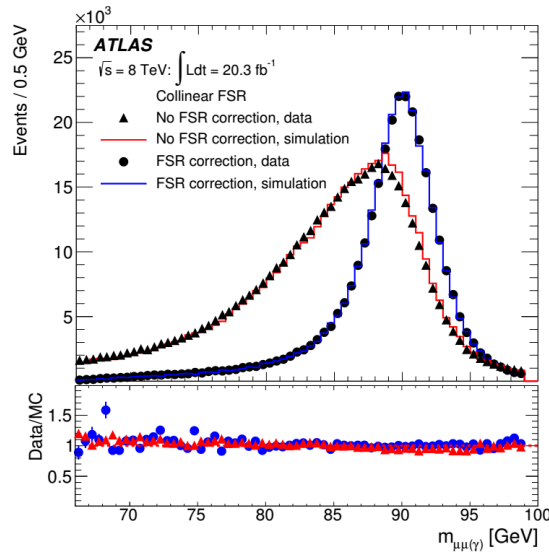
Figure 3.3: *Invariant mass distributions of Z → μ$^+$μ$^-$(γ) events in data before collinear FSR correction (filled triangles) and after collinear FSR correction (filled circles), for events with a collinear FSR photon satisfying SFR selection criteria. The prediction of the simulation is shown before correction (red histogram) and after correction (blue histogram).*

3.5   Reducible Background estimation

The reducible background affecting the H →ZZ*→4ℓ channel can be considered relatively weak. It mainly originates from processes involving a single true Z boson in the final state, associated with misidentified jets as leptons, usually at the low P_T region. Background evaluation is based

on simulation samples, combined with data-driven methods, essentially for the low mass region between 120 - 180 GeV. Since, in this low mass range, at least one from the H decay bosons is off-shell, it mainly decays to low transverse momentum leptons with important reducible background contribution. In the case where the sub-leading Z decays to a di-muon pair, principal background contributions are the pp→Z+$b\bar{b}$→4ℓ and pp→$t\bar{t}$→Wb→4ℓ processes since heavy quarks constitute the main muon background source. In the case of an electron pair decay, jets are the dominant contribution via pp→Z + 2 jets→4ℓ mechanism. Given the diverse background nature for the Z→e$^+$e$^-$ et Z→μ$^+$μ$^-$ channels, processes Z(QQ→μ$^+$μ$^-$) and Z(XX→e$^+$e$^-$) are separately investigated. In spite of their differences, both backgrounds are estimated using the same primary logic:

1. Control regions (CR) are formed, relaxing or inverting specific selection criteria such as to enrich each CR on one background while minimizing signal leakage.
2. The background composition in these regions is studied and compared to simulations
3. Probabilities are calculated for an event belonging to the control region to survive in the signal region ("transfer factors")
4. These probabilities are subsequently used to predict expected background events in the signal region

In the following paragraphs, the background estimation methods for the Z→e$^+$e$^-$ and Z→μ$^+$μ$^-$ are presented.

3.5.1   Z+μμ background estimation

The number and treatment of the different control regions has historically evolved. In the next, the baseline method introduced in 2012 is described, which allows for a better constraint on statistical uncertainties. In this implementation, four main orthogonal control regions are defined:

i.   A region where inverted isolation criteria are required for at least one of the muons of the sub-leading pair, while all standard analysis cuts are applied to leading di-leptonic (Z→μμ or Z→ee) pair. This region is enriched with light flavors (π/K decays).

ii.   A region where an inverted impact parameter significance criteria is required for at least one of the muons of the sub-leading pair, while all standard analysis cuts are applied to the leading di-leptonic (Z→μμ or Z→ee) pair. Because of the inversion of the primary vertex requirement, contributions from b decays (Z$b\bar{b}$ and $t\bar{t}$) are enhanced.

iii.   The eμ+μμ control region, where no isolation or impact parameter significance requirements are applied for the sub-leading muon pair. Standard analysis criteria are implemented for the leading di-lepton pair, while different flavor leptons are required between leading and sub-leading pairs. This region is mainly enriched in $t\bar{t}$ originating leptons.

iv.   The Same Sign control region, where no isolation or impact parameter cuts are applied for the sub-leading di-lepton pair, required to be composed of same sign muon candidates. Again, all standard analysis requirements are requested for leading di-lepton. This region is populated by all 3 main backgrounds (Z$b\bar{b}$, $t\bar{t}$, K/π).

The number of expected background events is extracted from a maximum likelihood fit applied simultaneously to all four control regions. The fit result also allows one to determine background composition of each control region and to evaluate the expected number of background events in the "Reference CR". The latter is defined by considering all events having the leading di-lepton satisfying all analysis criteria while isolation and d$_0$ are not applied to the sub-leading muon pair. Extrapolation factors are computed to estimate the background yields anticipated at the signal region.

The m$_{12}$ distributions are presented in *Figure 3.4* for the four CRs, together with the results of the combined likelihood fit. The corresponding value of m$_{12}$ is adjusted by a Breit-Wigner, convoluted either with a Crystal Ball (for Z +jets sample) or by a second order Chebyshev polynomial

(ttbar). The combined fit result was tested to give the same final yield as when applied in each CR individually. Background composition of the four control regions is presented in *Table 3-5*

Background	inv-d$_0$ CR	inv-iso CR	SS CR	eμ + μμ CR
$Z\,b\bar{b}$	32.8±0.5 %	26.5±1.2 %	30.6±0.7 %	0.3±1.2 %
$Z+light$	9.2±1.3 %	39.3±2.6 %	16.9±1.6 %	0.0±0.8 %
$t\bar{t}$	58.0±0.9 %	34.2±1.6 %	52.5±1.1 %	99.7±1.0 %

Table 3-5: *Expected contribution of the ll+μμ background sources in each of the control region*
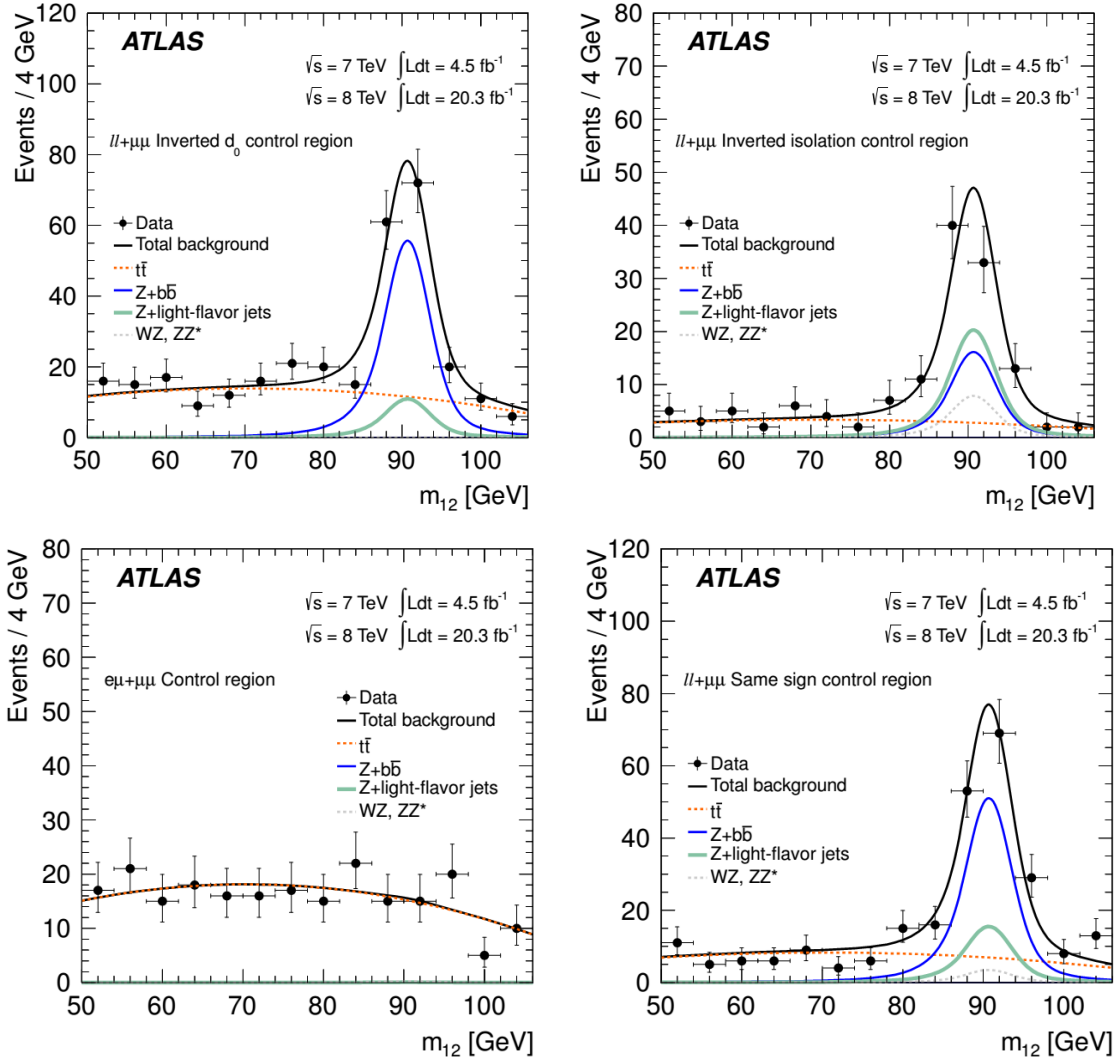
Figure 3.4: *The observed m$_{12}$ distributions (filled circles) and the results of the maximum likelihood fit are presented for the four control regions: inverted requirement on impact parameter significance (top left), inverted requirement on isolation (top right), eμ leading di-lepton, where backgrounds, except from $t\bar{t}$, are small and not visible (bottom left), and (bottom right) same-sign sub-leading di-lepton. The fit results are shown for the total background (black line) as well as the individual components: Z + jets decomposed into Z+b$\bar{b}$ (blue line) and Z + light flavor jets (green line), $t\bar{t}$ (dashed red line), and the combined WZ and ZZ (dashed gray line), where the WZ and ZZ contributions are estimated from simulation.*

To calculate the expected background in the signal region, transfer factors are determined using simulated datasets. These factors can be defined either by using the efficiencies of the control region events to be found in the signal region, or by calculating (through MC datasets) the ratio between

the number of events in the signal region versus the equivalent number of events in the background region. In the first case, the transfer factor is expressed as (*equation 3-2*):

$$f_{transfert} = \varepsilon_{iso}{}^2 \, \varepsilon_{d0}{}^2 \, /(1- \varepsilon_{d0}{}^2) \qquad (\, 3\text{-}2 \,)$$

where ε_{d0} and ε_{iso} are the efficiencies for the secondary muons satisfying the isolation and impact parameter requirements. In the second, more direct method, the ratio is computed by (*equation 3-3*):

$$f_{transfert} = n_{sr}/n_{cr} \qquad (3\text{-}3)$$

where n_{sr} and n_{cr} are the number of events in the signal and the control region respectively.

Although in both methods the transfer factors are computed with simulated data, the second approach is limited by statistics. If only a very small number of events survives the final selection in the MC samples, the transfer factor will have a large corresponding statistical uncertainty. Conversely, the first method utilizes global muon efficiencies ignoring any dependence on the position and transverse momentum. For the $t\bar{t}$ component, with very low statistics, the first method is selected, while for the $Zb\bar{b}$ part, estimations are conducted using the second method. The resulting transfer factors are presented in *Table 3-6*, while any differences between the two methods are included as systematic uncertainties.

Transfer factor (%)	
$Z\,b\bar{b}$	3.10±0.19
Z+light	3.0±1.8
$t\bar{t}$	0.55±0.09

Table 3-6: *Corresponding transfer factors for the $Zb\bar{b}$ and $t\bar{t}$ samples on events passing the Z+μμ selection with a sub-leading di-muon pair.*

Final values are presented in *Table 3-7* for the 2e2μ and 4μ channels separately in 7 TeV and 8 TeV data. Main contribution originates from Zbb events. Systematic and statistic uncertainties are separately calculated.

Run	Background	4μ	2μ2e
7 TeV	Z + jets	0.42 ± 0.21(stat) ± 0.08(syst)	0.29 ± 0.14(stat) ± 0.05(syst)
	$t\bar{t}$	0.081 ± 0.016(stat) ± 0.021(syst)	0.056 ± 0.011(stat) ± 0.015(syst)
	WZ expectation	0.08 ± 0.05	0.19 ± 0.10
	Z+jets Decomposition		
	$Z\,b\bar{b}$	0.36 ± 0.19(stat) ± 0.07(syst)	0.25 ± 0.13(stat) ± 0.05(syst)
	Z + light flavor jets	0.06 ± 0.08(stat) ± 0.04(syst)	0.04 ± 0.06(stat) ± 0.02(syst)
8 TeV	Z + jets	3.11 ± 0.46(stat) ± 0.43(syst)	2.58 ± 0.39(stat) ± 0.43(syst)
	$t\bar{t}$	0.51 ± 0.03(stat) ± 0.09(syst)	0.48 ± 0.03(stat) ± 0.08(syst)
	WZ expectation	0.42 ± 0.07	0.44 ± 0.06
	Z+jets Decomposition		
	$Z\,b\bar{b}$	2.30 ± 0.26(stat) ± 0.14(syst)	2.01 ± 0.23(stat) ± 0.13(syst)
	Z + light flavor jets	0.81 ± 0.38(stat) ± 0.41(syst)	0.57 ± 0.31(stat) ± 0.41(syst)

Table 3-7: *Number of $t\bar{t}$ events estimated and expected at the signal region by the transfer factor method.*

3.5.2   Z+ee background estimation

The Z+ee final state background mainly originates from what is defined as non-prompt or fake electron candidates in the sub-leading di-lepton pair. Such objects may primarily originate from:

- QCD jets misidentified as electrons during reconstruction
- Non-isolated electrons from heavy quark semileptonic decays
- Conversion electrons from photon interactions with detector material

The study and evaluation of these backgrounds is performed using both data and simulated samples, by defining two discreet control regions:

- ✓ The 3l + X control region, where selection criteria are relaxed for the lowest P_T electron (X)
- ✓ The Z+XX control region, where identification criteria are relaxed or inverted for both sub-leading pair leptons.

In simulated samples, access to the truth origin of each electron candidate is available at generator level. By exploiting this information, referred to as truth classification, four categories can be defined, denoted by e, d, f and c, for background analysis:

1. e – true electron: An isolated electron from a W or Z boson decay.
2. q – non-isolated electron: An electron from a b-quark semileptonic decay, usually accompanied by jets or additional tracks.
3. γ - conversion electron: A true reconstructed electron from a photon conversion. The photon may be generated by Bremsstrahlung radiation of one of the final electrons from a Z-decay, a pion decay or even due to FSR of the actual di-boson pair.
4. f – fake electron: Any object not corresponding to a true electron, mainly a misidentified jet.

In data samples, where no truth information is available for electron candidates, a different categorization is developed based on reconstructed variables. Electrons are subsequently quantified as E (electron) or F (fake) with respect to the following definition:

- **_E – Electron:_** In order for a reconstructed electron candidate satisfying Loose Likeli-Hood Particle Identification (LooseLHPID) to be considered as a true electron, the ratio of deposited energy in the strip layer with respect to total energy has to be larger than 0.1 while if the corresponding track traverses an active region of the b-layer, hits in that layer are required. If the object is in the barrel region ($|\eta| < 2.0$) an additional requirement on the ratio of the number of high-threshold hits in the TRT to the total number of hits therein is imposed (R_{TRT}). On the end-caps, a cut on the ratio of the energy distribution in the transverse plane is applied by the R_φ variable, representing the ratio of energy deposited in clusters of 3×3 over 3×7. This ratio is required to be at least 90 %.
- **_F- Fake:_** Any other electron candidate failing the Electron (E) criteria.

Similar to the muon background case, several control regions enriched in background events, are defined by inversing or relaxing normal selection criteria. Background events can subsequently be extrapolated to the signal region using the following three primary methods:

I.   **The 3l+X method,** where a control region is formed from three electrons satisfying all analysis criteria with relaxed cuts applied on the fourth lepton candidate.

II. **The transfer factor method** relying in the Z+XX control region in MC samples, from which background events are extrapolated to the signal region using transfer factors calculated using efficiencies derived from a Z+X control region.

III. **The Reco-truth unfolding method,** where the Z+XX control region composition is obtained by using truth information from simulation and final number of events is extrapolated to the signal region using rescaling factors.

The above methods were historically developed in different periods. Since initially no data statistics was available, only MC samples were used for background estimation. During the evolution of Run 1, a particular effort was devoted in estimating irreducible background with additional methods, in order to constrain uncertainties. It has to be noted that systematic uncertainties differ between the various methods. Although the 3l+X method was used as the baseline for the final Run 1 result, all alternative methods served as a systematic check and as an evaluation of the level of understanding on the estimation mechanism of the expected irreducible background.

3.5.2.1   *The 3l+X method*

In this control region, the three highest E_T leptons of the final quadruplet are required to fully satisfy all analysis cuts. For the lowest E_T electron identification criteria are relaxed and no isolation or impact parameter significance selection are applied. To suppress the ZZ contribution, same sign sub-leading di-lepton pairs are used in the final sample, while any remaining ZZ contamination is estimated at 6 %. If in an event multiple quadruplets can be formed, all combinations with the same leading di-lepton mass (m_{12}) are independently considered as individual events. Since in the 3l+X method only the composition of one lepton is examined, a two dimensional fit is sufficient to accurately investigate the background composition and distinguish between light jets faking electrons, conversion photons - FSR contribution and quark semileptonic decays. Variables used in this approach are the number of b-layer hits ($n_{B-Layer}$), to separate electrons and light jets from conversion photons, and the TRT ratio (R_{TRT}), to discriminate between electrons and light jets.

Using MC samples, an increased statistics Z+X control region is defined, requiring an on-shell Z along with an additional electron candidate satisfying only silicon selection criteria (more than six hit in the silicon tracker with at least one pixel hit). The R_{TRT} and $n_{B-Layer}$ distributions are extracted for each background component, while for the ZZ contribution, a Z+XX control region is defined. Extracted shapes are subsequently simultaneously fitted with data satisfying the 3l+X control region requirements in order to obtain the yield for each background component. For the heavy flavor contribution, due to reduced data statistics, the yield is constrained to the MC obtained one, including a 20 % statistical error and a correction factor of 1.39 and 1.33 for the 4e and 2μ2e channels respectively. The latter is introduced to match the expected yield in data, where individual contributions are estimated using the sPlot [38] method which takes into account kinematic variables of the forth electron according to the 2D fit of the R_{TRT} and $n_{B-Layer}$ variables. A probability is assigned to each event to belong to one of the four electron categories.. Corresponding fits in the 2e2μ and 4e channel separately are presented in *Figures 3.5 and 3.6*.

In order to extrapolate the expected background from the 3l+X control religion to the signal region, efficiencies for the fourth electron to survive the full analysis selection are calculated. These efficiencies can be estimated through MC simulation of on-shell Z boson decays accompanied with an additional lepton candidate (Z+X) and are subsequently rescaled with respect to data. Additional control regions are also defined to extract the data/MC scale factors (SF) in order to correct possible difference in the efficiencies of the γ and f component. For isolated electrons, the scale factors are included in the energy calibration, while for the very small q component, a 40 % uncertainty is assumed. Final efficiencies are computed in bins of P_T, using six different transverse momentum regions.
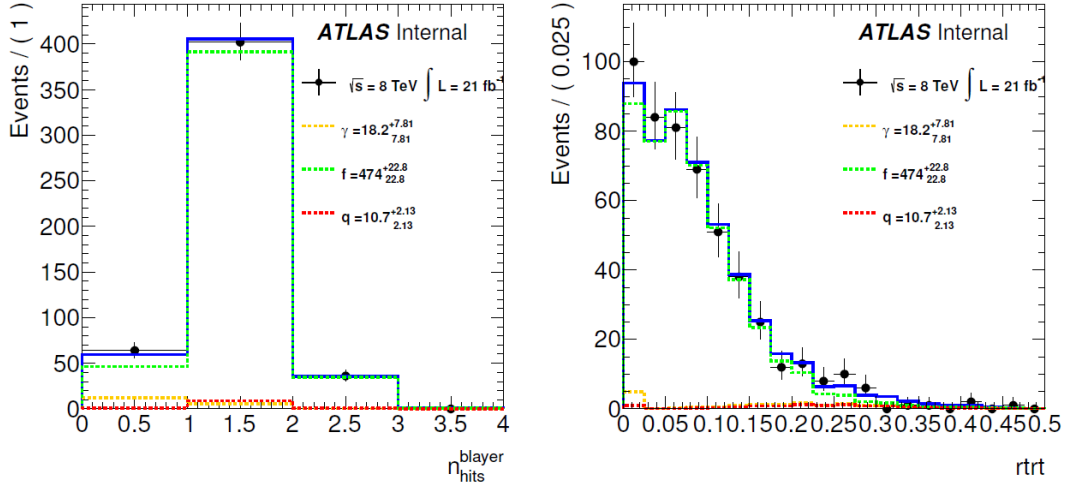
Figure 3.5: *Simultaneous fit result on R_{TRT} and $n_{B\text{-}Layer}$ variables on data and breakdown of the different background contributions for the 2μ2e channel.*
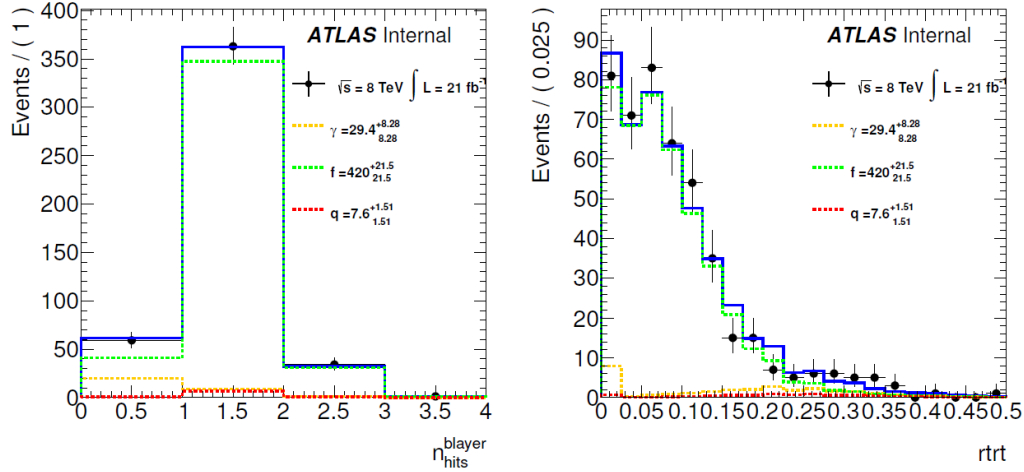
Figure 3.6: *Simultaneous fit result on R_{TRT} and $n_{B\text{-}Layer}$ variables on data and breakdown of the different background contributions for the 4e channel.*

Extrapolation of expected events from the control region to the signal region is performed using the transfer function (*equation 3-5*):

$$TF = \sum_{i=\gamma,f} \varepsilon^i(P_T) \times w^i_{sPlot} \qquad (3\text{-}4)$$

where w^i_{sPlot} is the individual probability of each background component for a single event as it is calculated by the sPlot [38] method and $\varepsilon^i(P_T)$ the P_T dependent efficiencies for the electrons, corrected with the appropriate scale factors. Because of the multiple quadruplets approach, a 10 % increase in the total yield is observed in the control region for both the 4e and 2μ2e modes. To deal with the small statistics of the heavy flavor component, a single inclusive transfer factor has been used.

Final estimated results with their corresponding systematic uncertainties are presented in *Table 3-8*. The latter, take into consideration uncertainties related to the fit quality and to the templates on the data, as well as those concerning the precision of the transfer factors. Transfer factor uncertainties

contain the statistical uncertainty of the MC samples and the scale factors uncertainty, estimated at 4 %. It has to be noted that transfer factor uncertainty is the dominant systematic. After subtraction of the remaining ZZ contribution, 2.88 ± 0.28 (syst) ± 0.54 (stat) events are expected for the 4e channel and 2.91 ± 0.33 (syst) ± 0.60 (stat) for the 2μ2e channel, in the full mass range.

	Type	Data	Fit efficiency	SR yield			
4e	f	$420^{+21.50}_{-21.20}$	0.0034 ± 0.0004	$1.43^{+0.07}_{-0.07}$	(stat)	$^{+0.47}_{-0.47}$	(syst)
	q	$7.60^{+1.51}_{-1.52}$	0.11 ± 0.02	$0.84^{+0.18}_{-0.18}$	(stat)	$^{+0.14}_{-0.14}$	(syst)
	γ	$29.36^{+8.28}_{-7.75}$	0.024 ± 0.004	$0.70^{+0.20}_{-0.20}$	(stat)	$^{+0.20}_{-0.20}$	(syst)
2μ2e	f	$473.7^{+22.8}_{-22.4}$	0.0034 ± 0.0004	$1.49^{+0.08}_{-0.08}$	(stat)	$^{+0.53}_{-0.53}$	(syst)
	q	$10.66^{+2.13}_{-2.13}$	0.09 ± 0.02	$0.96^{+0.26}_{-0.26}$	(stat)	$^{+0.16}_{-0.16}$	(syst)
	γ	$18.2^{+7.80}_{-7.19}$	0.024 ± 0.004	$0.44^{+0.19}_{-0.19}$	(stat)	$^{+0.21}_{-0.21}$	(syst)

Table 3-8: *Estimated yield of each component calculated from the fit on the data and average efficiencies and extrapolation of the yield for each component on the SR. Main systematic uncertainties are evaluated for the estimate of the f and γ contributions. Numbers correspond to 2012 data analysis (20 fb^{-1} at 8 TeV).*

3.5.2.2   *Transfer factor method using the Z+X$^\pm$X$^\mp$ control region with inverted cuts*

In this method, events are selected following the standard analysis criteria with relaxed identification requirements on the secondary di-lepton pair. Electrons used in quadruplet formation are required to pass the normal likelihood identification method. To form the Z+XX control region, subleading electrons have to fail at least the impact parameter significance requirement, isolation cut or likelihood identification process. Candidates used for the subleading di-lepton pair are nevertheless expected to satisfy a softer electron identification selection, *LooseLHID,* where the likelihood maximization threshold has been substantially lowered. Because of this inversion on the isolation and impact parameter significance requirements, irreducible ZZ$^{(*)}$ background contribution is essentially suppressed.

The electron background estimation with the transfer factor method is subdivided in four main steps:

- Using simulated samples, efficiencies are calculated for the sub-leading electron candidate objects of the Z+XX region to pass proper isolation, impact parameter and likelihood electron identification. To increase statistics, this calculation is performed in Z+X control regions, where the X additional object follows the same definition as the sub-leading leptons on the Z+XX region.

- The Z+XX control region is studied and contributions of each component are analyzed

- Transfer factors are calculated for an object in the Z+XX control region to be found in the signal region using calculated efficiencies.

- The number of background events in the signal region is extrapolated from the control region using the transfer factors.

Efficiency calculation from Z+X samples: Z+X samples are defined as events consisting of an on-shell Z boson with primary di-lepton pair satisfying all standard analysis criteria and only one additional electron candidate object passing a relaxed selection (relaxed Likelihood, no impact pa-

rameter, nor isolation cuts). The third electron candidate, which should be well separated with respect to leptons from the primary Z (ΔR > 0.2). Stricter constraints are imposed on the kinematic properties of the Z-boson, required to be within a mass window of 15 GeV from the Z-pole mass (91.1876 GeV), while leptonic decay products must have a transverse momentum greater than 20 GeV. A single lepton trigger is used, assuring that at least one of the final objects is correctly identified, whereas the requirement for exactly three leptons in the final state (two generated by the Z-boson decay and one additional electron candidate) assures the exclusion of the ZZ$^{(*)}$ contribution. Finally, rejection of WZ events is performed with a missing transverse momentum cut at E$_{T\text{miss}}$< 25 GeV.

For the Z+X efficiency calculation, a reconstructed categorization is applied to the third electron candidate. This categorization is restrained only to true electrons (E) and fakes (F), corresponding to the definition detailed in section 3.4.2. In *Table 3-9*, a breakdown of Z+X events is presented in truth categories for the MC samples.

Z+X control sample

[%]	e	q	γ	f
E	0.7±0.0	17.6±0.1	19.9±0.2	61.8±0.3
F	0.1±0.0	1.7±0.0	5.4±0.1	92.9±0.3

Table 3-9: *Composition breakdown of the Z+X sample in truth and reconstructed categories. Yields are presented in % values. Data analyzed from the 2012 Run (20fb^{-1} at 8TeV proton-proton collision energy).*

Efficiencies are computed in bins of P$_T$ and η to account for differences in the kinematic properties of the sub-leading electron candidates between the Z+X and Z+XX samples. Integrated efficiencies are presented in the following table (*Table 3-10*) for data and MC samples. A breakdown for different truth categories is applied in the simulation as well, while a 35 % increase is observed in data with respect to simulated samples.

Category	MC Z+X	Data Z+X
Reco		
E	7.2 ± 0.1	9 ± 0.1
F	1.9 ± 0	2.2 ± 0
Truth (E)		
e	96.1 ± 0.8	
q	17.3 ± 0.4	
γ	8.9 ± 0.2	
f	2.8 ± 0.1	
Truth (F)		
e	85.9 ± 3.4	
q	18 ± 0.8	
γ	7.7 ± 0.3	
f	1.2 ± 0.0	

Table 3-10: *Inclusive efficiencies (in %) for reconstructed (E, F) electron candidates depending on their truth origin (e, q, γ, f). Data corresponds to the 2012 Run (20 fb^{-1} at 8 TeV proton-proton collision energy).*

Definition of the Z+XX region: The Z+XX control region, referred as CR5a, is formed by events having one Z boson satisfying all analysis criteria and two additional electron candidates, both passing *LooseLHID* and failing at least one of the isolation, impact parameter or normal likelihood selection. Truth vs reco composition of the CR5a control region is presented in the following table (*Table 3-11*):

Z+XX control region

[%]	e	q	γ	f
E	0.2±0.0	34.8±1.1	16.1±1.0	48.9±1.9
F	0.0±0.0	4.1±0.3	5.3±0.4	90.5±2.6

Table 3-11: *Breakdown composition of the Z+XX sample in truth and reconstructed categories. Yields are presented in % values.*

A flavor analysis of the number of events in the CR5a region in data and Monte Carlo is presented in the following table (*Table 3-12*). An increase of 20 % is observed in the data with respect to the estimated MC events for the all-electron channel, while for the 2μ2e mode, the effect is less pronounced with only a 5 % difference. These differences are considered as corrections and also taken into account in the systematic uncertainties evaluation. Reconstruction categorization in the data samples is also presented in *Table 3-13* for the electron and muon leading di-lepton pair separately.

	4e	*2μ2e*
Data	653±26	707±27
Z+jets	448.1±15.9	552.0±19.8
Zbb	49.7±1.3	56.9±1.4
tt̄	52.8±0.9	65.0±1.0
WZ	2.3±0.9	2.3±0.2
Total	552.9±19.0	676.2±22.4

Table 3-12: *Number of events in CR5A, in data and in simulation..*

Category	*4e*	*2μ2e*
EE	100±10	99±10
EF	191±14	208±14
FE	117±11	131±12
FF	245±16	268±16

Table 3-13: *Composition of the CR5a events into the reconstruction categories in data.*

Transfer factor calculation: A difference is observed in the truth composition of Z+X and Z+XX Control Regions. Therefore, the efficiencies derived by the Z+X sample cannot be directly used. The overall efficiencies are calculated per truth category from the Z+X region and applied also per category in the ZZ+XX sample with respect to the following model (*equation 3-6*):

$$\varepsilon_x(P_T, \eta)=f_\chi^e(P_T, \eta)\times\varepsilon_x^e(P_T, \eta)+ f_\chi^\gamma(P_T, \eta)\times\varepsilon_x^\gamma(P_T, \eta)+ f_\chi^q(P_T, \eta)\times\varepsilon_x^q(P_T, \eta)+ f_\chi^f(P_T, \eta)\times\varepsilon_x^f(P_T, \eta) \qquad (3-5)$$

where X symbolizes reconstruction category (E, F), f_x^T are the P_T, η dependent fraction of each true category with respect to the reconstruction category and ε_x^T are the efficiencies for the different truth components of the Z+X region as presented in *Table 3-11*.

Individual component efficiencies need to be corrected to account for inconsistences between data and MC, resulting in a 35 % decrease for the latter. Through dedicated control regions, scale factors are calculated for each component, resulting in a factor of 1.0 - 1.2 for γ and 1.2 - 2.0 for fake electron contribution respectively. Finally, transfer factors composed by the above mentioned P_T, η and reconstruction category-dependent efficiencies, are defined with respect to *equation 3-7*). These factors reflect the probability of an event in the Z+XX region to be found in the signal region,

$$TF = \frac{\varepsilon_3 \times \varepsilon_4}{(1-\varepsilon_3)\times(1-\varepsilon_4)} \qquad (3\text{-}6)$$

where ε_3 and ε_4 are the P_T, η and reconstruction category dependent efficiencies of the two sub-leading electron candidates to pass the isolation, impact parameter and electron ID selection of the standard analysis.

Extrapolation in the signal region: Completed transfer factors are applied in an event by event basis to data events within the CR5a region in order to calculate the expected number of events to the signal region. Because of the applied cuts in the Z+X region, ZZ and WZ components are suppressed. To account for any remaining ZZ contribution, the entire method is also applied to a separate ZZ simulated sample and any events found are subsequently subtracted from the expected number of events in the signal region. The result is presented in *Table 3-14* along with the ZZ events to be subtracted, along with the final estimate separately for the muon and electron leading pair cases. Finally, the WZ component is also included to provide a global estimation of the reducible electron background.

Quoted systematic uncertainties take into consideration several contributions. Statistical uncertainties in the transfer factor calculation, which are negligible are considered as well as the statistical uncertainty on the composition of the Z+XX region, estimated in the order of 18 % - 23 %. Finally, the systematic and statistical uncertainties of the Monte Carlo scale factors to fit with data, estimated at 31 % and 33 % respectively is accounted. An additional check was also performed by applying the efficiencies directly as derived by the Z +X composition instead of the Z +XX one. The effect of the composition difference between the two samples results to a corresponding difference of 40 - 60 % in the final estimate.

	4e	*2μ2e*
Extrapolation from CR5a	1.90±0.07(stat)±0.89(syst)	2.09±0.08(stat)±0.90(syst)
ZZ extrapolation from CR5a	0.01±0.00	0.01±0.00
Expected WZ	0.56±0.06	0.44±0.07
Final estimation	2.45±0.10(stat)±0.89(syst)	2.52±0.10(stat)±0.90(syst)

Table 3-14: *Expected electron background events in the control region estimated using the transfer factor method.*

3.5.2.3   *Reco-truth unfolding method – relaxed cuts approach*

Using a similar approach to the Transfer Factor method, a Z+XX background enriched region is defined and its composition is established using both truth and reconstructed information. Subsequently, a more abundant Z+X sample is defined in an equivalent manner and efficiencies are calculated for each of the X candidates to be found in the single region. Finally, transfer factors are calculated and the final number of events is extrapolated for the data in the signal region. This method uses purely MC samples for computations and efficiency calculations.

Definition of the Z+XX region: A Z+XX control region is defined (CR0), where leptons of the sub-leading di-leptonic pair satisfy all analysis criteria with the exception of isolation and impact parameter requirements, while electron candidates pass the *LooseLHID* selection. The XX candidates of selected events are classified following reconstructed categories in EE, EF, FE, FF in descending order of P_T for the sub-leading X. Both data and MC samples are treated, with the latter being composed of the ZZ, ZW, Z inclusive, Z $b\bar{b}$ and $t\bar{t}$ modes along with the Higgs signal at a mass of 125 GeV. A comparison between data and simulations, presented in the following table (*Table 3-15*) demonstrates a good agreement between the two datasets.

	EF	EE	FF	FE	Total
Data	468±21.6	374±19.3	439±21	233±15.3	1514±39
MC	456±15	365.6±10	475±17	229.7±10	1526.4±26.7

Table 3-15: *Data and MC composition of Z+XX events in reconstructed categorization. Data analyzed from the 2012 Run (20 fb^{-1} at 8 TeV proton-proton collision energy).*

Events can be further classified to 16 categories, following the truth origin (e, q, γ, f) of the two additional electrons. The Z+XX sample also includes irreducible ZZ background and Higgs signal contributions, which are subtracted by removing the truth electron component from the final sample. The decomposition of the Z+XX sample is presented in *Table 3-16*, where reconstructed categories are further analyzed with respect to their truth component (4×16 possibilities). This representation is only applied for the $m_{4l} > 110$ GeV region, not including the single Z resonant contribution while, the entire range is presented in *Table 3-17*.

Z+XX

Categories	ee	eq	eγ	ef	qq	qγ	qf	γγ	γf	ff	qe	γe	fe	γq	fq	fγ
EE	121.2	4.3	1.6	4.2	40.5	11.3	42.1	8.3	18	49.4	1	0.4	0.7	9.7	16.9	17.2
FE	15.4	0.4	0.2	0.5	5.3	1.9	4.2	1.7	9.2	100.8	0.1	0.1	1.8	5.1	36.8	31.5
FF	3.3	0	0.1	2.3	1.1	0.4	20.6	1.5	28.4	347.2	0	0	0.3	0.9	17.5	19.1
EF	23.6	1.1	0.6	15.3	9.1	4.5	125	1	68.3	155.8	0.4	0	1.5	0.8	4.1	6.9

Table 3-16: *Z+XX truth composition of reconstructed categories. Uppercase letters correspond to reconstructed electron candidate classification while lowercase to truth origin information. Composition represents the mass range of $m_{4l} > 110$ GeV.*

Z+XXCR0

Categories	ee	eq	eγ	ef	qq	qγ	qf	γγ	γf	ff	qe	γe	fe	γq	fq	fγ
EE	130.3	4.5	1.8	4.5	44.4	11.7	44.3	8.2	20.1	52.4	1	0.4	0.7	10.6	17.9	17.7
FE	16.6	0.4	0.2	0.5	5.7	1.9	4.4	1.8	11.1	100.8	0.1	0.1	2.3	5.4	39.1	34.2
FF	3.6	0.5	0.1	2.5	1.2	0.4	21.9	1.5	31.3	371.3	0	0	0.6	0.9	18.2	21.3
EF	25.5	1.1	0.7	17.2	9.9	4.8	132.9	1.1	82.5	167	0.3	0	1.5	0.9	4.2	7.5

Table 3-17: *Same table as 3-18 but including the entire mass region. Truth category ee is later subtracted since it includes true electrons from the signal as well as ZZ irreducible and single Z resonance contributions. While most of the categories remain largely unaffected with respect to Table 3-17, an increase is observed for the ee category due to the single Z resonant decays.*

Efficiency calculation from Z+X samples: A Z+X sample is used in order to calculate efficiencies for each of individual electrons to be found in the signal region (*Table 3-18*). For the third lepton candidate passing the relaxed identification criteria, no isolation or impact parameter is requested, while, to suppress the WZ contribution, an additional requirement of $E_{T_{miss}} < 25$ GeV is imposed. This study is performed in simulated samples using not only reconstructed categorization but also truth information. In the evaluation of the overall efficiencies for reconstructed categories, truth efficiencies are applied to the composition of the Z+XX table, after being corrected to match data. This difference between the Z+X and Z+XX samples originates from the different definition of X additional objects, as in the Z+XX sample one requires two e-like candidates and therefore selects more non-isolated electrons coming from b-decays (category "q").

Composition in %	e	q	g	f
Z+X Reco-E	0.013±0.003	0.181±0.001	0.225±0.15	0.582±0.170
Z+XX Reco-E	0.031±0.001	0.335±0.006	0.178±0.008	0.457±0.010
Z+X Reco-F	0.001±0.000	0.0179±0.020	0.061±0.010	0.92±0.007
Z+XX Reco-F	0.001±0.000	0.047±0.002	0.055±0.002	0.893±0.005

Table 3-18: *Composition of Z+X and Z+XX control samples for the CR0.*

Use of the Z+X sample provides a more abundant secondary electron candidate pool for precise efficiency calculation, reducing statistical uncertainties. The agreement between data and Monte Carlo concerning reconstructed categorization is quite well with compatibility within statistical uncertainties for the composition (*Table 3-19*). Variation of the Z mass interval and of the lepton P_T allows to estimate systematic uncertainties. An alternative redefinition of the Z+X region includes a stricter selection on the first Z, required to be within a 15 GeV interval of the Z mass, and transverse energy of the leading di-leptonic pair electrons greater than 20 GeV. Although a slight modification of the composition is observed, mainly due to increased photon rejection, agreement between data and simulation stays in the same order as presented in *Table 3-19*. This stricter selection was also used to independently probe efficiencies and calculate the final number of expected events in the signal region.

Z+X	Events	Z+E (%)	Z+F (%)
Data	226217±476	32.11±0.1	67.89±0.1
MC	228550±451	32.36±0.1	67.64±0.1

Table 3-19: *Z+X events in data and simulated samples with composition percentage for the two reconstructed categories.*

To cancel out any kinematical differences between the Z+X and Z+XX samples, efficiencies (and equivalent transfer factors later on) are calculated in bins of transverse momentum and pseudorapidity of the X electron candidate for the Z+X sample. Five E_T bins are used ([7-8], [8-9], [9-12],[12-20] and > 20 GeV) and four distinct eta regions ([0, 1.37], [1.37, 1.52], [1.52, 2.01], [2.01, 2.47]), defined in a manner to equally distribute statistics. For each (E_T, η) bin and reconstructed versus truth category, an efficiency and equivalent transfer factor is computed. *Figure 3.7* demonstrates the truth-reco computed efficiencies in pseudorapidity bins for each E_T region. Reconstructed truth (E) efficiencies are presented on the left side with the F category on the right side, while for the case of the true electrons (category Ee), the efficiency is the highest as expected across all eta regions, ranging from 85 - 95 %.

Integrated numerical values of final efficiencies in data and MC are presented in *Table 3-20* for the reconstructed categorization. A 30 % difference is observed between the two, which has to be taken in to account when applying these efficiencies to data for final background extrapolation. Since the composition of data and MC in the Z+X region is similar (see *Table 3-19*), any incoherence is introduced by an efficiency difference in one or more of the individual categories.

Category	Standard Z selection		Strict Z selection	
	MC Z+e	Data Z+e	MC Z+e	Data Z+e
Global	4.4±0.1 %	5.3±0.1 %	3.6±0.1 %	4.3±0.1 %
Reco-E	8.9±0.1 %	11.3±0.2 %	7.3±0.1 %	8.8±0.1 %
Reco-F	2.2±0.1 %	2.1±0.1 %	1.8±0.1 %	1.9±0.1 %

Table 3-20: *Integrated efficiencies for the Z+e samples in data and MC taking into account two different leading Z selections.*
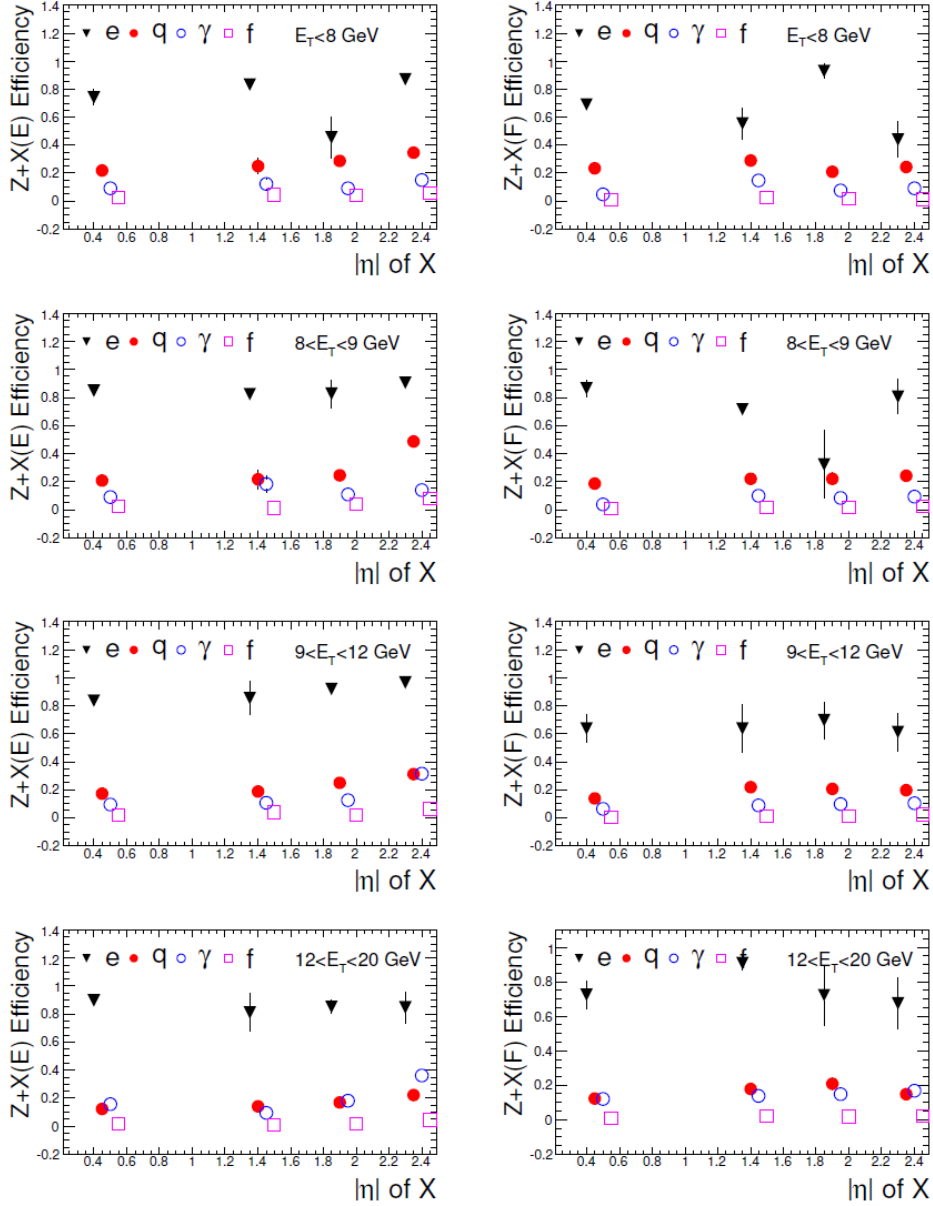
Figure 3.7: *Efficiencies of the Z+X electron candidate as a function of the |η| and E_T bins for the truth and fake reconstructed categories and for all four truth classifications of the additional electron candidate.*

Transfer factor calculation: Final transfer factor is derived taking into account both the composition of the Z+XX sample and the efficiencies extracted from the Z+X sample, in a four dimensional matrix. Two of the dimensions represent the (E_T,η) parameterization while, the other two are referring to the reconstructed versus truth categorization. In this representation, the transfer factor is expressed in the following way (*equation 3-8*):

$$TF_{XX'} = \sum_{xx'pairs} \left\{ f_{XX'}^{xx'} \cdot \varepsilon_X^x(\eta_3, E_{T3}) \cdot \varepsilon_{X'}^{x'}(\eta_4, E_{T4}) \right\} \qquad (3\text{-}7)$$

where X,X′ = E,F the reconstruction and x, x′ = e, q, γ, f the truth categories for the pair of XX electrons. The $f_{XX'}^{xx'}$ represents the fraction of each component in the Z+XX sample as presented in *Table 3-18,* while the ε_X^x correspond to the efficiencies of the third and fourth electron candidate in bins of η and E_T. The number of final events in the signal region is computed by multiplying the corresponding transfer factor to each event in the four dimensional matrix of the Z+XX events with respect to the formula (*equation 3-9*):

$$N_{SR} = \sum_{i=1}^{N_{CR}} TF_i \qquad (3\text{-}8)$$

Extrapolated yields in the signal region are presented in *Table 3-21*. The ZZ and Higgs signal contributions result in the large amount of events in the ee region. Results presented correspond to events with an opposite sign secondary di-electron pair and a strict primary Z selection.

To subtract the ZZ and Higgs contribution accounting for true electrons, one can consider the full mass range and subtract the true electrons. Alternatively, it is also possible to investigate only the mass region of interest between 110 GeV and 170 GeV, where the irreducible di-Z background is minimal, but an eventual subtraction of the true electrons accounting for the Higgs signal has to be made. In both cases, the considered mass range is larger than 110 GeV in order to avoid single Z resonance contribution. In the first case, simulation predicts 1422.8 ± 25.9 events in the control region and 132.4 ± 0.6 (148.9 ± 0.7) events in the signal region for the standard (strict) primary Z selection, dropping to 1259.2 ± 25.1 and 5.2 ± 0.2 respectively when rejecting true electrons. For the second case, a total of 1272.01 ± 25.2 and 15.9 ± 0.3 events are found in the control and signal region respectively, reduced to 10.9 ± 0.2 and 5.0 ± 0.2 accordingly when rejecting true electron contribution. Both methods preserve all other irreducible background components, while any remaining ZZ and Higgs signal contributions are further extracted by the application of the method to the corresponding MC datasets.

Z+e$^{\pm}$e$^{\mp}$ signal region yields (%)

	ee	eq	eγ	ef	qq	qγ	qf	γγ	γf	ff	qe	γe	fe	γq	fq	fγ
EE	99.4	0.6	0.2	0.1	0.8	0.2	0.1	0.2	0.1	0	0.1	0.1	0	0.3	0.1	0
FE	10.1	0	0	0	0.1	0	0	0	0	0	0	0.1	0.1	0.1	0.1	0
FF	1.8	0	0	0	0	0	0	0	0	0	0	0.1	0.1	0	0	0
EF	15.9	0.2	0.1	0.2	0.2	0	0.2	0	0.1	0	0	0	0	0.1	0	0

Table 3-21: *Extrapolated reconstructed category yields with respect to truth composition in the signal region, using efficiencies and transfer factors on the Z+XX control region for a strict primary Z selection. The single Z resonance and Higgs component are not subtracted, accounting for the large ee electron composition yield.*

Extrapolation in the signal region: The calculated transfer factors are applied in the Z+XX sample to extract the probability of an event to pass from the control to the signal region. Given the agreement of the Z+XX composition for the reconstructed categories between data and MC demonstrated in *Table 3-15*, integrated transfer factors in the truth categories can be applied on data to extrapolate the final number of expected background events in the signal region. In data, the H(125) and ZZ contribution cannot be a priori excluded and one can either set the ee equivalent transfer factor to zero or estimate these contribution from MC simulation. Another option would be the application of a Z-mass "veto" within a 30 GeV window, centered at the Z PDG mass value on the secondary di-electron pair. Nevertheless, the ZZ$^{(*)}$ contribution will still remain and will have to be still estimated by a dedicated simulation sample.

Before calculating final results, efficiencies are corrected to match data computed values for the photon and jet component. The final estimation is presented in the following table (*Table 3-22*), yielding 6.9 ± 0.2(stat data) ± 0.2 (stat MC) ± 0.5(syst) events for the standard Z selection and 5.4 ± 0.2 (stat data) ± 0.2 (stat MC) ± 0.5(syst) for the strict one. Using the ZZ sample and after true electron subtraction, it is expected that 1.2±0.4 events will survive to the signal region for the standard Z selection while the H(125) contribution can be considered negligible. As a result, the total number of final quoted reducible electron background is 5.7±0.4±0.5 events. Systematic uncertainties originate from the statistical uncertainty of the composition and efficiencies in the Monte Carlo samples as well as from the efficiency rescaling performed to match data.

m$_{4l}$ *range*	*4e*	*2μ2e*	*Total*
m$_{4l}$ >110 GeV including ZZ Residual	2.9±0.2(stat)±0.3(syst)	3.3±0.2(stat)±0.3(syst)	6.2±0.2(stat)±0.5(systa)
80 GeV < m$_{4l}$ < 600GeV including ZZ residual	3.3±0.2(stat)±0.3(syst)	3.6±0.2(stat)±0.3(syst)	6.9±0.2(stat)±0.5(syst)
Residual ZZ+H(125) for 80 GeV < m$_{4l}$ < 600GeV	0.5±0.2	0.7±0.3	1.2±0.3
80 GeV < m$_{4l}$ < 600GeV	2.8±0.3(stat)±0.3(syst)	2.9±0.3(stat)±0.3(syst)	5.7±0.4(stat)±0.5(syst)

Table 3-22: *Final estimation of the reducible electron background in the signal region. Data analyzed from the 2012 Run (20fb^{-1} at 8TeV proton-proton collision energy).*

The same analysis was also performed with Same Sign sub-leading dilation pairs, naturally excluding any ZZ$^{(*)}$ and H signal contributions. Such an analysis allows a verification of the previously quoted results and especially of the ZZ$^{(*)}$ simulated estimation. Results are calculated separately for the different decay modes of the leading Z:

- Z(ee) + X±X± : 2.4 ± 0.4 ± 0.5 events
- Z(μμ) + X±X± : 3.5 ± 0.6 ± 0.5 events

3.5.3   Final results on the background

In the previous sections, several reducible electron and muon background estimation methods were presented for the H→ZZ*→4l analysis. In the muon case, global and m$_{12}$ fits are performed separately for the jets and top-antitop component while an additional $t\bar{t}$ and WZ evaluation is also carried out using eμ+μμ events and dedicated simulation samples respectively. In the electron case, the 3l+X method is presented, as well as the data-driven transfer-factor method with inversed cuts and finally the reco-truth unfolding method with relaxed selection criteria. As a reference, the global fit method was selected for the muon background estimation while for the electron, the 3l+X process is used. In the following table (*Table 3-23*) an inclusive summary of results is presented for all background estimation methods in 8 TeV, 2012 data.

The total final expected reducible background in 2012 data, as calculated by the reference methods in the four lepton analysis is 13.33±0.74±1.02 events in all final states. In the following plots (*Figure 3.8*) invariant mass distributions of the four leptons are presented in the control region consisting of a Z boson passing full analysis selection and a sub-leading lepton pair of same flavor, where no isolation and impact parameter criteria are applied. Distributions are separately evaluated for the electron and muon case combining 2011 and 2012 data.

3.6   Systematic Uncertainties

For the estimation of systematic uncertainties, several components are considered. Electron and muon identification and reconstruction uncertainties, background estimation uncertainties but also uncertainties concerning delivered luminosity and Higgs production cross-section, used in Monte Carlo simulation weighting.

Luminosity: Normalized integrated luminosity uncertainty is estimated at 1.8 % and 3.6 % for 7 TeV and 8 TeV data respectively, determined using the method detailed in reference [39].

Estimation Method	Expected events
4μ	
Global fit : Z+jets contribution	**3.11±0.46±0.43**
Global fit : $t\bar{t}$ contribution	**0.51±0.03±0.09**
m_{12} fit : Z+jets contribution	2.88±0.83±0.22
m_{12} fit : $t\bar{t}$ contribution	0.42±0.06±0.09
$t\bar{t}$ from eμ + μμ	0.47±0.05±0.08
WZ expectation	**0.42±0.07**
2e2μ	
Global fit : Z+jets contribution	**2.58±0.39±0.43**
Global fit : $t\bar{t}$ contribution	**0.48±0.03±0.08**
m_{12} fit : Z+jets contribution	3.11±0.78±0.44
m_{12} fit : $t\bar{t}$ contribution	0.39±0.07±0.07
$t\bar{t}$ from eμ + μμ	0.44±0.04±0.07
WZ expectation	**0.44±0.06**
2μ2e	
ℓℓℓ + X	**2.91±0.33±0.60**
ℓℓ + XX Transfer Factor	2.52±0.10±0.90
ℓℓ + XX Reco - Truth	2.9±0.3±0.3
4e	
ℓℓℓ + X	**2.88±0.28±0.54**
ℓℓ + XX Transfer Factor	2.45±0.10±0.89
ℓℓ + XX Reco - Truth	2.8±0.3±0.3

Table 3-23: Combined results of all background estimation methods on data for the 2012, 8 TeV dataset in the 80 Gev < m_{4l} < 600 GeV range. The default method is represented by a bold description and a green background color.

Leptons: Lepton reconstruction and identification efficiency uncertainties, as well as transverse momentum resolution and energy scale uncertainties, are determined through W, Z and J/Ψ decay samples. Momentum energy scale and lepton energy uncertainties are estimated in the order of 0.2 %, 0.2 %, 0.3 % and 0.4 % for the 4μ, 2μ2e, 2e2μ and 4e channels respectively. Reconstruction and identification uncertainties are separately evaluated for each lepton flavor.

Electrons: Reconstruction and identification uncertainties on electrons originating from a m_H= 125 GeV Higgs boson are estimated in the order of 9.4 %, 2.4 % and 8.7 % in the 4e, 2e2μ and 2μ2e channels respectively. For electrons with E_T < 15 GeV, an additional 1 % uncertainty is considered.

Muons : For the muons, the corresponding uncertainties related to reconstruction and identification are estimated at 0.8 %, 0.4 % and 0.4 % in 4μ, 2μ2e and 2e2μ modes respectively for a Higgs mass of m_H = 125 GeV.

Additional analysis cuts: Impact parameter and isolation efficiencies are studied using data containing isolated and non-isolated leptons. Isolated leptons are obtained through the Z→ℓℓ process while any additional reconstructed leptons in these events are used as the non-isolated sample. Additional verifications with non-isolated leptons originating from b and c quark semileptonic

decays have been performed using di-jet samples. A good data - simulation agreement is observed and any corresponding systematic effect can be neglected.

Background estimation: Limits on background estimation precision mainly originate from uncertainties on transfer factor calculations of the control region towards the signal region and the number of events available in the control region. Corresponding uncertainties are estimated separately for each method in the previous section.

Theory uncertainties: These are detailed in section 3.2.2 along with the description of the used MC samples for the analysis for the signal and the $ZZ^{(*)}$ background.
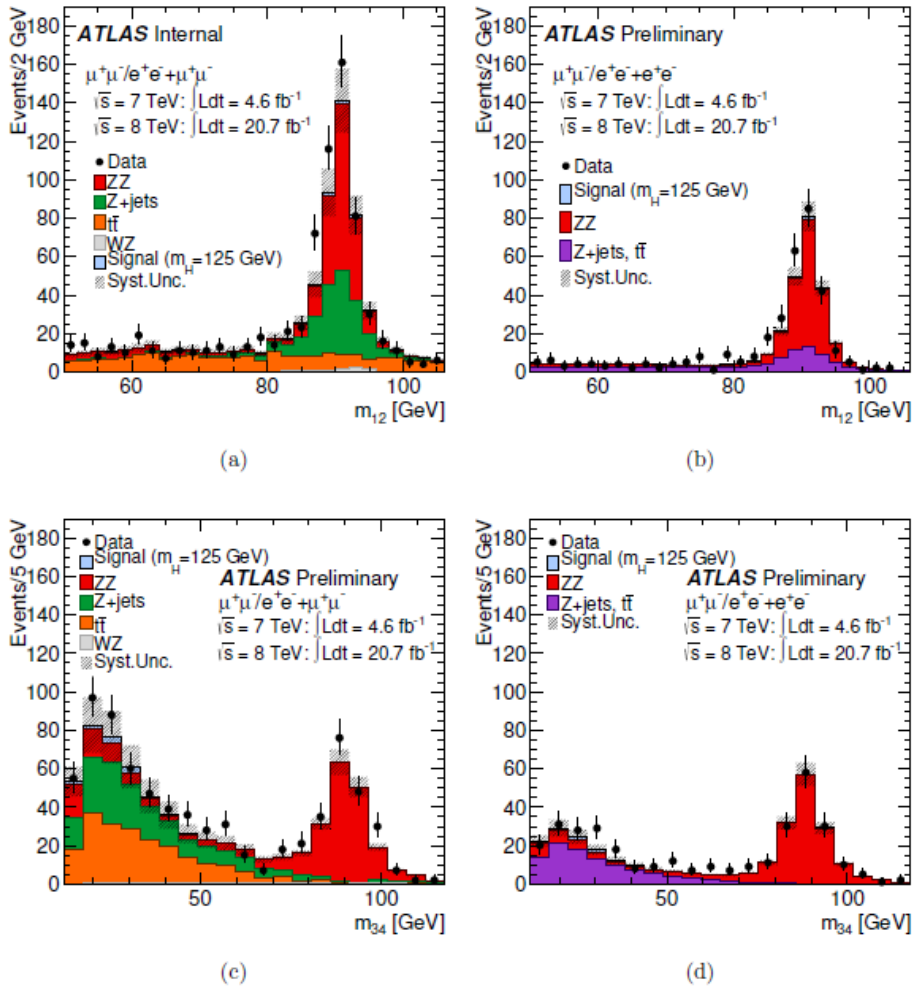
Figure 3.8: *The m_{12} and m_{34} distributions of the Z+ll control region at 8 TeV and 7 TeV data separately presented for the μμ+ee/μμ and ee+ee/μμ channels.*

3.7   Final results

Selection criteria presented at the beginning of the chapter are applied to 8TeV 2012 data representing an integrated luminosity of 20.7 fb^{-1}. A total of 459 candidate events are selected with an $m_{4l} > 100$ GeV, with 151 events in the four muon channel, 225 events in the 2μ2e mode and finally 83 events in the all-electron channel. At the same mass region, 397±14 events are expected through

background processes. A detailed presentation of the results is performed in *Table 3-24* separating the low (m$_{4\ell}$ < 160 GeV) and high (m$_{4\ell}$ ≥ 160 GeV) mass region. The invariant mass distribution of selected events is also presented in *Figure 3.9*.

Mode	4μ		2e2μ/2μ2e		4e	
	Low Mass	*High Mass*	*Low Mass*	*High Mass*	*Low Mass*	*High Mass*
ZZ$^{(*)}$	12.34±0.55	91.53±6.65	14.63±0.90	141.83±10.82	5.41±0.53	55.21±4.43
Z, Z b$\bar{b}$, t$\bar{t}$	1.92±0.63	0.47±0.15	6.14±1.50	1.49±0.36	2.52±0.63	0.61±0.15
Total Background	14.26±0.84	92.00±6.65	20.77±1.75	143.32±10.83	7.93±0.82	55.82±4.43
Data	27	93	28	169	13	55
m$_H$=125GeV	5.80±0.74		7.03±0.95		2.89±0.42	

Table 3-24: *Number of observed events as well as expected background, separated in low and high (m$_{4\ell}$ ≥ 160 GeV) mass regions for √s = 8TeV data. Expected signal events are also presented for the Higgs masse. Systematic uncertainties are included for the signal and background events estimations while all presented results are for m$_{4l}$ > 100 GeV.*
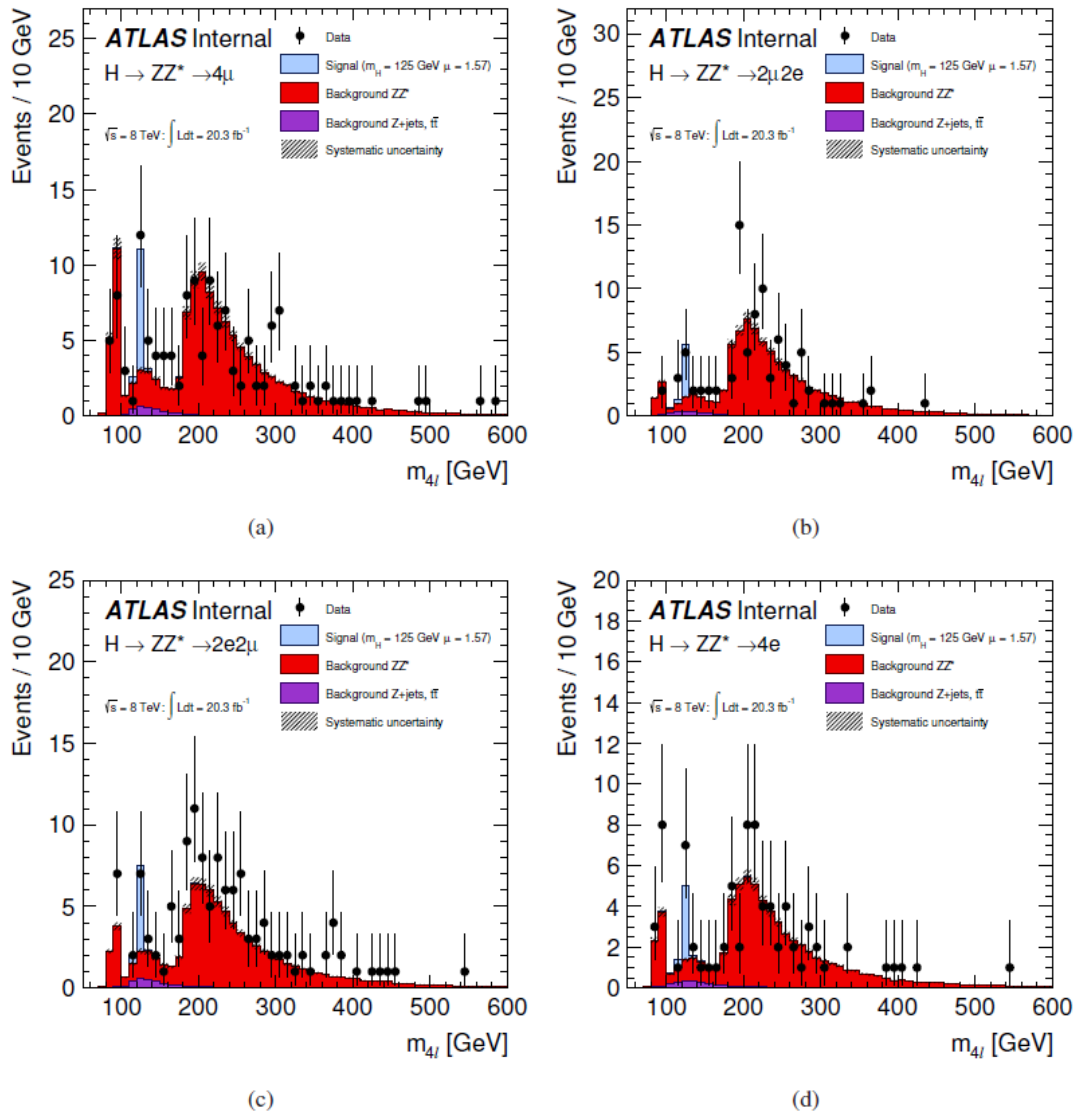
Figure 3.9: *The m$_{4\ell}$ distribution of the selected candidates on √s = 8 TeV data for the different sub-channels of the analysis, compared to the background expectation in the full range: (a) 4μ, (b) 2μ2e, (c) 2e2μ, (d) 4e.*

During data analysis in high energy physics, statistical tools are utilized to confirm or exclude a discovery. This is mainly performed by determining if data are compatible with a given hypothesis or what is the level of incompatibility. Exclusion of a certain hypothesis demands a Confidence Level of at least 95 %, while requirements for discovery are stricter, with the convention for any discovery announcement driven by a signal excess of at least 5σ observed significance. In this case, statistical fluctuations accounting for the observed signal excess represent a probability of one-in-three million.

In statistical procedures the frequentist approach is used while the Bayesian method is used as a check to establish the exclusion limits. The frequentist approach starts by defining a statistical test, t_μ, which aims to quantify the agreement between observed data and predictions. It is more interesting to study the "signal strength" parameter. This parameter is expressed as $\mu = \sigma / \sigma_{SM}$ where σ_{SM} represents the production cross-section of the Standard Model. The signal strength is defined as $\mu = 0$ at the background noise model only while $\mu = 1$ corresponds to the Standard Model signal. In our case, the statistical test is used to discriminate background noise events from signal.

The statistical test is evaluated using a maximum likelihood fit of the signal and background models to data. For higher limits, the Confidence Levels prescription is used, with a frequentist approach [40, 41]. The following plot (*Figure 3.10*) demonstrates the maximum expected and observed limits on the cross-section with respect to the Higgs mass (m_H) for a combination of 2011 and 2012 data. The probed region extends from 110 GeV to 600 GeV, with the major part being excluded apart the area with $m_{4l} < 129.5$ GeV where a large excess is observed.
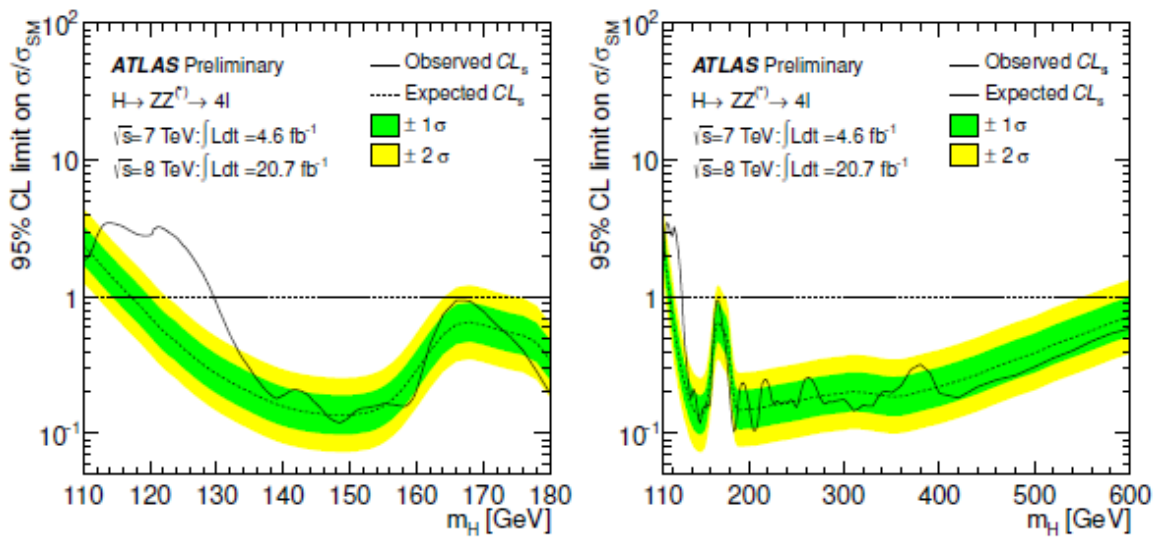
Figure 3.10: *Upper limit within 95 % Confidence level on the Standard Model Higgs production cross-section for 2011 and 2012 combined data. The dashed line represents expected values whereas the continuous presents measured data. The green and yellow regions are respectively the ±1σ and ±2σ limits. On the left plot, only the low mass region is presented while in the right, the entire probed mass interval is displayed.*

The significance of an excess is defined by the probability p_0, where 1 corresponds to the $\mu = 0$ value implying a purely background observed pattern. Thus, p_0 represents the probability that any data observation may be attributed to a background fluctuation. Consequently, the lower p_0 is, the more unlikely it is that any observed excess is due to local fluctuation generated by background noise and can be attributed to a signal. In *Figure 3.11* local p_0 is presented according to m_H, for the combination of $\sqrt{s} = 7$ TeV and $\sqrt{s} = 8$ TeV data. Local p_0 is obtained by using the asymptotic approximation detailed in reference [42].
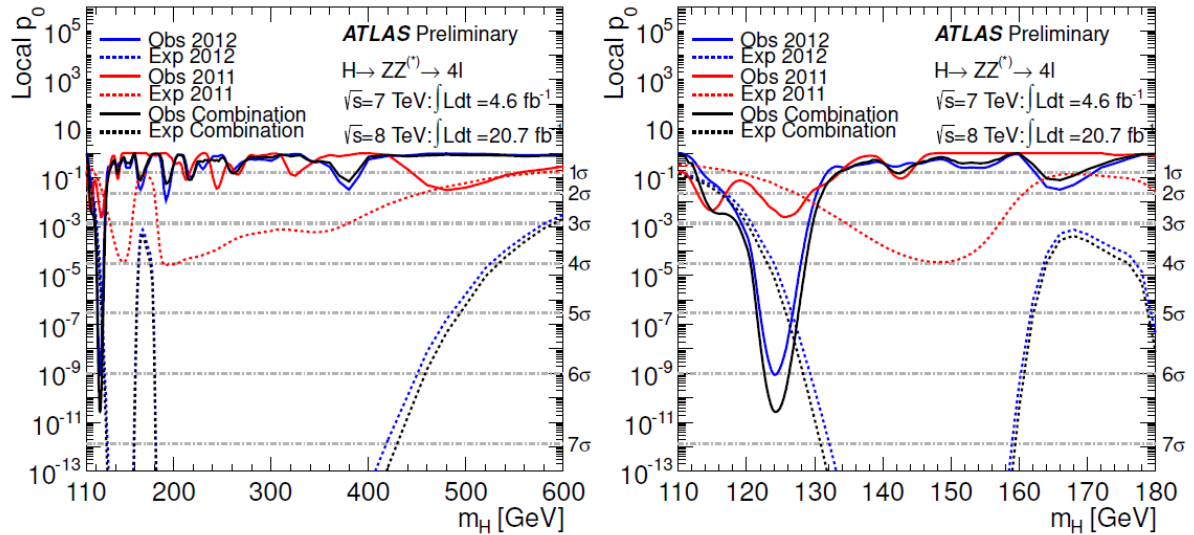
Figure 3.11: *Plots of the local p$_0$ value for 2011 (red curve), 2012 (blue curve) data and their combination (black curve) with respect to the Higgs mass. Dashed lines present the expected p$_0$ in the background only hypothesis with dashed horizontal lines corresponding to local significance. On the left hand side the entire mass range is presented while in the right figure only the lower region is plotted.*

Figure 3.12 shows the profiled likelihood based m$_H$ estimation is determined for the combination of the 2011 and 2012 data. The value of the mass adjusted from the profiled likelihood is m$_H$ = 124.3 +0.6/-0.5(stat) + 0.5/-0.3(system) GeV, where the systematic uncertainty is dominated by the energy and momentum scale uncertainties.
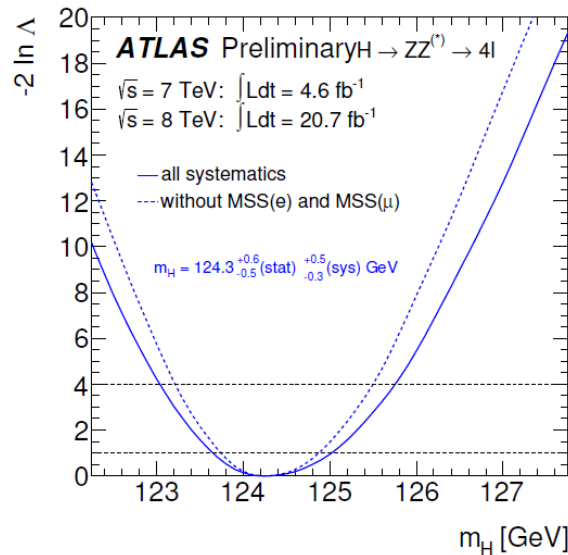
Figure 3.12: *Profiled likelihood plot with respect of the m$_H$ values for the combination of 2011 and 2012 data. The continuous line takes into account systematic uncertainties in the electron and muon energy scale while the dashed line is calculated without uncertainties. The 68 % confidence level is defined by the point where the curve intersects the horizontal line corresponding to 1.*

The overall signal strength, μ, acts as a global scale factor on the total number of events predicted by the Standard Model for each Higgs boson signal processes. *Figure 3.13 a*, presents the signal strength a function of m$_H$ for the combination of 2011 and 2012 data. In *Figure 3.13 b*, a simulated Standard Model Higgs boson signal is injected at the background. Blue strips represent

the range of statistical test -2lnλ(μ) < 1, where λ is the likelihood profiled ratio representing an approximately ±1σ variation.
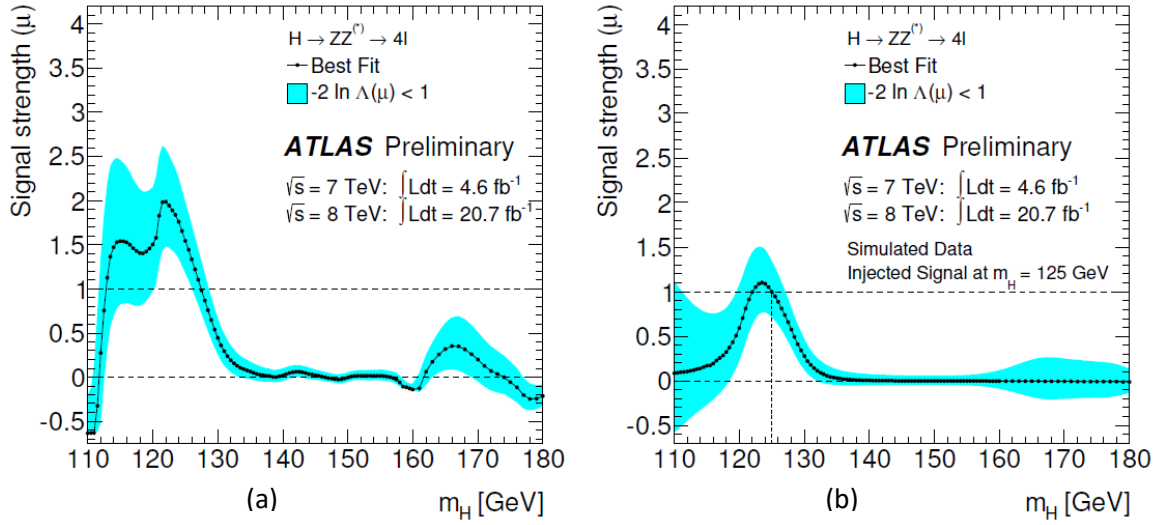
Figure 3.13: *On the right: signal strength μ = σ/σ$_{SM}$ with respect to m$_H$ for the combined 2011 and 2012 dataset. On the left: signal strength with respect to m$_H$ when a Higgs signal hypothesis for a m$_H$= 125 GeV is injected in the simulated background.*

Figure 3.13 presents the best signal strength fit with respect to m$_H$ using a profiled likelihood ratio approach, with 1 and 2 σ limits. The contours correspond to 68 % and 95 % confidence level at the asymptotic limit. Signal strength in the nominal mass value of m$_H$ = 124.3$^{+0.6}_{-0.5}$ (stat) $^{+0.5}_{-0.3}$ (syst) GeV is of 1.7$^{+0.5}_{-0.4}$.
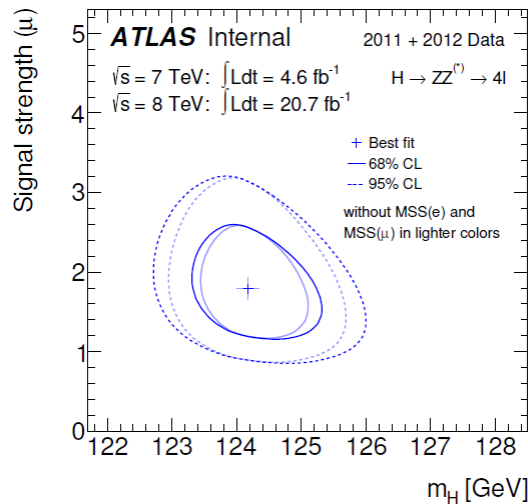
Figure 3.14: *Best fit between signal strength and m$_H$ as well as profiled likelihood ration contours corresponding to 68 % and 95 % confidence level at the asymptotic limit. Bold curve includes uncertainties on the electron and muon energy scale.*

3.8   Conclusions

The advantage of the H→ZZ*→4l channel is the low background pollution, in particular around 125 GeV. Nevertheless the reducible component, composed of misidentified or non-isolated objects

(muons or electrons), was the field of intensive studies during Run 1. The multiple methods developed during this period and aiming to constrain systematic uncertainties on background estimation have been extensively discussed. A special emphasis is attributed to the electron channel background.

The analysis allowing the discovery of the Standard Model Higgs boson in the H→ZZ$^{(*)}$→4l channel has been presented, based on 2011 LHC data of √s=7 TeV as well as 2012 data of √s=8 TeV with 4.8 fb^{-1} and 20.3 fb^{-1} integrated luminosity respectively. An excess of events with a significance of 8.1 standard deviations is observed, corresponding to a mass of $m_H \approx 124.3$ GeV. The profiled mass and signal strength (σ/σ_{SM}) for a Standard Model Higgs-like particle is m_H=124.3$^{+0.6}_{-0.5}$(stat.)$^{+0.5}_{-0.3}$(syst.) GeV and μ =1.7$^{+0.5}_{-0.4}$ respectively. In the mass search region of 125±5 GeV, a total of 37 events are detected while 10.36 are expected from background sources. In sub-channels with a sub-leading electron-pair (4e and 2mu2e), 14 events are observed with 4.08 expected from background. The fraction of the reducible background is estimated at 27%. A very good agreement between all reducible electron background estimation methods is observed. In particular, the developed truth-reco unfolding method is within 1% of the nominal 3l+X method, predicting 2.8 ± 0.3 ± 0.3 events over the full mass range (80 GeV – 600 GeV). Such an agreement allows to significantly lower systematic uncertainties on background estimation and demonstrates a good understanding of the physical processes.

3.9   References

[1]   The ATLAS collaboration, "Measurements of Higgs boson production and couplings in the four-lepton channel in pp collisions at center-of-mass energies of 7 and 8 TeV with the ATLAS detector", arXiv:1408.5191v3 [hep-ex], fEBRUARY 2015

[2]   The ATLAS collaboration, "Measurement of ZZ production in pp collisions at sqrt(s) = 7 TeV with the ATLAS detector and limits on anomalous ZZZ and ZZγ couplings", JHEP03 128, March 2013

[3]   ATLAS Collaboration, Eur. Phys. J. C 70 823 (2010), arXiv:1005.4568 [physics.ins-det]

[4]   S. Agostinelli et al., Nucl. Instr. and Meth. A 506 250 (2003)

[5]   P. Nason, J. High Energy Phys.11 040 (2004), arXiv:hep-ph/0409146

[6]   S. Frixione, P. Nason, C. Oleari, J. High Energy Phys.11 070 (2007), arXiv:0709.2092 [hep-ph]

[7]   S. Alioli, P. Nason, C. Oleari, E. Re, J. High Energy Phys.06 043 (2010), arXiv:1002.2581 [hep-ph]

[8]   S. Alioli, P. Nason, C. Oleari, E. Re, J. High Energy Phys.04 002 (2009), arXiv:0812.0578 [hep-ph]

[9]   P. Nason, C. Oleari, J. High Energy Phys.02 037 (2010), arXiv:0911.5299 [hep-ph]

[10]   D. de Florian, G. Ferrera, M. Grazzini, D. Tommasini, J. High Energy Phys.06 132 (2012), arXiv:1203.6321[hep-ph]

[11]   M. Grazzini, H. Sargsyan, J. High Energy Phys.09 129 (2013), arXiv:1306.4581 [hep-ph]

[12]   T. Sjostrand, S. Mrenna, P. Z. Skands, J. High Energy Phys. 05 026 (2006), arXiv:hep-ph/0603175

[13]   T. Sjostrand, S. Mrenna, P. Z. Skands, Comput. Phys. Commun. 178 852 (2008), arXiv:0710.3820 [hep-ph]

[14]   P. Golonka, Z. Was, Eur. Phys. J. C 45 97 (2006), arXiv:hep-ph/0506026

[15]   N. Davidson, T. Przedzinski, Z. Was, arXiv:1011.0937 [hep-ph]

[16]   S. Jadach, Z. Was, R. Decker, J. H. Kuhn, Comput. Phys. Commun. 76 361 (1993.

[17]   P. Golonka, B. Kersevan, T. Pierzcha la, E. Richter-Was, Z. Was, and M. Worek, Comput. Phys. Commun. 174 818 - 835 (2006), arXiv:hep-ph/0312240

[18]   A. Djouadi, M. Spira, P. M. Zerwas, Phys. Lett. B 264 440 (1991)

[19]   S. Dawson, Nucl. Phys. B 359 283 (1991)

[20]   M. Spira, A. Djouadi, D. Graudenz, P. M. Zerwas, Nucl. Phys. B 453 17 (1995), arXiv:hep-ph/9504378

[21]   S. Catani, D. de Florian, M. Grazzini, P. Nason, J. High Energy Phys. 07 028 (2003), arXiv:hep-ph/0306211

[22]   U. Aglietti, R. Bonciani, G. Degrassi, A. Vicini, Phys. Lett. B 595 432 (2004), arXiv:hep-ph/0404071

[23]   S. Actis, G. Passarino, C. Sturm, S. Uccirati, Phys. Lett. B 670 12 (2008), arXiv:0809.1301 [hep-ph]

[24]   M. Ciccolini, A. Denner, S. Dittmaier, Phys. Rev. Lett. 99 161803 (2007), arXiv:0707.0381 [hep-ph]

[25]   M. Ciccolini, A. Denner, S. Dittmaier, Phys. Rev. D 77 013002 (2008), arXiv:0710.4749 [hep-ph]

[26]   K. Arnold et al., Comput. Phys. Commun. 180 1661 (2009), arXiv:0811.4559 [hep-ph]

[27]   M. L. Ciccolini, S. Dittmaier, M. Kramer, Phys. Rev. D 68 073003 (2003), arXiv:hep-ph/0306234

[28]   CERN-2011-002 (2011), arXiv:1101.0593 [hep-ph]

[29]   A. Bredenstein, A. Denner, S. Dittmaier, M. M. Weber, Phys. Rev. D 74 013004 (2006), arXiv:hep-ph/0604011

[30]   T. Melia, P. Nason, R. Rontsch, G. Zanderighi, J. High Energy Phys. 11 078 (2011), arXiv:1107.5051 [hep-ph]

[31]   T. Binoth, N. Kauer, P. Mertsch, arXiv:0807.0024 [hep-ph]

[32] S. Dittmaier, C. Mariotti, G. Passarino, R. Tanaka (Eds.), "LHC Higgs cross-section working group", CERN-2012-002 (2012), arXiv:1201.3084 [hep-ph]

[33] M. Botje et al., arXiv:1101.0538 [hep-ph]

[34] H.-L. Lai, M. Guzzi, J. Huston, Z. Li, P. M. Nadolsky, J. Pumplin, C.-P. Yuan, Phys. Rev. D 82 074024 (2010), arXiv:1007.2241 [hep-ph]

[35] M. L. Mangano, M. Moretti, F. Piccinini, M. Treccani, J. High Energy Phys. 01 013 (2007), arXiv:hep-ph/0611129

[36] ATLAS Collaboration, ATLAS-CONF-2012-143 (2012). https://cds.cern.ch/record/1491697.

[37] ATLAS Collaboration, ATLAS-CONF-2012-123 (2012). https://cds.cern.ch/record/1473426

[38] M. Pivk, F. Le Diberder, "sPlots: A statistical tool to unfold data distributions", Nucl. Instr. and Meth. 555 (2005) 356–369

[39] Georges Aad et al., "Improved luminosity determination in pp collisions at $\sqrt{s} = 7 TeV$ using the ATLAS detector at the LHC", Eur.Phys.J., C73:2518, 2013

[40] A. L. Read, "Presentation of search results: the CLs technique", J. Phys. G, 28(10):2693–2704, 2002.

[41] G. Cowan, K. Cranmer, E. Gross, O. Vitells, "Asymptotic formulae for likelihood-based tests of new physics", European Physical Journal C, 71 :1554, February 2011

4   Beyond Run 1: Phase II HL-LHC upgrades

4.1   ATLAS Run 2 Upgrade

During the LHC 2012 - 2014 two year shutdown, several improvements where implemented to the ATLAS detector and computing systems in preparation for Run 2 and the increased energy of 13 TeV. Bunch spacing is 25 ns at 13 TeV, with estimated 1 - 1.7×10^{34} cm^{-2}s^{-1} instantaneous luminosity. The energy increase to 13 TeV, the reduced bunch spacing and the 20 % increase in the proton-proton interaction cross-section (*Figure 4.1*) lead to a factor of 2 increase in expected instantaneous luminosity. Combined with doubling of the hard interaction cross-section, a significant increase in the amount of single object triggers is also anticipated [1]. Upgrades where mainly implemented in the ATLAS trigger and inner tracker systems to cope with deteriorating experimental conditions and ensure pile-up rejection.
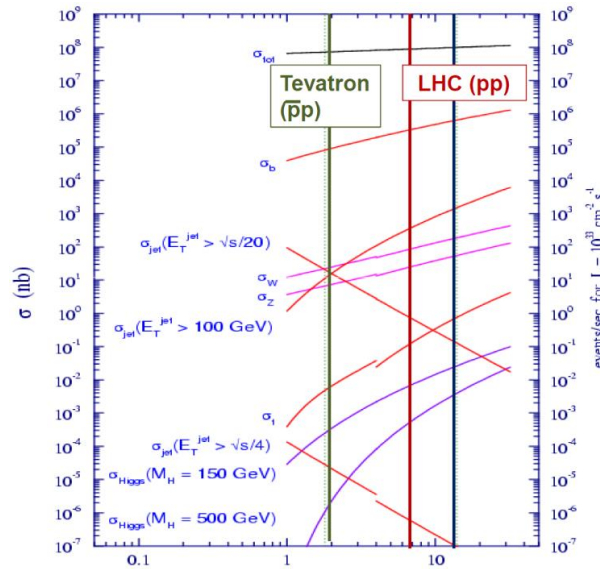
Figure 4.1: *Proton interaction cross-section for Tevatron (green line) and LHC at 7 TeV (red line) and 13 TeV (blue line). A 20 % increase with respect to 7 TeV cross-section is expected with the increase of energy.*

4.1.1   ATLAS Run 2 Upgrades

A major ATLAS upgrade was the installation of an additional pixel layer, the Insertable B-Layer (IBL), placed adjacent to the beam pipe at a radius of 30mm from the interaction point. [2]. Following the same principle as for the existing pixel detector, modules are arranged into 14 staves (*Figure 4.2*) combining planar sensors for central and 3D pixels for high eta regions. Pixel size was reduced to 50 μm × 250 μm, arranged in double (for planar) and single (for 3D) chip slim edge matrices. A new read-out front-end integrated circuit was designed (FE-I4) with a corresponding size of 2 mm × 2 mm and radiation tolerance up to 5×10^{15} n$_{eq}$/cm^2. Installation was completed at the end of 2014 while cosmic events have already been reconstructed with the use of the new layer. Because of its proximity to the interaction point, the IBL is susceptible to high radiation damage and increased occupancies. Expected fluence to the surface of the silicon sensors is estimated at 3.3×10^{15} n$_{eq} \bullet$ cm^2, assuming a 550 fb^{-1} integrated luminosity with very small variations with respect to the z axis.

During the LHC 2013-2015 shutdown, the muon Cathode Strip Chamber (CSC) readout system has also been upgraded [3]. The improved read-out design, based on the Reconfiguration Cluster Element (RCE) concept, allows for high bandwidth and is able to handle the higher Level-1 trigger

rate of 100 kHz and the higher occupancy at Run 2 luminosity. RCE design is centered on a new processor centric Xilinx Zynq series with an ARM processor embedded in FPGA fabric and high speed I/O resources. Coupled with auxiliary memories, the system forms a versatile DAQ bloc allowing applications to access both software and core firmware resources. A carrier board allows for the formation of a DDAQ cluster, hosting several RCE mezzanines interconnected via an embedded network [4]. System installation was completed in 2014.
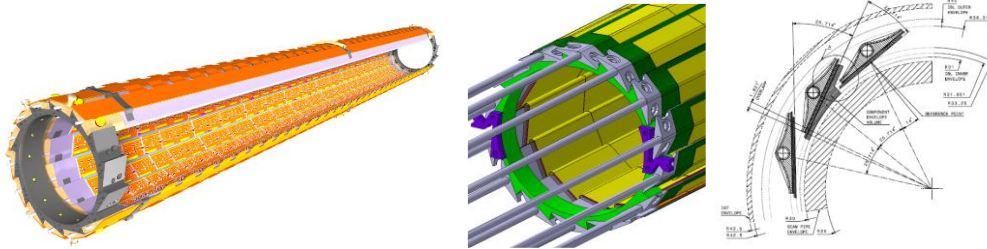
Figure 4.2: *IBL layout in the longitudinal direction (left and middle) and in the r-φ plane (right) with the pixel staves visible.*

4.1.2   Physics motivation beyond Phase I

The 2012 discovery of the Higgs boson at a $m_H \approx 126$ GeV marked the LHC era and presents opportunities for studying the electroweak symmetry breaking [5, 6]. The accumulated statistics allowed to verify to quite high level the compatibility of the discovered boson with the SM predictions, as far as its production, couplings to bosons, spin and parity are concerned (see 1.7.1-1.7.2). Not all production modes, nor all couplings have been identified, because of the lack of statistics. In order to further probe the new particles compatibility with the Standard Model Higgs boson, a vast quantity of data is needed, concerning its spin and parity, couplings determination and self-coupling studies through interference effects. In addition, Higgs scattering data can be used as probes for beyond the standard model phenomena and electroweak precision measurements [7]. Concerning BSM searches, no evidence has been reported in 7 - 8 TeV collisions, allowing limits to be placed for strongly produced SUSY in the TeV scale and up to 203 GeV for other new particles.

We are currently at the first part of the LHC Run at 13 TeV. The increase of collision energy opens wide the searches for new physics, combined with the higher expected luminosity (100 fb^{-1} till end 2018). On the Higgs boson side, confirmation of Standard Models predictions with higher precision and observation of remaining production and decay channels is the imminent priority. Several extended Higgs sector models predict coupling deviations from Standard Model values of arbitrary nature. While measurements have already started in LHC, an increase in luminosity by a factor of 10 will achieve precision improvement for already established channels. For the H→γγ in the 0-jet and di-jet VBF modes, the H→ ZZ*→4l, the H→WW*→ℓνℓν in the 0-jet and 2-jet VBF categories [5] and H→ τ$^+$τ$^-$ for the VBF mode [4] a 50 % improvement is anticipated [8]. Coupling ratio uncertainties (see section 1.7.2) are expected to improve by a factor of 2 in all cases, achieving a 5 % precision for the ZZ channel.

Rare production and decay modes, notably the WH(→γγ) / ZH(→γγ), H→μμ and ttH→(γγ) which can provide valuable contributions to the general couplings fit, will become available at increased statistics. A 6 σ sensitivity for the inclusive H→μμ channel and 100 events for each of the other modes are expected at 3000 fb^{-1} integrated luminosity while around 18 (ttH case) events are estimated at Run 2 using Run 1 extrapolations for 300 fb^{-1} at 13 TeV. At the end of LHC Run 2 with 300 fb^{-1} anticipated integrated luminosity, 3 % and 9 % uncertainties are estimated for the κ_v and κ_F factors included in the minimal couplings fit with no additional BSM contributions [9]. These experimental uncertainties are expected to evolve to 2 % and 3.5 % respectively, for a 10-times luminosity increase. Finally, a measurement of the Higgs self-coupling is needed to reconstruct the

corresponding potential and establish the mechanism as responsible for electroweak symmetry braking. Higgs pair production can be used as direct analysis probe for the trilinear self-coupling but, at hadron colliders and for a mass of $m_H \approx 125$ GeV, has a weak cross-section of 34^{+6}_{-5}(QCD Scale) $\pm$ 1(PDF) fb through gluon-gluon fusion. An increased luminosity is therefore required to probe this process at the clearest decay channel ratio of H(bb)H($\gamma\gamma$) which presents an increased branching. A significance of 3σ may be achieved in observation of this process, with essential improvements on identification efficiencies. An accuracy of 30 % is estimated at the most optimal case for the measurement of the λ_{HHH}, combining both ATLAS and CMS expected events at 3000fb^{-1}[10].

Rise of the weak boson scattering cross-section in the longitudinal mode at the TeV scale has always been an inspiration for new physics. While Higgs induced compensation is expected in the standard model, other processes are possible, like Technicolor, little Higgs or even models including the standard Higgs mechanism that may include an additional light scalar particle and TeV resonances. Using ZZjj channels in the 300 fb^{-1} luminosity expected at the end of Run 2, a 30 % statistical precision is estimated in the electroweak cross-section measurement for $m_{jj} > 1$ TeV, value that does not allow for definite conclusions on most of the alternative theories.

SUSY remains at the heart of all LHC experimental searches and most up-to-date exclusion limits originate from 7 - 8 TeV LHC datasets. Assuming a light LSP (Lightest Supersymmetric Particle), exclusion boundaries for squarks and gluinos are currently at 1.4 TeV and 1.0 TeV respectively [11]. Looser constraints have been placed on third generation squarks [8] gauginos and leptons [12, 13] where limits depend on the assumed SUSY mass spectrum. While limits will further improve with the expected 14 TeV dataset, exclusion will remain weak at 2.8 TeV exclusion mass for the gluino and 2.4 TeV for the squark at the end of Run 1 [14].
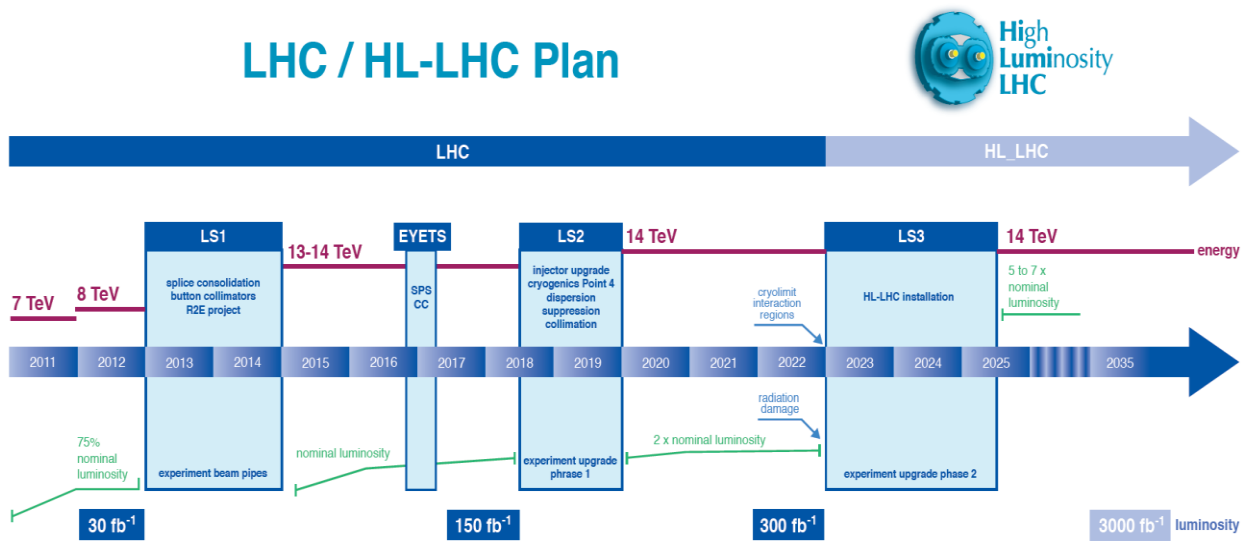
Figure 4.3: *CERN LHC long term operation schedule. Run 2 and 3 extend up to 2022 when the last programmed technical stop will take place to install HLL-LHC upgrades.*

Finally, a luminosity upgrade would substantially increase exotics discovery potential. Although several models exist with different features, high P_T leptons, photons, jets and missing ET are common ground and have to assure that any detector design maintains sensitivity to these signatures. High mass top resonances corresponding to a Kaluza-Klein gravitons in the Randall-Sundrum model as well as di-lepton resonances originating from a Z' at the topcolour model are referred as characteristic examples whose mass reach will significantly benefit from a luminosity increase.

Current LHC operations planning extends to end of 2022, including a prolonged technical stop between the third quarter of 2018 and the end of 2019 for injector and cryogenic systems replacement as well as cavern preparation work for ATLAS and CMS detector upgrades [15]. Concluding Run 2 at the end of 2022 (*Figure 4.3*), a total integrated luminosity of 300 fb^{-1} is expected since the beginning of data taking in 2011 [16].

With the strong physics incentive in various domains detailed above, an upgrade program has been decided to extend LHC operation for an additional 10-year period, with technical stops every 3 years, accounting for a cumulative 8 years data time. Phase II High Luminosity runs aim at a total integrated luminosity of 3000 fb^{-1} before LHC decommissioning. To achieve this figure, initial Phase II upgrade studies concentrated on a peak luminosity of 5×10^{34} cm^{-2}s^{-1} corresponding to an average of 140 interactions per crossing and 25 ns spacing. However, pushing up to the technical limits of the machine, a scenario for 7.5×10^{34} cm^{-2}s^{-1} peak value is suggested, corresponding to a value of μ=200 with a 300 fb^{-1} per year delivered luminosity.

4.2   HL-LHC Upgrade Scenarios

Design goals for ATLAS Phase II upgrades focus to an efficient detector operation under these conditions while dedicated studies are performed to investigate the physics potential of eventual detector extensions at high eta regions. Channels previously discussed impose different requirements on detector performances with respect to final state topology. Higgs studies in gluon-gluon production mode via the ZZ*and μμ channels strongly depend on lepton reconstruction and triggering efficiency while, good vertex definition and PileUp mitigation is imperative for the VBF production studies, characterized by forward jets at $|\eta| > 2.5$. Studies on the exotics and SUSY, including Z', are strongly affected by lepton trigger and reconstruction efficiencies, missing E$_T$ and flavor tagging as well as jet vertex association in conjunction with boosted objects identification. Finally, Kaluza-Klein searches are mostly affected by b-tagging performance since a b di-jet pair is expected at the final state [15].

Three upgrade scenarios were defined, with an attempt to satisfy operational and physics requirements for Phase II, based on LS1 detector improvements and representing evolutions in design and technology of already introduced techniques. These model scenarios, studied under the demand of the LHC Scientific Committee, correspond to different upgrade levels of the current layout and are presented in a decreasing order of estimated cost. While the physics case for the High Luminosity upgrade is solid, the extend of detector improvements depends on a combination of estimated cost and expected performances. In that context, the three following scenarios were individually studies and relevant physics performance and discovery potential were evaluated:

1. *Reference scenario:* A trigger update will be implemented for L0 and L1 triggers, working at 1Mz and 400 kHz rates respectively, while high level trigger is set at 100 kHz. Though the pixel tracker system is extended to η = 4.0 with 12 end-cap discs, barrel layers remain to the current number of 3 with a foreseen reduction in pixel size (*Figure 4.4*). A complete replacement of the TRT system is foreseen, with a total of six double strip layers including a stub layer for the barrel region and 7 end cap disks, covering the same pseudorapidity region as the pixel detector. Despite the fact that upgrade of the Liquid Argon Calorimeter electronics is essential due to radiation damage limits, in the reference scenario, a new finely segmented Forward Calorimeter (sFCal) with 100μm liquid argon gaps will be installed as well as a finely segmented precision timing detector, placed at the $2.4 < |\eta| < 4.3$ region, where current electromagnetic calorimeter segmentation is quite coarse. On the muon spectrometer stations, an acceptance extension up to $|\eta| < 4$ is expected combined with trigger system upgrades. New resistive plate and small tube diameter Monitor Drift Tube

(sMDt) chambers will be installed in the inner barrel region, with the first ones residing only in the central section while sMDTs will be placed on top of the preexisting ones. Finally, forward trigger calorimeter will be replaced in all three scenarios, and front-end MDT readout system will follow the natural eta extension at $|\eta| < 4$. The total cost of the upgrades is estimated at 275 million Swiss Francs.
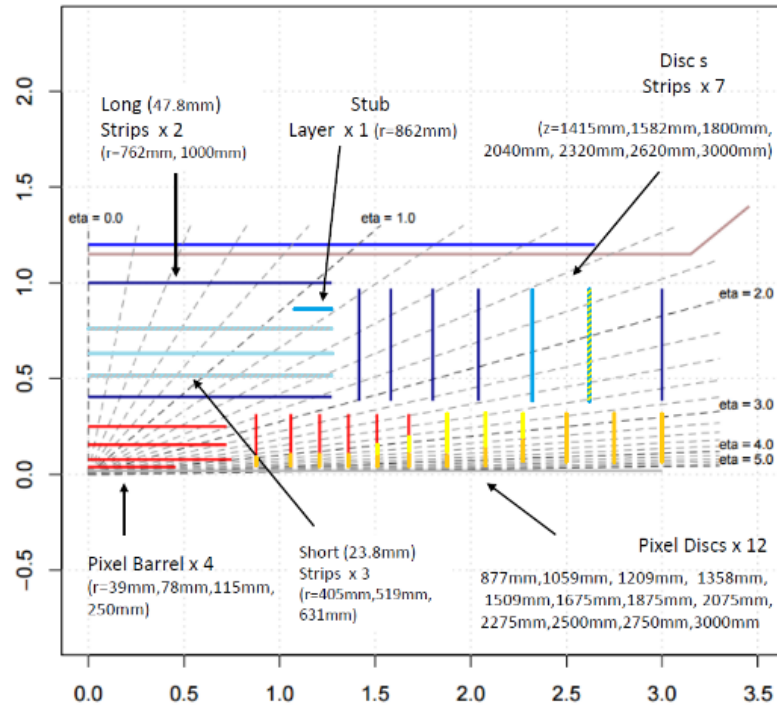
Figure 4.4: *A comprehensive representation the inner tracker scoping scenario geometry. For the Pixel detector, red demonstrates the geometry proposed for the low scenario, with yellow are denoted the additions proposed for the middle scenario and with orange the final additions proposed for the reference scenario. For the strip detector, blue depicts the low scenario with the blue green disk also included and light blue-gray regions being single-sided strip modules. Light blue symbolizes the middle scenario additions (three full barrel layers) while slightly darker blue denotes reference scenario additions, notable the two trip disks located next to the last in z direction.*

2. *Middle Scenario:* L0 and L1 trigger rates are reduced to 200 kHz while high level trigger will be operating at 50 kHz with a detector readout at 200 kHz for level 1 stage. On the strip tracker, one disk will be removed from each side with respect to the reference scenario as well as the stub layer, while for the pixel detector, an eta extension up to $|\eta| < 3.2$ will be implemented (*Figure 4.4*). Though the FCal will not be upgraded, a MiniFCal will be placed in front of the existing detector and all calorimetric electronics in the liquid argon and hadronic stations will be replaced. In spite of several performance improvements, mainly in the trigger system with finer granularity L0 MDTs and the addition of RPCs for redundancy and trigger acceptance coverage, no extension is foreseen for the muon tracker system. In the main barrel region, only easily accessible high eta MDTs and RPCs are replaced, since they are expected to receive higher radiation damage. The reduced pixel and strip layers contribute to a slight reduction of the estimated upgrade cost, which for the middle scenario is at the level of 235 million Swiss Francs.

3. *Low Scenario*: Reduced trigger rates to same values as for the middle scenario are expected but, acceptance extensions follow the inner tracker system up to $\eta < 2.4$. In

the pixel detector, no forward extension to the current η coverage will be installed, with six end-cap disks. Strip detector will consist of two full layers and two single sided ones following pixel detector for forward region coverage with six full end-cap disks. Though no calorimetric or muon extension is foreseen, electronics on all of these detectors will be replaced to cope with higher rates and radiation damage. In spite of the omission of several pixel and strip layers with respect to the other two scenarios and the dramatic downsizing in trigger and electronics upgrades, cost reduction is not analogous with an estimated 28 % reduction with respect to the reference scenario. The scenarios' total expected cost would therefore be at the level of 200 million Swiss Francs.

Given the tight timeline as well as the design, production and delivery delays for various detector components, production phase for silicon sensors needs to begin at early 2018. In that context, technical documentation and design layouts need to be finalized by mid-2017 with a final decision on the detector layout placed at the end of 2016-first half of 2017.

In the next two chapters, studies relative to the Phase II HL-LHC Run are presented in both analysis and hardware level. In particular:

- Chapter 5 details the observability potential of the bbH(γγ) mode in HL-LHC simulated conditions and under for 3000 fb^{-1} integrated luminosity hypothesis for each of the three defined upgrade scenarios. These studies, conducted in the context of the Higgs Prospects working group, aim to set limits and to be used as guidelines for upgrades scenario definition.

- In chapter 6, research and development activities towards a radiation hard, highly granular and efficient pixelated silicon tracker are detailed. My personal involvement is exposed in various development steps, from the simulation and design stage to testing, performance evaluation and radiation hardness studies. The scope of the this work is a contribution to the HL-LHC ATLAS pixel detector TDR, proof of concept and investigation of the potential of different innovative technologies within the ATLAS and RD50 collaborations.

4.3 References

[1] Peter Jenni, "The LHC Project and Discovery Physics", 11th Corfu Summer Institute on Elementary Particle Physics and Gravity, September 2011

[2] The ATLAS Collaboration, "ATLAS Insertable B-Layer Technical Design Report", CERN-LHCC-2010-013, ATLAS-TDR-19

[3] The ATLAS Collaboration, "A New ATLAS Muon CSC Readout System with System on Chip Technology on ATCA Platform", ATL-MUON-SLIDE-2016-004

[4] R. Claus, on behalf of the ATLAS Muon Collaboration, "A New ATLAS Muon CSC Readout System with System on Chip Technology on ATCA Platform"

[5] ATLAS Collaboration, "Observation of a new particle in the search for the Standard Model Higgs boson with the ATLAS detector at the LHC", Phys.Lett. B716: 1 - 29, 2012

[6] CMS Collaboration, "Observation of a new boson at a mass of 125 GeV with the CMS experiment at the LHC", Phys.Lett. B716: 30 - 61, 2012.

[7] ATLAS Collaboration, "Search for the Standard Model Higgs boson in the H to $\tau^+\tau^-$ decay mode in $\sqrt{s}$=7TeV pp collisions with ATLAS", JHEP 1209:070, 2012

[8] ATLAS Collaboration, "Letter of Intent for the Phase-II Upgrade of the ATLAS Experiment", CERN-LHCC-2012-022 ; LHCC-I-023

[9] LHC Higgs Cross Section Working Group, A. David et al., "LHC HXSWG interim recommendations to explore the coupling structure of a Higgs-like particle", arXiv:1209.0040 [hep-ph], LHCHXSWG-2012-001, 2012

[10] ALICE, ATLAS, CMS, LHCb Collaborations, "ECFA High Luminosity LHC Experiments Workshop Report: Physics and Technology Challenges", November 2013, ECFA/13/284

[11] ATLAS Collaboration, "Search for s-quarks and gluinos with the ATLAS detector in final states with jets and missing transverse momentum using 4.7 fb^{-1} of $\sqrt{s}$ = 7 TeV proton-proton collision data", Phys.Rev., 2012. arXiv:1208.0949 [hep-ex]

[12] ATLAS Collaboration, "Search for direct top s-quark pair production in final states with one isolate lepton, jets, and missing transverse momentum in $\sqrt{s}$ = 7 TeV pp collisions using 4.7 fb^{-1} ATLAS data", ATLAS-CONF-2012-07, 2012.

[13] ATLAS Collaboration, "Search for direct production of charginos and neutralinos in events with three leptons and missing transverse momentum in $\sqrt{s}$ = 7 TeV pp collisions with the ATLAS detector", ATLAS-CONF-2012-077, 2012

[14] ATLAS Collaboration, "Search for direct s-lepton and gaugino production in final states with two leptons and missing transverse momentum with the ATLAS detector in pp collisions at $\sqrt{s}$ = 7 TeV", ATLAS-CONF-2012-076, 2012

[15] ATLAS Collaboration, "ATLAS Phase-II Upgrade Scoping Document", CERN-LHCC-2015-020; LHCC-G-166

[16] R. Heuer, "LHC Schedule according to MTP2015", CERN Council 76th session, 18-19 June 2015, http://indico.cern.ch/event/397373/session/0/contribution/9/2/material/slides/0.pdf

5   Studies on the bbH(→γγ) channel at HL-LHC with 3000fb[-1]

5.1   Introduction

In the previous chapter, the upgrade program for the High Luminosity phase of LHC has been presented, together with its strong physics incentive and reach potential. In order to consolidate the different upgrade scenarios and validate the scientific motivation, dedicated physics studies were performed for the main channels to be studied in HL-LHC. In this context, an analysis aiming to identify the sensitivity of the ATLAS detector to the Higgs produced in association with b quarks has been conducted. This study concerned the Higgs decaying into two photons, taking profit from its clean and high resolution signal in the detector. The analysis was performed within the task force of the Higgs Prospects Working group.

5.2   Physics Case

The combined ATLAS and CMS results on the newly discovered boson at a mass of 125 GeV, strongly favor its compatibility with the particle predicted by the BEH mechanism. The already measured (H→γγ, H→ZZ*→4l, H→WW*, H→ττ) or constrained (H→μμ) decay channels, demonstrate that the new boson couplings behave as expected from the Standard Model theory within 10-20 % precision[1-2]. While this result is already an impressive outcome from Run 1, a lot remains to be achieved. A precise measurement of the couplings to all elementary particles could allow both a consistency check of the SM and testing the validity of various BSM models.

During Run 1, no evidence of a Higgs boson interaction to b-quarks has been observed. Although for a mass of 125 GeV, the H→bb mode dominates the total decay width (*see Figure 1.8*), its observation is rendered particularly challenging due to the huge QCD background. Alternative ways of probing Higgs coupling to b quark are also possible:

- The Higgs production by gluon fusion takes place through top and b quark loops. Because of its small mass, b contribution to the loops is limited in the SM to 10 % of the rate [3 - 7]. The Higgs coupling to b quarks could be measured by comparing the corresponding Higgs coupling in ttH production mode to the one measured for gluon fusion production mode. In principle, the difference of the two measurements would lead to the b coupling and to top-b interferences.

- The associated production of the Higgs with b-quarks (bbH) is of the same order as ttH (~ 0.5 pb at √s = 13 TeV). However, because of the low transverse momenta of the b quarks, the rate of bbH events surviving a typical analysis is significantly reduced with respect to ttH yields. It is well known that in some BSM models (SUSY), the Higgs coupling to bottom quarks can be enhanced. This brings a further interest for the measurement of the Higgs to b coupling.
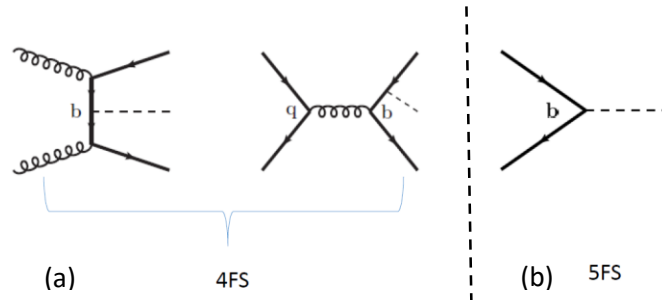
Figure 5.1 (a and b): *Four flavor scheme production diagrams where final b quarks are not part of initial partons (right, 5 a) and five flavor scheme LO diagrams (left, 5 b) were final Higgs boson is irradiated off b initial quark.*

Two computations schemes exist in the literature for the treatment of the large (wrt QCD scale) b-quark mass [8].In the so-called 4FS scheme, final bottom quarks are not considered as partons of the initial protons, while the bb̄H final state is generated through the diagrams presented at *Figure 5.1 a* in leading order computation. In the alternative 5FS scheme, the final Higgs boson is created by b-quarks from the colliding protons (*Figure 5.1 b*). For computations performed at all meaningful perturbation orders, the two schemes give similar results on inclusive cross-section.

At the expected center of mass energy of 14 TeV for Phase II LHC upgrade, the ratio of the expected Higgs associated production mode cross-section with respect to the current value at $\sqrt{s} = 8$ TeV nearly doubles (≈ 2.51) (*Figure 5.2*) [9]. Although this refers to all decay channels, the case of bb̄H(→γγ) is presented as a more viable alternative, since the di-photon channel provides a clean identification mode for the Higgs resonance, with a well-established analysis and efficient photon reconstruction and identification.
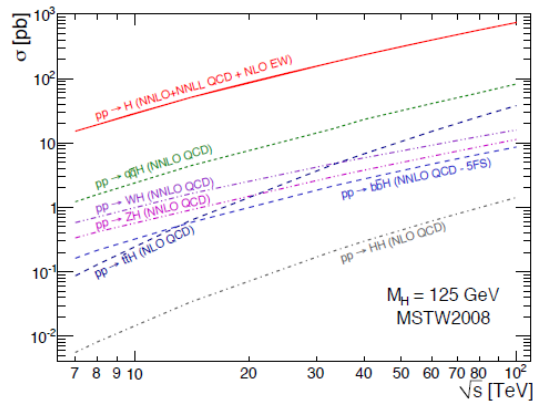
Figure 5.2: *Cross-section evolution for the different production modes with respect to center of mass energy for a $m_H \approx 125$ GeV.*

5.3   The bb̄H(→γγ) mode

Although strongly suppressed by the small Higgs to di-photon branching ratio, the bbH(→γγ) signature allows to profit from the excellent mass resolution of the electromagnetic calorimeter in order to improve the sensitivity of the measurement. Typical signal event signature consist of two photons originating from the Higgs decay, in conjunction with a b-jet pair, originating from b-meson decays within the detector fiducial volume. The narrow Higgs resonance is precisely reconstructed by the di-photon invariant mass at ≈ 125 GeV while no resonance in measured with the b-jet pair at the di-jet side.

Irreducible background consists of processes allowing for two genuine photons and b di-jet pair at the final state, with most prominent the bb̄γγ, H(→bb̄)H(→γγ), Z(→bb̄)H(→γγ) and t(→b)t(→b̄)H(→γγ) modes. The resonant peaks of H->bb and Z->bb have large widths (~25GeV) and donot allow an efficient rejection without killing an important part of the bbH signal. The ttH mode results to a non-resonant di-jet mass spectrum with more energetic b jets. The bbγγ mode gives continuum mass spectra for both di-photon and di b-jet systems.

In contrast with the irreducible background, the reducible background is mainly composed of one or more misidentified photon objects or wrong flavor attributed jets. Misidentified b-jets from charm or light jets, coupled with a di-photon pair, are major contributions from of ccγγ and jjγγ final states. In addition, misidentification of a jet or lepton to photon has to be considered. Since this contribution is represented by distinct misidentification probabilities (fake rates) separately for jets and electrons, main samples affected by this effect include ttlepton, bb̄ and ccj inclusive. In the very

busy environment expected at high PileUp (μ=200), jet inclusive background may also be taken into account. Nevertheless, since flavor misattribution of the di-jet pair and double fake photon selection have to occur simultaneously, the effect can be considered as negligible.

By extending Run 1 techniques in performance assessment and PileUp simulation, studies have been carried out for both μ = 200 and μ = 140 interactions per crossing, in all three scoping scenarios defined in the previous chapter (see section 4.2).

5.4   MC Samples

Official ATLAS 14 TeV MadGraph5 / Pythia8 NLO production at 14 TeV was used for all modes and detailed information are provided in the following table (*Table 5-1*).

Sample	Generator	σ x BR (fb⁻¹)	Eq. Lumi (fb⁻¹)	Nb. Events	Weight
$Z(b\bar{b})H(\gamma\gamma)$	Pythia8+Photospp	0.29683	3368932	9.80E+05	0.00091
$t\bar{t}H(\gamma\gamma)$	MC@NLO	1.39	83863	1.17E+05	0.036
$t\bar{t}\gamma$	MadGraph+Pythia8	2717.5	3680	9.95E+06	0.82
$t\bar{t}l$	MC@NLO+Herwig +Photos+Tauola	812260	18.45	1.50E+07	162
$jj\gamma\gamma$	MadGraph+Pythia8	22256	2247	4.83E+07	1.38
$b\bar{b}jj$	MadGraph+Pythia8	93680000	0.006	5.75E+05	48900
$b\bar{b}j\gamma$	MadGraph+Pythia8	264000	69.4	1.83E+07	43
$c\bar{c}\gamma\gamma$	MadGraph+Pythia8	1573.6	12710	2.00E+07	0.24
$c\bar{c}\gamma j$	MadGraph+Pythia8	2471300	10	2.50E+07	296
$b\bar{b}\gamma\gamma$	MadGraph+Pythia8	338.12	13309	4.50E+06	0.22
$H(b\bar{b})H(\gamma\gamma)$	MadGraph+Pythia8	0.1073	2795899	3.00E+05	0.00107

Table 5-1: *Detailed list of MC samples with generator information and scaling factor to 3000 fb⁻¹ used at the bbH analysis.*

Depending on the generated statistics and nominal cross-section anticipated at 14 TeV, a weight has been computed to scale the expected number of events from each process to the luminosity of interest according to the following formula (*equation 5-1*):

$$w = 3000 \times \frac{\sigma \times BR \, (fb^{-1})}{N_{generated}} \qquad (\,5\text{-}1\,)$$

where w is the corresponding sample weight for 3000 fb⁻¹ and $N_{Generated}$ the number of generated events. For several samples, especially the bbjj, $c\bar{c}\gamma j$ and $t\bar{t}l$, low available statistics resulted to a large normalization factor, inducing important fluctuations in several distributions. In most of the cases, the size of the needed additional samples was prohibitive with respect to the deadlines and the computing resources.

Lack of fully simulated samples at all streams imposed the use of truth level datasets with no reconstructed information available. Specific efficiency and smearing functions have been applied to the truth variables to model detector and reconstruction effects.

5.5   Object pre-selection and treatment

Key objects in this analysis include photons, jets, electrons and muons. Since the available simulation samples contain only truth information, energy (for all objects) and position (for photons)

is smeared to represent Phase II anticipated performances. Smearing studies are based either on fully simulated samples at 14 TeV or on extrapolations from current detector resolution. Functions derived from fully reconstructed MC samples are subsequently used to apply trigger, identification and fake efficiencies to leptons and jets. To emulate truth experimental conditions, any such functions are applied in a probabilistic way, with seeds generated in a per event manner, to ensure reproducibility. Finally, in order to evaluate the fake rates of jet→γ, jet→e, P_T/η dependent functions are being provided for photon and electron cases separately. Subsequent fake objects are uniformly treated with their real counterparts in the rest of the analysis.

A comprehensive description of the most relevant objects and their applied corrections is presented below:

- *Photons* are measured by the electromagnetic Liquid Argon calorimeter with an acceptance extending up to $|\eta| = 2.47$. Object energy and position are smeared in accordance with extrapolated performances for photons with a generated $P_T > 10\,\text{GeV}$. *Figure 5.3* demonstrates the smearing effect for photons in the bbH sample before any pre-selection. Overall energy resolution is in the order of 5.4 % (*Figure 5.3 a*) while for the position a 3 % resolution is observed (*Figure 5.3 b*).
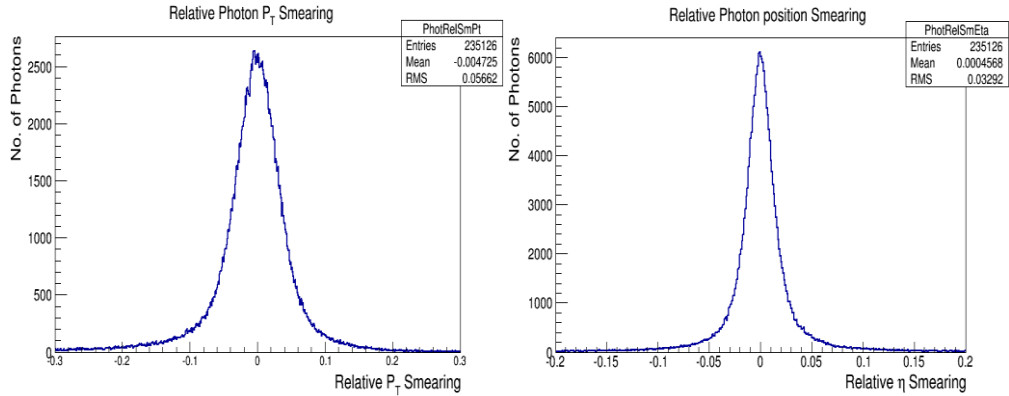
Figure 5.3 (a and b): *Energy resolution (left) and resolution in pseudorapidity (right) introduced by the smearing functions for photons. Distributions generated for the optimal scenario using 10^5 bbH events.*

- *Electrons* can be identified and characterized by both the electromagnetic calorimeter (energy) and the tracking system (pixel and strip inner trackers). Similarly to the photon case, they undergo a truth energy and position smearing while, detection fiducial region remains unchanged ($|\eta| < 2.47$). Electrons and other leptons included in the used simulation samples, originate from heavy flavor semileptonic decays and are later used to veto such events. Electrons are also considered to estimate the fake photon misidentification.

- *Muons* are measured by both the muon spectrometer and the inner detector. A transverse momentum smearing with an acceptance up to the region of $|\eta| < 4$, depending on the probed scenario. Muons within the analyzed datasets originate from heavy flavor semileptonic decays and serve to reject such events through an isolated lepton veto, at the last stages of the pre-selection.

- *Jets* are defined by the *Anti$_{KT}$40* algorithm [10], evaluating energy deposits and distributions in both the hadronic and electromagnetic calorimeter, contained within a cone of $\Delta R = 0.4$ with respect to the selected jet barycenter. In the reconstruction process, it is quite common for a photon or electron to also be represented as a jet candidate, with

slight position and energy variations. Resulting overlapping objects are subsequently excluded by requiring maximum jet proximity to leptons and photons no less than ΔR = 0.1 within the calorimeter, defined as:

$$\Delta R = \sqrt{(X_\gamma - X_{jet})^2 + (Y_\gamma - Y_{jet})^2} \qquad \textbf{(5-2)}$$

Whenever this requirement is not respected, the electromagnetic energy fraction of the photon/lepton is calculated. If this fraction is found to be within 15 % of the jet energy, the jet is considered as the primary object while the photon/electron is rejected. Smearing is applied to surviving jets in a transverse momentum interval between 15 GeV and 1.5 TeV, as a function of their truth energy and position, within a respective momentum resolution of ~ 25 %. An additional energy rescaling, referred as JES, is also performed, accounting for parton radiation outside the jet cone. This process is subsequently controlled by requiring the position of the invariant $b\bar{b}$ mass in Z-boson events to be in its nominal PDG value. *Figure 5.4* demonstrates the effect of smearing while energy rescaling can be observed on *Figure 5.5*. Jets are measured along the acceptance of the tracking system as defined by the various upgrade scenarios. In the studies concerning the scoping document, three acceptance regions are considered, one for each of the three proposed detector upgrade scenarios, with |η| < 2.4, |η| < 3.2 and |η| < 3.8 respectively.
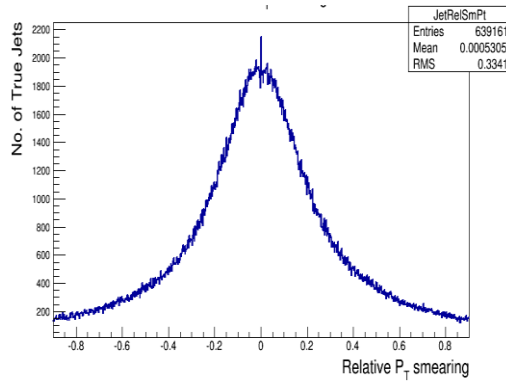
Figure 5.4: *Jet transverse momentum smearing resolution with a width of 30 % computed for the reference scenario with 10⁵ bbH events.*
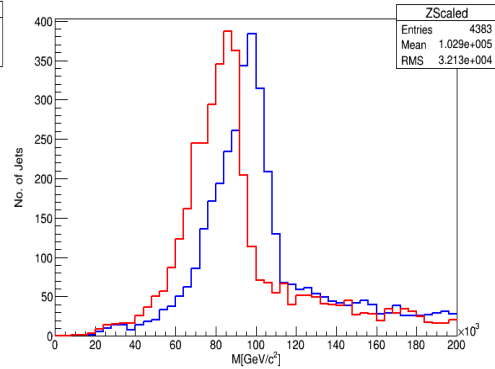
Figure 5.5: *Jet energy before and after parton rescaling (Reference scenario, using complete ZH sample).*

- *Pileup* response in HL-LHC conditions is emulated for instantaneous intensities corresponding to a μ = 140 and μ = 200 interactions per crossing. A superposition of additional jets in the physics simulated samples is performed, on an event by event basis. PileUp jets are thereafter referred as "PU" to distinguish from true hard scatter processes QCD produced jets, referred as "HS". Dedicated PU libraries have been produced integrating expected Phase II conditions while, complete energy rescaling is already applied at generator level. Since no true level information is available for the PU part, special handling is required with respect to flavor tagging, identification performances and fake object generation. PU jets have in general lower energy than the HS ones. Their pseudorapidity distributions exhibits distinct patterns, depending on the scoping scenario and the considered instantaneous luminosity (*Figure 5.6 b*). As expected, the number of PU jets per event increases when passing to higher μ values (*Figure 5.6 a*).
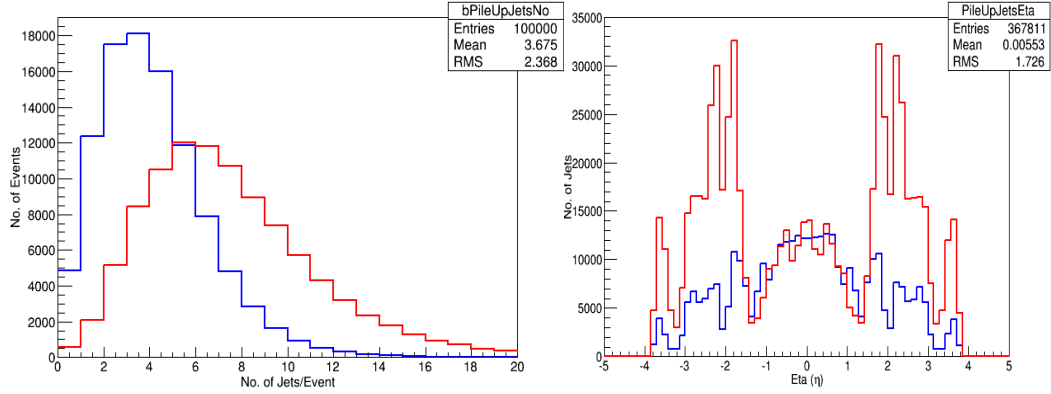
Figure 5.6 (a and b): *Number of per event PU jets (left, Figure 5.7 a) and their pseudorapidity distribution (right, Figure5.7 b) contained in the libraries corresponding to μ= 140 (blue) and to μ = 200 (red). Distributions are generated for the optimal scenario using 10^5 bbH events.*

- *Fake jet→photon* probability application is performed on all available jet objects after PU addition and jet-photon-electron overlap removal. Photon-like energy and position smearing is performed in the original truth jet quantities to all selected objects and are subsequently treated as true photons. In the case of PU jets, rescaling is applied in the already smeared jet energy itself, since no true information is available in the library. The effect of this additional smearing has been evaluated thought a truth jet study on the bbH sample. A 1 % difference is observed on the final photon quantities originating from already smeared jet energy with respect to those computed from purely truth information.

- *Fake jet→electron* transformation is performed in an equivalent manner to the jet→fake photon case. The same limitations as previously mentioned apply for the PU component and electron-like rescaling is performed with respect to pre-smeared jet energy. The effect was also evaluated in an equivalent as in the fake photons case study, using true electrons from the bbH sample. A 0.7 % deviation was observed to final electron energy when the appropriate smearing was applied on jet-rescaled quantities.

- *Fake electron→photon* misidentification probability, corresponding to truth electrons without reconstructed tracks, is in the order of 2 % in the barrel ($|\eta| < 1.37$) and 5 % in the end cap calorimeter ($1.52 < |\eta| < 2.47$). The effect is taken into consideration after jet overlap removal while, photon smearing is performed to truth electron quantities.

5.6   Analysis Requirements

After smearing application to object energy and position, a series of cuts is employed to increase signal to background ratio. In detail:

1) *Spatial isolation:* In order to guarantee optimal energy measurement, objects are required to be well separated in the calorimeter. An isolation of $\Delta R = \sqrt{\Delta \Phi^2 + \Delta \eta^2} = 0.2$ between electromagnetic objects (electrons and photons), corresponding to the electromagnetic cluster cone used for the electron and photon reconstruction, is required. Since jet definition is performed using the *AntiK$_T$40* algorithm, an additional separation of $\Delta R = 0.4$ is required between any pair of HS or PU jets. Nevertheless, since the PU library was produced separately from any of the physics samples, the isolation requirement is not present between PU and HS jets and has to be applied as an additional cut at the final stage of the analysis.

2) **B-Jet identification:** Jet b-flavor tagging probability is estimated using P_T/η dependent functions derived for expected Phase II run conditions. Extrapolations are performed using fully simulated $t\bar{t}$ events including complete PU implementation. Three different variants are utilized: one characterizing the probability of a truth b-jet to be tagged as such, with a 70 % acceptance yield while rejecting 98 % of PU jets; a second corresponding to the probability of a truth charm jet to be tagged as b; and a third, evaluating the rate of light jets surviving the b-tagging process. A fourth function has also been implemented specifically for PU jets, because of the difference between the used frameworks for the production of physics samples and the PU libraries. These functions have different forms depending on jet transverse momentum and pseudorapidity.
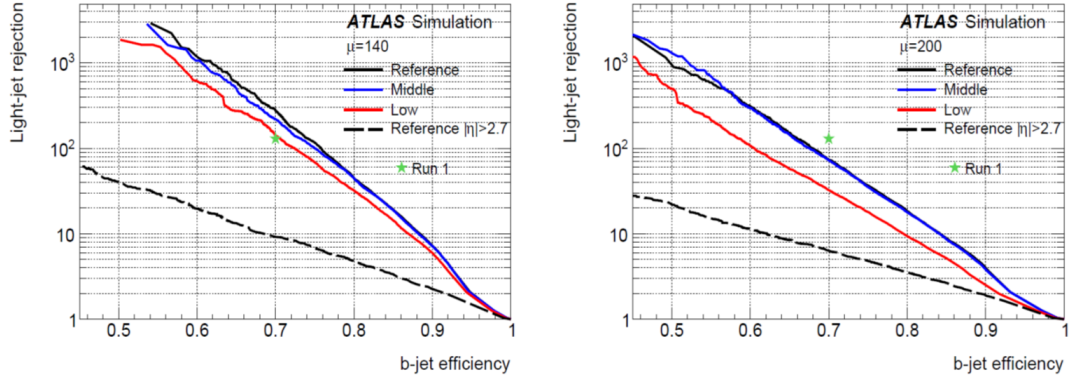
Figure 5.7: *The light-flavor jet rejection versus the b-jet efficiency for the MV1 b-tagging algorithm in the Reference (black), Middle (blue) and Low (red) scenarios for a pile-up of 140 (left) and 200 (right) for jets with $P_T > 20$ GeV and $|\eta| < 2.7$. The dashed curves are for jets in the Reference layout for $|\eta| > 2.7$. The equivalent Run 1 operating point is shown by a green star [11].*

In *Figure 5.7* light jet rejection with respect t b-tagging efficiency is presented for all three scenarios. Quoted results are extracted using the MV1 tagging algorithm [12], combining track impact parameter and secondary vertex information in a neural network approach. Training is performed using Run 1 b-jet events as signal and light jets as background. Due to limitations on the number of events of the fully simulated samples (50.000), tagging efficiency is parameterized in order to construct a smooth continues map [13] using a two dimensional fit as a function of P_T and $|\eta|$. Flavor tagging was optimized for all physics analysis channels, including compromises to accommodate an acceptable level of efficiency in all jet categories.

Concerning the different scoping scenarios, structural differences on the pixel and strip trackers heavily effect flavor tagging performance. All relevant efficiencies as a function of pseudorapidity are presented in *Figure 5.8* for each one of the three scenarios and jet flavor. Little performance difference between the middle and reference scenarios for $|\eta|<2.7$ is observed, but a small degradation for the later is seen at higher eta, with respect to the for the truth b-jet component. For the central region, tacking performances for the reference and middle scenarios are similar, leading to comparable b-tagging efficiencies. Nevertheless, extensions in forward calorimeter and tracker for the reference scenario allow for a higher number of PU jets to be reconstructed in these regions, effect that degrades the true b-jet yield. For the low scenario, tracking efficiency drops by 5% with respect to the other two and fake rate increases by a factor of ten. The b-tagging performance is subsequently heavily affected, with an increase in mis-identification and PU tagging for the fixed working point of 70%. Although these results did not use any re -optimization for the number of hits pre track as a function of η per scenario due to lack of statistics in the simulated samples, preliminary cross-checks demonstrate a potential for 30% improvement in mis-tagging for the central region.
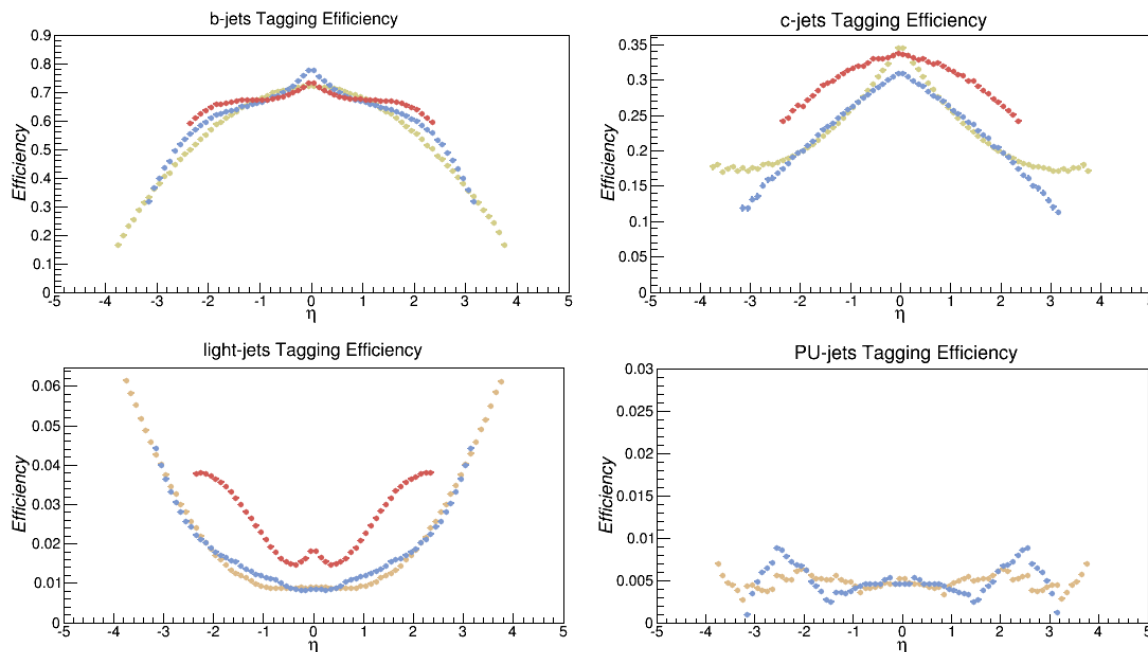
Figure 5.8: *B-tagging efficiency for truth b-flavor (top left), c-flavor (top right), light jets (bottom left) and PU jets (bottom right) for the optimal (gold), middle (blue) and low (red) scenarios. Efficiencies are derived using the bbH complete sample in the μ = 200 case after object preselection and isolation requirements.*

3) **Photon identification:** Photon identification criteria are defined with respect to their rejection power over jets. A tight selection is applied through corresponding transverse momentum dependent functions, yielding a mean efficiency of 70 % (*Figure 5.9 a*). A significant efficiency reduction is observed for the low energy region. This decrease, starting at $P_T < 90$ GeV, reaches a value of 40 % at the lowest allowed limit of 25 GeV. In the eta region, (*Figure 5.9 b*) identification efficiency remains stable with the exclusion of the calorimeter crack positions, excluded from photon definition.
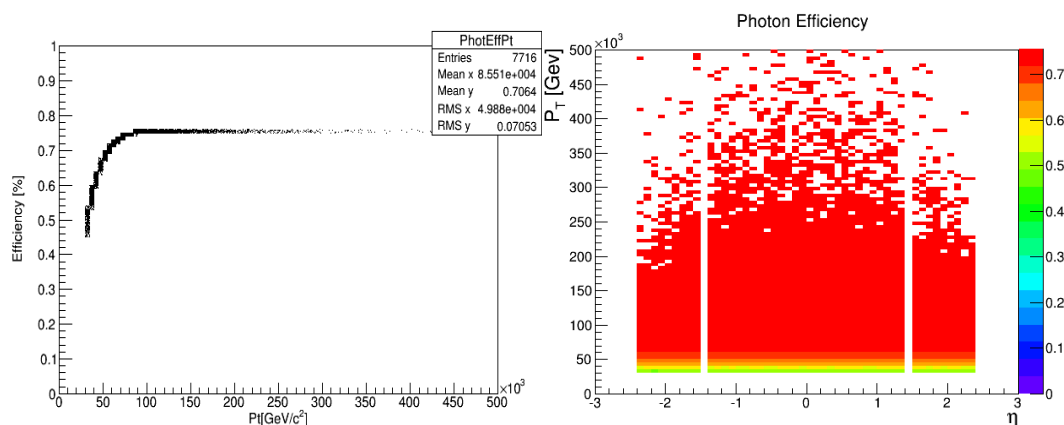
Figure 5.9 (a and b): *Tight identification efficiency for photons with respect to transvers momentum (left, Figure 5.9 a) and pseudorapidity (right, Figure 5.9 b) distributions.*

4) ***Fiducial* cuts:** While for photons, electrons and muons no difference across scenarios is expected, extensions of the inner tracker at high eta regions, would increase jet acceptance when passing from the low to the reference scenario (*Table 5-2*). For the photon and fake-

photon cases, the calorimeter crack region is excluded to recover decreasing efficiency. Final acceptance is fixed for leptons and photons to the current $|\eta| < 2.4$ across all scenarios while, the minimum allowed jet P_T is imposed from the jet energy calibration uncertainties, extrapolated for Run 2 conditions, at 30 GeV.

Object	Reference	Middle	Low
Jets	$P_T > 30\text{GeV}$		
	$|\eta| < 3.8$	$|\eta| < 3.2$	$|\eta| < 2.4$
e⁻ and jet→ e	$P_T > 30\text{GeV}$		
	$1.52 < |\eta| < 2.4$ and $1.52 < |\eta| < 2.4$		
μ	$|\eta| < 4$	$|\eta| < 3.2$	$|\eta| < 2.4$
	$P_T > 25\text{GeV}$		
γ, jet→ γ, and e⁻→γ	$|\eta| < 1.37$ and $1.52 < |\eta| < 2.4$		
	$P_T > 30\text{GeV}$		

Table 5-2: *Final object kinematic cuts for all three scoping scenarios.*

5) ***Final Cut-flow Overview:*** The analysis is completed with a di-photon trigger requirement at the minimum expected Run 2 threshold of 25 GeV for both objects.. The linear order of sequential analysis steps is detailed in the following:

1. Energy and angle smearing on photons, true electrons, jets and muons.

2. PU jet overlay

3. Jets overlap removal with respect to photons and electrons

4. e→γ and jet→γ fake generation

5. Photon, electron and muon candidates' isolation with respect to jets

6. Final kinematic cuts on isolated objects

7. P_T/η dependent efficiency functions application on all objects

8. ≥ 2 b-tagged jet requirement

9. Trigger requirement for the di-photon pair per combination (see below)

10. Event rejection in presence of additional isolated muon or electron per combination (see below)

5.7   Event treatment and multiple combinations.

As previously described, P_T/η dependent efficiencies concerning fake rates, photon reconstruction efficiency, flavor identification and electron-muon efficiencies are applied in a probabilistic manner. Surviving objects are used to form di-jet and di-photon combinations. It is quite usual that more than one quadruplet can be formed in a single event, satisfying all imposed analysis criteria. In an attempt to increase statistics, especially for the more problematic $t\bar{t}l$, $b\bar{b}jj$ and $c\bar{c}\gamma j$ samples, a multiple combination approach is implemented, considering all surviving jet and photon objects as final quadruplet candidates. For each individual combination, an additional condition is applied to ensure that the two photon and b-jet candidates originate from different truth–level objects. Isolated lepton veto and di-photon trigger are independently applied in a combination level, especially since a truth electron can also be considered as a photon. Finally, an individual combination weight is computed, equal to 1 over the total number of combinations passing the selection per event. In samples with relatively high PU or jet contamination, the number of individual combinations can have tails up to several hundred per event.

Sample	Initial Nb. of Events	Selected Combinations		
		Low	Middle	Nominal
$Z(b\bar{b})H(\gamma\gamma)$	9.80E+05	40562	42887	42209
$t\bar{t}H(\gamma\gamma)$	1.17E+05	14033	13751	13675
$t\bar{t}\gamma$	9.95E+06	13020	13236	13370
$t\bar{t}l$	1.50E+07	271	284	290
$jj\gamma\gamma$	4.83E+07	84992	73805	77965
$b\bar{b}jj$	5.75E+05	3	4	4
$b\bar{b}j\gamma$	1.83E+07	7907	8856	8907
$c\bar{c}\gamma\gamma$	2.00E+07	169113	142515	146921
$c\bar{c}\gamma j$	2.50E+07	2318	1927	2080
$b\bar{b}\gamma\gamma$	4.50E+06	91515	99285	98750
$H(b\bar{b})H(\gamma\gamma)$	3.00E+05	29457	30949	31137
$b\bar{b}H(\gamma\gamma)$	9.50E+05	36211	40237	40745

Table 5-3: *Available statistics per sample and final number of selected combinations for each of the three scenarios.*

While the sum of jet identification probability, jet to photon fake probability and jet to electron fake probability can in several cases exceed unity, an intrinsic rescaling is imposed by the probabilistic nature of the applied selection. Highest priority is given to true identified b-jets, followed by fake jets→photons and jet→electrons. The same selection procedure also applies for electrons, with the highest priority given to true identified electrons followed by fake electron to photon.

Table 5-3 presents available event statistics for each sample in terms of initial number of events and final selected quadruplet combinations. While one would expect combinations to increase while moving to a higher acceptance scenario, this is not always the case (for ex ZH. ttH, bbγγ samples). Actually, the PU rejection is improved due to better tracker implementations. Nevertheless, an increase on weighted events is observed when extending detector acceptance. Although angular distributions are different for background modes, a truth-level study on the bbH sample demonstrated a 10 % increase when the outermost forward region is included [14].

5.8   TMVA Analysis

A TMVA based analysis has been used to maximize signal to background separation, The Boosted Decision classification algorithm is implemented using 3000 trees and 3-level training depth.

Available dataset was divided into two equal portions, with one half used for training and the other for testing. During the training procedure, negative interference weights, present at the ZH sample, were not taken into consideration. However, in order to avoid biasing, they corresponding events were consecutively considered during application on the testing sample. A series of kinematical variables were used to identify the most discriminant ones, like the position and energies of photons and jets, their spatial separation, the quadri-vectors of di-photon and di-jet systems, and the four-object quadri-vector. Analysis was run in two consecutive iterations with most of the available variables introduced in the first attempt, where the ten most discriminating were defined. These variables were subsequently used during the second iteration for the BDT training (*appendix 5.1*). Given the large rescaling factor of the $b\bar{b}jj$ sample, it was not considered in the TMVA analysis while, pre-training normalization is performed with respect to the signal for individual backgrounds, to minimize statistical fluctuations. For each Scoping scenario, a specific training was performed since the kinematic distributions differ. Reference scenario training was used to define the optimal BDT cut point, giving the best sensitivity. The same BDT-cut was also applied to extract the sensitivities of the two other scenarios.

The full analysis was performed for both, the mu=140 and mu=200 cases. Results are shown below.

5.8.1   Results with a μ = 200 value

Jets and -especially- sub-leading photons exhibit a particularly structured distributions at high values of pseudorapidity. The effect originates from the distinctive PU jets pseudorapidity distributions, available in the μ = 200 library, convoluted with the dedicated b-tagging efficiency functions. The effect is more pronounced for the sub-leading b-jet, often originating from PU pollution. In *Figure 5.10*, pseudorapidity distributions of the final selected jets are presented for the reference scenario using the complete bbH sample. In addition, PU originating fake-photon pollution is introduced in the di-photon object selection, affecting all three scenarios at different levels. Corresponding pseudorapidity distribution for di-photon pair suffer, as a result, from the PU characteristic structures in the extended eta regions, with respect to the μ = 140 and the no- PileUp analysis case.
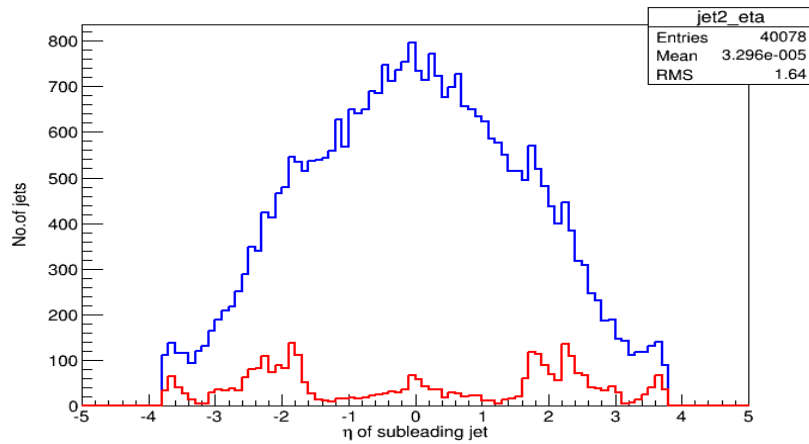
Figure 5.10: *Pseudorapidity distribution of the sub-leading jet (blue line) for the bbH full sample. The high η structures as well as the particular increase at η ≈ 2 are characteristic of the PileUp contamination. In red, the fraction of the PU jets is shown.*

In *Figures 5.11, 5.12 and 5.13*, the most relevant variables for the photons, jets, di-photon, di-jet and quadruplet objects are presented. Except for the jet isolation applied at an annulus of 0.4 for the final di-jet pair, no additional pre-selection cuts are requested. While the signal is composed of a clearly distinguishable di-photon mass resonant distribution at the Higgs mass value, background is comprised both of a non-resonant part, corresponding to inclusive di-photon processes and a 2γ resonant one, composed of the $t\bar{t}H(\gamma\gamma)$, $Z(b\bar{b})H(\gamma\gamma)$ and $H(b\bar{b})H(\gamma\gamma)$ samples. The di-photon mass of the H→γγ decay is clearly visible at the $m_{\gamma\gamma}$ distribution on the Higgs mass value while, the non-resonant component of the background is extended over a large region. Signal and background contributions in the following figures have been normalized.

Concerning the leading and sub-leading jets, no important discrimination power can be observed for the transverse momentum and eta distributions (*Figure 5.11*). To evaluate PU contamination of the final selected events, a negative indexing was used for all PileUp originating objects. Corresponding distributions for photons and jets are also presented. Though the sub-leading jet is slightly more affected, in general the percentage of PU jets at the final stage is less than 1 %. Such a behavior can be explained by the increased PU rejection of the flavor tagging algorithm and the lower transverse momentum threshold of the PU component. Finally, the only di-jet variable of discriminating value is the separation of the selected jets (ΔR_{bb}), with the signal and background distributions differing substantially. Nevertheless, the strong peak at $\Delta R < 1$, seen for the signal is a simulation effect, derived by the fact that non final-state b-hadrons are considered as individual jets. In that sense, along the cascade of b-hadronization, several jets can be constructed from the same b-

quak with slightly different positions and energies, resulting in a very close final di-jet pair. Although this effect is at a generator level, an additional pre-selection cut ad $\Delta R_{bb} > 1$ was introduced to compensate.
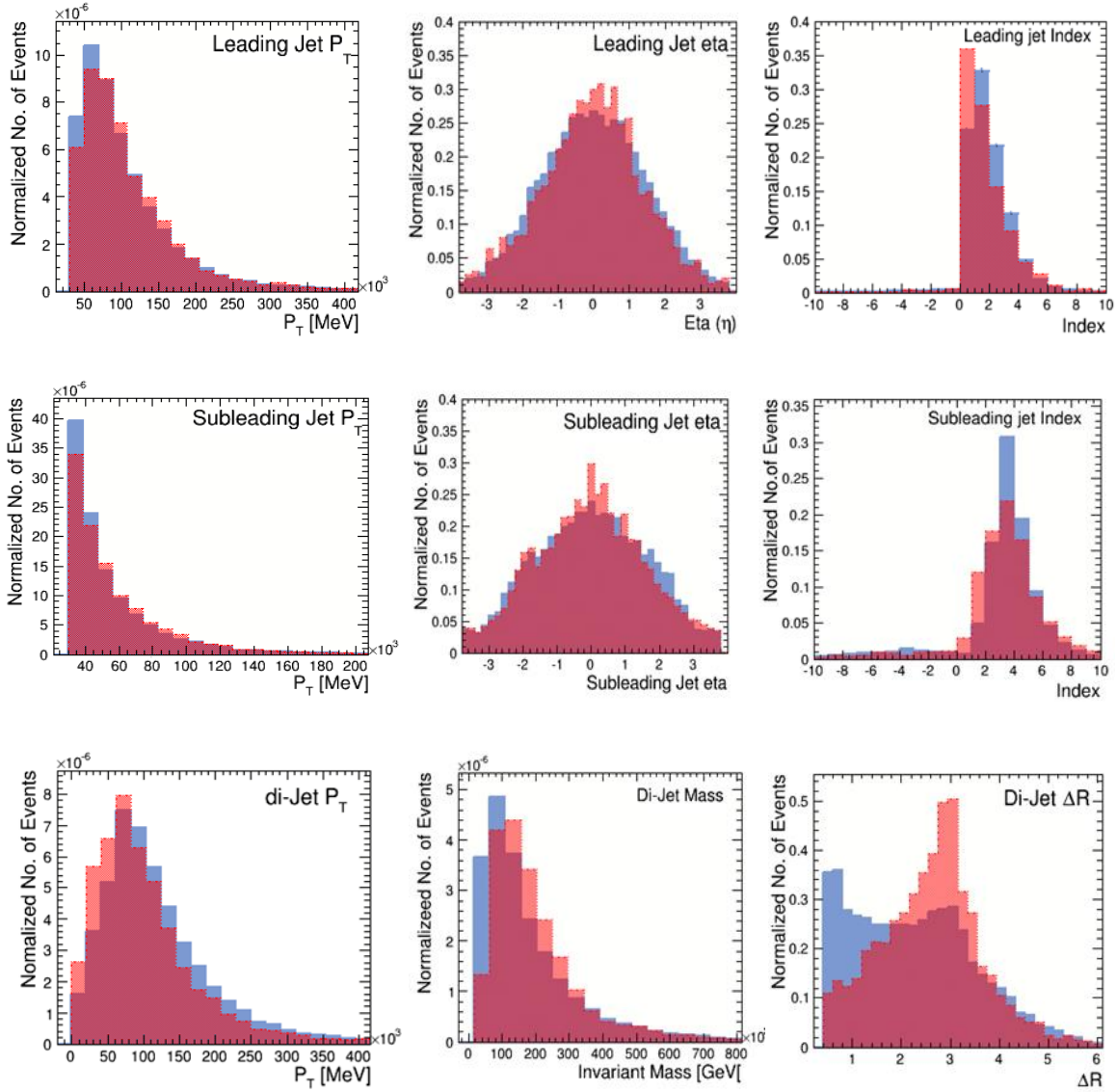
Figure 5.11: *Transverse momentum, eta and index distributions for leading and sub-leading jets as well as mass, transverse momentum and separation distribution of the combined di-jet pair. Signal is presented in blue while in red is plotted the combined background.*

On the photon side (*Figure 5.12*), the separation power of the pseudorapidity for both leading and sub-leading photons is very weak, since differences between signal and background seem to be primary of statistical nature. Concerning the transverse momentum, on both the leading and sub-leading photon, the signal seems to exhibit higher P_T values than the background. One can therefore suggest a cut at 75 GeV for the leading photon and around 40 GeV for the sub-leading as an option to consider for a cut based approach. Evaluating the PU contamination from the index distributions, one can infer that the sub-leading photon is significantly affected for background samples. As a result, a large percent of the sub-leading photons on background events are actually misidentified PU jets, effect that reflects to the final background composition. On the di-photon pair side, the photon separation and the combined mass are the most discriminating variables, especially because of the resonant nature of the signal.
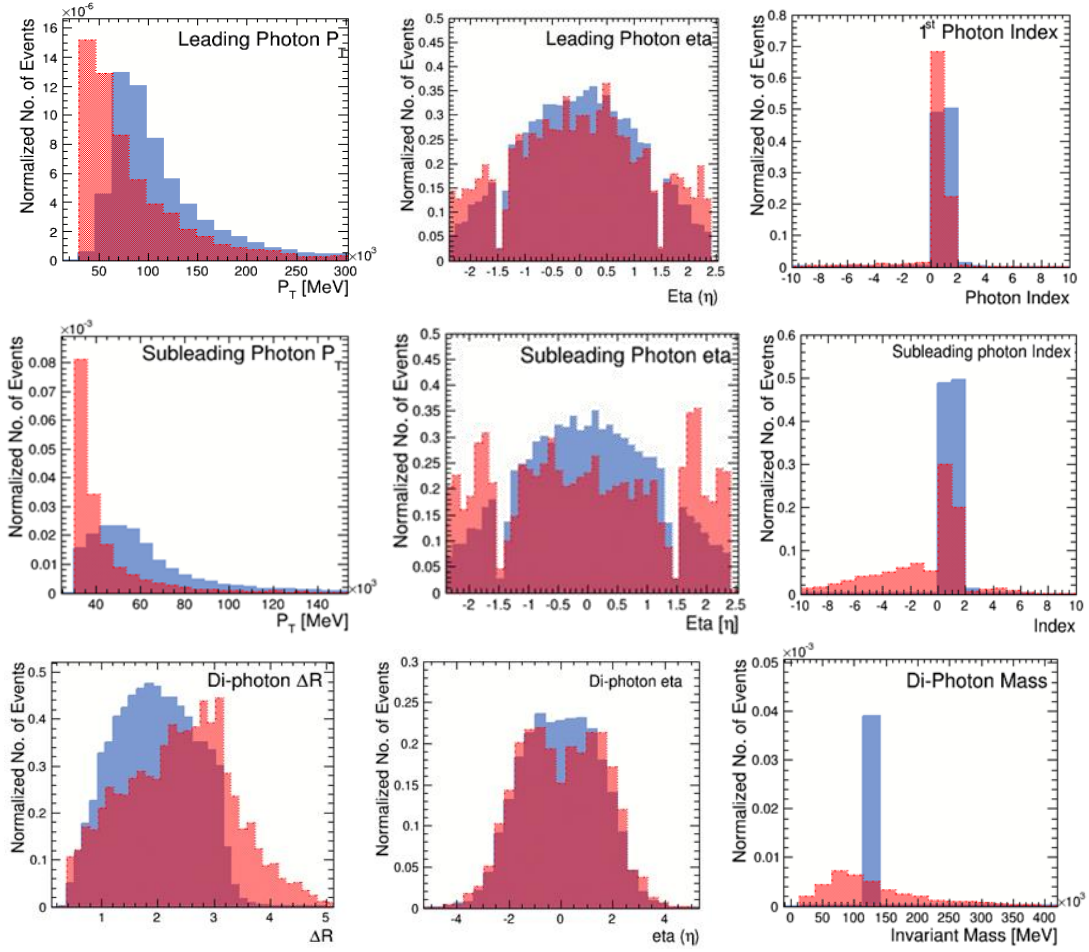
Figure 5.12: *Transverse momentum, η and index distribution of leading and sub-leading photons as well as η, ΔR and invariant mass distribution of the di-photon pair. Signal is presented in blue while in red is distinguishable the combined background. Normalization is performed with respect to training weights.*
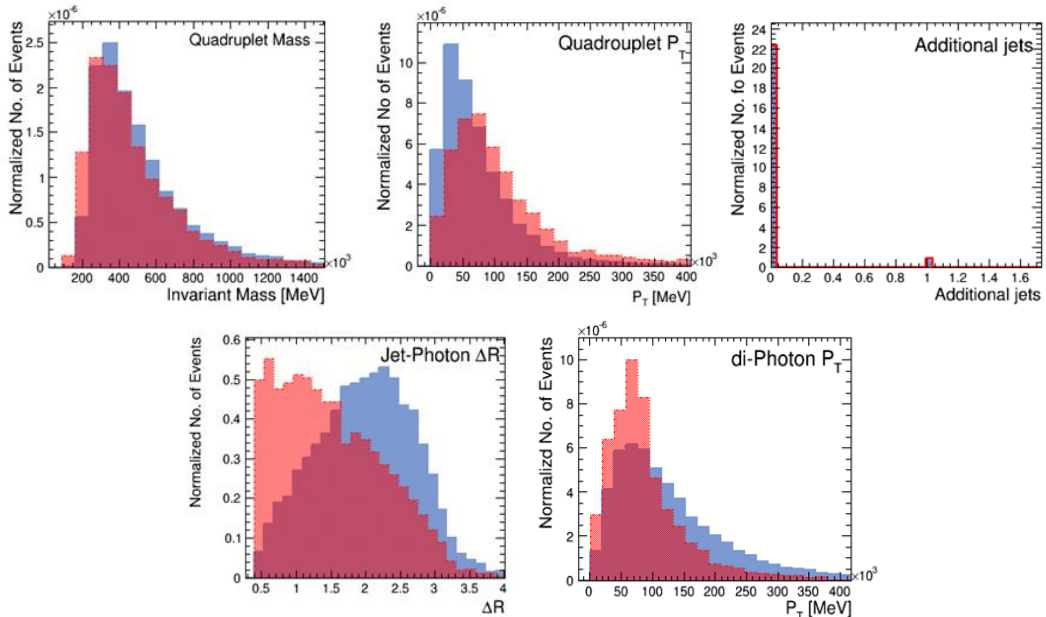
Figure 5.13: *Invariant mass and transverse momentum distributions of the combined quadruplet, additional jets in the final event, di-photon pair transverse momentum and leading-photon jet separation distributions for signal and background.*

Finally, several reconstructed quadruplet variables are presented in *Figure 5.13*, with only the leading photon-jet separation ($\Delta R_{\gamma 1j1}$) demonstrating a potential use for signal to background discrimination. This is mainly a result of the particular bbH system topology. Higgs photons are mainly expected in the central region while, for the bb system, forward geometries are favored. On the other side, the number of additional jets per event, the quadruplet invariant mass and its transverse momentum are not of any significant discrimination value, especially due to the large number of background process considered, which generate a continuum spectra.

By evaluating the discrimination power of the variables presented on *Figures 5.11 - 5.13* only ten were considered for the final TMVA training and optimization. These include separation of the di-photon pair ($\Delta R_{\gamma\gamma}$), di-jet pair (ΔR_{bb}) and leading photon-jet ($\Delta R_{\gamma 1j1}$), pseudorapidity of all four objects separately, di-photon mass, transverse momentum of the final quadruplet and the of the sub-leading photon. Index distributions are presented for evaluation purposes exclusively and to explain background compositions but, since they constitute truth level information on object origin, they cannot and are not considered in any stage of the analysis.

Considering the significant separation power of the di-photon mass, an additional TMVA analysis was performed where a pre-selection cut was applied for the region of 120 GeV $< m_{\gamma\gamma} <$ 130 GeV. In spite of this pre-requirement, the di-photon mass was still included as a variable during BDT training. A significant background reduction is obtained for all non-resonnant 2gamma processes. The price to pay is the introduction of important fluctuation of the template shapes of the discriminating variables, as shown in *Figure 5.14*.
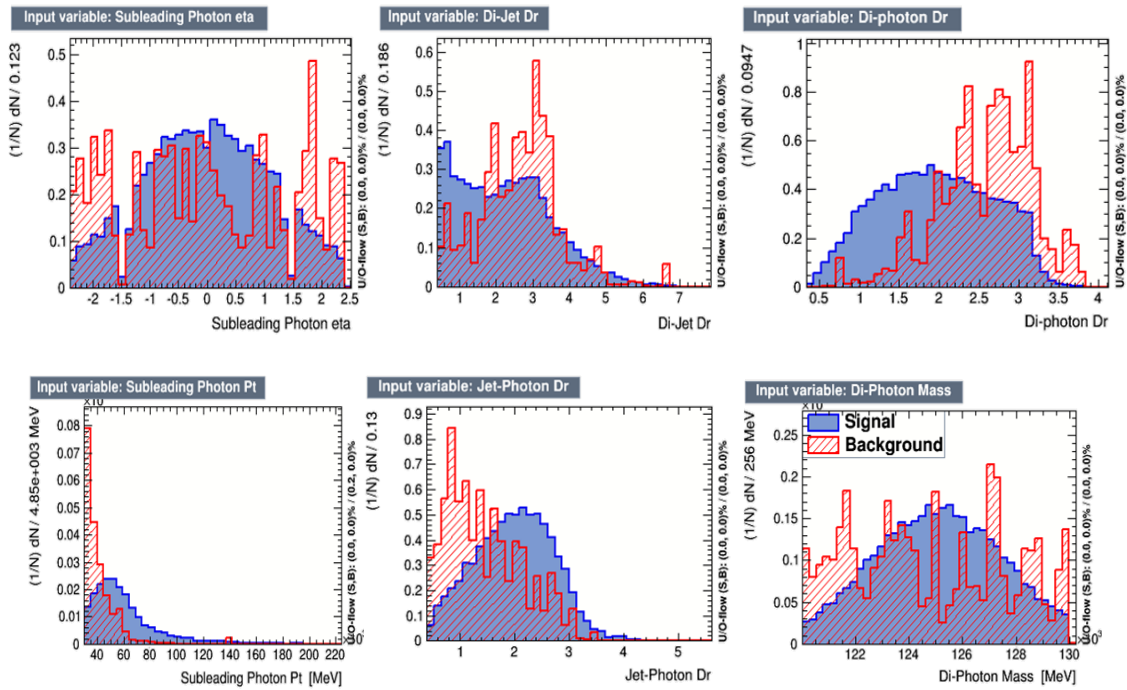
Figure 5.14: *Input variable distribution of the η_γ2, ΔR_bb, ΔR_γγ, P_T(γ₂), ΔR_γ1j1, m_γγ for the nominal scenario in the case of a a 120 GeV < mγγ < 130 GeV cut. The blue area represent the single region while with red is represented the combined background.*

The effect of the di-photon mass cut on the final BDT distribution is clearly visible on the signal and background probability distribution functions, presented for the reference scenario in *Figure 5.15*. On the left hand side, the non-resonant background component is located towards negative BDT values and dominates the background population. The signal, as well as the resonant background contribution, are situated on the positive end of the plot. On the right hand side of *Figure 5.15*, where a mass range of 120 – 130 GeV has been required for the di-photon mass, the major part

of the non-resonant background is suppressed. Some tails still survive together with almost all events from the resonant contributions, mainly the HH, ZH and ttH processes. Strong statistical fluctuations are observed in this case for the background BDT distribution. In both figures, the signal and background distributions are normalized.
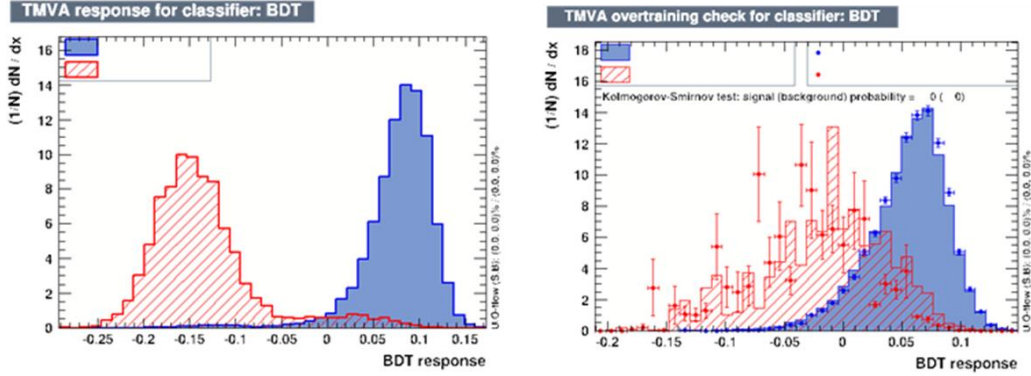
Figure 5.15: *BDT response and output PDFs for the signal in blue and the background in red at the reference scenario. All distributions are normalized with respect to signal while, training and testing samples are plotted together, with testing data represented as points. Left hand plot corresponds to no di-photon mass preselection cut BDT output while right hand to a 120 GeV < $m_{\gamma\gamma}$ < 130 GeV cut.*

For each value of BDT response, the expected combined background and signal events are computed in all three scenarios while, the anticipated significance is calculated with corresponding uncertainty. In a simplistic Analysis of Variance approach, where a statistical test is applied, the null hypothesis for the observation of a specific signal corresponds to the background only observation [15]. On the other hand, the median hypothesis would correspond to a signal plus background observation. In this case, assuming considered data respect a Gaussian distribution, the p_0-value can be expressed as:

$$p_{0,b} = \int_{s+b}^{\infty} Gaussian(n|b,\sigma)dn \ \text{ with } \ \sigma = \sqrt{b} \qquad (5\text{-}1)$$

By performing a variable modification under the definition u=(n-b)/σ, the Gaussian can be reduced to an error function, allowing to identify the expected significance as:

$$p_{0,b} = \int_{s/\sqrt{b}}^{\infty} Gaussian(u|0,1)du \qquad (5\text{-}2)$$

In this case, the number of events, defined always as a positive number, is consequently expressed as:

$$p_{0,b} = 1 - \int_0^{\frac{s}{\sqrt{b}}} Gaussian(u|0,1)du = 1 - \Phi(s/\sqrt{b}) \qquad (5\text{-}3)$$

The final significance of the observation hypothesis is subsequently defined as the number of signal events divided by the square root of the expected background events (*equations 5-4*).

$$\boldsymbol{Significance} = \frac{N_{sig}}{\sqrt{N_{bkg}}} \qquad (5\text{-}4)$$

While Monte Carlo statistical uncertainties were not introduced to the significance computation, they have been taken into account in the calculation of the corresponding uncertainty, thus contributing to the end result. The equivalent formula for the significance uncertainty is presented in *equation 5-5*.

$$\sigma_{significance} = \sqrt{\frac{\sigma_{sig}^2}{N_{bkg}} + \cdot \frac{N_{sig}^2}{4 \cdot N_{bkg}^3} \cdot \sigma_{bkg}^2} \qquad (5\text{-}5)$$

where N_{sig} represents the number of signal events with score greater than the selected BDT value

N_{bkg} the number of background events with score greater than the selected BDT value

σ_{sig} the uncertainty on the signal

σ_{bkg} the uncertainty on the background

To compute the statistical uncertainty of the signal and background events one needs to take into account not only the normalization weight of each sample as defined in Table 5-1 but also the individual weight of each quadruplet combination, as described at the beginning of section 5.1 Corresponding uncertainties are described by *equations 5-6 and 5-7*: The index j on the first summing term of *equation 5-7* runs through all of the different background samples.

$$\sigma_{sig} = \sqrt{F_s^2 \cdot \sum_{i=1}^{N_{sig}} w_i^2} \qquad (5\text{-}6) \qquad \sigma_{bkg} = \sqrt{\sum_{j=1}^{bkg} F_{bj}^2 \sum_{i=1}^{N_{bkg,j}} w_i^2} \qquad (5\text{-}7)$$

where F_s is the signal normalization factor

F_{bj} is the background sample normalization factor

w_i the individual weight of each combination

N_{sig} the total number of signal events

N_{bkg} the total number of background events for the specific sample (denoted as j)

Significance distributions with respect to different BDT cut values for all three scenarios are presented in *Figure 5.16. S*ignal and background un-normalized PDFs for each case are also included. A stable BDT cut point is selected such as to achieve significance maximization for the reference scenario, while avoiding any instabilities on neighboring bins at the higher end of the distribution. Such fluctuations are to be expected due to lack of background statistics, especially for the increased normalization factor datasets.
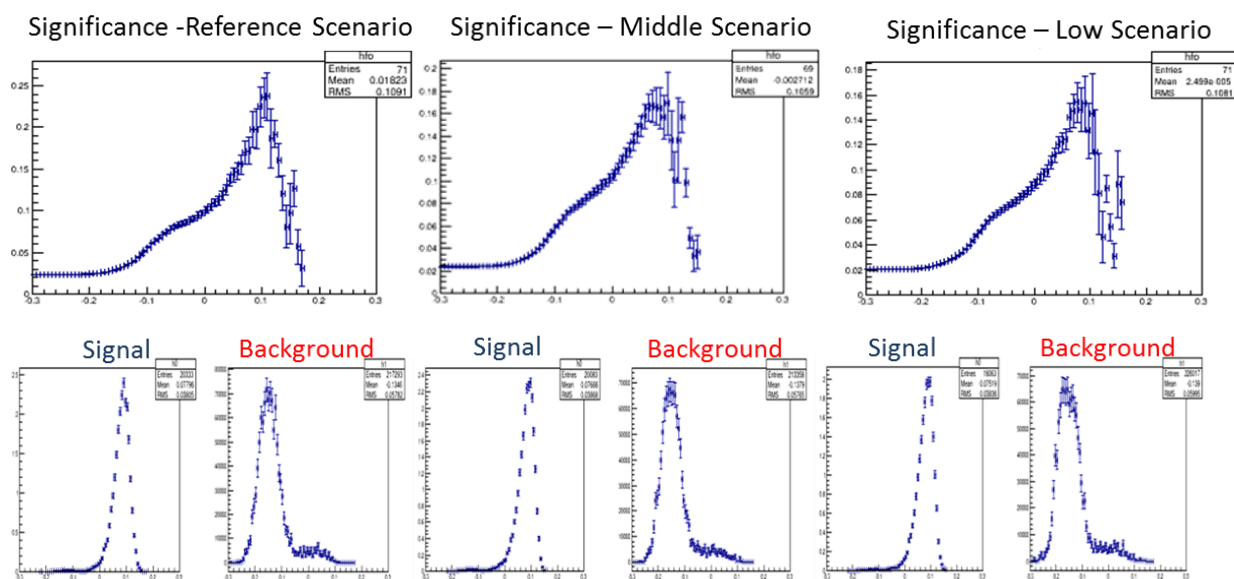
Figure 5.16: *Significance distributions, signal and background PDFs for all three scenarios when no mass cut is applied for a μ = 200 value. From left to right: Low, Middle and Reference scenarios are presented Fluctuation on the higher end of the significance distributions are due to lack of background statistics in the increased weight samples.*

At the higher end of the significance distribution, where background and signal events are reduced, slight variations of the BTD cut value may induce important variations, by exclusion or inclusion of a single high weight background event. Once the significance is recalculated and the excluded event weight is factored, large jumps can be observed, leading to discontinuities in the corresponding distributions. To avoid inconsistent regions, the optimal cut point is defined as the one presenting high significance but not situated to the proximity of fluctuating neighbor bins. This optimization is performed only for the reference scenario and the selected point is applied to all other cases, with the constraint of always remaining within a stable region of the significance distribution. Statistical fluctuations tend to increase towards the low scenario, partially because of background and signal events reduction due to acceptance limitations of the detector volume.
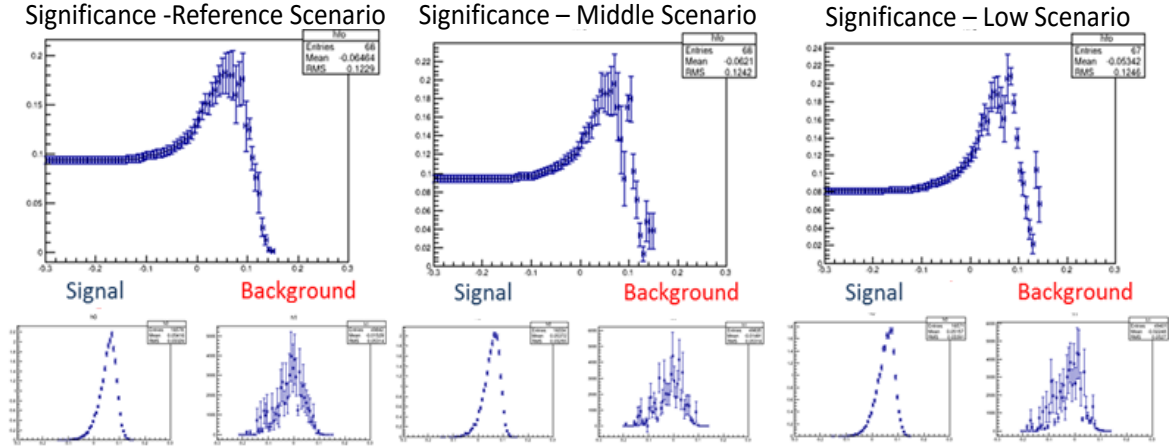
Figure 5.17: *Significance distributions, signal and background PDFs for all three scenarios when 120 GeV < $m_{γγ}$ < 130 GeV is required for a µ = 200 value. From left to right: Reference, Middle and Low scenarios are presented Fluctuation on the higher end of the significance distributions are due to lack of background statistics in the increased weight samples.*

In the case of 120 GeV < $m_{γγ}$ < 130 GeV cut TMVA analysis, the optimal cut point can be found in lower classifier values, since a large portion of the previously background dominated region has been removed. However, the presence of fluctuations at the high end of the distribution is still apparent, following the same trend per scenario as in the no mass cut analysis case (*Figure 5.17*). Since the di-photon mass pre-selection is mostly removing non-resonant background situated traditionally at lower classifier values (*Figure 5.15*) it is expected that fluctuations induced due to reduced background statistics will become more prominent with respect to the no $m_{γγ}$ cut analysis.

Final results for all three scenarios are presented in *Table 5-4*. For the no mass cut case, the analysis clearly favors the reference scenario with an increased significance and a marginal increase in the increase expected signal and background events with respect to other two scenarios. The ascending order of improvement coincides with the pseudorapidity extension foreseen in each case, while the three scenarios are incompatible within uncertainty limits. By applying a di-photon mass pre-selection, a large part of the non-resonant background is absent, allowing for a lower cut value, accounting for an observed increase in the expected signal and background. Nevertheless, relaxing the BDT cut introduces additional fake photon backgrounds, resulting in a degradation of the overall significance. Since fake background follows the jet pseudorapidity distribution, an increase is observed when the acceptance is extended, resulting in an inverse order of scenario ranking, with respect to the no $m_{γγ}$ cut case. In the di-photon mass cut case, all three scenarios remain compatible within the uncertainties, not allowing any definitive conclusions. IN spite of this initial interpretation, increased uncertainties due to lack of statistics make all three scenarios compatible and may account of the observed ordering effects.

		Reference	Middle	Low
Mass Cut	Significance	0.182 ± 0.030	0.185 ± 0.032	0.188 ± 0.029
	signal	12.77 ± 0.13	12.53 ± 0.13	10.70 ± 0.12
	Background	4922 ± 1134	4561 ± 1100	3219 ± 702
No mass cut	Significance	0.225 ± 0.034	0.170 ± 0.040	0.131 ± 0.031
	Signal	8.78 ± 0.11	8.75 ± 0.11	7.38 ± 0.10
	Background	1516 ± 324	2659 ± 880	3153 ± 1060

Table 5-4: *Significance value and expected signal and background events for all three scenarios in the two TMVA cases, with and without the di-photon mass cut pre-selection at μ = 200.*

Although in significance calculation only a statistical error is included, a large systematic uncertainty is also expected. Given the ~ 5 ‰ signal to noise ratio of the analysis, an evaluation of a systematic uncertainty on signal and background samples would induce an increased uncertainty on the final calculated significance. For the simplest case where the same value is assumed for all background and signal samples, a conservative 10% systematic would induce a 30% increase on the uncertainty of the final significance. This level drops to 8% uncertainty increase if a 5% systematic is evaluated for all samples.. With respect to the relevant distributions (*Figure 5.17)*, such an issue can introduce systematics directly to the significance, up to the order of 30% depending on the stability of the classifier at the selected BDT cut value.

Stream	Reference		Middle		Low	
	Events	**Yield %**	**Events**	**Yield %**	**Events**	**Yield %**
$b\bar{b}\gamma\gamma$	120 ± 8	(7.9 ± 1.8) %	130 ± 8	(4.9 ± 1.7) %	103 ± 8	(3.3 ± 1.1) %
$b\bar{b}j\gamma$	274 ± 159	(18 ± 4.0) %	374 ± 175	(14 ± 4.7) %	329 ± 167	(10 ± 3.6) %
$H(b\bar{b})H(\gamma\gamma)$	9.8 ± 0.1	(0.6 ± 0.2) %	9.1 ± 0.1	(0.34 ± 0.2) %	8.5 ± 0.1	(0.27 ± 0.1) %
$jj\gamma\gamma$	537 ± 39	(35 ± 7.7) %	558 ± 41	(21 ± 7.0) %	556 ± 41	(18 ± 6.0) %
$t\bar{t}\gamma$	4 ± 2	(0.3 ± 0.2) %	8 ± 4	(0.32 ± 0.2) %	4 ± 2	(0.13 ± 0.1) %
$t\bar{t}H(\gamma\gamma)$	43.7 ± 1.6	(2.9 ± 0.8) %	42.7 ± 1.6	(1.6 ± 0.6) %	37.7 ± 1.5	(1.2 ± 0.4) %
$t\bar{t}l$	0 ± 0	(0 ± 0.) %	0 ± 0	(0 ± 0) %	0 ± 0	(0 ± 0) %
$Z(b\bar{b})H(\gamma\gamma)$	11.20 ± 0.14	(0.7 ± 0.3) %	10.79 ± 0.14	(0.41 ± 0.2) %	9.00 ± 0.13	(0.29 ± 0.1) %
$c\bar{c}\gamma\gamma$	120 ± 8	(8 ± 1.8) %	141 ± 9	(5.3 ± 1.8) %	128 ± 8	(4.1 ± 1.4) %
$c\bar{c}j\gamma$	395 ± 280	(26 ± 5.7) %	1384 ± 862	(52 ± 17.3) %	1977 ± 1046	(63 ± 21.1) %

Table 5-5: *Background composition for all three scenarios when no di-photon cut is applied.*

Stream	Reference		Middle		Low	
	Events	**Yield %**	**Events**	**Yield %**	**Events**	**Yield %**
$b\bar{b}\gamma\gamma$	231 ± 11	(4.7 ± 1.1) %	224 ± 11	(4.9 ± 1.2) %	167 ± 9	(5.2 ± 1.2) %
$b\bar{b}j\gamma$	1111 ± 330	(23 ± 5.2) %	760 ± 270	(17 ± 4.1) %	690 ± 244	(21 ± 4.7) %
$H(b\bar{b})H(\gamma\gamma)$	12.55 ± 0.16	(0.25 ± 0.1) %	12.52 ± 0.16	(0.27 ± 0.1) %	11.80 ± 0.15	(0.37 ± 0.1) %
$jj\gamma\gamma$	1173 ± 59	(24 ± 5.5) %	1057 ± 56	(23 ± 5.6) %	1031 ± 56	(32 ± 7.0) %
$t\bar{t}\gamma$	12 ± 4	(0.24 ± 0.1) %	18 ± 5	(0.39 ± 0.1) %	7 ± 3	(0.21 ± 0.1) %
$t\bar{t}H(\gamma\gamma)$	62.2 ± 2.0	(1.26 ± 0.3) %	57.0 ± 1.9	(1.25 ± 0.3) %	61.6 ± 1.9	(1.91 ± 0.5) %
$t\bar{t}l$	0 ± 0	(0 ± 0) %	0 ± 0	(0 ± 0) %	0 ± 0	(0 ± 0) %
$Z(b\bar{b})H(\gamma\gamma)$	15.01 ± 0.16	(0.30 ± 0.1) %	15.22 ± 0.16	(0.33 ± 0.1) %	13.69 ± 0.15	(0.43 ± 0.1) %
$c\bar{c}\gamma\gamma$	265 ± 12	(5.4 ± 1.3) %	243 ± 11	(5.3 ± 1.3) %	249 ± 11	(7.7 ± 1.8) %
$c\bar{c}j\gamma$	2040 ± 1083	(41 ± 9.6) %	2175 ± 1065	(48 ± 11.5) %	989 ± 656	(31 ± 6.7) %

Table 5-6: *Background composition for all three scenarios for the 120 GeV < $m_{\gamma\gamma}$< 130 GeV cut case.*

In a di-photon mass cut analysis, no ordering can be concluded between different scenarios since all three remain compatible within statistical uncertainties. However, this is not the case for the no diphoton mass preselection analysis. The reference scenario seems to be 30 % better in terms

of significance with respect to the low scenario, whereas ranking between scenarios follows detector extension in eta within statistical uncertainties (*Table 5-4*). More interesting conclusions can be derived by studying the background compositions (*Tables 5-5*). For the no mass cut analysis, the dominant contribution for the reference scenario is likely the jjγγ sample, in which two true photons are present and any b-jets are of incorrectly tagged nature. When switching to the middle and low scenarios, the dominant background contribution presents a tendency towards the ccjγ sample. The substitution of a true photon object by a jet faking a photon, may be partially attributed to poorer tracker implementations. If however this is regarded as the dominant issue, one would expect indications of the bbjγ being the most important background and not the ccjγ. A possible increase of the allowed PU jets at the final state may account for this behavior, effect that significantly amplifies the fake photon misidentification issue, to an extend that seems to be more important than any flavor tagging issue.

Uncertainties on background composition yields presented on *tables 5-5 and 5-6* are taking into account the correlations between the total number of background events and the number of events in each component [16]. An additional contribution is also considered corresponding to the statistical uncertainty of the initial number of events. The final estimation is derived using the following formula (*equation 5-8*):

$$\sigma_{yield} = \sqrt{\frac{yield \cdot (1-yield)}{\sum_{i=1}^{N} N_{bkg,i}} + \cdot \left(\frac{\sigma_{\sum_{i=1}^{N} N_{bkg,i}}}{\sum_{i=1}^{N} N_{bkg,i}} \cdot yield\right)^2} \qquad (5\text{-}8)$$

where yield corresponds to the per-cent contribution of each background sample
σ_{yiel} the uncertainty of the per-cent background contribution

On the other hand, in the case where a di-photon mass preselection is applied, the dominant non-resonant jjγγ component seems to be largely suppressed. In this case, the previously identified effects, poor jet-to-photon misidentification, increased PU contribution of the ccjγ sample and poor tagging implementation appear to be affect all three scenarios, promoting the ccjγ as the most important background within statistical uncertainties. In addition, the fact that bbjγ appears to consists the second most important contribution, denotes the potential issue of the jet-to-photon misidentification. By combining the conclusion from both analysis, with and without di-photon mass cut, it is possible to order the three main issues in a decreasing order of severity. Jet flavor mis-identification is the most important issue, yielding primary contribution a sample with no true b-jets (either jjγγ or ccjγ). The fake jet identification follows, with samples containing one true photon and one jet being either primary or secondary backgrounds in all cases. Finally, the particularity of the ccjγ sample with the forward geometry adds to the previous effects, especially because it is increasingly effected by PU jet high pseudorapidity.
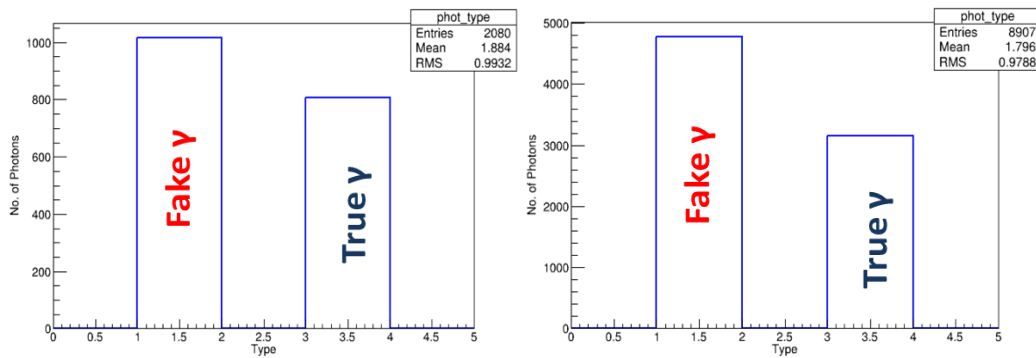
Figure 5.18: *Photon type in the cc̄jγ and bbjγ background samples for the full statistics on the nominal scenario. Type "one" denotes fake photons originating from a jet object while type "three" denotes truth generated photons. On the selected quadruplets, fake photons consist the majority of events.*

A detailed study of the origin of photons in the two samples, the ccjγ and the bbjγ confirms the issue (*Figure 5.18*). It is evident that in both cases, fake photons originating from jets constitute the majority of the selected quadruplets. Furthermore, referring to the nominal scenario with the highest acceptance, it is can also be seen that the final size of the ccjg sample is higher than that of the bbjγ within relevant uncertainties. Taking into consideration the dropping b-jet tagging efficiency at high eta (50% after $|\eta| = 2.0$) and the increased c-efficiency at the same region (40%) according to *Figure 5.8*, one can understand that the extension in eta further enhances the ccjγ background. Finally, the inequality between fake and true photons in both bbjγ and ccjγ samples actually suggest that a significant portion of quadruplets are composed not of one but two fake photons.

5.8.2   Results with a μ = 140 value

Although a value of 140 interactions per crossing is not the first option for the HL-LHC maximum targeted peak luminosity, it provides a significantly cleaner PU environment to study in detail the behavior of the physical quantities and accounts for a more technically feasible LHC operation point. Furthermore, such a study serves as a crosscheck, especially on the linearity and validity of the P_T/η dependent efficiencies, smearing functions and PU emulation tool. In that sense, the full analysis has been repeated at μ = 140 for all scoping scenarios and equivalent cases. Reduced PU component results into cleaner jet pseudorapidity distributions with absence of the characteristic PU structures at high eta and $\eta \approx 2$ regions (*Figure 5.19*) in both leading and sub-leading jets.

As for the μ = 200 case, input distributions of the six most discriminating variables are presented for jet isolation only pre-selection requirement and the di-photon mass cut case (*appendix 8.1*) in the reference scenario. No significant variations are apparent on the single distributions. On the contrary, because of reduced PU pollution, background statistics significantly decreases, due to the large number of different processes included. Thus, background variable fluctuations are increased with respect to μ = 200 case.
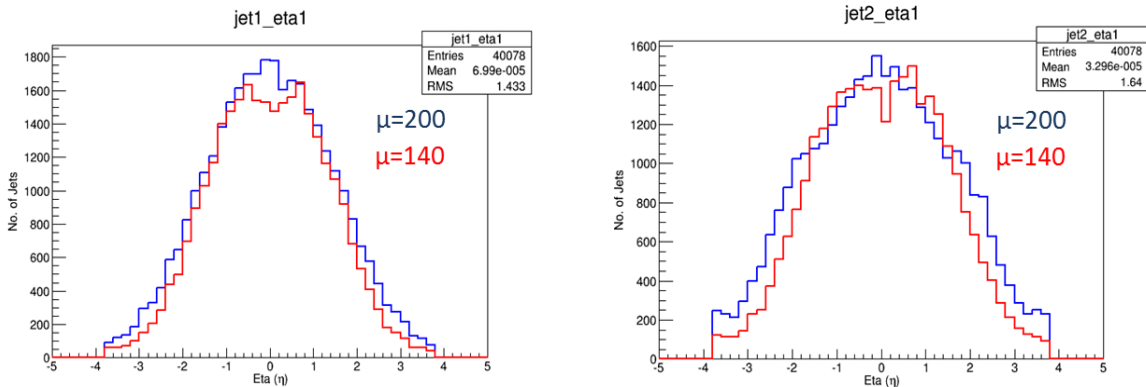
Figure 5.19: *Pseudo rapidity distribution of the leading (left) and sub-leading (right) jets on the bbH sample for the reference scenario at the two μ values.*

BDT classifier PDFs are represented for training and testing sample at the reference scenario (*Figure 5.20*). As previously, an analysis with no additional cuts is performed and one where the di-photon mass is requested to be within the 120 GeV $< m_{\gamma\gamma} <$ 130 GeV interval. While a cleaner background should account for a better separation, more pronounced fluctuations in the corresponding PDFs than for the μ = 200 case do not allow to take advantage of the cleaner environment during classifier training.

Selection of the optimal BDT cut point is performed with respect to the reference scenario and applied to all three cases. Since PU contamination, which affects significantly high eta regions, is lower, it can be observed that the optimal point for all three scenarios is in fact identical (*Figures*

5.21 and 5.22). In high PU conditions, an increase in pseudorapidity acceptance introduces larger background and forces BDT selection to become stricter when passing to more forward extended detector implementations. For a $\mu = 140$ value, this effect is not yet sufficient to affect optimal classifier cut value. As a result, the optimal point is identical for all three scenarios.
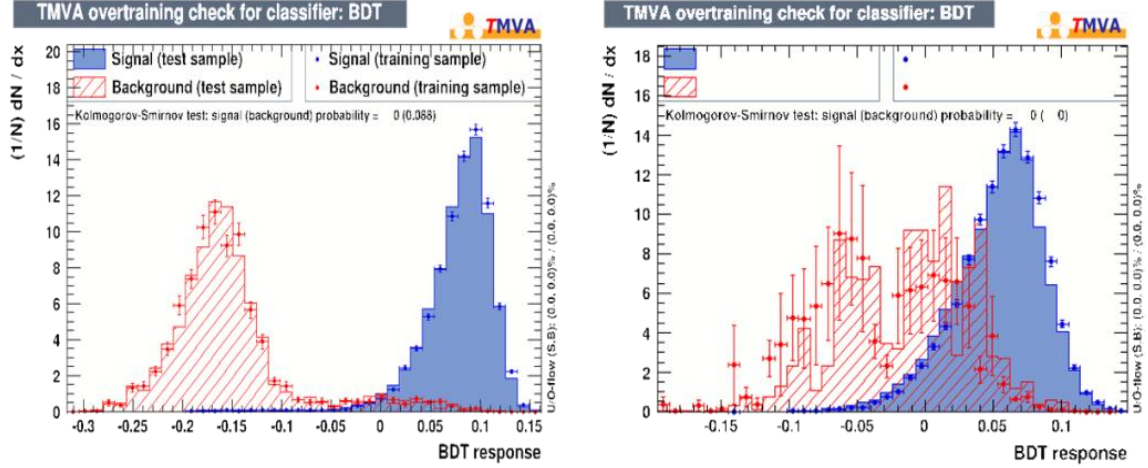
Figure 5.20: *BDT response and output PDFs for the signal in blue and the background in red on the reference scenario at $\mu = 140$. All graphs are normalized while training and testing samples are plotted together, with testing data represented as points. Left hand plot corresponds to no di-photon mass cut case while right hand to 120 GeV < $m_{\gamma\gamma}$ < 130 GeV cut.*

In the *Table 5-7,* significance and expected signal and background events are presented for all scenarios. An overall improvement is observed towards the reference scenario independently of the $m_{\gamma\gamma}$ pre-selection application in both TMVA cases, which is no longer compatible within statistical uncertainties. In addition, by studying the background composition tables (*Tables 5-8 & 5-9*) as well as the tendency on the efficiency, the effect of fake jets to photons becomes in this case also apparent. In the $\mu = 200$ analysis, the most prominent background contribution is the ccγj, where two effects are combined: incorrect jet flavor tagging and jet-photon fake rates. For $\mu = 140$ conditions with the reduced expected PU, wrongly attributed flavor becomes a secondary effect since the number of per event jets is dramatically reduced. In spite of the 2 % b-tagging efficiency corresponding to the PU component, this value is sufficient to introduce a large number of wrongly attributed objects for $\mu = 200$ case while in the $\mu = 140$ conditions, the effect is significantly reduced. On the other hand, fake jet-photon misidentification becomes the most significant issue in lower PU conditions, promoting bbjγ channel that includes three true analysis objects, as the primary background component.

		Reference	Middle	Low
Mass Cut	Significance	0.24 ± 0.03	0.18 ± 0.04	0.167 ± 0.034
	Signal	10.93 ± 0.12	11.38 ± 0.13	9.44 ± 0.12
	Background	2057 ± 341	3810 ± 1070	3192 ± 912
No mass cut	Significance	0.24 ± 0.02	0.20 ± 0.03	0.18 ± 0.04
	Signal	13.46 ± 0.14	13.07 ± 0.14	11.26 ± 0.13
	Background	3047 ± 406	4310 ± 946	3735 ± 1092

Table 5-7: *Significance value and expected signal and background events for all three scenarios in the two TMVA cases, with and without the di-photon mass cut pre-selection for $\mu = 140$.*
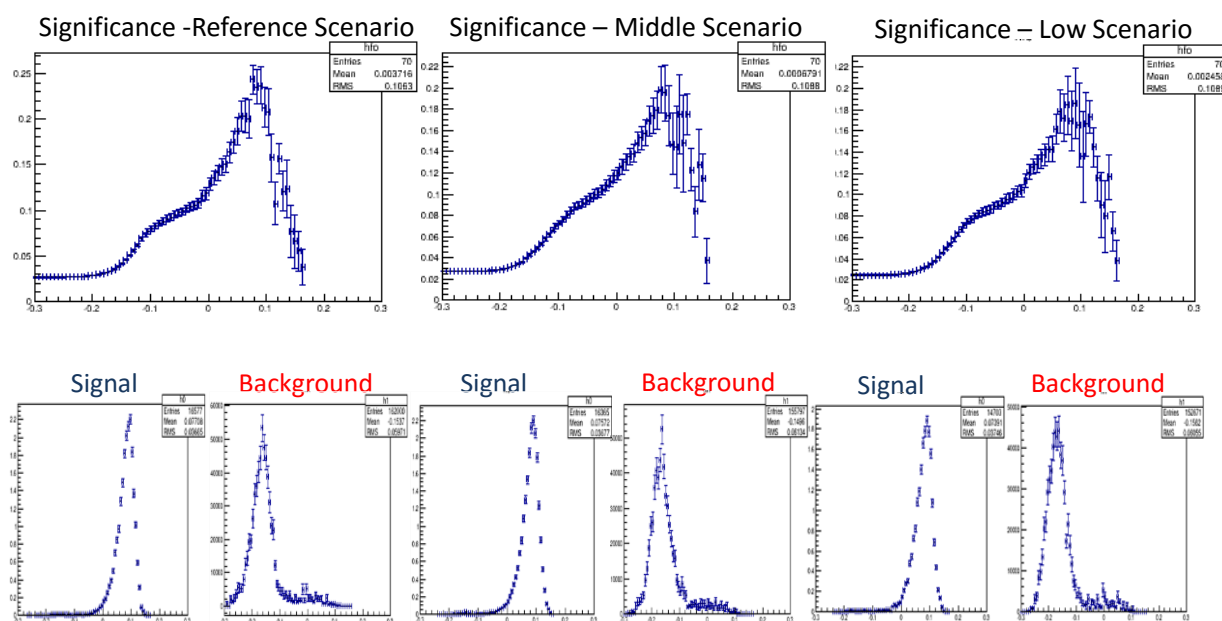
Figure 5.21: *Significance distributions, signal and background PDFs for all three scenarios when no mass cut is applied for a μ = 140 value. From left to right: Reference, Middle and Low scenarios are presented Fluctuation on the higher end of the significance distributions are due to lack of background statistics in the increased weight samples*
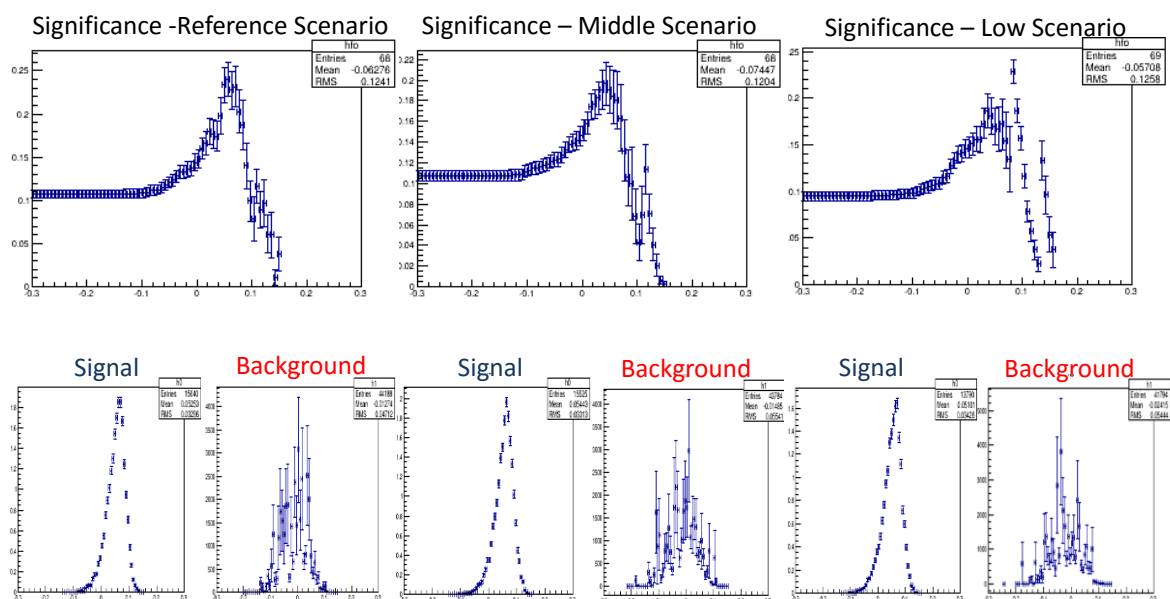
Figure 5.22: *Significance distributions, signal and background PDFs for all three scenarios when a 120 GeV < $m_{γγ}$ < 130 GeV is required for a μ = 140 value. From left to right: Reference, Middle and Low scenarios are presented Fluctuation on the higher end of the significance distributions are due to lack of background statistics in the increased weight samples.*

Overall a 30 % improvement is observed with respect to the μ = 200 value across all scenarios and TMVA configurations. A clear tendency is demonstrated towards the reference scenario while background compositions are still dominated by fake jet to photons. The reduced number of PU jets renders flavor tagging mis-identification a secondary issue, shifting the balance towards true b-jets and the bbγj sample which becomes the most dominant background contribution.

Stream	Reference		Middle		Low	
	Events	Yield %	Events	Yield %	Events	Yield %
$b\bar{b}\gamma\gamma$	286 ± 12	(9.4 ± 1.4) %	269 ± 12	(6.2 ± 1.4) %	232 ± 11	(6.2 ± 1.9) %
$b\bar{b}j\gamma$	1368 ± 350	(45 ± 6.0) %	1638 ± 386	(38 ± 8.4) %	961 ± 302	(26 ± 7.6) %
$H(b\bar{b})H(\gamma\gamma)$	14.49 ± 0.17	(0.48 ± 0.1) %	13.53 ± 0.17	(0.31 ± 0.1) %	12.57 ± 0.16	(0.34 ± 0.1) %
$jj\gamma\gamma$	834 ± 50	(27 ± 3.7) %	709 ± 46	(16 ± 3.7) %	619 ± 43	(17 ± 4.9) %
$t\bar{t}\gamma$	27 ± 7	(0.88 ± 0.2) %	18 ± 5	(0.42 ± 0.1) %	10 ± 4	(0.27 ± 0.1) %
$t\bar{t}H(\gamma\gamma)$	78.6 ± 2.2	(2.6 ± 0.4) %	64.4 ± 2.0	(1.5 ± 0.4) %	65.9 ± 2.0	(1.8 ± 0.6) %
$t\bar{t}l$	0 ± 0	(0 ± 0) %	0 ± 0	(0 ± 0) %	0 ± 0	(0 ± 0) %
$Z(b\bar{b})H(\gamma\gamma)$	17.78 ± 0.18	(0.58 ± 0.2) %	16.82 ± 0.17	(0.39 ± 0.1) %	15.34 ± 0.17	(0.41 ± 0.2) %
$c\bar{c}\gamma\gamma$	224 ± 11	(7.3 ± 1.1) %	197 ± 10	(4.6 ± 1.1) %	187 ± 10	(5.0 ± 1.5) %
$c\bar{c}j\gamma$	198 ± 198	(6 ± 1.0) %	1384 ± 862	(32 ± 7.1) %	1632 ± 1048	(44 ± 12.8) %

Table 5-8: *Background composition for all three scenarios when no di-photon cut is applied for μ = 140.*

Stream	Reference		Middle		Low	
	Events	Yield %	Events	Yield %	Events	Yield %
$b\bar{b}\gamma\gamma$	191 ± 10	(9.3 ± 1.7) %	210 ± 11	(5.5 ± 1.6) %	165 ± 9	(5.2 ± 1.5) %
$b\bar{b}j\gamma$	849 ± 275	(41 ± 6.9) %	1002 ± 295	(26 ± 7.4) %	961 ± 297	(30 ± 8.6) %
$H(b\bar{b})H(\gamma\gamma)$	10.59 ± 0.15	(0.51 ± 0.2) %	10.19 ± 0.15	(0.27 ± 0.1) %	9.76 ± 0.14	(0.31 ± 0.1) %
$jj\gamma\gamma$	599 ± 43	(29 ± 4.9) %	587 ± 42	(15 ± 4.4) %	479 ± 38	(15 ± 4.3) %
$t\bar{t}\gamma$	12 ± 4	(0.58 ± 0.2) %	16 ± 5	(0.42 ± 0.2) %	8 ± 3	(0.24 ± 0.1) %
$t\bar{t}H(\gamma\gamma)$	48.9 ± 1.8	(2.4 ± 0.5) %	48.8 ± 1.8	(1.3 ± 0.4) %	45.6 ± 1.7	(1.4 ± 0.5) %
$t\bar{t}l$	0 ± 0	(0 ± 0) %	0 ± 0	(0 ± 0) %	0 ± 0	(0 ± 0) %
$Z(b\bar{b})H(\gamma\gamma)$	13.29 ± 0.15	(0.65 ± 0.2) %	13.29 ± 0.15	(0.35 ± 0.1) %	11.58 ± 0.14	(0.36 ± 0.1) %
$c\bar{c}\gamma\gamma$	135 ± 8	(6.6 ± 1.2) %	144 ± 9	(3.8 ± 1.1) %	128 ± 8	(4.0 ± 1.2) %
$c\bar{c}j\gamma$	198 ± 198	(10 ± 1.7) %	1779 ± 1027	(47 ± 13.1) %	1384 ± 862	(43 ± 12.4) %

Table 5-9: *Background composition for all three scenarios when 120 GeV < m_γγ < 130 GeV and μ = 140.*

5.9   Cut Based Analysis

A cut based approach was also applied by imposing thresholds on the most discriminant variables, with respect to their discriminating power as defined by the TMVA analysis. The strength of such an analysis in terms of sensitivity is expected to be significantly lower while the addition of the PU jets for an environment with μ = 200 further deteriorates the result. Nevertheless, the aim of this analysis is to validate the general observations performed with the TMVA method by a more robust procedure. Used variables (*Table 5-10*) concern, in the kinematic aspec, sub-leading photon transverse momentum and minimal photon-jet and photon-photon separation. The 2γ invariant mass is required to be compatible with a Higgs decay, to dramatically reduce dominant non-resonant diphoton background candidates. Thresholds have been placed cording the observations on section 5.7 and *Figures 5.11 to 5.12*.

120 GeV < $m_{\gamma\gamma}$ < 130 GeV
$P_T(\gamma_2) > 40$ GeV
$\Delta R(j_1\text{-}\gamma_1) > 1.6$
$\Delta R(\gamma_1\text{-}\gamma_2) < 2.8$

Table 5-10: *Order and applied cuts in the cut based analysis.*

Analysis was performed for both μ = 200 and μ = 140 cases (*Tables 5-11 and 5-12*). An equivalent improvement with respect to the TMVA analysis was observed in the significance, in the order

of 30 % when passing from the higher to lower μ value. Nevertheless, scenario ranking and preference is unclear and within statistical uncertainties. An overall 50 % - 60 % reduction in significance can be deducted in all cases when compared with results obtained using the TMVA method.

Scenario	Significance	Signal	Background
Reference	0.127 ± 0.010	13.07 ± 0.09	10521 ± 1238
Middle	0.131 ± 0.011	12.97 ± 0.09	9805 ± 1187
Low	0.121 ± 0.010	11.35 ± 0.09	8867 ± 1109

Scenario	Significance	Signal	Background
Reference	0.144 ± 0.014	11.85 ± 0.09	6774 ± 902
Middle	0.146 ± 0.015	11.88 ± 0.09	6650 ± 936
Low	0.136 ± 0.013	10.41 ± 0.09	5820 ± 795

Tables 5-11 & 5-12: *Cut based significance and expected signal and background events for μ = 200 on the left hand side and μ = 140 on the right hand side.*

A detailed cut flow table is presented (*Tables 5-13 and 5-14*) for both μ cases and all three scoping scenarios.. The di-photon mass cut as well as the sub-leading photon P$_T$ demonstrate the strongest background rejection, while subsequent closet photon-jet separation performs poorly in signal region An important remark is that the photon-jet separation strength abruptly increases when PU contamination is moderate, suggesting that fake photons are effecting cut's performance.

Applied Cut	Reference		Middle		Low	
	Signal	Background	Signal	Background	Signal	Background
Initial events	24.32 ± 0.13	1.07E+06 ± 13509	24.22 ± 0.13	1.03E+06 ± 13163	21.75 ± 0.12	1.11E+06 ± 14261
P$_T$(γ_2) > 38 GeV	21.15 ± 0.12	455666 ± 8163	21.04 ± 0.12	442493 ± 8022	18.88 ± 0.11	476635 ± 8647
120 GeV < m$_{\gamma\gamma}$ < 130 GeV	19.71 ± 0.12	26838 ± 2045	19.58 ± 0.12	26146 ± 2009	17.65 ± 0.11	29155 ± 2222
ΔR(j$_1$-γ_1) > 1.6	14.12 ± 0.10	12476 ± 1342	13.97 ± 0.10	11508 ± 1286	12.13 ± 0.09	10383 ± 1210
ΔR(γ_1-γ_2) < 2.8	13.07 ± 0.09	10521 ± 1238	12.97 ± 0.09	9805 ± 1187	11.35 ± 0.09	8867 ± 1109

Table 5-13: *Cut flow for all three scenarios at a μ = 200 value.*

Applied Cut	Reference		Middle		Low	
	Signal	Background	Signal	Background	Signal	Background
Initial events	21.17 ± 0.12	637365 ± 9605	21.06 ± 0.12	609842 ± 9244	19.02 ± 0.11	597834 ± 9357
P$_T$(γ_2) > 38 GeV	18.40 ± 0.12	332054 ± 6513	18.31 ± 0.11	315729 ± 6229	16.53 ± 0.11	311694 ± 6379
120 GeV < m$_{\gamma\gamma}$ < 130 GeV	17.54 ± 0.11	18731 ± 1590	17.56 ± 0.11	17934 ± 1537	15.66 ± 0.10	18435 ± 1612
ΔR(j$_1$-γ_1) > 1.6	12.61 ± 0.09	8128 ± 987	12.65 ± 0.09	7872 ± 1015	11.03 ± 0.09	7026 ± 887
ΔR(γ_1-γ_2) < 2.8	11.85 ± 0.09	6774 ± 902	11.88 ± 0.09	6650 ± 936	10.41 ± 0.09	5820 ± 795

Table 5-14: *Cut flow for all three scenarios at a μ = 140 value.*

Although background compositions uncertainties for both μ values (*Tables 5-15 and 5-16*) do not allow for a definitive conclusion, they further point towards the fake jet to photon effect. The most prominent background component seems to remain the ccγj contribution, followed by the bbγj. The latter, corresponds to a true tri-object final state where the additional forth photon originates from a true or PU jet. In this case, PU jet component does not seem to play an important role, especially since the situation remains unaltered for the lower μ value with decreased contamination.

While in the TMVA case the BDT training partially compensates for wrongly attributed flavor PU jets, a cut based approach does not allow any selection combinations that could mitigate the effect.

Stream	Cut Based Analysis, μ=200	
	Expected events	% of total background
$b\bar{b}\gamma\gamma$	340 ± 9	(3.2 ± 0.4) %
$b\bar{b}j\gamma$	3056 ± 380	(29 ± 3) %
$H(\to b\bar{b})H(\to \gamma\gamma)$	16.16 ± 0.13	(0.15 ± 0.04) %
$jj\gamma\gamma$	1749 ± 51	(16.6 ± 2.0) %
$t\bar{t}\gamma$	45 ± 6	(0.43 ± 0.08) %
$t\bar{t}H(\to \gamma\gamma)$	94.4 ± 1.7	(0.90 ± 0.14) %
$t\bar{t}l$	0 ± 0	(0 ± 0) %
$Z(\to b\bar{b})H(\to \gamma\gamma)$	16.39 ± 0.12	(0.16 ± 0.04) %
$c\bar{c}\gamma\gamma$	401 ± 10	(3.8 ± 0.5) %
$c\bar{c}j\gamma$	4804 ± 1177	(46 ± 5) %
$b\bar{b}jj$	Not Used	Not Used

Table 5-15: *Background composition for the reference scenario at μ = 200*

Stream	Cut Based Analysis, μ=140	
	Expected events	% of total background
$b\bar{b}\gamma\gamma$	320 ± 9	(4.7 ± 0.7) %
$b\bar{b}j\gamma$	2398 ± 333	(35 ± 5) %
$H(\to b\bar{b})H(\to \gamma\gamma)$	16.25 ± 0.13	(0.24 ± 0.07) %
$jj\gamma\gamma$	1062 ± 40	(15.7 ± 2.1) %
$t\bar{t}\gamma$	37 ± 5	(0.55 ± 0.12) %
$t\bar{t}H(\to \gamma\gamma)$	90.5 ± 1.7	(1.34 ± 0.23) %
$t\bar{t}l$	163 ± 162.56	(2.4 ± 0.4) %
$Z(\to b\bar{b})H(\to \gamma\gamma)$	16.35 ± 0.12	(0.24 ± 0.07) %
$c\bar{c}\gamma\gamma$	252 ± 8	(3.7 ± 0.5) %
$c\bar{c}j\gamma$	2419 ± 821	(35 ± 5) %
$b\bar{b}jj$	Not Used	Not Used

Table 5-16: *Background composition for the reference scenario at μ = 140.*

5.10 Conclusions

A study on the observability of the bbH(→2γ) mode with ATLAS in HL-LHC conditions (μ = 200 and μ = 140) with an integrated luminosity of 3000 fb⁻¹ has been performed. All three scoping scenarios were studied with a TMVA and cut base approach.

With the current framework of performances and the available simulation samples, the sensitivity to this mode remains week (significance 0.22 (0.11)) for μ = 200 and 0.24 (0.13) for μ = 140 with TMVA (cut-based) selection translating to a μ limit of ~ 4 (9) for a no diphoton mass- cut analysis approach. Passing from Low to Reference scenario, the number of expected events increase in both signal and background samples. A sensitivity improvement of up to 25 % is observed for the no mass cut analysis in both μ values, although current uncertainties may account for half of this estimate (*Table 5-4*).

In the high PU conditions of $\mu = 200$, incorrect jet flavor attribution for the PU part is driving main background contribution. At lower μ values where reduce PU is expected, the effect becomes of secondary nature. An improvement on the PU jet b-tagging efficiency would significantly benefit the $\mu = 200$ analysis. Jet to photon misidentification accounts for main background contribution in all scenarios and μ values. An evaluation of the photon fake rate is would be necessary at this point with pointing vector consideration to increase non primary vertex photon rejection.

A significant increase of available statistics in certain background sample would allow safer conclusions to be extracted and stringer limits to be imposed on expected significance and signal events. An attempt to further treat the Monte Carlo statistical poverty can be established through a fully weighted approach. For this method, efficiencies and tracking algorithms would no longer be applied in a cut based probabilistic manner. A global weight would be formed, extrapolating efficiencies and combining all identification probabilities. Although the final weight of an individual combination would be the product of the weights of its constituents, a normalization is imposed by the fact that several objects are recused into multiple combinations. In such an approach, additional attention is needed to correctly account for correlations occurring form the use of the same object in several combinations.

5.11 References

[1]   CMS Collaboration, S. Chatrchyan et al., "Precise determination of the mass of the Higgs boson and studies of the compatibility of its couplings with the standard model".

[2]   ATLAS-CONF-2013-009,   ATLAS-CONF-2013-010,   ATLAS-CONF-2013-012, ATLASCONF-2013-13 (2013).

[3]   E. Bagnaschi, G. Degrassi, P. Slavich, and A. Vicini, "Higgs production via gluon fusion in the POWHEG approach in the SM and in the MSSM", JHEP 1202 (2012) 088, [arX"iv:1111.2854]

[4]   H. Mantler and M. Wiesemann, "Top- and bottom-mass effects in hadronic Higgs production at small transverse momenta through LO+NLL", Eur.Phys.J. C73 (2013) 2467, [arXiv:1210.8263]

[5]   M. Grazzini and H. Sargsyan, "Heavy-quark mass effects in Higgs boson production at the LHC", JHEP 1309 (2013) 129, [arXiv:1306.4581]

[6]   A. Banfi, P. F. Monni, and G. Zanderighi, "Quark masses in Higgs production with a jet veto", JHEP 1401 (2014) 097, [arXiv:1308.4634]

[7]   M. Aivazis, J. C. Collins, F. I. Olness, and W.-K. Tung, "Leptoproduction of heavy quarks. 2. A Unified QCD formulation of charged and neutral current processes from fixed target to collider energies", Phys.Rev. D50 (1994) 3102–3118, [hep-ph/9312319]

[8]   M. Wiesemann et al., "Higgs production in association with bottom quarks", CERN-PH-TH-2014-182, arXiv:1409.5301v1 [hep-ph], 18 Sep 2014

[9]   LHC Higgs Cross Section Working Group, https://tlwiki.cern.ch/twiki/bin/view/LHCPhysics/CrossSections

[10]   Pavel Weber, "Jets in Atlas experiment (reconstruction and calibration)", University of Heidelberg, http://www.kip.uni-heidelberg.de/atlas/seminars/SS2009_JC/jet_algorithms.pdf

[11]   ATLAS Collaboration, "ATLAS Phase-II Upgrade Scoping Document", CERN-LHCC-2015-020; LHCC-G-166

[12]   ATLAS Collaboration, Calibration of the performance of b-tagging for c and light-flavor jets in the 2012 ATLAS data, ATLAS-CONF-2014-046, http://cds.cern.ch/record/1741020

[13]   ATLAS Collaboration, Performance assumptions based on full simulation for an upgraded ATLAS detector at a High-Luminosity LHC, https://cds.cern.ch/record/1604420

[14]   The ATLAS Collaboration, "ATLAS Large eta task force report", ATL-COM-UPGRADE-2015-013, 2015

[15]   Marc Escalier, "Recherche et découverte du boson de Higgs avec son mode de désintégration en pair de photons avec l'expérience ATLAS au LHC: une introduction", Mémoire présenté en vue d'Obtenir l'Habilitation à Diriger des Recherches, LAL 15-30, 2015

[16]   C. Blocker, "Uncertainties on Efficiencies", 2004, CDF/NEMO/STATISTICS/PUBLIC/7168

6 Planar Pixel development

6.1 Introduction

In this chapter an integrated comprehensive approach of silicon pixel development will be presented. After the necessary theoretical introduction, a full pixel fabrication process 3D simulation is performed for the basic current pixel design of the ATLAS detector. Conclusions are subsequently applied to the next stage of sensor design. Four innovative active edge geometries with top electrode modifications are implemented. To test production result, both process evaluation through Secondary Ion Mass Spectroscopy Measurements and functional detector assessment with electrical characterization are performed. A special library was developed for the purpose of in-depth post-process and in-situ evaluations along with the simulation and data analysis methodology. Progressing towards a fully functional particle detector, issues of the completed sensor assembly bonded with readout electronics are treated. In particular, the effect that different interconnection technologies can introduce to the final signal is examined. Finally, radiation damage is treated, both in its elementary effects through irradiated dopant profile characterization, but also with respect to detector functionality, via the study of a diode test production, irradiated at various fluences (up to $10^{16} n_{eq}/cm^2$).

To cover the entire conception circle of the final detector, activities are also presented in two additional domains. In the data acquisition side, a new system was designed and developed, capable of use in a wide range of technological application. This personal investment, not only covers the needs for a suitable test platform for future developments, but is also conceived as a contribution to the pixel community. On the future and alternative technologies aspect, a detailed process evaluation and development on a new kind of detector known as the Low Gain Avalanche Diode (LGAD) is presented. Although their radiation resistance remains to be proven, LGADs are considered a promising technology for future application due their attractive timing characteristics, embedded signal amplification potential and relatively simple fabrication process.

To summarize, the six main axis of sensor development are presented. From simulation to design and production quality testing, to interconnections and data acquisition system development, concluding with the problematic of radiation damage and relevant effects. This approach consists a continuous project, evolving trough all development steps with increased personal involvement.

6.2 HL-LHC Requirements

Planned LHC Phase II upgrades (HL-LHC) aim at extending the physics reach of ATLAS and CMS experiments by a factor 5 increase in instantaneous machine luminosity. Values of up to 7×10^{34} $cm^{-2}sec^{-1}$ are expected with a final estimated integrated luminosity at 3000 fb^{-1} [1]. Fluences at the tracker system will reach or exceed $\sim2\times10^{16}$ n_{eq}/cm^2 for the innermost layers (*Figure 6.1*) while 10^{15} n_{eq}/cm^2 is anticipated at the outer regions [2]. In those harsh conditions, an innovative radiation hard and geometrically efficient design is required for the planned complete replacement of the semiconductor tracker.

A complete replacement of the ATLAS inner tracker is envisaged, in order to cope with the high multiplicity environment, passing from the current area of 1.6 m^2 to 8 m^2 surface of silicon detectors. Increased occupancy may be addressed by adjusting the silicon detector unit cell (pixel, strip or short strip) size in conjunction with the use of active edge technology. On the other hand, radiation hardness constraints impose the exclusive use of electron collecting technologies (n-in-n or n-in-p). The latter, is proven to be significantly less affected by charge trapping due to reduced drift time and increased electron velocities [3, 4].

In preparation for this future demanding environment, variable geometry and implantation configurations are under consideration. Using simulations, targeted characteristics of the final device, response to radiation damage and efficiency can be probed with respect to fabrication process. An extensive evaluation of the simulation framework was performed. Subsequent instructive conclusions were applied in modifying the fabrication process in order to achieve optimized results. In a first approximation, implantation, oxidation and annealing steps are being extensively simulated. Simulation results are compared with experimental data, obtained using the Secondary Ion Mass Spectroscopy (SIMS) method, to determine dopant profiles.
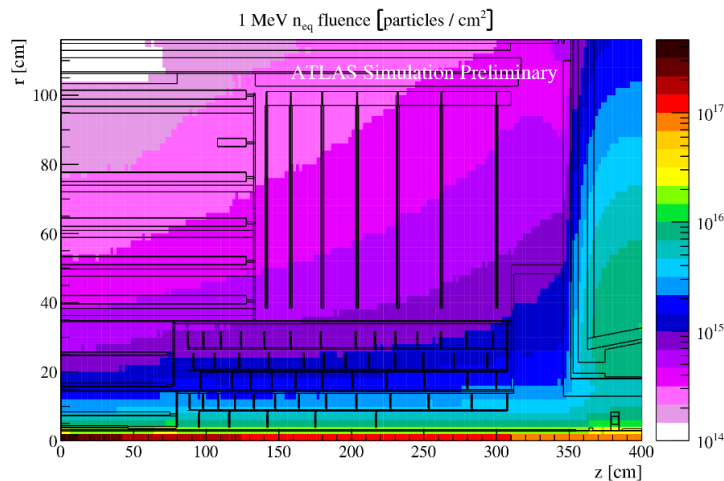
Figure 6.1: *Estimated equivalent fluences for the ATLAS inner tracker with respect to distance from the interaction point [5].*

6.3   Introduction to Silicon Detector Fundamentals

Electronics Grade Silicon (EGS) is of crystalloid type, organized in a faced-centered cubic crystal structure (*Figure 6.2*). Developed through the Czochralski (Cz) or Floating Zone (Fz) crystallization process in perfect mono-crystalline structures of defined orientation, it is most commonly organized in flat circular structures, referred as wafers [6]. Wafers are characterized by their thickness (in the order of several μm), their crystallographic orientation defined by the corresponding Miller indexes [7], their purity, assessed by electrical resistivity and the conduction type of substrate impurities (n for negative and p for positive types). EGS has a reference purity of a 100 ppb (parts per billion), which compared to metallurgical grade silicon commonly used is 10^6 times more refined.
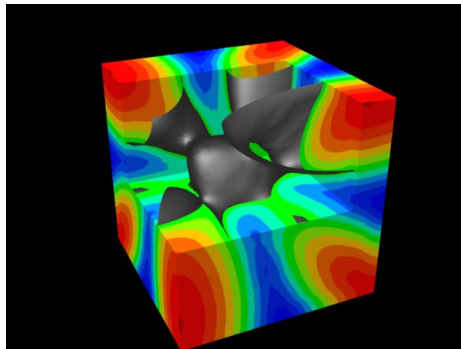
Figure 6.2: *Representation of the face-centered silicon crystal lattice with the band structure zones around the lattice positions.* The first Brillouin zone is represented *that demonstrates the strict influence of crystallographic axis to carrier motion [8].*

Quantum energy state superposition of silicon atom outer electrons in a lattice cell forces reorganization of energy levels (*Figure 6.3*). This hybridization effect, due to interactions between atoms, splits the original energy levels to additional states. In an infinite dimension approximation when considering a large number of interacting atoms, allowed energy states form a quasi-continuous spectrum with permitted energy zones and prohibited band gaps. This structural reorganization introduces semi-conductivity in the lattice, where electrons can, under certain conditions, traverse band-gaps and find themselves in a higher momentum-energy state. The width of the prohibited zones is an intrinsic property of each semiconductor material. Valence electrons of silicon atoms are responsible for lattice coherence and their movement is restrained close to the crystal structure. On the other hand, electrons in the conduction band of the collective structure, can propagate freely thought the crystal volume. In a first order approximation, conduction electrons can be considered as a fermionic gas whose energy distribution may be approximated by the Fermi-Dirac equation. This leads to a temperature dependent energy distribution, in which at low temperatures, all states can be populated. On the other hand, as temperature increases, electrons acquire sufficient kinetic energy that may allow them to jump from the valence to the conduction band. Conduction electron concentration in pure silicon is described by the following equation (*equation 6-1*) [9]:

$$n_i = 3.9 \times 10^{16} T^{3/2} e^{-0.605(keV)/kT} \qquad (6\text{-}1)$$

where n_i is the electron concentration in cm^{-3}, T the temperature and *k* Boltzmann's thermodynamic constant. As it is evident, in zero temperature all states are occupied and no free electrons exist to populate the conductive region. The exponent on the last term of *equation 6-1* is material specific and represents half of the energy gap between the conductive and valence zones while an additional multiplication factor is introduced to account for the band's dependence on temperature.
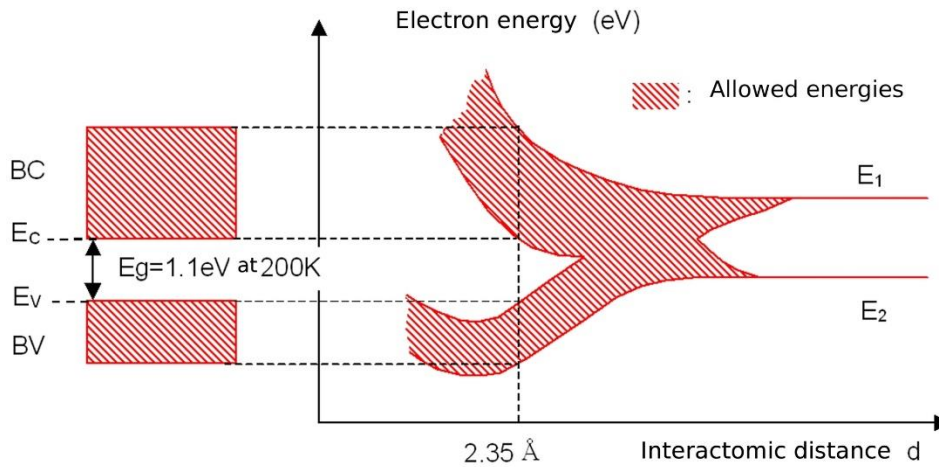
Figure 6.3: *Reorganization of atomic electron energy levels in a crystal lattice structure. Once atoms reach their atomic equilibrium distance of 2.35Å two continuous energy bands form (CB and VB), separated by a forbidden band, which is not accessible for electrons. Band gap, E_g is a characteristic of the material. The lowest energy level of the conduction band is denoted E_C while highest energy level of the valence band is called E_V so that we have the relationship $E_g=E_C-E_V$. Conduction and valence bands CB and VB represent the energies accessible to electrons, or the energies of the states potentially occupied by electrons [10].*

This fact inevitably leads to the introduction of a "hole" term, which in principle is the absence of an electron from the valence zone of the crystal. Since four electrons are available in the outer structure of the silicon atom, the introduction of foreign elements in the lattice with different number of valence electrons (N_{va}) will lead to either the absence of a lattice bond (a hole) if $N_{va} < 4$, or to the excess of an electron if $N_{va} > 4$. Such elements are called dopants and may be of two distinct types:

Acceptor: a dopant with less than four outer electrons that introduces an excess of holes in the structure. Most common p-type dopant is Boron but other alternatives may be used as Gallium.

Donor: for elements with an excess of valence electrons therefore introducing possible negative contributions to the structure. In this category phosphorous is mainly used.

Usually, both dopant types are found in a semiconductor crystal, but their contribution will cancel each other in such a way that only the net dopant is electrically active. A net p type doping (acceptor) will subsequently shift the Fermi quasi-energy level towards the valence band, while a net n-type doping (donor) will have the opposite effect. In each case, the barrier will be shifted since additional introduced carriers will fill energy levels not normally occupied. Given the band gap dependence with temperature, in higher values, the narrower gap allows for more carriers to pass to the conductive band reducing substrate resistivity. On the other hand, the narrower band-gap at low temperatures increases resistivity. The effect becomes more complex in a strongly doped silicon ($>10^{18}$ atoms/cm^3), where the amount of carriers is so high that states in the valence (conductivity) bands have a unitary probability to be filled by holes (electrons), resulting in a high electrical conductivity even at very low temperatures.

To describe the behavior of any semiconductor material, the drift-diffusion model has been developed, relying on a set of three equations [6]. In principle it is a combination of classical electrodynamics with diffusion and continuity additions expressed by the Maxwell and Poisson equations respectively. While model validly can be extended to degenerate semiconductors under the assumption that Fermi's statistics is respected, for the following equations, we assume a non-degenerate electron density that can be approximated by the Boltzmann distribution. In this case the Fermi level is assumed to have at least a 3kT distance from the closest band limit (conductive/valence). Dopants are also assumed to be ionized, which is the case for a shallow implantation while a stable temperature is supposed. The corresponding diffusion equations for electrons and holes are as follows (*equation 6.2 and 6.3*):

$$\frac{dp}{dt} = \nabla D_h \nabla_p + \nabla\left(p\mu_h \vec{E}\right) + G_h - R_h \qquad (6\text{-}2)$$

$$\frac{dn}{dt} = \nabla D_e \nabla_n + \nabla\left(\eta\mu_e \vec{E}\right) + G_e - R_e \qquad (6\text{-}3)$$

where D_h and D_e are the diffusion coefficients for electrons and holes in silicon, p and η represent the density of electrons and holes respectively in cm^{-3} and μ the mobility in cm^2/V/sec. The coefficients G and R account for the generation and recombination rates in cm^{-3}s^{-1}.

An additional equation is introduced to the system by the expression of the field-potential equation coupled with the Poisson continuity theorem and the total charge density ρ (*equations 6.4 and 6.5*):

$$-\nabla^2 V = \overrightarrow{\nabla E} = \frac{\rho}{\varepsilon} \qquad (6\text{-}4)$$

$$\rho = q(p - n + N_d^+ - N_a^-) \qquad (6\text{-}5)$$

where p and n are the number of intrinsic holes and electron concentration and N_d, N_a the number of donors and acceptors introduced by the dopant into the semiconductor material.

Generation effect is important for the description of leakage current in semiconductor detectors under bias. Recombination occurs between free charge carriers with a proportional rate to carrier concentration. Since in silicon semi-conductivity is achieved through doping indirectly creating the band gap region, recombination mainly occurs in defect centers present along the silicon band-gap.

6.3.1   Operating Principals

The use of silicon detectors in high energy particle physics was historically introduced by the NA11 and NA32 collaborations at CERN [7]. The operating principle of such a structure is based on a segmented p-n junction matrix.

When two regions of silicon of different doping type are in contact, an area is formed along the transition boundary, where opposite type carriers are combined. This, in the n-p case, would mean that under normal conditions, excess electrons from the n-side will recombine with holes in the p-side. An electric field is generated at the surrounding area, in a way that no other synchronized charge movement is permitted. The number of incoming and outgoing charges to the region due to thermal diffusion becomes equal once thermal equilibrium is established (*Figure 6.4*). This region is referred to as being "depleted" since no free charge carriers can be found within. In a general manner it is possible to control the span of the depletion region by means of an external electric field, referred as "biasing". There are two possible ways of biasing a p-n junction:
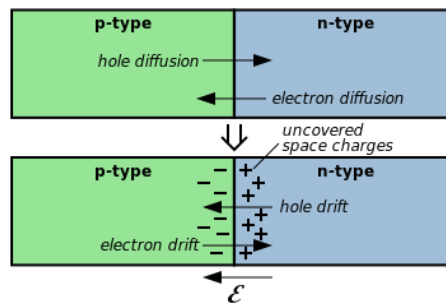
Figure 6.4: *Diagram of the diffusion across a p-n junction, with the resultant uncovered space charges, the electric field and the drift currents [11].*

Forward Biasing: If a positive potential is applied in the p-side and a negative to the n-side (*Figure 6.5*), then the corresponding carriers are moving away from the electrodes and towards the interface, repopulating energy states and reducing the width of the depletion region. Effective material resistance is dropping and it becomes conductive with an exponentially increased current with respect to the applied voltage. This act is referred as forward biasing.
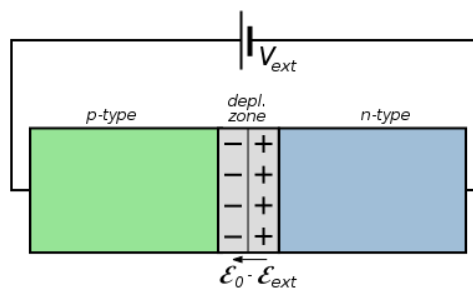
Figure 6.5: *Representation of an n-p junction in forward bias [12].*

Reverse Biasing: If a positive potential is applied to the n region and a negative potential to the p one (*Figure 6.6*), charge carriers are moving towards the electrodes, emptying larger portions at the central region of the material. The depletion zone expands and the conductivity subsequently drops. The current will increase in the initial stages of the polarization exponentially, because of free carrier movement. Once an equilibrium has been reached, it will remain stable with respect to the voltage since only thermal diffusion is allowed (*Figure 6.7*). This is referred to as reverse biasing.
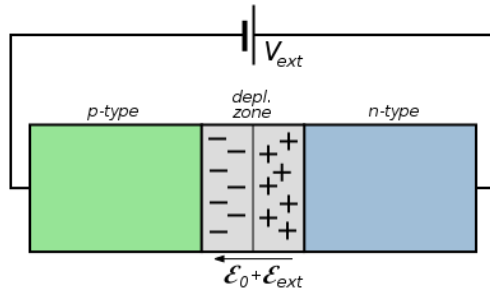
Figure 6.6: *Representation of an n-p junction in inverse bias [13].*
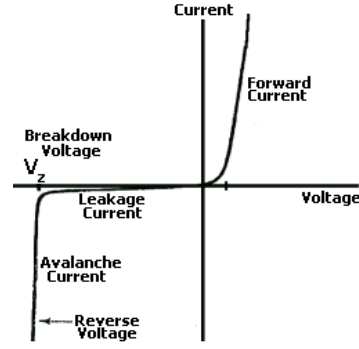
Figure 6.7: *Current vs voltage curve for a forward and inversed biased diode [14].*

In the case of a reversed biased p-n junction, the applied voltage will virtually appear in its full value across the depletion region, because of the much higher material resistivity with respect to n and p doped regions. As a result derived by the Poisson's equation, the space charge will also increase and extend further along both sides of the junction. The thickness of the depletion region therefore increases. Although the following calculation is performed with the assumption that the depletion region does not reach the wafer surface, the results are applicable in completely depleted structures as well, with the caveat that the eventual depletion region has to be geometrically limited by the wafer thickness.

Charge distribution in a reverse biased junction can be represented as (*equation 6-6*):

$$\rho(\chi) = \begin{cases} |e|N_D & (-a \leq x \leq 0) \\ -|e|N_A & (0 \leq x \leq b) \end{cases} \qquad (6\text{-}6)$$

where –a and b are the limits of the depletion region in each side of the junction (placed at the relative coordinate 0) and N_A, N_D the concentration of acceptors and donors respectively. The assumption is made that the electron diffusion results in a positive space charge in the n-region $-a \leq x \leq 0$ of the junction, while a corresponding negative space charge due to hole diffusion extends in the p-region over the area $0 \leq x \leq b$ [9]. The total charge is equal with sum of the number of holes and free electrons (p and n respectively), and the number of ionized donors and acceptors. With the assumption that all donor/acceptor atoms are fully ionized and their number is significantly higher than that of free electrons/holes, total neutrality can be respected under the condition $N_Da=N_Ab$.

By applying the Poisson equation in the above charge distribution, it can be derived that (*equation 6-7*):

$$\frac{\partial^2 \varphi}{\partial x^2} = -\rho(\chi) \Rightarrow \frac{\partial^2 \varphi}{\partial x^2} = \begin{cases} -\dfrac{eN_D}{\varepsilon} & (-a \leq x \leq 0) \\ \dfrac{eN_A}{\varepsilon} & (0 \leq x \leq b) \end{cases} \qquad (6\text{-}7)$$

To determine the electric potential an integration is sufficient by applying the boundary condition that the electric field must vanish at both ends of the distribution. This can be represented as (*equation 6-8*):

$$\frac{\partial \varphi}{\partial x} = \begin{cases} -\dfrac{eN_D}{\varepsilon}(x + a) & (-a \leq x \leq 0) \\ \dfrac{eN_A}{\varepsilon}(x - b) & (0 \leq x \leq b) \end{cases} \qquad (6\text{-}8)$$

With a secondary integration we can determine the electric potential. The boundary conditions can be established since the difference of the potential between the n and the p region should be equal to the bias voltage, assuming a relatively small junction contact potential. As a result it can be derived that (*equation 6-9*):

$$\varphi(x) = \begin{cases} -\frac{eN_D}{2\varepsilon}(x+a)^2 + \frac{eN_D}{2\varepsilon}a^2 & (-a \leq x \leq 0) \\ \frac{eN_A}{2\varepsilon}(x-b)^2 - \frac{eN_D}{2\varepsilon}b^2 & (0 \leq x \leq b) \end{cases} \qquad (6\text{-}9)$$

and by applying the potential difference V at any point within the depletion refion, is deducted that (*equation 6-10*):

$$V - \frac{eN_D a^2}{2\varepsilon} = \frac{eN_A b^2}{2\varepsilon} \iff N_D a^2 + N_A b^2 = \frac{2\varepsilon V}{e} \overset{N_A = N_D}{\iff} (a+b)b = \frac{2\varepsilon V}{eN_A} \qquad (6\text{-}10)$$

To calculate the total width of the depletion region, d = a + b, we can assume that the n-doping level is much higher that the p-one [15]. Consequently, since $N_A \ll N_D$ while $N_A b = N_D a$ we need to assume that b >> a and therefore the space charge extends much further on the p-side than on the n. In this case d ≈ b and we can deduct (*equation 6-11*):

$$d \cong \left(\frac{2\varepsilon V}{eN}\right)^{1/2} \qquad (6\text{-}11)$$

The result would have been the same even if the initial assumption was the inverse, assuming a dominant p-region. The resistivity of a semiconductor material can be expressed as ρ=1/eμN and by substituting to *equation 6-11* it can be inferred that:

$$d \cong (2\varepsilon V \mu \rho_D)^{1/2} \qquad (6\text{-}12)$$

Because of the semiconductor resistivity direct relation to active dopant concentration, when measuring the resistivity of the material in different depth once can deduce an accurate active dopant profile. Since one would like the largest depletion region with the lowest possible voltage, it is advantageous to use high resistivity substrate materials in semiconductor detector fabrication. Resistivity is limited by the substrate purity [16], since the amount of original substrate doping (before any lithographic process) must be high enough to counteract any material residual non-uniform effects.

An inversed biased junction presents a charge built-up in either side of the depletion region, resulting to properties similar to a charged capacitor. If the bias voltage increases, the depletion region is enlarged and the capacitance is reduced. The value of capacitance per unit area is defined as (*equation 6-13*):

$$C = \frac{\varepsilon}{d} \cong \left(\frac{e\varepsilon N}{2V}\right)^{1/2} \qquad (6\text{-}13)$$

Good energy resolution in an environment where electronic noise is important depends on achieving a small capacitance and thus applying the highest possible operating voltage, up to the full depletion point. Maximum electric field occurs at the point of transition between the n and p type material and can easily reach 10^6-10^7 V/m. For partially depleted detectors, the width of the depletion region is proportional to $V^{1/2}$ while the electric field value increases with the applied voltage also proportionally to $V^{1/2}$.

In a situation where complete depletion is reached, no free charge carriers are available within the detector junction. Nevertheless, an energy deposit by an external cause at a defined region of the

structure, can create free electron-hole pairs. Those would be directed towards the contact electrodes under the influence of the applied field, until all charge is evacuated from the silicon volume. As a result, a current will appear between the contacts electrodes, for the exact duration of the charges drift time. This energy deposit, in particle physics case, is a signature of a high energy charged particle traversing the sensor volume.

6.3.2   Technologies and radiation damage

Actual tracking sensors are finely segmented n-p junction matrices, allowing for an accurate position measurement. The sensor is inversely biased by applying a potential at one side while keeping the other to the ground. Signal extraction is performed by measuring evacuated charges towards the grounded side and an energy measurement is possible by integrating the collected charge.

P-n junctions can be formed in the following four ways (*Figure 6.8*):

1. On an n-type silicon substrate we can create an n^+-implanted region containing an excess of negative carriers. In that case, it is necessary to form a p-implanted region on the opposite side of the substrate, in order to create a p-n junction. This is referred to as an n-in-n technology.

2. On an n-type silicon substrate a p-implanted region is created. The junction is formed directly between the implanted region and the substrate itself. This is referred to as a p-in-n technology.

3. On a p-type substrate, it is possible to create n-implanted regions, in a way that the junction will be formed between the implanted region and the substrate itself. Such a technique is defines as n-in-p.

4. Finally, in a p-substrate, one can implant p^+ regions to create the pixelated geometry. In this case an additional n-implants required on the back side of the wafer to form the junction and is characterized as the p-in-p technique.

(a) n-in-n sensor

(b) p-in-n sensor

(c) n-in-p sensor

(d) p-in-p sensor
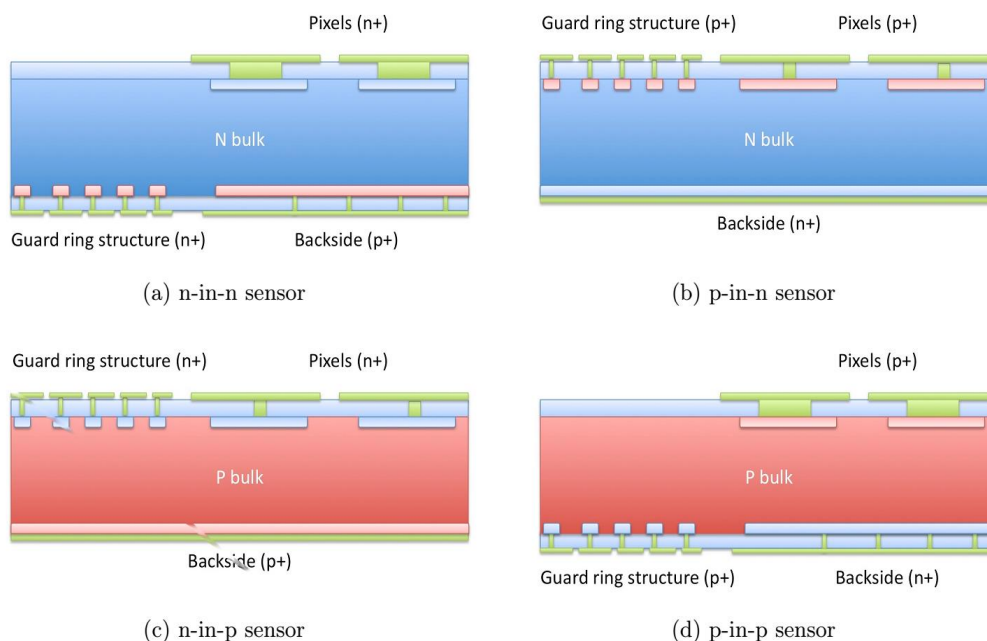
Figure 6.8: *Different planar pixel production technologies [17].*

Currently, out of the four described technologies, only the n-in-n and n-in-p is considered as the present option for the Highly Luminosity tracker upgrades of the ATLAS and CMS experiments. The radiation tolerance of the n-in-n technology has established it as the main solution while the economic benefits of the single sided lithography in the n-in-p process make it an attractive alternative. P-in-p sensors are only a theoretical concept since the combine the disadvantages of hole collection along with a double-sided lithography [18]. Additional structures at the outer region of the pixelated matrix are created to gradually lower the electric potential from the central region to the edges in order to avoid conductivity sparks when several matrices are placed in close proximity. These specialized structures, in form of implanted rings surrounding the matrix, are referred as Guard Rings (GR).

When referring to dopants and to the functionality of a p-n junction on the previous section, N_A and N_D were always referring to the acceptor and donor concentration respectively. While this simplistic approach is true for modern detectors where on each side only one spices is dominant, after irradiation or when several doping and electrically active defects are present, these quantities have to be replaced by the net doping or effective doping N_{eff}. This refers to the difference in concentration of all the donor –like states with respect to all acceptor-like state 3s and can be defined by the depletion voltage under the following condition (*equation 6-14*):

$$|N_{eff}| = \frac{2\varepsilon_0 \varepsilon_{si} V_{dep.}}{ed^2} \qquad (6\text{-}14)$$

where apart from the normal dielectric constants ε_0 and ε_{si}, e is the electron charge and d the length of the depletion region. Since by definition effective doping is positive for n-type materials and negative for p-type, only its absolute value is used in calculations.

In a non-irradiated silicon detector, effective doping (N_{eff}) is mainly defined by the shallow pixel implant on the front side of the sensor. Radiation damage effects introduce additional energy levels in the forbidden band –gap close to the mid-region, referred as deep levels. Experimentally, it is proven that deep level defects are primarily acceptor level. In the case of n-type silicon, this will reduce the initial effective doping concentration. As N_{eff} decreases, the so-called inversion fluence is reached, where the negative space charge of radiation induced donor impurities, compensates the initial positive space charge of the phosphorus implanted atoms. If the fluence increase further, the material behaves increasingly like a p-type silicon. This effect, not due to physical active dopant removal, is attributed to an increase of acceptors [19]. For an n type substrate, this would translate to a decrease in effective dopant concentration, up to the point of type inversion, where the material behaves as p-type silicon. On the contrary, for p-type substrates this effect is not manifested. The effective dopant concentration can be parameterized with respect to the fluence in the following way [20] (*equation 6-15*):

$$N_{eff}(\Phi) = N_{eff,0} e^{-c\Phi} - \beta\Phi \qquad (6\text{-}15)$$

where Φ is the fluence, $N_{eff,0}$ represents the initial effective dopant, while c and β correspond to donor compensation and acceptor generation respectively. The result of operating a heavy irradiated n-type silicon detector is that the junction moves from the front side to the back region. The device remains operational but if it is under-depleted, generated charges traverse through a non-depleted layer before reaching the read-out electrodes on the pixel side.

After irradiation the effective dopant changes over time. Two different effects are distinguished:

1. Immediately after irradiation N_{eff} decreases as a result of the decay of active radiation induced acceptor sites back to neutral level. The decrease continues until a minimum is reached and is referred to as "beneficial annealing".

2. After the minimum of N_{eff} has been reached, it again start to increase over time. This is believed to be due to diffusion of defects that create deep acceptor levels and reactions between them [21]. This process, referred to as reverse annealing, takes place in a larger time scale but introduces greater changes to the active dopant.

Both processes are very temperature sensitive, with reverse annealing mostly halted below 0^0C. At high temperatures the process is accelerated leading to increased depletion voltages [22]. As a result of these effects, a time depend change on the effective dopant is observed, which can be described in the following form (*equation 6-16*):

$$\Delta N_{eff}(\Phi, t, T) = N_{eff,0} - N_{eff} = N_b(\Phi, t, T) + N_c(\Phi) + N_Y(\Phi, t, T) \qquad (6\text{-}16)$$

where $N_{eff,0}$ represents the initial dopant concentration, N_b is related to beneficial annealing, N_c is related to the time-independent changes induced by radiation and N_Y corresponds to the inverse annealing component [23, 24].

A model describing the time and temperature dependence of the inverse annealing was developed by a group at Hamburg University (referred as the Hamburg model) [22, 23, 24]. It is based on the idea that the effect is produced by the transformation of originally electrically inactive defects into acceptor like states. Consequently, ΔN_{eff} saturates at a certain value, when all inactive defects have been transformed [25]. Using as a baseline *equation 6-15*, the stable time-independent irradiation component can be parameterized as (*equation 6-17*):

$$N_c(\Phi) = N_{c,0}[1 - e^{-c\Phi}] - g_c\Phi \qquad (6\text{-}17)$$

where the right term represents the introduction of acceptor like states as a function of the fluence and the exponential function corresponds to the compensation of the original donor concentration ($N_{c,0}$). For high fluences, greater than 10^{13} n_{eq}/cm^2, the exponential term can be neglected.

The reverse annealing on the other hand is treated by a second order approach. We assume two originally inactive defects X_1 and X_2 of equivalent concentrations N_{X1} and N_{X2} which for simplicity are considered equal. They can interact with each other to form an electrically active defect Y, following a decay of $N_{X1}=N_{X2}=N_{X0}$. The concentration of Y is described as (*equation 6-18*):

$$N_Y(t) = N_{X,0}[1 - \frac{1}{1+kN_{X,0}t}] \qquad (6\text{-}18)$$

were k is the N_{X0} decay constant defines as (*equation 6-19*):

$$k = k_0 e^{-E_a/k_B T} \qquad (6\text{-}19)$$

In this latest equation, E_a indicates the activation energy, k_B is the Boltzmann constant, and k_0 is a constant related to the phonon frequency in the lattice. Via k, the active defect concentration N_Y is strongly temperature dependent. N_Y will saturate at the concentration level $N_{X,0}$ if t→∞. $N_{X,0}$ can therefore be represented as $N_{Y,\infty}=gY\times\varphi$, where g_Y is referred to as the reverse annealing introduction rate.

6.3.3   Charge Collection and Signal extraction

Electron-hole pairs, created by energetic particles traversing the silicon volume will propagate to the closest readout electrode. Following the Shockley–Ramo theorem [26, 27], the current induced to the electrode itself is instantaneous, due to change of electrostatic flux lines ending on the electrodes surface. The amount of carriers arriving at the electrodes becomes a secondary effect. Using the method of Green functions, Shockley and Ramo independently derived a highly useful domain

integration formula for terminal currents induced by charge motion in an arbitrary multidimensional structure with multiple contacts (*equation 6-20*):

$$I^{(k)} = \sum_j q_j \cdot E_j^{(k)} \cdot v_j \qquad (6\text{-}20)$$

where the summation j runs over all particles within the volume, q_j and v_j represent particle charge and velocity, respectively, and the index k indicates the contact number for which the current is to be evaluated. The variable $E_j^{(k)}$ is defined as the weighting field, corresponding to the field evaluated at the position of particle j if all other charges were removed from the detector volume and all contacts were grounded, except from contact k which would be set to 1 V [28]. Its application has been widespread, ranging from hot carrier noise in bulk semiconductors and submicron semiconductor structures to generators and detectors of electromagnetic radiation, to terminal currents in Monte Carlo device transport simulation [29]. The theorem allows one to easily calculate the instantaneous electric current induced by a charge moving in the vicinity of an electrode.
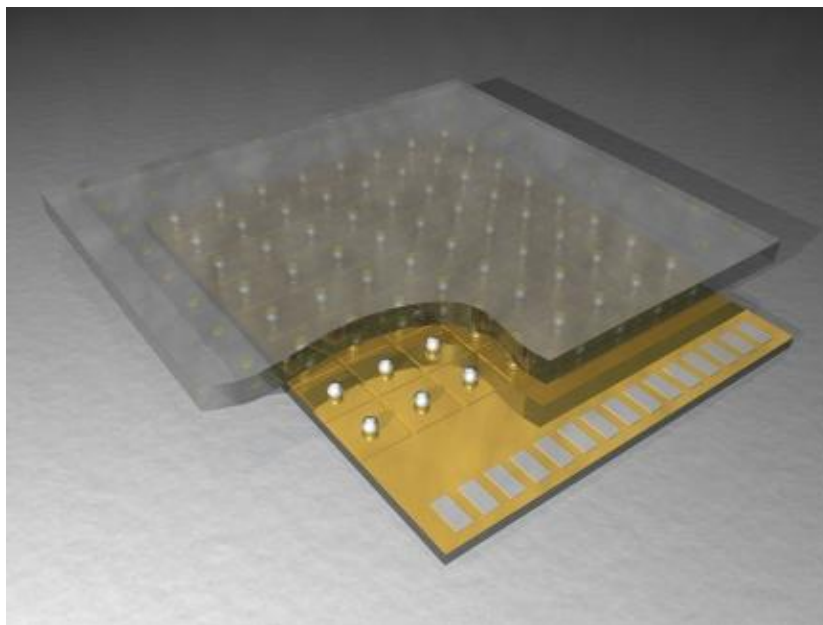
Figure 6.9: *Sensor-readout ASIC interconnection geometry. The sensor matrix is visible on the top part of the assembly while the small silver spheres correspond d to the solder bumps interconnecting the detector with the read-out ASIC (bottom orange plane). The consecutive metal gaps on the right side of the ASIC correspond the digitized read-out electrodes [30].*

In order to extract the signal, an electronic circuit is directly coupled to each pixel (*Figure 6.9*) through vertical interconnection points. A preamplifier, amplifier and shaper are typically included for analog treatment while a digital to analog converter and a certain level of logic are also implemented. Since one requires to have as many channels as pixels in the sensor matrix, readout electronics are organized in integrated circuits sharing the digital logic and data encoding parts. To ensure proper operation, it is important to maintain a conductive connection with the two parts with no additional resistive elements introduced by the interconnecting layers.

During charge propagation within the sensor itself, several effects may occur. It is commonly accepted that several generations and recombinations will occur while the charges propagate through the detector volume. While in normal silicon these effects will be in equilibrium, if a point defect is introduced in the crystal structure, charges may be absorbed and trapped. Furthermore, cross-talks between different pixels are possible, especially if the particle passes in the space covering several elements.

6.4   Introduction to fundamentals of Pixel Sensor Simulation

Producing a semiconductor device is a complicated, time consuming and costly procedure that cannot be realized in short time intervals. Prototyping in sensor optimization is therefore a significant issue especially for non-commercial applications where small profit margin are expected for the producer. In a typical sensor development process only a few different designs and technologies can be tried given the cost and production timescale. Subsequently, extensive simulation has to be carried out before any design implementation, to ensure final functionality and desired characteristics.

6.4.1   Frameworks and available algorithms

Simulation algorithms in semiconductor device development are commercial derivatives of institutionally developed packages of electrical field calculations, Monte Carlo implantation and analytical resolution algorithms. Current software is available in the form of Technology Computer Aided Design (TCAD) packages, grouping several elements and algorithms from different fields. Two main derivations are available, SYNOPSYS® Sentaurus™[a] [31] and SILVACO® TCAD™[b] [32] frameworks, both grouping the main elements for Monte Carlo simulation, finite element solution algorithms, electrical field calculations, geometry generation and active domain simulations. The SYNOPSYS® package, used in all simulation studies performed in this work, allows for a full 3D electrical field and process simulation through both Monte Carlo or analytical models, making it possible to probe efficiency and charge propagation in complex structures that cannot be represented in a two dimensional transverse plane. Two main kinds of simulations are possible:

Process simulation: Using a combination of diffusion equations, advanced Monte Carlo algorithms and a variety of data libraries, it is possible to accurately simulate the production process of a final semiconductor structure. Since production involves several steps, mainly dopant introduction on the substrate, an extensive knowledge of the technological process is needed. Lithographic masks and layer deposition techniques along with thermal diffusion and chemical reaction process are used. Main steps within a process simulation are:

1. Initial oxidation for the development of a mask layer to be used as pattern for subsequent doping operations

2. Deposition of a photosensitive resin on top of the oxide layer, usually of 1.5μm thickness through high velocity spinning.

3. Exposure of the coated surface to Ultra Violet light through a mask, or to an electron/laser beam to activate specific areas of the photosensitive layer

4. Chemical etching of the oxide layer at specific regions. The previously activated regions of the photosensitive layer provide no longer protection to the chemical agent (hydrofluoric acid), leaving the subsequent underlying silicon dioxide layers unprotected.

5. Ion beam, Plasma or chemical implantation affecting only the areas not protected by the oxide layer

6. Thermal diffusion and implant activation either through standard high temperature exposure or through an additional oxidation or other high temperature reaction strep.

---

[a] *Synopsys® Inc.* a Silicon to Software ™ Company for developing electronic products and software applications. Synopsys TCAD offers a comprehensive suite of products including process and device simulation tools, with Sentaurus being the main framework component. It offers a multidimensional simulation approach.
[b] *SILVACO® Inc.* is a privately owned provider of TCAD process and device simulation software. With Athena™ and ATLAS™, a silicon process and electrical simulation framework is provided.

These processes can be repeated several times through an actual production while technological parameters are not disclosed by foundries. As a result, it is of extreme importance to create a reference library (*see annex 8.3*) and to confirm simulator validity for a precise development.

Functional/electrical simulation: Charge propagation and diffusion is simulated inside the already defined sensor geometry though resolution of Maxwell's equations. They are additionally coupled to diffusion models and boundary conditions, defined by applied potential at fixed points. Finite element solutions algorithms are utilized while, results depend on carrier concentration within the simulated volume. Additional radiation model are also available either by the introduction of acceptors in the substrate to simulate defects or by applying more complex radiation damage simulation.

These two types of simulation can be interfaced and sequenced, feeding the result of a process simulation to the subsequent electrical model. Nevertheless, it is also possible to complete each phase independently of the other. In this approach, sensor geometry for a functional simulation can be hard-coded while, dopant distributions are provided as an external input. The most accurate result however can be obtained by interfacing the two stages such as final electrical characteristics are intransigently defined by the followed process steps. This is the adopted approach in this work and detailed process simulations are performed.

6.4.2   Meshing strategy

All available simulation frameworks take advantage of the diffusion, continuity and Maxwell partial differential equations [33, 34], with respect to the applied model, to describe carrier mobility and interactions within the simulated volume. Calculations are coupled with a finite element approach in order to successfully simulate the physical parameters within the device. The algorithm approaches the problem by considering a linearized version of the transport equation to describe the global calculation as an algebraic combination of a system of linear equations (*Figure 6.10*). Solutions for any given geometry can be obtained by subdividing the structure to finite regions, of a small enough size that allows for the local solution to be approximated by a polynomial function. Within a finite element, the partial differential equations are approximated with a polynomial solution Φ. Once individual solutions are calculated for each cell, a global representation is created by (*equation 6-21*):

$$V_{glob} = \sum_{l=1}^{n} a_i \ \Phi_i \ (V) \qquad (6\text{-}21)$$

where i corresponds to the indices of the intersections between two sub-elements, $\Phi(v)$ the polynomial function of the simulated parameter and α the multiplication factor. Polynomial functions $\Phi(v)$ can be defined as having a unitary value in any interaction point i between two elements while, being having a zero value to all surrounding area.
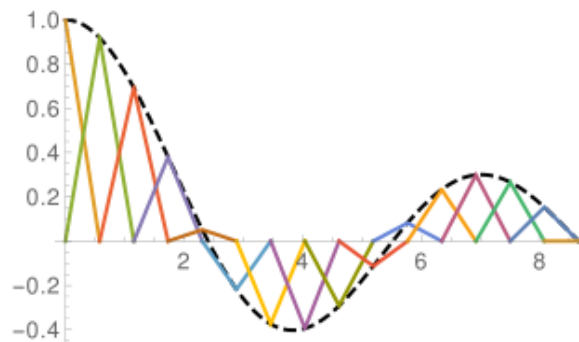
Figure 6.10: *A zeroeth order Bessel function J_0.interpolated in by a 16 dimension triangular function base [35].*

To produce accurate results, the cell size, called mesh element, needs to be sufficiently small to be able to apply the polynomial approximation. For regions where the probed physical parameter varies abruptly, finer meshing is required. If an extremely precise meshing strategy is used throughout the entire simulated volume, then the number of generated cells will exceed computing capacity. On the other hand, not accurate enough meshing will result in divergence of the global solution.

Although all TCAD frameworks do have an automated meshing algorithm supporting dynamic and adaptive meshing to take into account geometry variations along the simulation evolution, several constraints have to be imposed for a successful result. This include the predefinition of smaller and larger cell sizes as well as evolution steps for regions of interest.

6.4.3   Dopant Implantation Models

Dopant implantation is one of the most crucial production steps. It is in this stage that the actual doping of the substrate, defining its final electrical properties, takes place. In process simulation, two approaches can be used for dopant implantation:

1. *A library-based implantation simulation* where the outcome is calculated using extrapolations from experimental datasets and available measurements libraries. It can provide an accurate approach for typical conditions with a very fast processing speed [36].

2. *A Monte Carlo approach* by binary interaction approximation between incoming particles and silicon lattice cells. The total dose is extrapolated from a limited number of generated pseudo-particles per mesh element, whose trajectories start from a plane parallel to the silicon region above the wafers' surface with a defined incidence angle. Final number of trajectories can be further increased by allowing splits in mesh elements with low trajectory density. Splitted trajectories originating from the same particle have half the initial statistical weight and start under identical conditions at the splitting point. Trajectory splitting decreases statistical fluctuation and provides better modeling for transitional regions. To improve performance and processing time trajectory replication is also possible in order to avoid physical calculation of all available tracks and particles. In this approach, equivalent trajectories are rather copied than recalculated. Trajectory replication provides quite accurate results for 1D simulations, but is unsatisfactory in a 3D case where elementary mesh elements differ fundamentally. Final crystal damage accumulation is estimated using the binary collision approximation, where it is assumed that, if the transferred energy exceeds a certain threshold, the target atom is displaced and, at this lattice site, a vacancy is generated. When the displaced atom comes to rest, it is identified as an interstitial. Defect production rate is evaluated by simulating the full collision cascade. The main Monte Carlo engine of both simulation frameworks is based on the CristalTrim algorithm, an evolution of the Transport of Ions in Matter (TRIM) simulator [37], developed to calculate interaction of ions with matter. Latest versions were specifically optimized to simulate ion implantation in single crystalline semi-conductive structures and perform dynamic crystal damage calculations.

After implantation, a diffusion step is required to properly integrate the implanted dopant to the silicon crystal lattice and to force a recrystallization in order to repair possible lattice dislocations provoked by incoming ion impact. Four main physics models are available in a simulator level:

1. *Constant model:* It is based on Fick's diffusion law [38] assuming that the flux propagates from regions of high concentration to regions of low concentration proportionally to the concentration gradient (*equation 6-22*):

$$\mathbf{J} = -\mathbf{D}\nabla\Phi \qquad (6\text{-}22)$$

where j is the flux, φ the concentration and D the diffusivity of the implanted spices. Diffusivity is proportional to the square of the velocity of diffused particles, which in terms is proportional to the particle size and the viscosity of the medium. The evolution of the concentration with respect to time calculated by the second order derivative of the previous equation as (*equation 6-23*):

$$\frac{\partial \Phi}{\partial t} = D \Delta \Phi \qquad (\text{6-23})$$

2. *Fermi diffusion model:* The quasi-hydrodynamic carrier transport equations for semiconductive materials, extended to Fermi–Dirac statistics are considered. In the high injection case, these equations reduce to a drift-diffusion model with non-linear diffusion terms.

3. *Pair diffusion model:* The pair model does not only describe the influence of charged dopants on each other but also the reactions of dopants and the host lattice including its point defects.

4. *React model:* This model considers the pair model case with the addition that it can account for chemical reactions in multi-dopant implantations or in matrices where the crystalline structure is chemically active [39, 40, 41].

Although the constant model is a good approximation for low doping concentrations, at higher values, collective effects are highly important, as well as reactions with crystal damage. For intermediate and medium doses, the charged Fermi model is sufficient. The addition of pair interaction simulation for the pair model readjust the behavior to accurately describe experimental data up to implantation doses of 10^{15} atoms/cm^2. In the studies that follow, all four models are used to simulate diffusion process while, their level of consistency with experimental data on doping profiles is examined.

6.4.4   Application of 3D Simulation to the IBL sensor case

As a first step of detector development, simulation was carried out to the implemented n-in-n IBL sensor architecture in order to have a common ground base for comparison and result interpretation. Using the SYNOPSYS® 3D TCAD framework, I present the complete simulation of a single pixel structure included in the current detector. The process flow is simulated with extreme attention to adjust meshing and back-side process in an appropriate manner. Since not all technological parameters were available in detail, several steps are implemented using standard procedures in industry.

Initial simulation parameters were adjusted to known standards. A high resistivity, phosphorous doped, Czochralski silicon substrate was used as the base for further processing. Initial dopant concentration was set at 10^{14} atoms/cm^3, corresponding to an equivalent resistivity value of 5kΩ×cm. Although any processing steps only affect the wafer surface, simulation was performed throughout the entire substrate region, extending to the full depth of 250 μm. On the surface level, the simulation domain covers the entire pixel region, extending to an area of 50μm × 250μm. Since this particular production process (n-in-n) includes double-sided lithography, both front and back-end processes were simulated simultaneously.

In order to improve meshing and optimize computation speed, several fixed points were introduced (*Table 6-1*). During the various steps, the simulated geometry changes and the meshing has to be adapted. This process is time consuming and may generate inconsistences. By defining fixed lines, the simulator can only adapt mesh elements between them while, always respecting the ratio of the cell size that has been predefined. Fixed lines are therefore placed in the transition from a region of interest to a region where simulated quantities do not vary significantly. For instance, a fixed line is placed 200 nm form the surface, where all transition effects take place and meshing has

to be accurate and another at 3 μm depth, were a more coarse mesh is required. A final fixed line is placed at the total depth with an enlarged cell size (25 μm), since no interesting effects can be seen in this area. Additional meshing optimizations include a lateral cell accuracy at 0.5 μm and a vertical accuracy of 100 nm.

Fixed Lines Placement					
Depth (250 μm)		Horizontal direction (250 μm)		Vertical Direction (50 μm)	
Region	Cell Size	Point	Cell Size	Point	Cell Size
0 nm - 200 nm	100 nm– 200 nm	0 μm – 89 μm	1 μm – 10 μm	0 μm - 10 μm	1 μm – 20 μm
200 nm - 3 μm	200 nm – 1 μm	89 μm – 144 μm	10 μm	10 μm - 25 μm	20 μm – 40 μm
3 μm - 250 μm	1 μm - 25 μm	144 μm – 244 μm	10 μm	25 μm - 40 μm	40 μm – 20 μm
		244 μm – 250 μm	10 μm – 1 μm	40 μm - 50 μm	20 μm - 1 μm

Table 6-1: *Fixed points and cell sizes for different regions of the simulated structure*

Implantation was performed using the CristalTRIM MC algorithm with a generation of a 1000 pseudo-particles. This number was subsequently normalized to the defined dose both for the phosphorus and the boron implants. To achieve a reasonable accuracy in doping profile determination, adaptive meshing during implantation was used. Because of the significantly smaller boron dose, the minimum cell size during implantation simulation was readjusted to 100 nm for phosphorous and 10 nm for boron Target concentration uncertainties for both boron and phosphorus implants were set at 10^{18} atoms/cm^3. To simulate implant diffusion, the default model, an implementation of the Fermi model taking into account spices charge, was used.
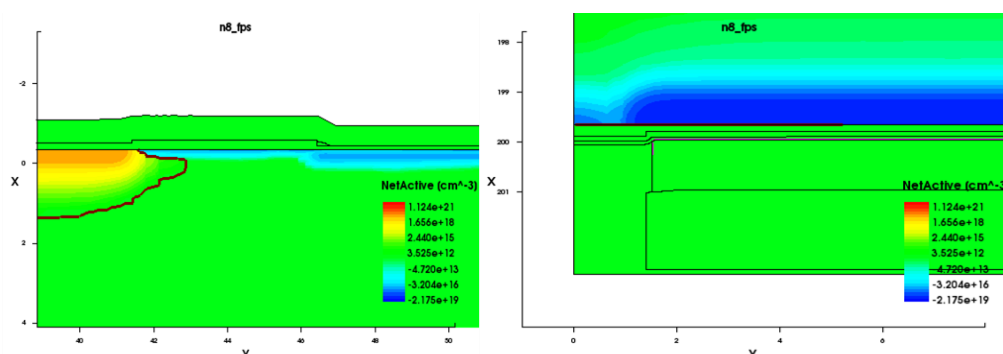

Figure 6.11: *Phosphorus and boron simulated doping profile cross-sections at the front bias-rail region (left figure) and on the sensor back side (right figure). Topological details of different non-silicon layers are represented with green color. On the front side doping profile (left plot) a lateral diffusion of the implant to a 0.5 μm distance after the end of the top metal electrode is visible.*

Fabrication process involves five lithographic steps in each side of the wafer. Through an initial oxidation, 120 nm of silicon dioxide (SiO_2) are deposited. Additional 0.5 μm photosensitive layer was added in conjunction with a mask to pattern the pixel regions. An etching step was used to remove the excess oxide and to expose the regions to be subsequently implanted. The pixel region is defined by the phosphorus implant, and a diffusion step through thermal exposure follows. Finally, the photosensitive layer is removed and the structure passes to the second production step.

A Silicon Nitride layer of a 50 nm thickness is deposited and through the use of a photoresist layer followed by an etching step, is patterned to allow for the boron implantation. Boron in this production is introduced as a very low implant to stop charge sharing between neighboring pixels (p-spray). After implantation, a thermal exposure is used to integrate the implant to the silicon lattice and the photoresist layer is removed. The 2-dimensional doping profile distribution of both implants are extracted (*Figure 6-11*) after all implantation and thermal steps.

The three remaining steps include opening of contacts though etching of the previously deposited oxide and nitride layers, deposition of a metal layer to serve as a contact electrode and introduction of a final silicon oxide layer as passivation. A passivation is frequently used in silicon production, to insulate and protect areas not required to contact any external circuitry. Thought-out the curse of the simulation procedure, all additional layers are treated as epitaxial depositions and no detailed oxidation simulation is performed.

The completed 3-dimentional geometry as well as the meshing elements and the doping profiles for both implants are presented in *Figure 6-12*. The metal region, represented with blue color on the upper right part of *Figure 6-12*, is slightly retracted with respect to the pixel boarders. Concerning the meshing elements, on the lower part of the same figure, it can be observed that a large area above the silicon surface is finely segmented. This area, corresponding to several layers that were deposited and removed along the process simulation, is always treated by the algorithm as an integral part of the substrate. As a result, computational time and resources are consumed. It is therefore a good practice to try to minimize such effects by altering the simulation in such a way to avoid removal of thick layers.
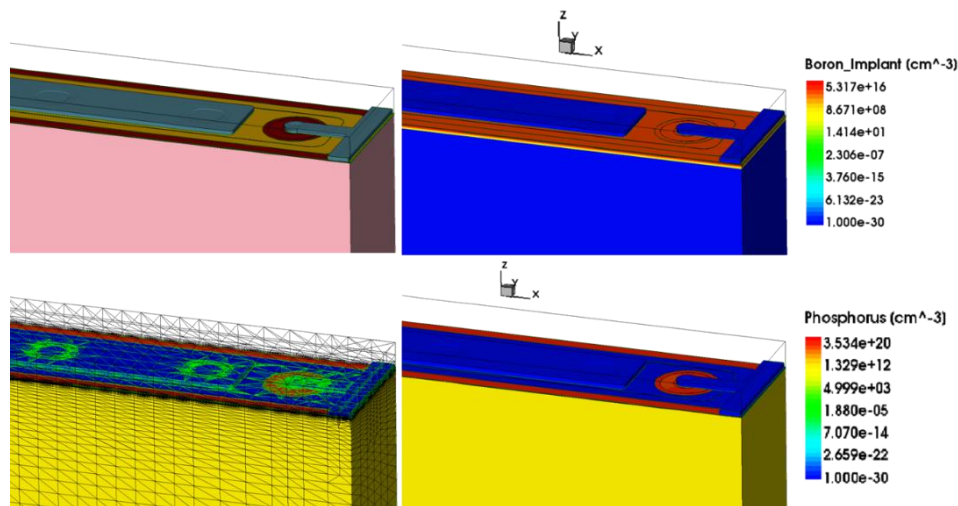
Figure 6.12: *Complete 3D representation of the biasing region of an IBL-type pixel. On the top left figure only a geometrical representation is shown, with pink representing the silicon region, red Silicon Nitride, brown the Silicon dioxide and blue the final aluminum layer. On the top right plot, a boron three dimensional doping profile is presented with meshing element details. Meshing extends over the surface of the simulation region to account for layers that were deposited and removed along the fabrication process. On the tow bottom figures, a 3D boron (left) and phosphorus doping profile is presented, while used colors correspond to the dopant concentration scale.*

To conclude, initial oxidation and subsequent etching and deoxidizing steps result in alternating deposition and removal of several layers of material. Interface region is therefore displaced with respect to its initial wafer surface resulting in an unwanted meshing on top of the silicon region which reduces calculation efficiency (*Figure 6.11*). Using a complete 3D and 2D process flow implementation, the lateral diffusion of the implants is extracted. A 0.4 μm lateral diffusion overshooting the metalized electrode is observed (*Figure 6.12),* resulting in field non-uniformities and distorted dynamic lines. The effect is taken into consideration for future production by implementing lateral metallization layer extension of the order of 1 μm.

## 6.5   Sensor Designs for ATLAS Upgrade and Active Edge Technology

In the previous section, I have studied design effects in the case of the IBL using a 3D simulation approach. Implementation of these results is presented in several designs using the innovative

active edge technology. A common production run, with participation from several groups was defined within the ATLAS planar pixel community. This Multi-Project wafer, commissioned in 2014, was assigned by ADVACAM[c], who has demonstrated a proven experience in active edge sensor development [42]. As a designer of the LAL contribution, I have introduced four key variations, centered on an in-house developed ASIC.

6.5.1 The Active Edge Technology

Large area hybrid silicon detectors are widely used in high energy physics experiments. To increase geometrical coverage and combine several layers of tracking information, large arrays of silicon sensors are stacked and tiled together to provide the needed sensitivity and coverage. However, the drawback is the formation of a dead region between individual modules. The inactive region usually consists of guard rings and as well as an additional gap between the active area and the cut region. Guard rings are structures that gradually decrease the electrical field towards the detector edge and protect the active area form high electrical currents. The additional gap is usually designed with a fairly large dimension, in order to minimize edge leakage effects, caused by conventional dicing methods.

A large effort is devoted in decreasing sensor dead regions. While optimizing dicing quality through laser dicing or other methods is possible, additional process complications are introduced [43]. The introduction of the active edge technology treats both issues and enables the fabrication of large area detection systems with seamless images. A dry etching technique is used to open deep trenches around the detectors, thus eliminating the need for a dicing process. A subsequent doping of these trenches renders detector edges active [44].
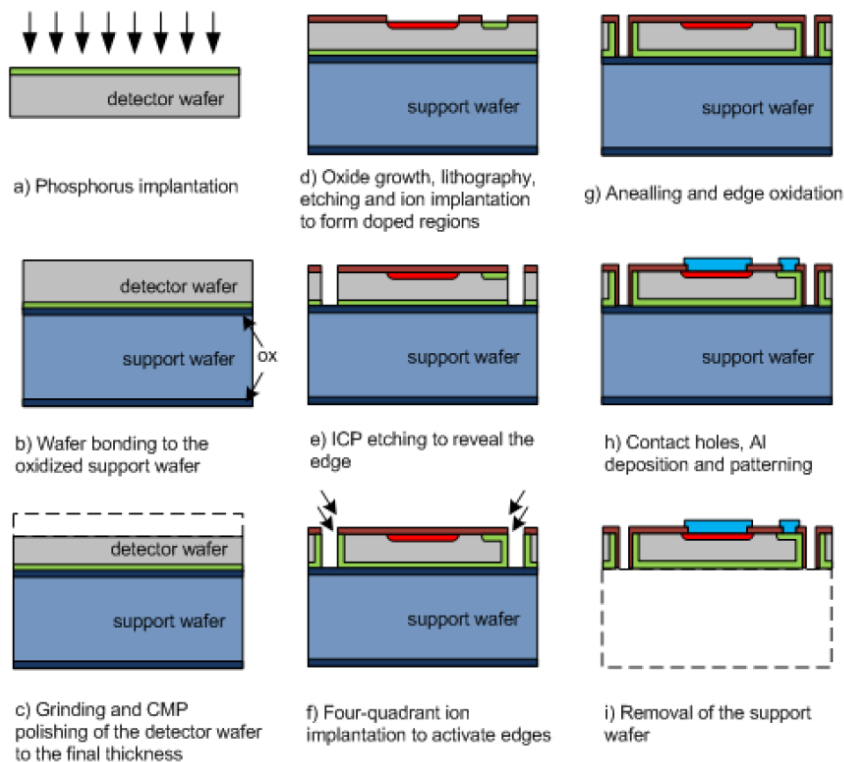
Figure 6.13: *A brief representation of the active edge process flow applied on n-in-p detector fabrication [45].*


The sensor wafer is firstly implanted on its back side and subsequently attached to an oxidized support wafer. Additional thinning may occur at this stage, to further minimize the thickness of the final sensor. Silicon oxide is grown at the top side of the wafer assembly, and through lithography and implantation, the active area is defined. Deep trenches are then created at the edges of the sensor the using Ion Coupled Plasma technique. These trenches extend all the way down to the support wafer. A four quadrant implantation with appropriate tilt angles is then performed in order to dope the trench walls. A subsequent activation through oxidation follows. Final production steps include metal contact deposition and detachment from the support wafer [46]. A brief schematic of the process is presented in *Figure 6.13*.

6.5.2   Design variations for the Multi-Project Run

Initial focus of the multi-project run was the evaluation of the edgeless technology on thin sensors. As a test production, several designs covering a wide range of research subjects, were assembled to a single wafer. In the general production characteristics, three thicknesses were decided, 50 μm, 100 μm and 150 μm, using 10 kΩ floating zone p-doped Cz wafers. The larger surface area provided by the six-inch diameter wafers allowed for flexibility in terms of included designs. The additional advantage of providing diced structures as a result of the active edge production process also allowed individual management of each design.

From the LAL perspective, four different designs where included, all compatible with the in-house developed ASIC Omegapix [47]. Representing a 3D implemented demonstrator chip, it corresponds to a relatively small detection area of 5 ×5 mm, comprising of 2304 channels. Pixels are organized in 23 columns and 96 rows, with a horizontal distance of 10 μm and a 12 μm vertical separation. The pixel dimension has been reduced to 25×200 μm, which is a factor of two smaller in comparison with current ATLAS IBL pixels in the vertical direction.

During the design phase, several technology limitations where imposed. To allow for testing and also provide a virtual grounding to non-interconnected pixels, a standard bias rail was introduced. It consists of a grid of metal rails in contact with every pixel at a specially implanted region. In addition, metallization regions on top-side pixel electrodes where extended to account for the 0.5 μm implant lateral diffusion surrounding the pixel (*Figure 6.14*). Nevertheless, the width of all metal regions posed a particular problem due to the Omegapix reduced pixel size. Because of the chemical etching technique used to form the metal layer, all structures needed to allow for a 1 μm tolerance in each direction. On the other hand, the minimum recommended width of an aluminum metal connection should not be less than 5 μm. For this limit downwards, the connection is no longer purely conductive and stars having a resistive behavior. As a result, taking into account the tolerances of the lithographic technology, a minimum of 7 μm width was implemented. This also represents the maximum width that can geometrically fit on the sensor matrix.

0.5 μm
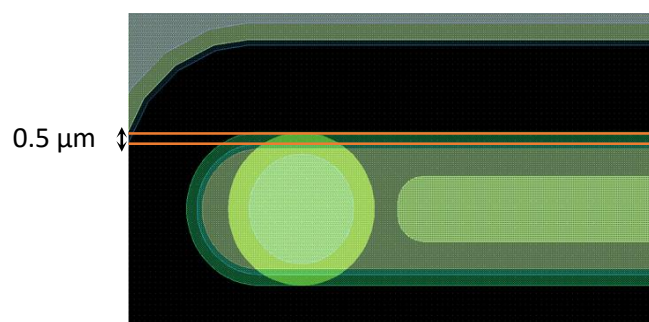
Figure 6.14: *Detail form a pixel mask where the metal layer is extended 2 μm with respect to the end of the implant in order to account for the lateral diffusion and the required tolerances of the chemical etching technology.*

The four final variants designed are listed below (*Figure 6.15*):

- *No guard ring and no bias rail:* Taking full advantage of the active edge technology, this design features no protective guard ring or biasing grid. The total distance from the edge of the last pixel to the sensor edge is 47 µm. Taking into account the interpixel distances, such a value corresponds to a 35 µm dead region, accounting for 3.6 % of the total area.
- *One guard ring with no bias rail:* The width of the Guard ring was reduced to 16 µm while the distance from the last pixel is set at 6 µm. Finally, a 25 µm spacing is allowed between the end of the guard ring and the edge of the sensor, accounting for the 57 µm inactive region.
- *One bias rail and no guard ring:* The bias rail width is set at 37 µm while the distance of the last pixel from the structure is fixed at 16 µm. The bias rail is kept 25 µm from the edge zone of the sensor, accounting for 65 µm inactive region (5.2 % inactive area)
- *One bias rail and one guard ring:* being the most conservative design, a 16 µm width guard ring and a 37 µm width bias rail are include. Keeping the distances form the last pixel of the matrix at 16 µm, the 25 µm separation form the sensor edge and a 5 µm spacing between the guard ring and the bias rail, increases the dead region to 88 µm (8 % of the total area)
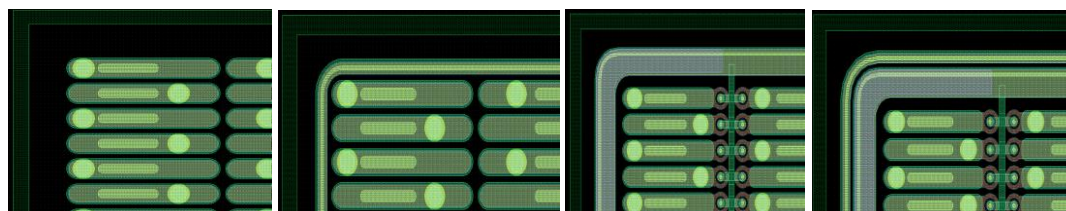
Figure 6.15: *The four design variations of the active edge production. From left to right: no Guard Ring - no Bias Rail design, no Bias Rail - one Guard Ring design, no Guard Ring - one Bias Rail design and one Guard Ring – one Bias Rail design.*

	No BR – No GR	*BR – No GR*	*No BR - GR*	*BR - GR*
Guard Ring Width			16 µm	16 µm
Bias Rail Width		37 µm		37 µm
Bias Rail – Guard Ring distance				5 µm
Last pixel distance	47 µm	16 µm	6 µm	16 µm
Distance to sensor edge	47 µm	25 µm	25 µm	25 µm
Total inactive region	47 µm	78 µm	57 µm	100 µm
% of inactive region	3.8 %	6.2 %	4.6 %	8 %

Table 6-2: *Summary of the geometrical characteristics of the four Omegapix sensor designs*

A respective summary of all design characteristics is presented in *Table 6-2*. Four samples of each design were included per wafer, resulting to a total of sixteen Omegapix compatible sensors. Taking into account the three different thicknesses as well as the wafer multiplicity, 70 sensors were delivered.

6.6   Doping profile Characterization

6.6.1   Motivation

Developing efficient design and fabrication techniques as well as building confidence level in simulation output, requires rigorous testing and evaluation of the final detector. While by electrical measurement one can evaluate functional characteristics of a device, no conclusion can be drawn

concerning neither the fabrication procedure, nor on its efficiency or the impact of dopant diffusion to the observed electrical behavior. As a result, knowledge of the dopant profile distribution within the detector is required to complete electrical characterization and explain operational behavior. Depletion voltage, leakage current, proportional or avalanche operation and to some extend breakdown boundaries are directly dependent on the shape and concentration of the dopant distribution within the substrate. While production testing is only half the intended outcome of doping profile measurements, accurate simulation and benchmarking of any conception accounts for the other half. The final goal is to have a complete knowledge of the detector quality from fabrication to electrical characteristics and signal response through simulations. Before even a single wafer is produced, one needs to establish a library and calibrate the simulator framework before any viable design can be produced.

The acknowledged dependence of functional characteristics of a silicon detector from the doping profile distribution as well as the close relationship of the later with charge generation process, mandates detailed modeling of the implantation process. Using simulation tools, it is possible to approximate with great detail the fabrication processes. Nevertheless, deviation in both doping profile distributions and expected electrical characteristics from those generated by simulations, require further modeling and understanding.

6.6.2 Secondary Ion Mass Spectroscopy as Tool for Simulation Validation

The SIMS measurements described in the following section is a very powerful tool, allowing a detailed characterization of the dopant profile [48]. This information is of vital importance in detector design. Since the final purpose is to have a complete functional and process simulation of a device before undertaking a production, implantation parameters to produce the appropriate dopant profile distribution with the required properties are essential. Technological parameters are not communicated by different manufacturers. To create a reference library, calibrate the simulation framework and consolidate its validity, three test productions involving different implantation parameters, specifically defined were made. The values were kept close to bibliographic reference value in sensor production while the three main implants and substrates used in the industry are probed: n-implant on an n–type wafer, n-implant on a p-type wafer and p-spray implant on a p-wafer. Measurements of wafer properties were conducted in the laboratory of the GEMAC group (Group d'Etude de la Matière Condensée) of the University of Versailles.

6.6.2.1 Measuring Basics

Secondary ion Mass Spectroscopy is an analytical technique allowing to characterize impurities in the surface and near surface (~10μm) region with a nominal sensitivity of 10^{13} atoms/cm³. The method consists of sputtering an energetic primary ion beam (0.5-20 keV) on the sample surface and on subsequent analysis of produced ionized secondary particles by mass spectrometry (*Figure 6.16*). This allows multi - element detection with a depth resolution of 1 to 5 nm depending on abrasion seed and beam characteristics. Surface information about the probing region can also be obtained, since the affected area extends up to 150×150 μm with respect to the sample surface. However, it is a destructive method, since removing material by sputtering leaves a crater in a sample, rendering impossible any further treatment on the affected region.

Determining the total dopant profile with SIMS is subjected to a number of constraints, primarily in relation with the stability, polarity and intrinsic characteristics of the primary ion beam. Boron, Phosphorus and Gallium are the most commonly used elements for doping in semiconductor industry. Probing each one of these analytes requires beam reconfiguration and is subject to different constraints for each case.

For the phosphorus case, bombardment with the usual negative oxygen ion beam would only allow a concentration resolution of about 10^{18} atoms/cm³ [49]. At the same time, using an oxygen

jet to deposit a secondary oxide on the sample surface in order to increase ionization yield would be problematic. The H_2O contamination induced from ambient humidity, would dramatically increase the SiH signal in the silicon substrate, degrading resolution beyond any useable limit. In contrast, one can take advantage of the high negative ionization yield exhibited under electropositive Cs^+ ion bombardment by replacing the oxygen ions in the primary beam with cesium. In such a setup, resolution limits of 10^{13} atoms/cm^3 can be achieved for a thick silicon target.
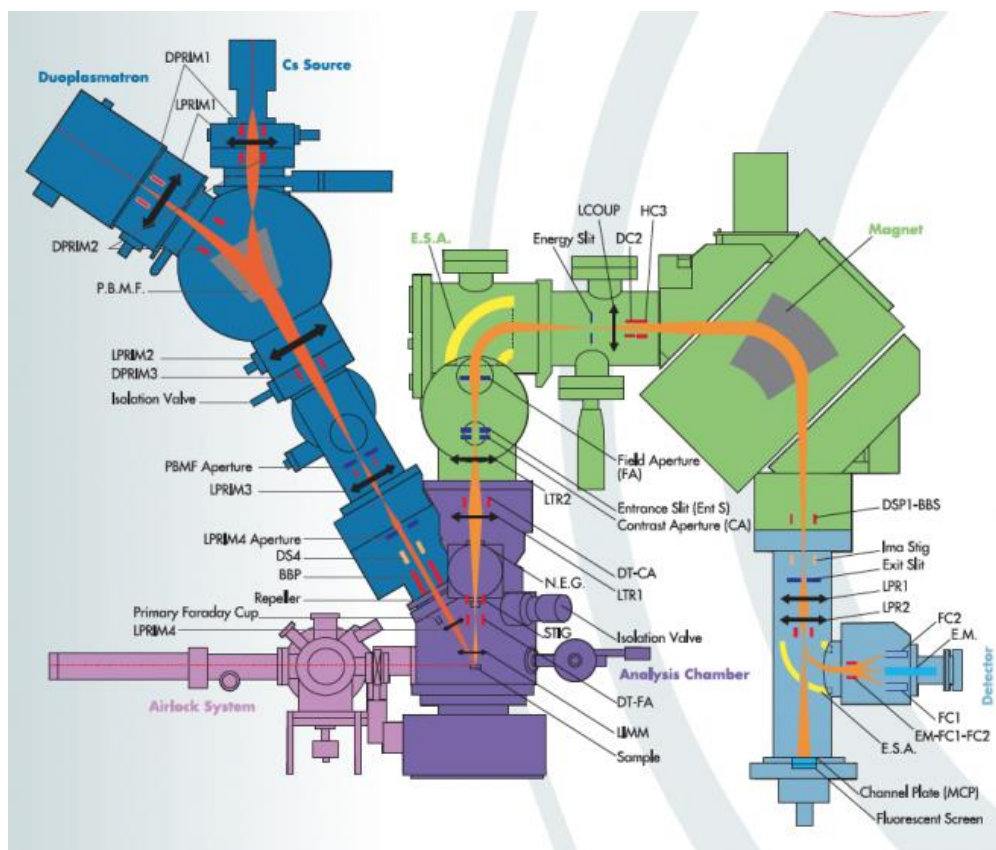

Figure 6.16: *Operating principal of the SIMS Spectrometer [50].*

In the case of non-conductive sample, no effective path is available for the incoming charge to be evacuated. As a result, the probed area will become positively charged, suppressing negative ion production yield. Furthermore, beam instabilities will be induced and secondary ion resolution will be degraded by the increase of the evacuation field. To neutralize the charging effect and stabilize the surface potential at the necessary (close to the ground) value, introduction of an additional negative charge, in the form of low energy electron beam, is necessary at the sample vicinity [51]. A correct adjustment of the charge compensation mechanism is required at the early steps of the measurement serving as guideline for subsequent corrections. In the case of negative secondary ions, partial charge compensation is achieved by the secondary beam itself, rendering the effect less significant.

While an electronegative element was used for Phosphorus analysis, in the Boron case, electropositive Oxygen ions are exploited to produce a B^+ secondary beam. Since in any case the primary ion bean is positively charged while the electropositive nature of oxygen will create positively charged boron secondary ions, the charge compensation mechanism described in the previous paragraph becomes significantly important in boron analysis. No self-stabilization mechanism by using secondary ions exists in this case and if no action is taken, produced ions are scattered and their energy altered. In this case, the introduction of the negative electron beam is important to re-stabilize the potential on the sample surface.

Figure 6.17: *The CAMECA IMF 7F System where measurements were performed [52].*

To achieve an initial reference potential needed to correctly calibrate the charge compensation mechanism, a non-insulating metal layer is deposited on all samples where a silicon dioxide layer precedes the substrate. Using palladium or gold Plasma Enhanced Chemical Vapor Deposition a reduced thickness (~50 nm) surface metal film is deposited on top of the SiO_2 layer. To develop an accurate understanding of the compensation mechanism, in several samples with superficial oxide layers SIMS measurements were also conducted after chemically etching any process induced regions. Results were subsequently compared with the ones obtained when no etching is performed and necessary adjustments were made. Individual series of measurements were performed to determine the interface of each layer (palladium/gold, oxide and silicon) and the relevant ion velocities in order to have an exact depth extrapolation.

An additional limitation of the technique is the maximum probing depth achievable under normal conditions. Although a uniform beam exposure to the target surface is performed, beam non-uniformities as well as non-crystalline surface structures can result in exposure to ion beam under various angles. Furthermore, as the measurement progresses and the induced crater deepens, ion reflection on the sidewalls degrade beam stability and introduce collisions at a wide variety of angles and energies. The effect is more prominent in polycrystalline materials since no uniform refraction plane exists. Combination of non-perpendicular surface collisions with crater side-wall reflections roughen the surface at the bottom of the crater preventing a continuously uniform sputtering. While at the initial stages the effect is not significant, the more the measurement progresses and the target surface becomes non-uniformed, the phenomenon is self –amplified due to the variation of primary ion incidence angle. At extreme cases the end of the crater becomes "dark" – non reflective for secondary ions – while, the resolution and the precision degrades with respect to depth. To treat this effect, all depth measurements were limited to a maximum depth of 4 μm, well below the expected 10 μm limit value of maximum penetration depth [53].

6.6.2.2 Concentration Quantification

During SIMS measurements, secondary ion intensity of elements of interest is recorded in using an electron multiplier, in the form of an electron induced current. In order for these values to be converted to actual element concentrations, a multiplication factor is needed, known as the Relative Sensitivity Factor (RSF). Since ionization yield depends on probed element, matrix composition, ion beam nature and measurement conditions, special reference samples of nominal consecrations have to be used in each series of measurements to calibrate the results and calculate the RSF. Those samples need to be of the same matrix and to contain the same element of interest as the ones been analyzed. Consequently, to quantify for example phosphorous concentration in silicon, an accurately phosphorous doped silicon calibration target is measured at the same conditions as the probed sample. Then corresponding multiplication factor is extracted.

To avoid depth imprecision in the determination of the reference profile, measured ion intensity (S_M for the matrix and S_i for the element of interest) is integrated along the total elapsed measuring

time. The average intensity is calculated for the matrix (I_M) and the element of interest I_i by dividing the signal integral with the total duration of the measurement (*equations 6-24 and 6-25*). The latter, is defined as being the time interval between the first and last recorded data point of the corresponding element, thus accounting for any time differences due to magnetic field adjustments. The average implant concentration (C_i) is computed by dividing the known implanted dose with the crater depth, created by the ion beam during the measurement (*equation 6-26*). Finally, the RSF is calculated by multiplying the average implant concentration with the ratio the average secondary ion signal for the matrix over the secondary ion signal related to the element of interest (*equation 6-27*). Expected units of the final factor are atoms/cm^3 since multiplied by detector counts should yield dopant concentration in the matrix.

Average secondary ion signal for matrix: $$I_M = \frac{\int_0^{T_M} S_M \partial t}{T_M} \qquad (6\text{-}24)$$

Average secondary ion signal for implant: $$I_i = \frac{\int_0^{T_i} S_i \partial t}{T_i} \qquad (6\text{-}25)$$

Average implant concentration: $$C_i = \frac{implanted\ dose\ (C)}{Crater\ depth\ (D)} \qquad (6\text{-}26)$$

Relative Scale Factor: $$RSF = C_i \frac{I_M}{I_i} \qquad (6\text{-}27)$$

Given the non-continues nature of data points, secondary ion signal integral can be approximated by a sum of all recorder intensities multiplied by the time interval between two consecutive values. Corresponding uncertainty can be evaluated as the square root of the quadratic sum of individual uncertainties in each bin, which, assuming stable beam conditions, should be identical. They are defined as the square root of the quadratic sum of time and signal uncertainties. Time uncertainty can be approximated as half the interval between two consecutive data points while for the total measuring time, the quadratic sum of the uncertainties at the start and end points is used. Implantation dose precision is typically one half of the last referred unit, while for the crater depth, it represents the convolution of the profilometer's precision definition with the statistical deviation of three consecutive measurements. A cumulative description of all considered uncertainties as detailed in *Table 6-3*.

Measurement time:	$\delta T = \sqrt{2 \cdot \left(\frac{t_{i+1} - t_i}{2}\right)^2}$
Crater depth:	$\delta D = \sqrt{\delta d_{stat}^2 + \delta d_{syst}^2}$
implanted dose:	Half of the last referred unit
Secondary ion signal integral:	$\delta S = \sqrt{\sum_{k=0}^{n} \delta t^2 + \delta s^2}$

Table 6-3: *Uncertainties for the various quantities used in RSF determination*

By propagating all contributing factors, a total uncertainty can be estimated for the RSF determination with respect to the following formula (*equation 6-28*):

$$\delta RSF = \sqrt{\frac{(I_M T_i \delta C)^2 + (C T_i \delta I_M)^2 + (C I_M \delta T_i)^2}{(I_i T_M D)^2} + \left(\frac{C I_M T_i}{I_i T_M D}\right)^2 \left(\left(\frac{\delta D}{D}\right)^2 + \left(\frac{\delta I_i}{I_i}\right)^2 + \left(\frac{\delta T_M}{T_M}\right)^2\right)} \qquad (6\text{-}28)$$

An unfortunate side-effect of the technique is that only elements with preexisting calibration targets can be quantified. Since the matrix has to be the same in both the measured and reference samples, there is a limited amount of possible applications. In that sense, although we can quantify phosphorous concentration in silicon, it is impossible to accurately determine its density in the preceding silicon oxide or other layers on top of the substrate. Although dopant concentrations are always presented quantified in the entire region, a conservative approach has to be taken concerning measurements in any silicon oxide, nitride or passivation layers where silicon substrate approximation is made.

In the following table (*Table 6-4*) typical phosphorous and boron in silicon RSF values are represented with their respective evaluated uncertainties for measurements conducted at the GEMaC facility of the university of Versailles:

Element	RSF Value (atoms/cm³)
Boron in Silicon	$(5.50\times10^{22} \pm 1.24\times10^{21})$ atoms/cm³
Phosphorous in Silicon	$(8.80\times10^{22} \pm 1.84\times10^{21})$ atoms/cm³

Table 6-4: *Typical RSF values calculated in silicon sensors measurements*

Since for the estimation of the RSF the secondary ion intensity of the matrix element is taken into account, during measurement quantification we need to use not only the ions intensities of the analyzed element but also that of the matrix. The concentration of the analyte can then be derived in the following manner (*equation 6-29*):

$$C_i = RSF \frac{S_i}{S_M} \qquad \text{(6-29)}$$

where S_i and S_m are the ion intensities for the element and the matrix and C_i the final extracted concentration in atoms/cm³. Corresponding uncertainty is mostly dominated by limits on the precision of the RSF value which are mainly affected by the accuracy on the determination of the implantation dose on the reference sample. As a result, precision on the final concentration calculation is of the same order as initial dose uncertainty on the calibration target for regions where the secondary ion signal is significant. A 2 % precision can be obtained for phosphorus and boron implanted silicon, assuming a uniform matrix.

6.6.2.3 Depth Quantification

Secondary ion intensity of probed elements is recorded as a function of time, generating a time profile. By measuring the depth of the SIMS crater created by the primary ion beam on the sample, time intervals can be converted to depth values. Assuming stable experimental conditions, mainly concerning the primary ion beam, a fixed abrasion speed is considered throughout the entire measurement. Once the crater depth is evaluated, it can be divided by the total exposure time to determine average abrasion speed. Depth can then be computed for each data point by multiplying the corresponding time value with the average speed.

Crater depths are measured using a mechanical fixed tip profilometer, calibrated to a precision of ± 5.3 nm. An average of three values is used per crater depth while total final uncertainty includes both statistical and systematic contributions. Concerning the thickness of the initial plasma deposited metal layer for ion beam stabilization, a sharp trench is created through surface scraping with a controlled load platinum tip. On silicon targets, surface layers are composed of silicon dioxide and/or silicon nitride with increased density that cannot be affected by the applied weight. It can be therefore safely be assumed that only the metal layer is removed and the trench corresponds to the thickness of the layer.

Although this method gives accurate results for homogeneous substrates, in case of multiple superimposed layers, the fixed speed approximation cannot be applied. Material sputtering and penetration depth depend on layer density and can vary substantially between different compounds. Abrasion speeds need to be determined for each layer separately through dedicated measurements. By starting on the top layer, the first measurement will stop exactly at the interface between the first and second matrix material. Subsequent measurement will again start on the surface but will stop at the interface between the second and third material and so on until the final layer is reached. At the end, there will be as many craters as layers, each one traversing all preceding deposits. Each layers' thickness can then be estimated by measuring the corresponding crater's depth and subtracting the depth of the previous layer's crater. Using the consecutive obtained datasets, beam time on each layer is extrapolated by looking for point of abrupt change on secondary ion intensities (several orders of magnitude). Finally, using determined layer thickness and spent time in each one, a single penetration speed per compound is determined.

During actual conditions, multiple elements are monitored. To determine transition point between consecutive layers, the first derivative of the secondary ion intensity is plotted for all elements. Because of the different extraction potential in each layer, Dirac-like peaks are expected to form in the derivative at the interface edge. For a perfectly separated interface layer and in measuring intervals infinitesimally close to zero, a perfect Dirac form is expected (*Figure 6-18)*. Nevertheless, because of the time resolution limits as well as atomic layer mixing at the transition region, a narrow width Gaussian approximation can be applied (*Figure 6-19*). By applying a statistical fit at the transition point, the time position is defined as the position of the Gaussian distribution maximum for every monitored element. Using all available maxima, an average transition point is estimated while, standard deviation of the values convoluted with half of the time interval between two data points is considered as uncertainty.
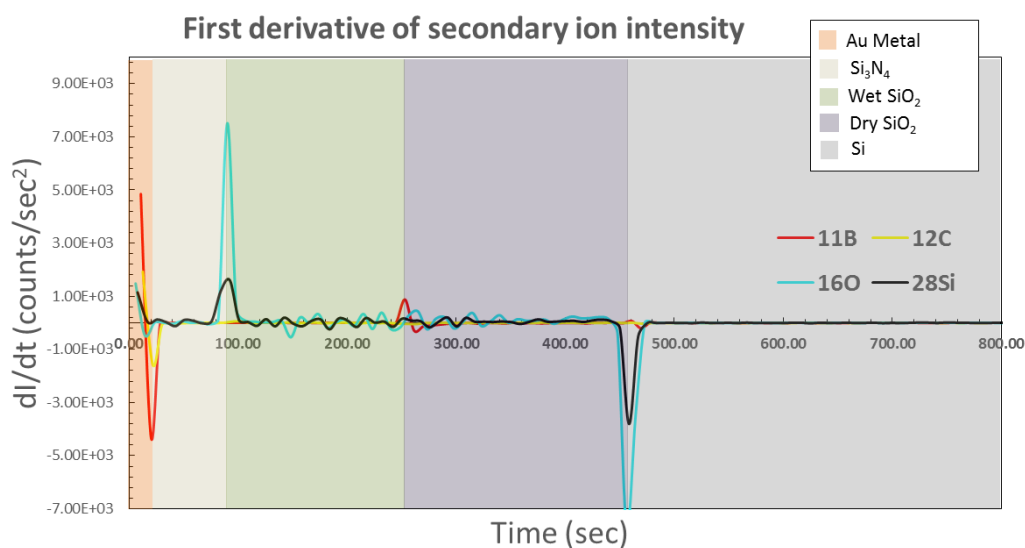

Figure 6.18: *First order derivative of secondary ion intensity for all monitored elements on a typical silicon sensor sample. Abrupt changes are observed in layer interface regions which are marked with different shading colors. Oxygen and silicon curves are scaled to a factor of 10^{-2} and 10^{-5} respectively for representation purposes.*

After the definition of transition time between consecutive layers and the measurement of associated thicknesses, an average abrasion speed is computed for each region along with the corresponding uncertainty. In contrast with the RSF, which is globally fixed for a series of measurements concerning the same element, abrasion speeds are separately calculated for each profile, since they heavily depend on the primary ion beam configuration. Parameters like the primary ion current, beam acceleration potential and focusing configuration can impact the depth determination accuracy

for each sample. A typical set of values is presented in *Table 6-5*. Although precise values are not of particular interest since they can vary significantly, their scale as well as the ratio of speeds between different layers is interesting.
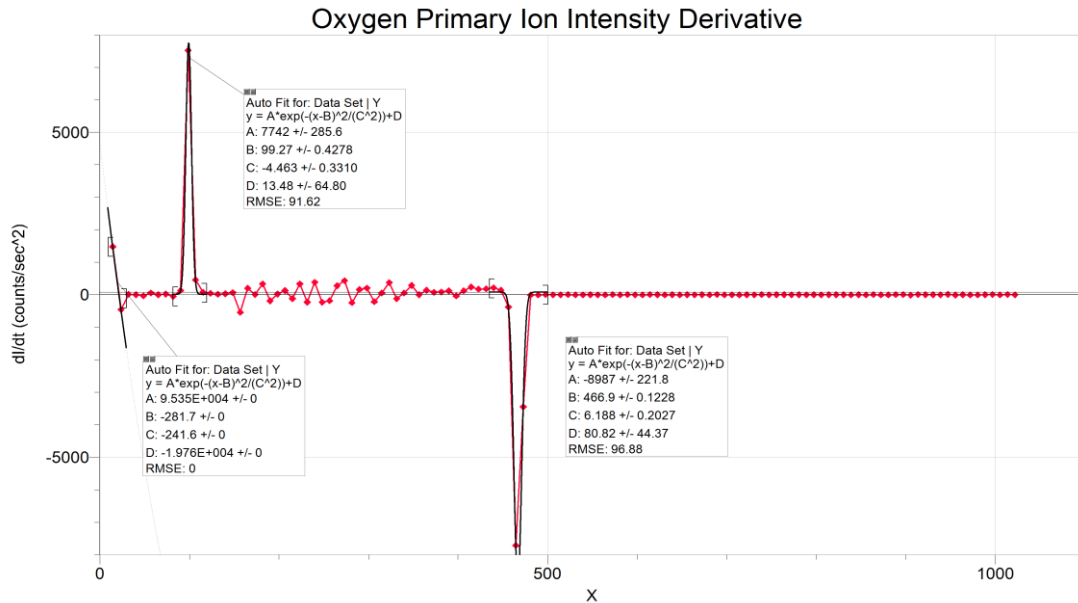
Figure 6.19: Narrow width Gaussian fit for the oxygen *secondary ion intensity derivative for the metal, oxide and silicon interfaces on the same sample presented at Figure 6.18. Transition time is considered to be at point where the peak of the Gaussian observed.*

Layer nature	Penetration speed (nm/sec)
Au Layer	2.8±1.0
Wet SiO$_2$	2.6±0.3
Dry SiO$_2$	2.4±0.4
Si$_3$N$_4$	3.1±0.6
Si	2.5±0.1

Table 6-5*: Primary ion calculated abrasion speed for different layers on a standard sensor Silicon sample*

Penetration speeds never exceed a few nm per second. Since Silicon dioxide density is lower than that of the silicon itself, the expected abrasion speed is slightly increased. For samples having undergone both wet and thermal SiO$_2$ growth, slightly different penetration speed values are determined. Because of the better quality of the dry oxidation process and the more regular structure of the produced layer, extraction potential is expected to be higher and beam penetration less efficient than in the wet SiO$_2$ region. Finally, silicon nitride layers most commonly used as passivation have similar densities and penetration efficiencies as wet silicon dioxide layers.

Final quantification is performed through multiplication of the penetration speed with each time point. When different layers are involved, the transition time is used to define layer change and the time in the new layer is calculated as the difference of the data point with respect to the average define transition time. Layer time is multiplied by the corresponding velocity and thicknesses of any previous layer as defined from crater measurements are added. In that way uncertainties can be kept under control, since preceding layer's speed and time estimations do not propagate to the following layer. In a four layer sample, a cumulated relative uncertainty of 4 % can be established for depth calculation, when combining uncertainties for all four regions.

6.6.3   Test production characterization

The above described technique is applied to three different test productions corresponding to the two main technologies currently used in sensor production, the n-in-n and n-in-p variety. Through a close collaboration with CiS[d] and VTT[e], producers of the ATLAS pixel sensors, test production were defined with well-known technological parameters tailored to our specifications. The main motivation is to compare the measured profiles with the simulated ones and to extract a process library for future simulations while calibrating the framework.

Wafers were diced in quadrants using a diamond saw and each quadrant was subsequently divided in 5mm wide strips. In one of the quadrants, screen oxide was etched using a 14 % hydrofluoric acid (HF) solution in an ammonium fluoride (NH_4F) solvent. Exposure time varies between 3 to 6 minutes with respect to the oxide layer thickness. Finally, two 5×5 mm^2 pieces where cut from the region closer to the wafer center where implantation is expected to be the most uniform, one with the oxide layer and one where the latest had been removed. Sample dimensions where selected taking into account the SIMS machine holder geometry, in order to ensure alignment and planarity with respect to the retaining mechanism. Although smaller dimension samples could have been used, a risk of introducing an incidence angle with the primary ion beam had to be considered.

Although for a purely semiconductor target, no significant preparation is needed prior to secondary ion spectroscopy, when addition layers isolating layers are involved, a reference surface is needed for initial beam adjustments. For samples where surface silicon dioxide layers were not removed, a ~50 nm PECVD palladium layer was introduced. Argon atoms, accelerated by a 5kV potential, vaporized a palladium anode ring which was deposited on the oxide surface. Layer uniformity was controlled at a 10 % precision level, but its thickness was subsequently measured.

6.6.3.1   n - in - n Test Wafer Samples

As described in section 6.3.2, four pixel fabrication technologies are currently available with the n-in-n being the one selected for the ATLAS pixel detector implementation. Being of a proven radiation hardness and effectiveness in terms of functionality and performance, it constitutes the base benchmark for any future developments. To understand process and dopant profile effects on final sensors as well as to calibrate the simulation framework and validate results in the larger context of passing to a purely simulation based pixel sensor development, the LAL pixel group decided to implement a basic n-in-n production to be used as a reference library. This implementation, with well-known technological and process parameters, not only is used to acquire experience in the basic process level, but also as a base for further irradiation studies in the most basic level, with no intervention of any additional complex effects induced by geometrical or conceptual issues. Given the motivation of this study as a reference and calibration for doping profiles in simulator and measurements and profile study with respect to irradiation, no lithographic masks were used. Selected doping concentrations and other process parameters vary around values commonly used in sensor production, which are not communicated to the final user.

6.6.3.1.1   Sample Production Process

Two series of wafers where manufactured, implanted under different conditions. For the first series, a low resistivity substrate was used with a nominal dopant concentration of 3×10^{16} /cm^3 corresponding to an equivalent resistivity of 0.25 $\Omega\cdot$cm and a thickness of 380 $\pm$ 5 μm. The second series of wafers was produced using a high resistivity substrate, equivalent to the silicon type on

---

[d] CiS Forschungsinstitut für Mikrosensorik GmbH, Konrad-Zuse-Straße 14, 99099 Erfurt, Allemagne, http://www.cismst.org

[e] Teknologian tutkimuskeskus VTT, Vuorimiehentie 3, Espoo, Finlande, http://www.vtt.fi

which sensors are produced, with a resistivity greater than 4 kΩ·cm, corresponding to a dopant concentration of 1.1×10^{12} atoms/cm^3 and of a thickness of 525 μm. Resistivity values are directly connected to radiation hardness, since higher resistivity substrates have a proven better tolerance to radiation damage [54]. The reduced number of charge carriers in the bulk provides less points where complex crystal defects can form, due to impacts from energetic particles or radiation absorption. Although wafer thicknesses are substantially greater than current sensor thickness, for the purpose of a doping profile study this has no actual effect, since all phenomena of interest take place in the first 10-15μm of the wafer depth, while the additional high thinning cost was also a contributing factor. All wafers where of n-type, phosphorous doped, <100> orientation Czochralski grown silicon, polished in both sides.

As no lithographic masks where involved, initial uniform thermal silicon dioxide layers of 100 nm and 200 nm thickness were developed on the primary substrate. While the 100 nm SiO2 layer was achieved using only a dry oxidation step, catalyzed by the presence of HCl, time and cost constraints of growing a 200 nm dry thermal oxide layer imposed the use of a wet-dry combination oxidation. It has to be noted that silicon dioxide does not grow on the surface of any preexisting layer but rather on the bottom, at the interface with the silicon substrate. Oxygen atoms need to diffuse through any material already on top of the wafer surface until they reach the silicon region. There, they react with Si atoms and form new layers of SiO_2 that expand outwards, under any previous layer. The thicker the layer that O_2 atoms have to traverse, the more time consuming the process becomes, with an exponential increase in time as the oxide grows. Since it is preferable to have a very good layer quality close to the silicon interface, one would rather prefer to have a dry thermal oxide (which is in general of better uniformity and more organized structure than the more rapidly grown wet SiO_2) developed at the last stages of oxidation. This is crucial to avoid non-uniformities during implantation as well as multiple scattering close to the interface and other transition effects.

After oxidation, wafers where implanted with phosphorous, using different doses and energies (*Table 6-6*). The oxide was used for screening the silicon wafer to avoid sputtering and crystalline amorphisation due to impact ionization, but inevitably part of the implant remained in the oxide region. Nevertheless, using the Bethe-Bloch formula for the stopping power of phosphorous ions at keV energies range, less than 5 % of total implant is considered to remain in the oxide region. After implantation, a thermal annealing step is performed to activate the dopant by integrating the implanted species to crystalline centers and recrystallize damaged regions. Processes of that type usually can be initiated at temperatures greater than half the fusion point of the material, which for silicon is 1414°C, and intensify as we approach 80 % - 85 % of this temperature. Nevertheless, one should keep in mind that a total fusion of the lattice should be avoided, especially in semiconductor grade silicon where mono-crystalloid structures are used and any random recrystallization will degrade the wafer. Thermal treatment temperature was set at 975°C for a 4h period in an inert atmosphere to avoid any chemical reactions.

N-IN-N, CIS WAFERS, <100> ORIENTATION													
Oxide thickness	100 nm							200 nm					
Implantation dose	10^{13} cm^{-2}		10^{14} cm^{-2}		10^{15} cm^{-2}		10^{16} cm^{-2}	10^{13} cm^{-2}		10^{14} cm^{-2}		10^{15} cm^{-2}		10^{16} cm^{-2}
Implantation energy (keV)	130	240	130	240	130	240	130	130	240	130	240	130	430	130
Annealing	4hours, 975 °C													

Table 6-6: *CiS test wafer production for dopant profile calibration. A series of 28 total wafers where produced in both low and high resistivity substrates.*

6.6.3.1.2   *Process Simulation*

Using the SYNOPSYS® Sentarus™ package, a complete simulation of this simplified production was performed. In the geometrical plane, since this is a uniform structure, an 1D approach is used by enforcing periodicity on the x and y direction with the z axis perpendicular to the wafer surface. Oxidation was both emulated by a simple oxide layer deposition and through a complete process simulation using the relevant thermal steps and active gas components composition information.

Implantation was performed using the Crystal Trim Monte Carlo algorithm [37], where penetration depth was estimated through a statistical approach. The total dose was extrapolated from a 1000 generated pseudo-particles per mesh element, whose trajectories started from a plane parallel to the silicon region above the wafers' surface. Real time clock randomization was used while the number of trajectories was further increased by allowing up to four splits in meshing elements with low trajectory density. Splitted trajectories originating from the same particle have half the initial statistical weight while they start under identical conditions at the splitting point. Up to four splits per particle where authorized but not more than 2 per mesh element and only within the silicon region. Trajectory splitting decreases statistical fluctuation and provides better modeling for transitional regions. In addition, a replication was activated to avoid physical calculation of all available tracks and particles. In this approach, equivalent trajectories are rather copied than recalculated, method that is quite accurate for 1D simulations like in this case. Final crystal damage accumulation was performed using the binary collision approximation, where it is assumed that, if the transferred energy exceeds a certain threshold, the target atom is displaced and, at this lattice site, a vacancy is generated. When the displaced atom comes to rest, it is identified as an interstitial. Defect production rate was evaluated by simulation the full collision cascade. Incident ion beam angle was set to a tilt of 7 % in the horizontal plane and a 30 % rotation as these are values commonly used in semiconductor fabrication to avoid implant channeling. The idea is to ensure that the incident ion beam is not oriented with respect to the crystal lattice and ions cannot use aligned empty spaces between elementary crystal cells to propagate deeply into the substrate. Although this is not really necessary due to the SiO_2 layer presence, which has a mostly irregular structure, it is always used as a precautionary measure for penetrating particles. No photosensitive resin was simulated at any step since there are no lithographic mask involved. Nevertheless, in actual circumstances, implantation takes place with the developed photosensitive layer still in place, as an additional sputtering protection mechanism. Final calculated concentration errors where set to 10^{18} atoms/cm^3 for phosphorous within the implanted region.

Concerning diffusion, four different readily available models where used (constant, Charged Fermi, Charged React, Charged Pair) as described in the simulator section 6.4.3, to better investigate the description potential with respect to experimental data. Thermal treatment steps where simulated using the closest possible approximation to actual increase, decrease and stabilization intervals while inert atmosphere was simulated throughout the treatment.

6.6.3.1.3   *Simulation – SIMS comparison on etched silicon samples*

In a first attempt, only low resistivity samples on which the oxide layer has been removed where measured. Initial simulations, performed with deposition of a 100nm oxide layer and not complete oxidation simulation, demonstrated good agreement in the initial silicon region but deviated from actual experimental results at higher substrate depths. In particular (*Figure 6.20*) a systematic deviation is observed in the simulated results towards shallower depths in all samples, independently of the implanted dose and energy. In a second approximation, the exact oxidation process was simulated (*Figure 6.21*) and the systematic tendencies were restored. Differences in oxide layer densities [55] between dry and wet grown layers have to be taken into account to reproduce accurately the implantation process.
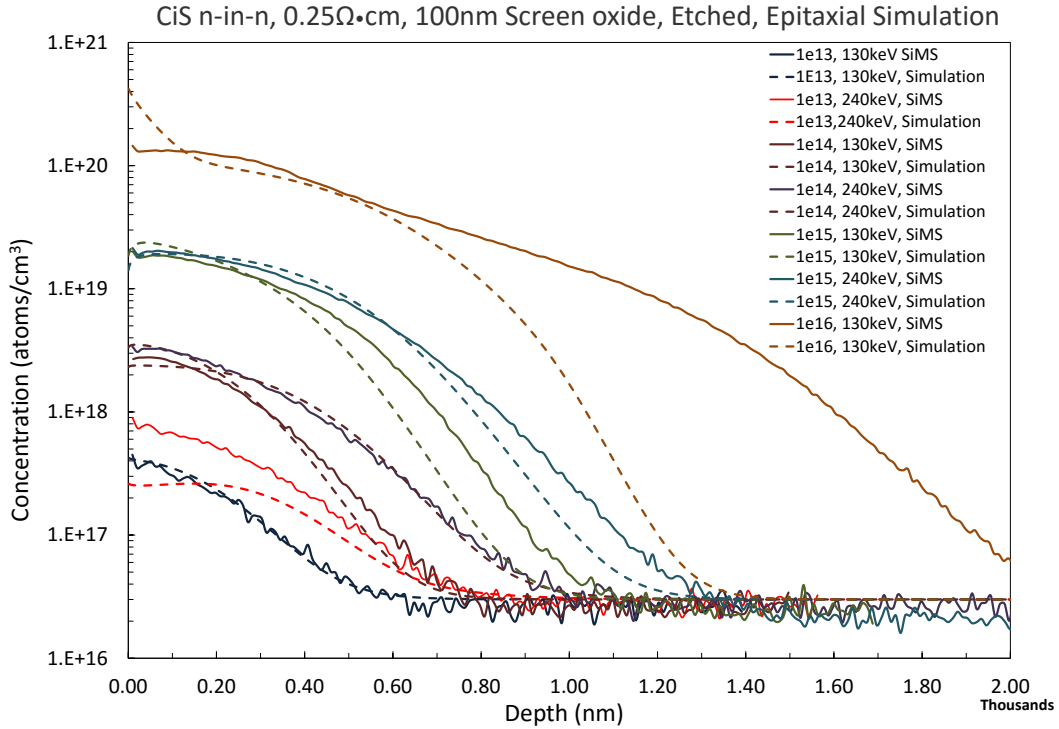
Figure 6.20: Simulated vs SIMS measured doping profiles for the CiS n-in-n production. Simulation was run with deposition of a 100nm silicon di- oxide layer using the charge pair diffusion model. A systematic deviation is observed on the simulated curve towards shallower distributions.
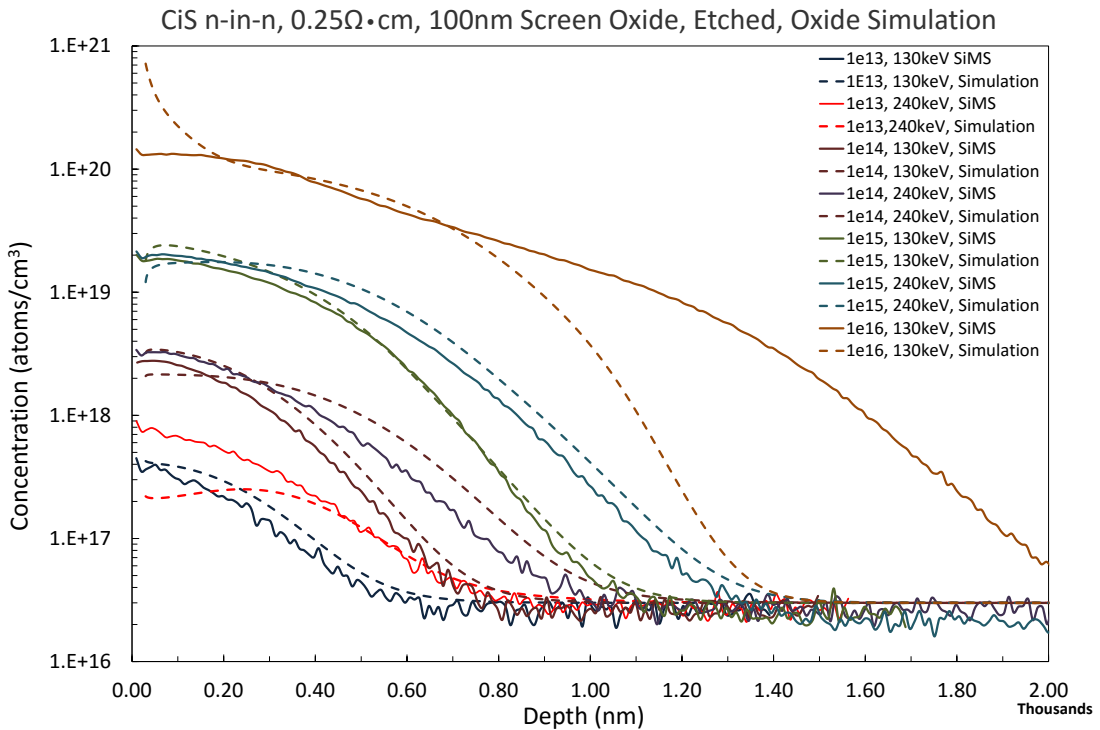
Figure 6.21: *Simulated vs SIMS measured profiles when complete oxidation process was simulated us-ing the charge pair diffusion model. Statistic deviations are still present but no systematic behavior is ob-served. Simulated results are represented with dotted lines while measurements are drawn with continues cures.*

Even after accurate oxide simulation, deviation of non-statistical nature are still observed for the 10^{13} atoms/cm^2 sample at 240 keV implantation energy and the 10^{16} atoms/cm^2 implanted sample at 130keV. For the 10^{13} atoms/cm^2 sample, divergence is observed at the first stages of the profile curve. In theory, when passing from 130 keV implantation energy to 240 keV while maintaining the same dose, ions have a deeper penetration depth due to their increased kinetic energy. Resulting profile should extend deeper in the substrate, while, to maintain the same dose integral, surface concentration is expected to drop. With respect to the Bethe-Bloch approximation for the phosphorous case, the relative difference between the 130 keV implanted sample profile and the 240 keV one, does not suggest the two implantations where performed at the same dose. The implanted dose can be extrapolated by calculating the integral of the measured concentration along the probing depth for each SIMS profile. In the following table *(Table 6-7)* doses are estimated for all samples within the silicon region:

Nominal Implantation Dose	Nominal implantation energy	SIMS Computed implantation dose
10^{13} atoms/cm^2	130 keV	1.19×10^{13} atoms/cm^2
	240 keV	2.597×10^{13} atoms/cm^2
10^{14} atoms/cm^2	130 keV	7.847×10^{13} atoms/cm^2
	240 keV	1.128×10^{14} atoms/cm^2
10^{15} atoms/cm^2	130 keV	7.094×10^{14} atoms/cm^2
	240 keV	8.866×10^{14} atoms/cm^2
10^{16} atoms/cm^2	130 keV	7.27×10^{15} atoms/cm^2

Table 6-7: *Calculated surface dose from the SIMS measured profile for all samples inside the silicon region. Lower dose value than the specifications is expected because of the implant retained within the oxide layer.*

Since the relative sensitivity factor was extrapolated for a pure silicon sample implanted with phosphorus, the implanted dose can only be estimated within the silicon region. Any concentration quantifications for the oxide layer would be incorrect. Computed total implant concentrations for within the silicon region demonstrate a general 20 % deviation from nominal values. This deviation corresponds to dopant been trapped within the screen oxide layer. Taking into account that phosphorous diffusivity in silicon is in the order of $\sim 8 \times 10^{-15}$cm^2/sec [56] while the corresponding value in silicon dioxide is several orders of magnitude higher ($\sim 5.73 \times 10^{-5}$cm^2/sec) [57] for 975°C, it is evident that phosphorus initially within the SiO$_2$ layer will get more diffused and find its way across the interface within the silicon substrate. In parallel, the phenomenon is amplified by the segregation value, representing the ratio of phosphorous concentration within the silicon versus concentration in the oxide layer at a state of equilibrium, which is significantly higher than one. This can be translated to a tendency of phosphorus rejection outside the silicon dioxide layer and within the substrate itself. Combining these two mechanisms, it is safe to infer that the initial amount of phosphorous trapped within the 100nm screen oxide, before any thermal annealing step, is quite higher than the final 20 % observed during SIMS.

For the sample with implantation dose of 10^{13} atoms/cm^2 at 1240keV, the total computed dose in the silicon exceeds the nominal value, pointing to an implantation mis-calibration. Since the penetration depth seems to be accurate, several simulation attempts were performed, where the energy was kept close to the reference of 240keV, but the dose varied from 1 to 3.2 times 10^{13} atoms/cm^2 *(Figure 6.22)*. A dose variation alone does not succeed in reproducing the effect, especially since the observed disagreement with simulations is situated at the initial part of the profile and does not extend in depth. To accurately replicate the curve form using a higher implantation dose, a lower energy would be needed. Hence, the energy was fixed at 180keV and different doses where simulated *(Figure 6.23)*. Although none of the simulated dose-energy combinations precisely matches the data points, the most accurate approximation, within 5 %, is obtained for a dose of 2.4×10^{13} atoms/cm^3 using an energy of 160keV (solid curve *Figure 6.23*). This behavior could be explained by a beam instability of the implanter. It was known that the machine was not sufficiently stable

under highly energetic conditions. Variations of beam parameters (magnetic field in the monochromatic separator, beam current e.c.t.) can account for the observed increase in the implanted dose and decrease in energy.
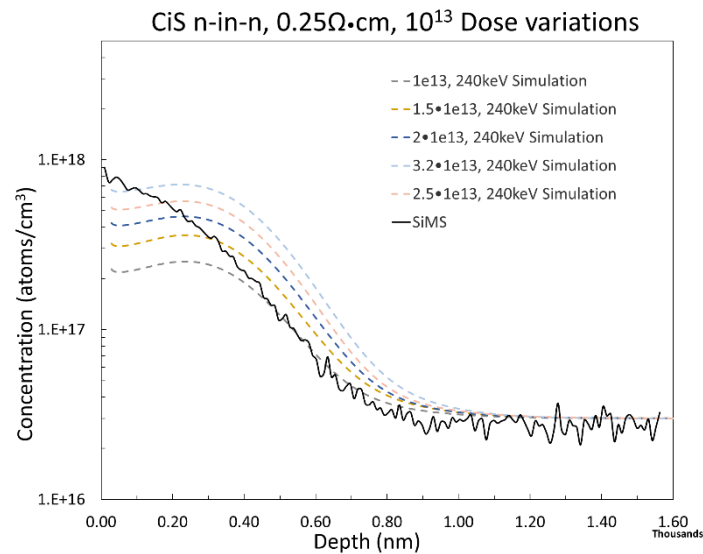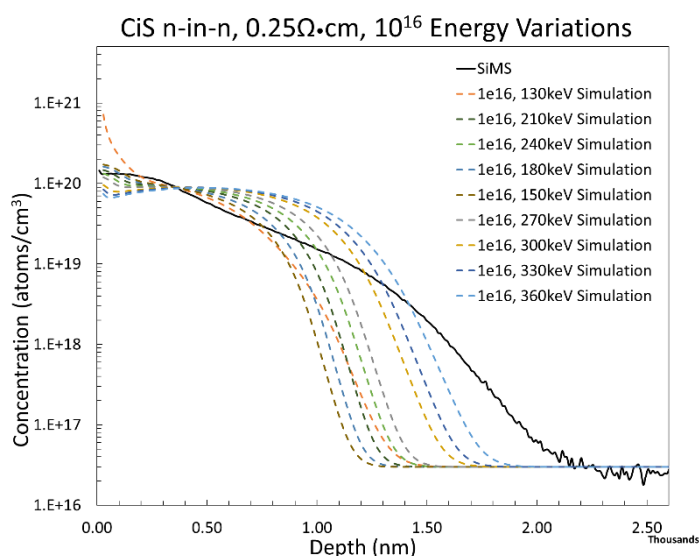

Figure 6.22: *Simulated profiles for the 10^{13} atoms/cm^2 @240 keV sample using different implantation dose values and the charged pair diffusion model. None of the simulated curves can describe the observed behavior of the sample, in spite of the increase in the surface concentration.*
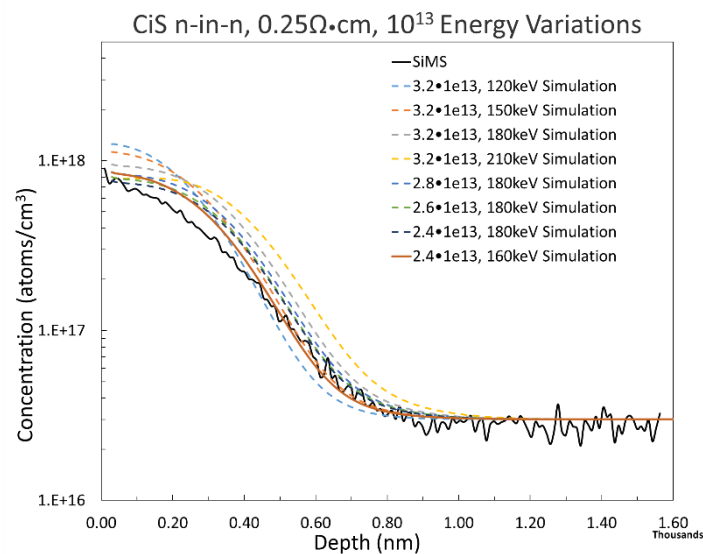
Figure 6.23: *Simulated doping profiles for the 10^{13} atoms/cm^2 @240keV sample, the dose was kept relatively close to the experimental value of 2.5×10^{13}atoms/cm^2 while energy varied while the charged pair diffusion model is used. Best agreement can be observed for a dose of 2.4×10^{13} atoms/cm^2 at an energy of 180keV (continues orange curve).*

To explain deviations in the behavior of the 10^{16} atoms/cm^2 implanted sample, a different approach is necessary. The computed dose from the measurements seems to be in agreement with the nominal value. Concerning the implantation energy, an increase would lead to a deeper distribution and would reduce surface concentration closer to the actual value. Nevertheless, it could not account for the shape of the profile curve (*Figure 6.24*). In addition, such large differences from the defined value during implantation would have easily been noticeable and corrected. The deeper distribution in the SIMS profile seems to be a diffusion issue, the origin of which could either be due

to insufficient cooling during ion bombardment or to the improper description of crystal damage by the default Charged-Fermi diffusion model used in the Synopsys simulator. A model study was performed using the four available models in the Sentaurus simulator as well as three additional, available in the SILVACO® Athena algorithm, keeping the same simulation parameters (*Figure 6.25*). None of the models seems to completely describe experimental results, however, the SILVACO® PLS[(f)] [58, 59] model, seems to approximate the deeper behavior of the profile. In the PLS approach, the dopant-vacancy pairs are not considered as an isolated system in high dopant concentration since, because of the increased amount of dopant atoms, each vacancy can interact with more than one of them A more complete approximation would include a more evolved implementation of the PLS model, were its core diffusion engine would be replaced by the standard Synopsys charged Fermi. The latest can sufficiently describe surface effects and initial diffusion, part on which the Fick's approach implemented in the PLS algorithm is not as effective. Nevertheless, the model is particularly successful in describing the deeper diffusion part.


Figure 6.24: *Simulated profiles for the 10^{16} implantedsample using different ion energies using the charged pair diffusion model. None of the curves can reproduce the deep diffusion while surface concentration decreases with energy increase.*

---

[f] The SILVACO PLS model was developed with the aim to consist a unique model for simulation of dopant diffusion and activation. It is a physical model coupled with a single set of parameters that can provide accurate simulation with an ease of use and flexibility. The high concentration of point defects, created by a high dose implantation, induces a fast acceleration of the diffusion. Although simple diffusion models can simulate defect-dopant coupling diffusion, Frenckel pair annihilation and recombination at the surface or bulk levels, they fail to correctly describe more complex effects. These include in particular, defect clusters formation, dislocation loops and mixed dopant/defect clusters cluster.

To effectively describe all phenomena, the PLS model is a combination of three main constituents:
A core diffusion mode, a defect cluster model and a dopant-defect clusters model.

- The core diffusion model is based on the Fick's diffusion law taking into account any reactions during annealing. Dopant migration is realized through point defects while charged states are take into account. Recombination and surface exodiffusion are also considered.
- The Defect Model is based on the Ostwald Ripening theory. Various type of extended defects are taken into account, such as small clusters, <311> defects, perfect and faulted dislocation loops It has the ability to accurately predict diffusion acceleration.
- Mixed dopant-defect cluster model is based on ab-initio calculations. For Boron, various types of clusters are considered, including B2I, BI2, B3I and B4I2. Arsenic vacancy clusters are also implemented while the ability is provided to easily add some new reactions i to improve simulations
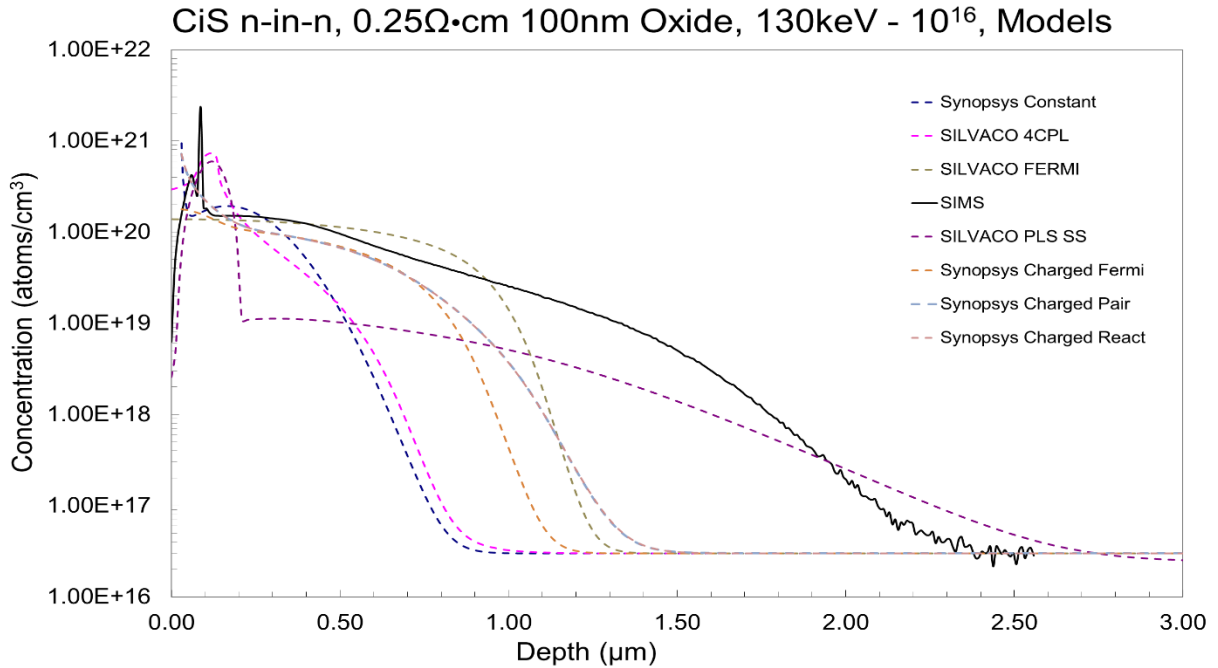
Figure 6.25: *Simulations performed for the 10^{16} sample using all the Available models in the two main simulation frameworks. Synopsys Fermi model better describes the shallow part of the distribution while the SIVACO PLS model accounts for the deep diffusion in the substrate.*

#### 6.6.3.1.4   *Oxide Layer Evaluation*

While initial measurements where performed in samples where all additional oxide layers were removed, subsequent data were taken though the screening oxide region. Since the relative sensitivity factor in the SIMS measurements was calibrated using a Phosphorus implanted silicon matrix, no comparison can be performed prior to the silicon interface in terms of dopant concentration. Nevertheless, an excellent agreement is observed with respect to the interface position in the target depth, suggesting a correspondence of oxidation process with the simulator for a fully simulated oxidation. The slight systematic disagreement in *Figure 6.26* towards the surface side of the profile distribution, is an effect of the additional deposited metal layer prior to any measurements. Upon subtraction of the mean layer thickness, one can confirm the exact results found with no oxide layer.

6.6.3.1.5   *High Resistivity Samples*

Additional set of measurements was performed on certain high resistivity substrate samples. With respect to implant distribution, no alteration is expected since the dopant concentration in the substrate itself, (10^{12} atoms/cm^3) is several orders of magnitude below any implanted dose while the increase in resistivity does not affect any diffusion mechanisms. Since SIMS sensitivity does not allow probing doses lower than 10^{15} atoms/cm^2 (*Figure 6.27*), the substrate distribution cannot be studied. Upon reaching these low values, uncertainties become dominant. As a result, the substrate concentration value cannot be probed. For economic and time management reasons, the complete set of high resistivity samples was not measured, especially since no variation was expected with respect to previously observed data. Selected samples included those with implantation characteristics close to actual values used in sensor production (10^{15} atoms/cm^2 @ 130keV, 10^{15} atoms/cm^2 @ 240keV), a reference sample for which simulation and data agreement was considered optimum (10^{14} atoms/cm^2 @ 130keV) and finally the problematic 10^{16} atoms/cm^2 @ 130keV sample, to confirm the behavior detailed in the previous section. All results are similar with respect to the low resistivity substrate data.
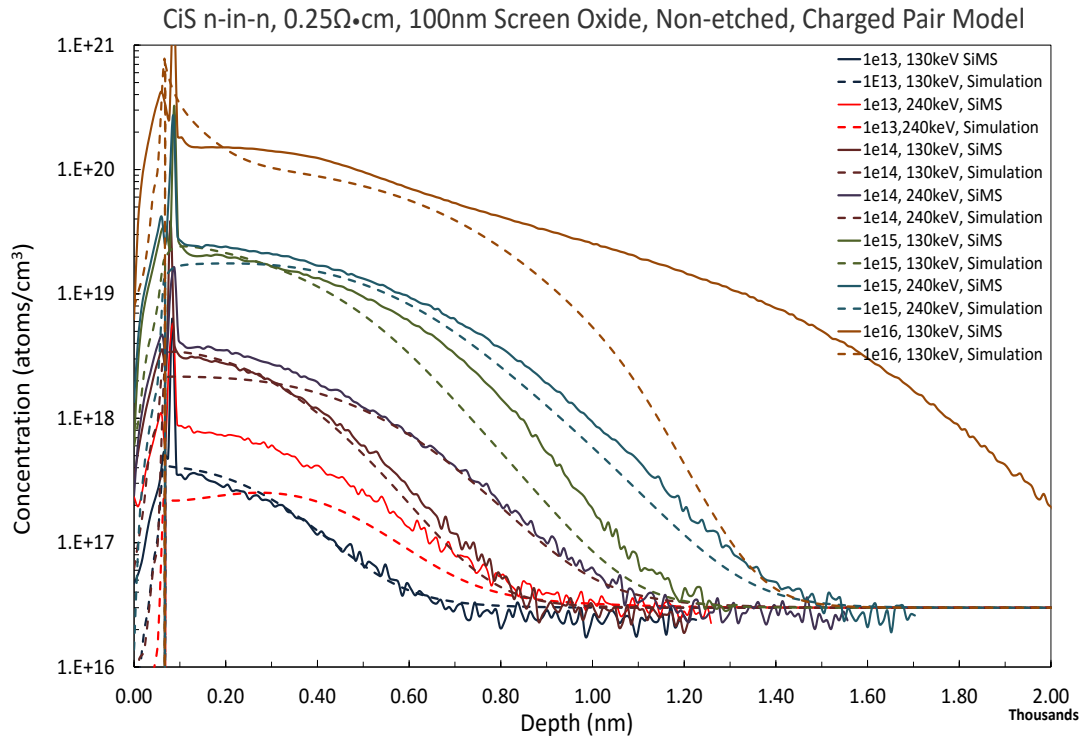
Figure 6.26: *SIMS measurements in CiS low resistivity wafers through the screening oxide layer and simulations using the charged pair diffusion model. A good agreement is observed between simulations and measurements with respect to the oxide-silicon interface position.*
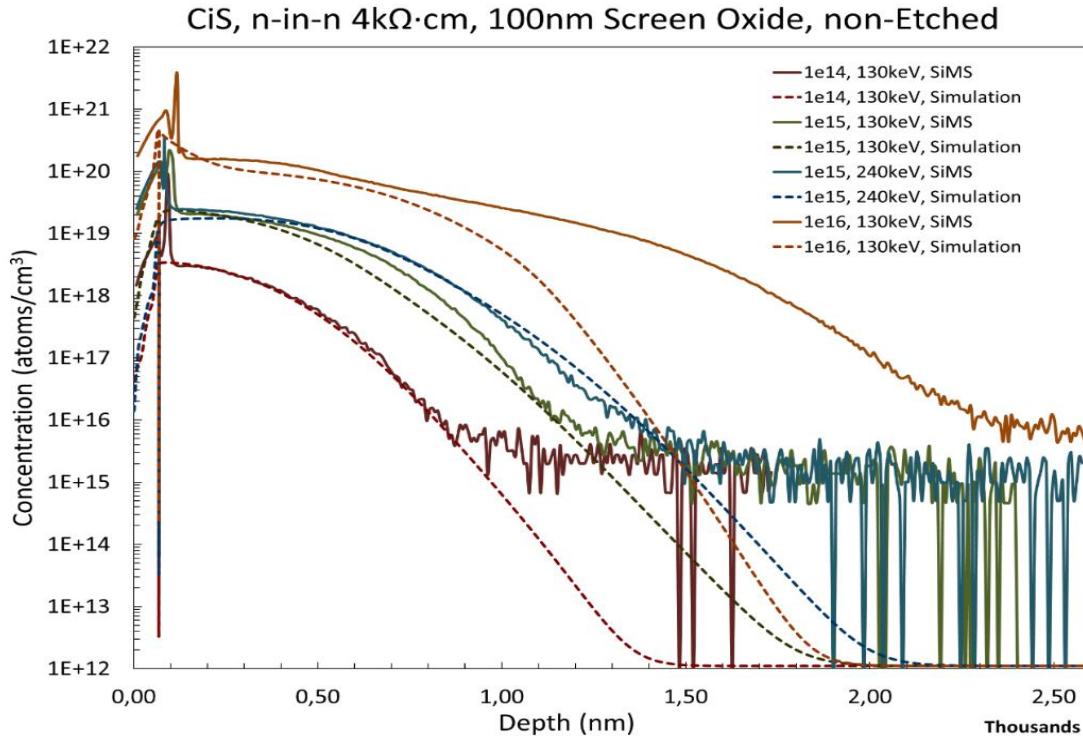
Figure 6.27: *SIMS measurements and simulations using the charged pair diffusion model on selected high resistivity samples. No variation observer with respect to the low resistivity measurement while low substrate concentration exceeds instrument accuracy.*

6.6.3.1.6   Conclusions

In general, a depth of up to 2.6 μm is observed for the profile distribution for the highest dose case. For the intermediate doses, closer to actual production values, no accountable concentration of the implant can be observed after 1.4μm. While an energy increase will reduce concentration on the surface regions and result in a deeper profile, an increase in dose will induce increase statistics in the tails of the penetration distance and stopping power distributions. As a result the amount of deposited particles becomes significant enough to be observed by the measurements. In any case, for a standard sensor production, all interesting phenomena develop at less than 5 μm from the wafer surface, demonstrating a huge margin in wafer thickness reduction (from 385 μm - 525 μm to 50 μm – 150 μm).

To conclude, a good comparison of simulation versus SIMS measurement is performed for low and intermediate doses, whereas at high doses (10^{16} atoms/cm^2) implant diffusion model needs modifications to accidently describe binary interactions. For the 10^{13}@240keV sample, a possible implantation instability could account for the observed deviations. No difference in the final acquired doping profile is observed between high and low resistivity substrates, while an accurate oxidation simulation is needed for better precision, to account for the density and quality differences between wet and dry developed silicon dioxide.

6.6.3.2   n - in - p Test Wafer Samples

Sensor production can be performed either on n-type substrate, in which case a double sided process is needed to create an n-p junction, or on a p-substrate, where only one implantation step is needed to introduce the n-type dopant. The junction is formed in the interface between the implant and the substrate itself, which is now of opposite type with respect to the implanted species. N-in-p process is one sided, with less lithographic steps and substantially less expensive than n-in-n productions. To have a complete understanding of the various methods, the same methodical work was performed as in the n-in-n case but in collaboration with a different foundry, currently competing for Phase II upgrade production. ADVACAM, a spin-off of the national technology center of Finland VTT, is also a pioneer in the new active edge technology and an understanding of their processes is increased interest for future productions.

6.6.3.2.1   Wafer fabrication

To investigate a p-substrate production, as in the n-in-n case, a series of <100> orientation boron-doped wafers were used for two different resistivity values. The lower resistivity substrate, ~ 0,25 Ω·cm, corresponds to a boron substrate concentration of 7×10^{15} atoms/cm^3 and a thickness of 675±5 μm, and is a Czochralski grown silicon wafer, polished on its top side. For the high resistivity wafers, the thickness changed to the standard value of 525±5 μm with a dopant concentration on the substrate in the order of 1.3×10^{12} atoms/cm^3. Since only dopant profile distributions are investigated, no lithographic masks where used in any production stage. An initial screen oxide layer was developed upon all wafers prior to implantation. Thickness of screen oxide varies between 100 and 200nm, in accordance with the n-in-n test production specifications.

To achieve a more complete and uniform understanding, implantation parameters for the n-in-n and n-in-p productions where kept identical (*Table 6-8*). Dose varies between 10^{13} atoms/cm^3 and 10^{16} atoms/cm^3 for the two distinct energies of 130 keV and 240 keV per oxide thickness. Initial oxidation and implantation steps are no different from the n-in-n production.

A substantial difference was introduced in the activation of the implant species. Rather choosing a standard thermal cycle in an inert atmosphere, a combined process was used. At the beginning, wafers where submitted to an one hour standard thermal cycle at 1000ºC in N$_2$ atmosphere. Then

two subsequent oxidation steps followed. A wet oxide was initially developed at the same temperature, followed by a dry silicon oxidation afterwards, for the same duration of 1h. This variable process is of double interest. In most sensor production processes, several implantation steps are implemented and for each one of them, a different lithographic mask is needed. In a standard process, after thermal activation of the first implant, a new screen layer would have to be placed, either through normal or low temperature oxidation (LTO - low thermal oxidation) or Si_3N_4 deposition. The thermal dose would have to be carefully monitored to avoid any over-diffusion of the implant. In order to overcome such problems and to reduce costs, it is possible to develop subsequent screen layers and activate the implant at the same time using high temperature layer development processes. An oxidation is therefore performed at 1000ºC, although in our case no additional step follows. Nevertheless, if the duration of the oxidation process is maintained for as long as the normal thermal exposure would have lasted, the thickness of the developed oxide layer would largely exceed any useful value. In addition, a side-effect of this oxidation process is that it actually consumes substrate layers, by transforming silicon molecules to SiO_2 acting on the implanted surface of the wafer affectively removing implant from the final region. This effect can be both beneficial and detrimental at the same time. Beneficial in the sense that first layers of implanted silicon, where most of impact damage, transition effects and mis-modeling occur, will be removed. Diffusion through oxide development is also more efficient since oxidation has been proven to increase dopant diffusivity within silicon due to the exercised pressure on the crystal structure under the oxidized region and the disassociation of the lattice related to the oxygen-silicon reaction [55, 58]. The detrimental part consist of the implant extraction from the final substrate. One has to be certain that after oxidation, enough implant will remain for a functional device (see the Gallium LGAD case).

n in p, VTT production, <100> orientation, thickness of 675 μm or less,

	100 nm								200 nm							
Oxide thickness																
p implantation doses	10^{13} cm^{-2}		10^{14} cm^{-2}		10^{15} cm^{-2}		101^{6} cm^{-2}		10^{13} cm^{-2}		10^{14} cm^{-2}		10^{15} cm^{-2}		10^{6} cm^{-2}	
Implantation energy (keV)	130	240	130	240	130	240	130	240	130	240	130	240	130	240	130	240
Annealing	3hours, 1000 °C (1h annealing + 1h wet oxidation +1h dry oxidation)															

Table 6-8: *ADVACAM n-in-p test wafer production characteristics. A total of 32 wafers were produced in both low and high resistivity substrates.*

To account for these three issues, a normal thermal activation was implemented for 1h at 100C, a wet (fast) oxidation step for 1h at 1000C and finally a slower but better quality dry oxidation step for the same time and temperature. The interest of the dry oxide at the last step is to create the best possible transition between the silicon and preceding layers, since new oxide layers always develop from the silicon interface onwards, as preparation layers for any subsequent processing steps.

6.6.3.2.2   Sample Process Simulation

Samples where simulated using the same general flow parameters as for the n-in-n case with respect to implantation model, meshing strategy and optimizations. The entire substrate was simulated using a much coarser meshing after the first 20μm of silicon, where the region of interest is. Differences are present at the final steps of dopant activation. An oxide is developed on the already implanted silicon wafer. Nevertheless, the oxidation speed and efficiency depends on the dopant concentration on the silicon surface. For silicon dioxide to form, oxygen atoms need to diffuse within Si lattice and encounter an atom in a crystal position that favors interactions. An increase in the dopant concentration results in more defects in the silicon lattice due to mismatch. In a defect region, atoms are more loosely connected to the crystalline structure and present higher reactivity with respect to a conical crystal [59]. To account for the effect, a dopant dependent oxidation model was used, demonstrating higher oxidation rates in the most heavily implanted samples.

6.6.3.2.3   Simulation – SIMS Doping Profiles Comparison

Initial measurements where performed in oxide-free samples. A good overall agreement in the order of 5 %, at the low and intermediate doses, is demonstrated between simulations and measurements (*Figure 6.28*). The four available diffusion models in Synopsys were studied (Fermi, Charged Pair, Constant and Charge React) in their charged variations, attempting to further investigate deviations observed at doses higher than 10^{16} cm^{-2}. Although the charged react and charged pair models provide adequate results for intermediate range, they fail to provide a reasonable description for higher doses. The constant model, based in Fick's diffusion law, gives very poor agreement for all samples while the charged Fermi model seems to be sufficiently adapted for intermediate doses but diverges for higher values providing significantly shallower profiles with respect to the measured ones. Doses of 10^{15}/cm^2 present a uniform deviation of 0.3µm towards shallower depths in both implantation energies (130keV and 240keV) for all models, while for the most energetic implantation of 10^{16} at 240keV a deviation towards higher depth is observed, equivalent to that detailed in the n-in-n implanted sample of same dose.
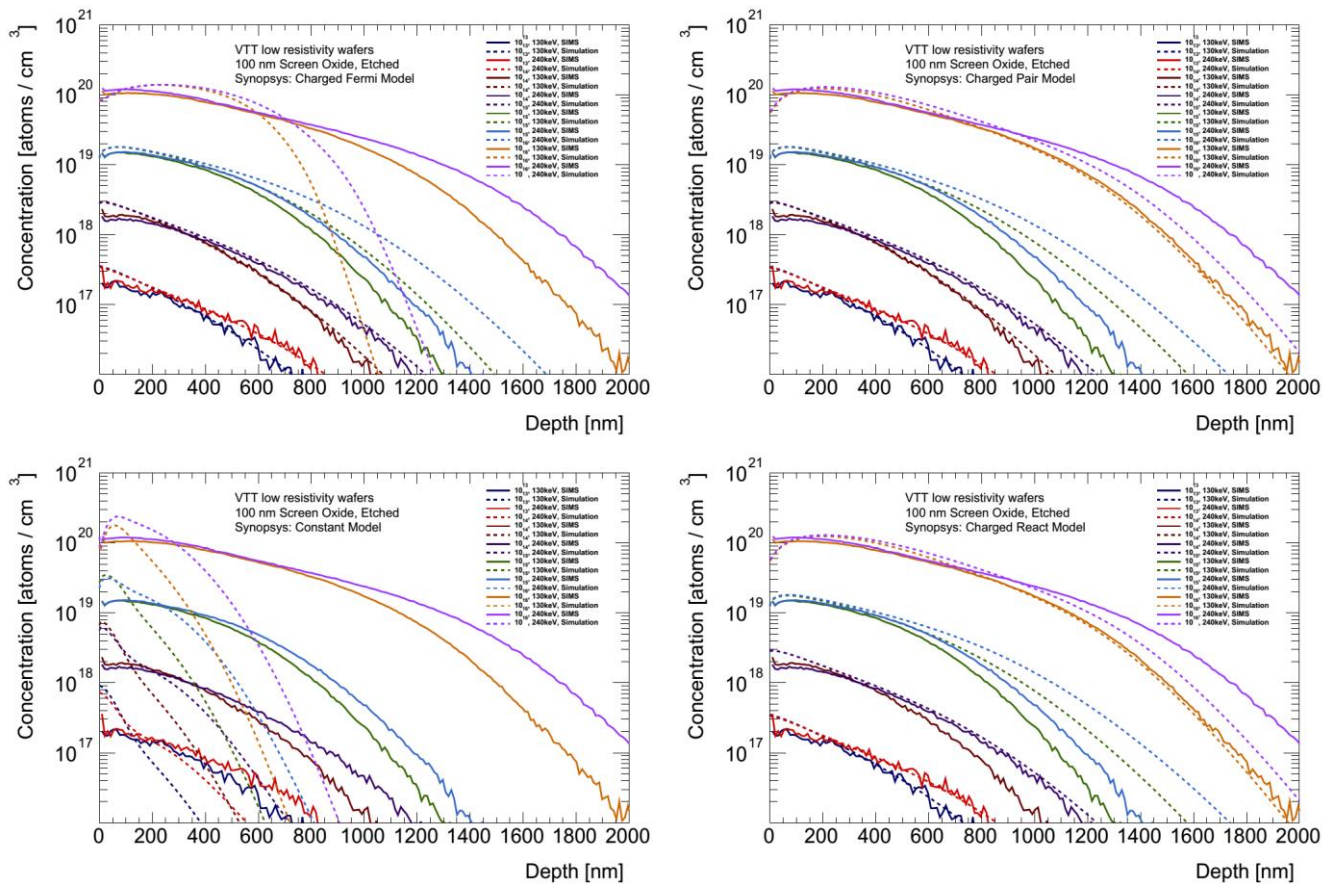
Figure 6.28: *N-in-p doping profile measurements and simulations using different diffusion models. From left to right (clockwise): Charged Fermi diffusion model, default Charged Pair model, Constant Model and Charged React model. Simulations are plotted with dashed lines while SIMS measurements are represented with continuous curves. Although the Charged Pair model provides very good agreement, there is a discrepancy on highest dose modelling. Results are slightly better that the Charged Fermi model, where disagreements are more pronounced even for intermediate doses. Charged react essentially provides the same analytical description as charged pair model taking into account possible chemical reaction between species. Finally, the constant model only provides an adequate description for weakly implanted wafers.*

A first order evaluation of the nominal dose values is derived by the calculation of integrated doses from SIMS data (*Table 6-9*). A general difference of 30 % with respect to the reference is

observed for all samples. This difference is slightly increased with respect to the 10 % - 15 % observed in the n-in-n case, mainly because of the final oxidation steps which consume the surface layers of implanted silicon and transfer that implant within the silicon dioxide region. In spite of any variations between samples, this tendency is rather uniform suggesting correct dose adjustment between different implantations. For the dopant concentration within the silicon dioxide, no accurate estimation can be made since the SIMS calibration was only performed using pure silicon implanted samples.

Screen layer	Nominal Dose	Energy	Computed Dose
100nm	10^{13}atoms/cm^2	130keV	6.67E+12
		240keV	8.28E+12
	10^{14}atoms/cm^2	130keV	7.35E+13
		240keV	7.35E+13
	10^{15}atoms/cm^2	130keV	6.80E+14
		240keV	7.48E+14
	10^{16}atoms/cm^2	130keV	6.93E+15
		240keV	7.76E+15
200nm	10^{14}atoms/cm^2	130keV	7.37E+11
		240keV	4.91E+13
	10^{15}atoms/cm^2	130keV	6.23E+12

Table 6-9: *Surface dose calculation using the SIMS profile for all samples. The calculation is valid only within the silicon region.*

For the 10^{15} atoms/cm^2 samples, a shallower profile than expected is measured. Both samples exhibit the same measured profile shape while, observed differences with respect to simulation are in both cases of the same order (~0.3 μm). The depth where a concentration of 10^{16} atoms/cm^3 is reached for the lowest energy sample (10^{15} @ 130 keV) is unexpectedly similar to the equivalent depth for the lower dose sample (10^{14} @ 240 keV). These three observations, the same curve form for all 10^{15} atoms/cm^2 implanted samples, the shallower diffusion depth than expected and the same observed same systematic deviation from simulations, point to a possible implantation issue. To further investigate the effect, the 10^{15} @ 130 keV sample was chosen and simulations were performed with one of the four main implantation parameters (energy, dose incident angle, diffusion time) modified in each trial.

The shallower nature of the profile points to lower implantation energy. By keeping the dose fixed at the nominal value, a series of simulations were performed with energies varying from 10 to 130 keV (*Figure 6.29*). Initial part of the distribution seems to be in accordance with expected results from a 100 keV implantation whereas in depth diffusion seems to follow the 80 keV distribution, but since none of the curves completely matches the data, an energy variation alone is not sufficient to describe the effect.

The second investigated parameter was the post-implantation diffusion time. Assuming a shorter thermal exposure would explain the shallower profile. Implant activation in these samples is performed via a classical thermal annealing of 1h and two oxidation steps while there is no indication that the oxide thickness is less than foreseen (see later paragraph). As a result, any annealing time variations could only be in the first of the three steps that does not include oxide development. Several annealing times were simulated (*Figure 6.30*) ranging from 20 to the original 60 minutes. Diffusion effect seems to be minimal, as one should expect, since the subsequent steps are significantly longer in time and are mainly responsible for the implant diffusion.

The third controlled parameter was the beam incidence angle with respect to the wafer surface. It has already been noted that a small angle of 7° is introduced to avoid channeling effect within the silicon crystal. Nevertheless, channeling should not occur in samples already covered with oxide layer because of the irregular nature of these regions. Indeed, several angles where simulated (*Figure*

6.31) and no significant variation is seen between an angle of 0 and 7 degrees. When the incidence angle becomes steeper, surface scattering and geometrical acceptance reduce the amount of implant within the wafer. Departing from the logical hypothesis that an angle that could cause this effect would be significantly large to be noticed and could not have occurred by accident, this is not an effect to be considered.
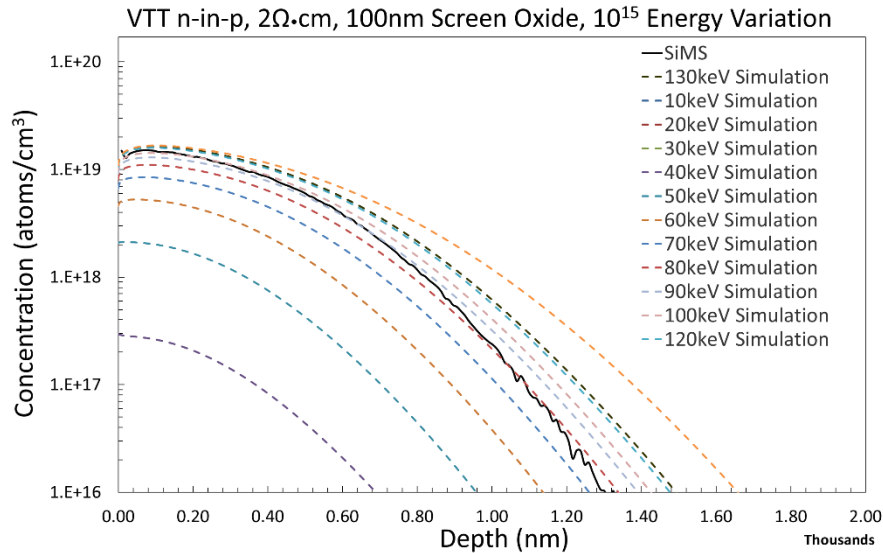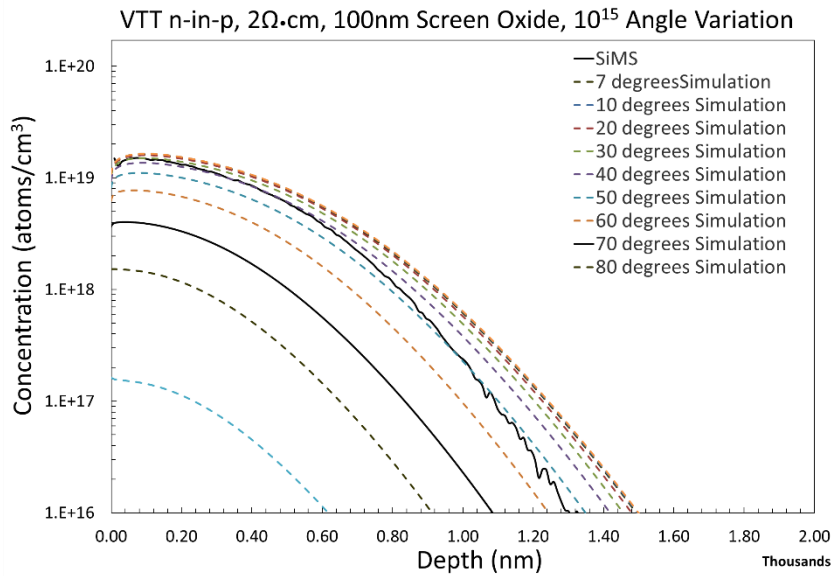

Figure 6.29: *Simulations using different implantation energies for the 10^{15}atoms/cm^2 at 130keV sample using the charged pair diffusion model.*
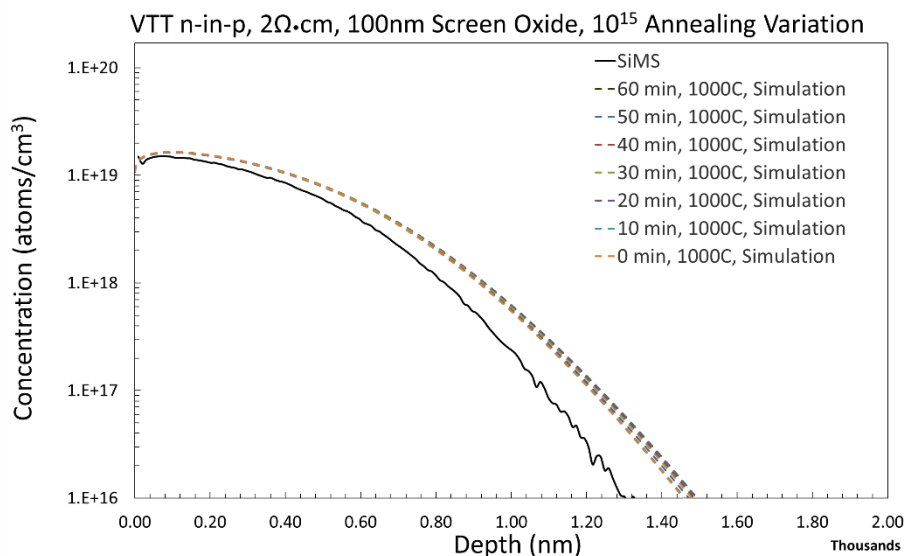
Figure 6.30: *Simulations assuming different annealing duration of the first step of implant activation for the 10^{15}atoms/cm^2 at 130keV sample using the charged pair diffusion model.*

Finally, several variations on implanted dose where simulated (*Figure 6.32*). Although none of simulated values seems to reproduce the observed profile form, a tendency is established towards lower implantation doses. As for the 10^{13} atoms/cm^2 sample of the n-in-n CiS test run, the observed deviation is a combination between lower energy and a small dose variation resulting from a mis-handling of a beam parameter. Since most foundries sub-contract implantation steps to external companies, no control over the parameters is possible. While additional test protocol with well-established implantation procedure is needed to allow for final conclusions, in normal CMOS and transistor production, a variation of this scale would have no observable effect on the final product.

Figure 6.31: *Simulations performed assuming different primary ions beam incidence angles for the 10^{15} at 130keV sample using the charged pair diffusion model.*
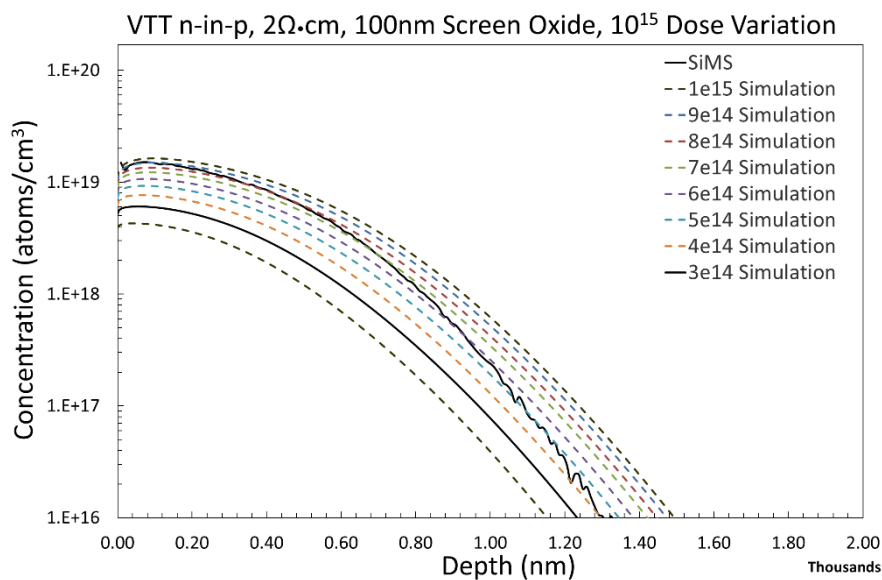
Figure 6.32: *Different doses were simulated while the implantation energy was kept at 130keV for the10^{15}at 130keV sample using the charged pair diffusion model.*

On the other hand, for the highest dose and energy (10^{16}/cm^2 at 240KeV) a tendency towards deeper profile is apparent. As in the precious case, integrating the available implant quantity determined by SIMS data is in agreement with production reference parameters. The nature of this deviation is nevertheless different and is induced by the used diffusion model, proven to be inaccurate in high doses. The reason for which the model seems to work for the 10^{16} at 130keV sample in this production (while it is reminded that for the same sample at the n-in-n case results deviated significantly from simulations) is the substrate type. The p substrate is of opposite nature with respect to the n-implant and donor-acceptor concentrations counterbalance to some extent. Nevertheless, implanted donor densities are not high enough for binary interaction modeling to no longer sufficiently describe the behavior within the substrate. Therefore, the default charged pair model still gives reasonable results for the 10^{16} atoms/cm^2 at 130keV implanted sample while it starts failing from thereafter.

6.6.3.2.4   Oxide Layer Evaluation

To control the understanding of the oxidation process, SIMS where also performed in samples where the oxide layer was left intact. Because of the implant activation through oxidation, the oxide layer is expected to be thicker than the 100nm specifications. In *Figure 6.33,* SIMS measured doping profiles and simulations are presented including the oxide layers. Four main remarks can be made:

- A very good agreement is observed between measurements and simulations for the oxide-silicon interface values. As expected two oxide regions are visible, with the first of 100nm being the screen oxide through which the implantation was performed, and the second of about 400nm been developed during implant activation.

- The position of the first oxide interface is identical for all samples, whereas the second oxide interface is deeper for higher dose samples. Because of different doping, higher dose samples sustained increased crystalline damage which accelerates post-implantation oxidation. Since all samples where submitted to the same conditions, more doped samples will have a thicker secondary oxide layer.

- Implant concentrations between SIMS and simulations in the oxide regions do not agree since data calibration is only valid for the silicon region.

- The characteristic distribution of the implant in each oxide region gives an indication of the type of fabrication process utilized. In the first oxide region we can find a Bragg-like peak corresponding to the implant trapped within this layer during ion bombardment. Since phosphorous diffusivity in oxide is tree orders of magnitude less than its diffusivity in silicon (10^{-17}cm^2/sec in SiO$_2$ versus 10^{-13}cm^2/sec) [6] at 1000 C and at the reference concentrations, the dopant profile within the oxide region remains unaltered during post-implantation thermal steps.

However, in the second oxide region we observe a much lower phosphorous concentration presenting a slow descent. This corresponds to the phosphorus implant trapped at the first layers of silicon and during oxidation was pushed out. The implant concentration is subsequently lower because of the oxide to silicon volume ratio, having a value of 2/3. As a result, for every two volumes of silicon consumed three volumes of oxide are produced and the implant gets "diluted" within the oxide. Finally, the distribution seems to present a very mild descent because in this oxide region because the initial dopant concentration in the first layers of silicon is stable (*see Figure 6.26*).

6.6.3.2.5   High Resistivity Samples

While all results presented on the n-in-p test wafers where obtained using a low resistivity (2 Ω·cm) implanted substrate, the same dose - energy characteristics where also implemented on high resistivity wafers (10 kΩ·cm). Because of the substantial experience gain on through-oxide measurements and the proven ability to correctly quantify and manage SiO$_2$ layers demonstrated on the previous study, SIMS measurements on high resistivity substrate where directly performed without any oxide etching. Nevertheless, only the four most commonly used energy-dose combinations in sensor production where investigated, given the fact that no actual deviation from any low resistivity results is expected. As it can be seen from the following figure (*Figure 6.34*), the comparison between measurements and simulation yields the same issues and discrepancies as for the low resistivity production. Dopant concentration within the original silicon wafer is several orders of magnitude smaller than any of the implantations performed thus limiting any differences to electrical characteristics.
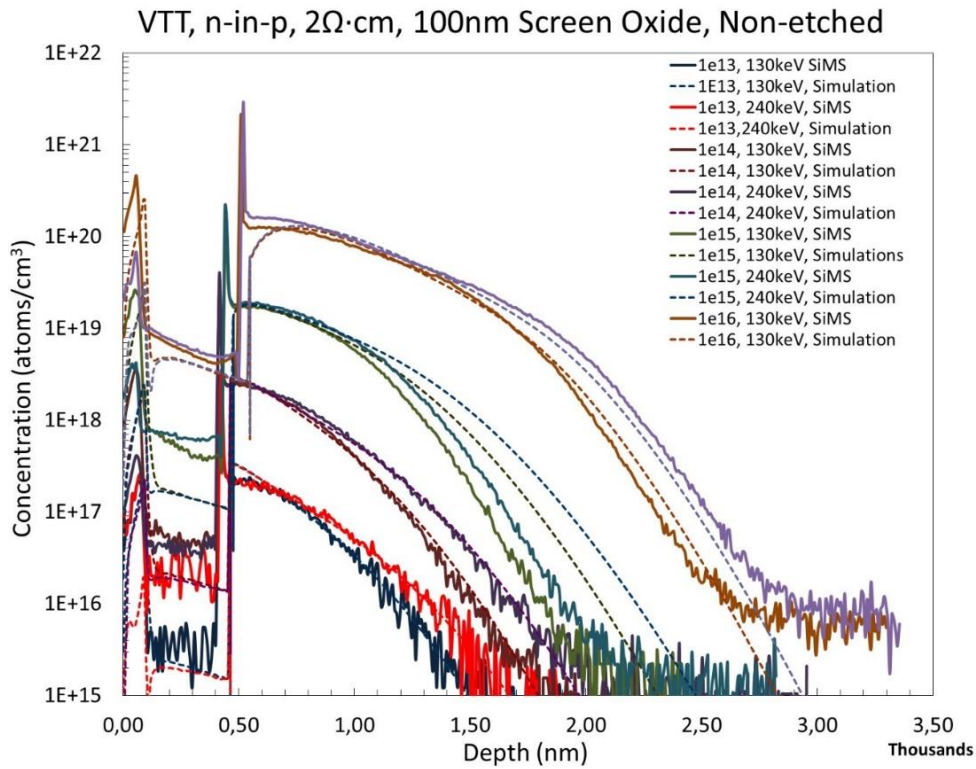
Figure 6.33: *Simulations and SIMS measurements of phosphorous implanted ADVACM samples where the oxide region was not removed and the charged pair diffusion model. Distinctive dopant distributions separate the two oxides, initial screen oxide in the beginning and thermal oxide developed during activation.*
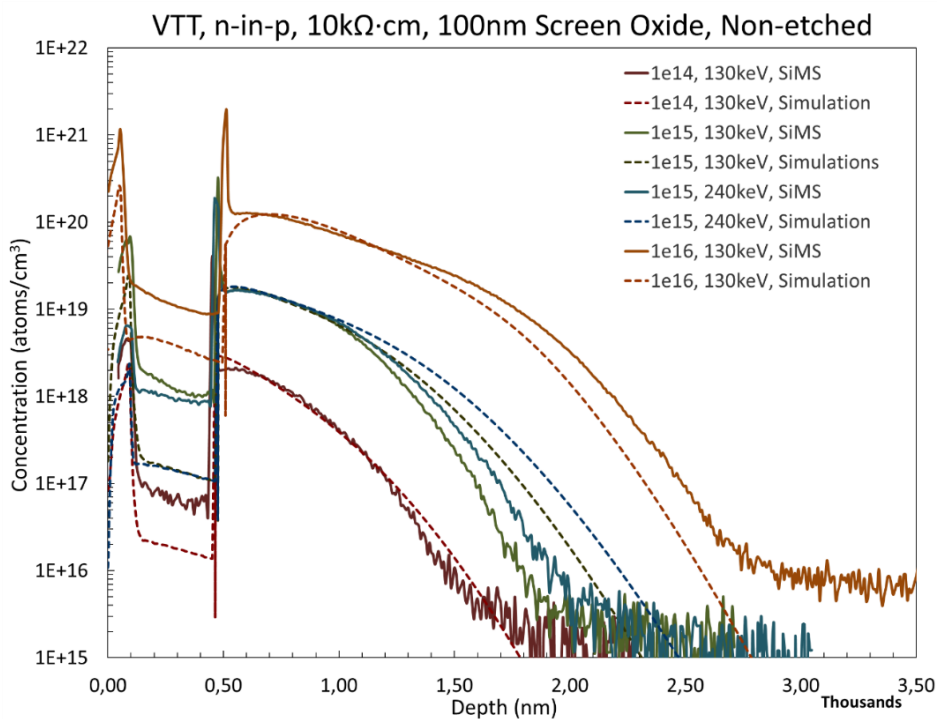
Figure 6.34: *Simulations and SIMS measurements of phosphorous implanted ADVACM samples on high resistivity substrate wafers with the charged diffusion model. The oxide region has not been removed while only the four most commonly used dose-energy combinations where probeds.*

6.6.3.2.6   Conclusions

To conclude, a very good agreement between SIMS measurements and simulations was observed for the n-in-p production, when using the charged pair diffusion model. The post implantation activation via oxide development improves the uniformity in the first silicon layers and the agreement with the simulations. A systematic deviation for doses of 10^{15}atoms/cm^2 was observed and can be attributed to instabilities during implantation process. Model validity extends up to 10^{16}atoms/cm^2, where a deeper profile than predicted is observed for the highest energy. In the n-in-p production, this systematic model disagreement appears in slightly higher concentrations because of the nature of the substrate that compensates partially the effect.

6.6.3.3   p-Spray Test Wafer Samples

When designing a pixel, a series of implants are used to define the matrix and form the functional element of the sensor itself. Essentially, a pixel sensor is a matrix of diodes, vertically aligned and sharing one of the implants. Modern trend, for radiation hardness reasons, is to use an n-type implant to form the pixelated part while the necessary p-type implant is either introduced on the back side of the substrate, as in the n-in-n case, or is the substrate itself, as in the n-in-p case. Because of the uniform nature of the p part and the physical proximity of individual pixels in the sensor matrix, it is possible for charges induced underneath one pixel to drift and induce a signal on neighboring cells. This effect is more pronounced if the trajectory of the particle generating these charges traverses close to a pixel's edge. To isolated pixels from one another, limit crosstalk and control charge sharing, and additional, opposite type implant, is introduced between the pixels. This p-type dopant of low concentration, is primarily boron and is most commonly known as p-spray. To have a complete reference for developing a sensor production, a p-spray test production was implemented on a p-type substrate using the ADVACAM process.

6.6.3.3.1   Sample Production Processing

A low resistivity (~0.25 Ω·cm, 7×10^{15} atoms/cm^3) p-type substrate, of <100> orientation and 675±5 μm thickness was used for the boron p-spray test production. A uniform initial silicon dioxide layer of 200nm-300nm was developed and the samples were implanted with boron in different energy and dose, resulting in a total 6 wafers (*Table 6-10*). As in the previous cases, no lithographic masks where implemented while post-implantation activation was performed in accordance with the procedure described at the n-in-p test production, involving thermal oxidation.

P SPRAY, VTT PRODUCTION, <100> ORIENTATION						
Oxide thickness	200nm			300nm		
p implantation doses	1×10^{12} cm^{-2}	3×10^{12} cm^{-2}	6×10^{12} cm^{-2}	1×10^{12} cm^{-2}	3×10^{12} cm^{-2}	6×10^{12} cm^{-2}
Implantation energy	60 KeV			90 KeV		
Annealing	3hours, 1000 ^{o}C					

Table 6-10: *P-Spray test production parameters. A total of 6 low resistivity substrate wafers were produced.*

6.6.3.3.2   Process Simulation

The exact same simulation procedure was used as in the n-in-p case. Given the low concentration expected in the substrate, the absolute dopant concentration error was set to 10^{15}atoms/cm^3. To increase statistics, the maximum authorized particle trajectory splits were set to 4 with two allowed per meshing element. Implantation was performed using the Monte Carlo Crystal Trim algorithm. In this case, the initial oxide layer was not completely simulated but emulated by a deposition of 200 or 300nm of silicon dioxide. For the final oxidations steps used for implant activation, no dopant

specific oxidation was used because of the reduced implant expected to be found in the silicon region.

6.6.3.3.3 SIMS – Simulation Doping Profile Studies

Given the substantial experience obtained, measurements were performed directly through the oxide layer n all samples. The two distinct oxide regions are visible (*Figure 6-35*) referring to the primary oxide on the top and the secondary, developed during activation. Unfortunately, the use of high resistivity substrates strongly degrades the discriminating power of the measurement because of its high boron content, which is higher than the SIMS resolution limit. Given the lower concentrations of 10^{12} cm^{-2}, an extreme accuracy was achieved for the silicon region were simulations and data are in perfect agreement. Discrepancies of the dopant concentration at the first 500 nm of the sample, within the oxide region, are due to the absence of silicon oxide calibration targets for the SIMS measurements. Nevertheless, alignment of the interface regions between simulation and measurements is perfect, while the initial overshoot of the measured curves correspond to beam instabilities as charge compensation effect is optimized. The initial palladium layer deposited in all samples with oxide for charge compensation purposes, has been subtracted from the available data since it is not simulated neither part of the original production.
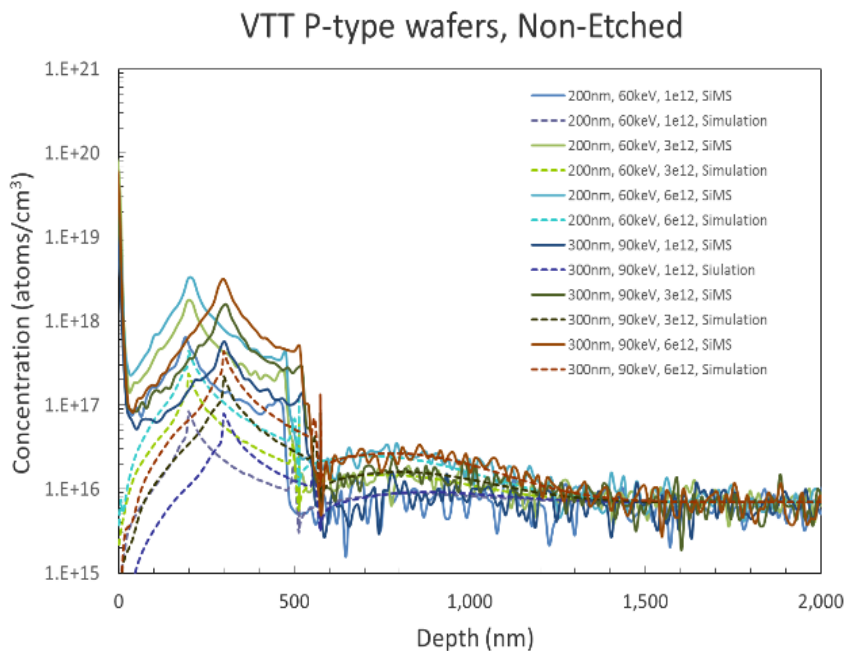
Figure 6.35: *P-spray doping profile in low resistivity p-type substrate. The two oxidation steps are separated by the sharp pics at the left part of the plot, with the further left region corresponding to the screen oxide and the region that extends up to 500 nm, to post-implantation annealing. Simulations are run using the charged pair diffusion model.*

6.6.3.3.4 Conclusions

P-spray implantation is of low energy and as a result, quite shallow. The major part of the dopant is situated at the first micrometer of the silicon layer. This is the result of an active choice, since most of the charge propagation to neighboring pixels takes place at surface layers. In addition, a quite low dose is selected in order not to disturb the effective pixel diode. As such, it has to be several orders of magnitude less than the pixel implant itself. From a production process side of view, it is observed that a very large portion of the implant is within the secondary oxide. Because of the low energy and the thick screening layers, most of the original implant stays at the first layers of the substrate. Subsequent oxidation transforms these layers to silicon dioxide and transfers the majority of the dopant outside the substrate. This technique constitutes an engineering choice, one

allowing only the smooth tail part of the profile distribution to remain within the final silicon region, in order to avoid abrupt changes of the electrical field within the sensor.

### 6.6.4 Low Gain Avalanche Diodes Production evaluation

After having successfully validated both the simulation tool and proven the application of SIMS analysis in production evaluation, the method was applied to an innovative detector technology, the Low Gain Avalanche Diode (LGAD). Using the acquired experience, an appropriate test structure to be introduced in all wafer production of LGAD type was designed, one that would allow evaluation of the final result through SIMS measurements. In addition, in close collaboration with CNM[(g)], an additional simulation and measurement campaign was undertaken in an effort to replace boron traditional doping with gallium implantation.

6.6.4.1 LGAD Principles

The use of silicon detectors in particle detection applications provides good performance and accurate particle tracking information. Given the intrinsic properties of silicon, a reverse biased detector operated in the proportional region, provides an amount of charge relative to the primary ionization in the semiconductor. In addition, due to the small energy gap of 1.11 eV between the valence and conduction bands, a large amount of carriers (80 e$^-$/μm) are produced per ionizing particle. This provides a good efficiency and a large detection rate. Nevertheless, silicon sensors operating in the linear region remain extremely sensitive to thermal and electronic noise and the signal to noise ration degrades heavily with irradiation.

A way of overcoming this issue is the introduction of some mechanism of charge amplification within the detector. This will allow to produce a signal much higher than primary ionization by increasing the yield of generated carriers. Subsequently, the use of a lower gain for the electronics amplifier would be possible. Such a behavior is achieved by a multiplication stage within the silicon bulk for avalanche diodes, used in photon detection (APD). However, in an avalanche operation mode, no information can be extracted for the initial particle energy.

A new detector, similar to a reverse biased diode operating in avalanche mode, was proposed [60], operating with a lower gain. The Low Gain Avalanche Diode (LGAD) detectors, structurally resemble a normal p-n junction with the addition of a multiplication layer, providing typical gain of 10 - 100. Internal structure can be compared to that of a planar n-in-p pixel technology with the addition of a p type pad diffused under the top n$^+$ implant region (*Figure 6-36*). As a result an n$^+$/p/p$^-$/p$^+$ is created at the center of the geometry [61]. Once the detector is reverse biased, a higher electric field in the central region will enhance electrons reaching the n$^+$ electrode. The gain of the structure crucially depends on the dopant distribution of the p multiplication layer, responsible for electric field amplification.
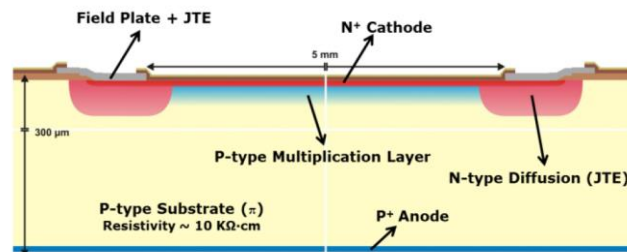
Figure 6.36: *Schematic representation of an LGAD cross-section. The p-multiplication layer is diffused below the n+ implant of the top electrode. Special structures (JTE) are included to reduce the field at the edges of the structure between the n$^+$ and p regions [61].*

An additional structure is needed to reduce electric field intensity at the n^+/p-type junction region towards the edge of the structure. At this point, the high filed curvature and increased dopant concentration are susceptible to induce an early breakdown. The edge structure, referred as JTE, consists of an additional n-diffusion that overlaps the main n-type contact. Thanks to this implementation, the electric field is reduced to values that allow for the breakdown voltage to be higher than the depletion voltage of the main region [62].

6.6.4.2   *Test Structure design*

Following the LGAD cross-section scheme defined in *Figure 6.36,* six different areas can be identified, each with a different doping profile. Four of these doping distributions correspond respectively to the n^+ surface electrode, the p^+ multiplication region, the n implant defining the JTE structure and the backside p electrode [63]. Two further regions are defined at the superposition points of the n^+ top implantation with the JTE n-type diffusion and with the p+ multiplication region [64]. Consequently, to correctly evaluate any LGAD production, a six region test structure needs to be defined, with each region reserved to one of the previous profiles.

A 10 mm $\times$ 10 mm structure (*Figure 6.37*) was introduced to each production wafer, divided into six 2.75 mm $\times$ 3.65 mm equal regions. Each region was subsequently matched to the required process step in order to correspond to one of the six doping profiles. In particular, the following reference scheme was applied:

Region L1: p-stop implantation, corresponding to backside and guard ring implants
Region L2: p-well implantation, corresponding the p^+ multiplication region, situated under the n^+ central anode.
Region L3: n-implant corresponding to the JTE region implantation
Region L4: n^+-implant of the central anode region.
Region L4+L2: Combination of the n^+ anode region implant and the p^+-implantation of the multiplication layer.
Region L4+L3: Combination of the n^+ central anode region implant and the JTE n-implant
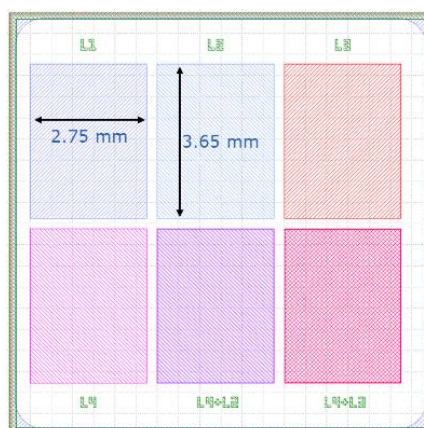
Figure 6.37: *Layout of the LGAD doping profile test structure with the various implanted regions .From left to right in the top row the L1, L2 and L3 regions are placed while the L4, L4 + L2 and L4+L3 are located on the bottom row.*

The structure was specifically conceived for SIMS measurements with the size of each region kept sufficiently large for at least five distinct iterations. Any additional material layers deposited through the fabrication process flow were not removed, since their respective thickness was also of interest in this study. Finally, no top metallization layer was introduced, in contrast with the full production process flow of an LGAD sensor.

6.6.4.3   *Sample preparation and measurements*

Each region of the structure was individually diced and undergone an ultrasonic surface clean prior to measuring, Because of the additional silicon dioxide and passivation layers deposited, an additional gold layer was deposited to regulate potential at the surface layer during SIMS measurements. Through PECVD (Plasma Enhanced Chemical Vapor Deposition) technique, 60nm of gold were introduced, with 10 % uniformity. Samples were subsequently measured in a five stage approach for each region. This was necessary to evaluate the different thicknesses of each layer as well as the corresponding ion velocities. For regions where a single dopant is present, only one concentration calibration was performed. However, since in layer L4+L2 a combination of p and n type implantation is used, the measurement process is repeated twice, using different ions species. Crater thicknesses were evaluated for all regions, through mechanical profiling. Final depth is extracted combining values for three individual linear fits performed on the profile on the crater bottom. This also allowed to verify the uniformity of the beam and exclude any secondary effects.

6.6.4.4   *Results for Boron LGAD Run*

Structures included a phosphorus implantation for the n-type regions and a boron implant on the p-type. Since detailed process flow was not known for the run under investigation (CNM run 7859, wafer 5), an initial exploratory measurement was performed to identify different layers and deposited materials. Given the high importance of the dopant distribution of the multiplication region, implantation parameters (boron doped with an energy of 100 KeV at a dose of 2.2×10^{13} atm/cm^2) were provided for validation. By monitoring secondary intensities of several elements (^{11}B, ^{12}C, ^{16}O and ^{28}Si) it is possible to identify transition layers between different materials. Oxygen and Silicon intensities are useful for defining interfaces between SiO$_2$ layers and the substrate. On the other hand, Carbon is monitored not only for its close mass proximity to boron which is the element of interest, but because it is used as a catalyst in several deposition processes. By inferring to *Figure 6.38* top plot, representing secondary ion intensities with respect to measuring time, it is possible to clearly distinguish the silicon, silicon oxide, metal and passivation layers. The metal layer is the one deposited as preparation for the measurement and is the first to be encountered by the primary beam. In the subsequent layer, silicon and oxygen intensities stay relatively low, while no implant can be identified. This is clearly a region deposited at the end of the process, containing a lower amount of silicon than the substrate matrix itself. It is a passivation layer consisting of Si$_3$N$_4$. Because of the increased signal of both silicon and oxygen in the three subsequent layers their composition can be attributed to silicon dioxide.

A caveat concerning the growth process is the dopant distribution within this region. While by studying the form of the oxygen and silicon secondary intensities it is not possible to distinguish any structure, the boron distribution clearly points out three different regions. Silicon oxidation is performed from the silicon interface upwards, displacing any preexisting layers outwards. Since the amount of boron in the first oxide region is minimal, it is certain that this was the initially deposited oxide, served as a mask for the subsequent implantation. On the second and third oxide regions, boron intensities are extremely high but present a discontinuity. These oxides were developed after the implantation while they also served as diffusion steps for the initial implant. The outermost layer corresponds to the first of these oxidation processes while, the inner region was the final oxidation – diffusion step. One can even evaluate corresponding thermal treatment exposure by measuring the thickness of each layer. The final region is attributed to the silicon substrate.

Although reverse engineering is not the aim of this measurement, it is possible for an unknown sample to define with detail the process flow by carefully analyzing SIMS results. Layer thicknesses and corresponding ion penetration velocities are presented in *Table 6-11* for the first region (L1). After the initial exploratory measurement and the identification of all regions, further data allowed precise determination of layer thicknesses. On the middle plot of *Figure 6.38* a depth calibration is performed and measuring time is transformed to equivalent depth. Finally, using the definition of

the RSF through a suitable calibration sample and the integrals of the matrix and dopant intensities, a concentration calibration is performed. The bottom plot of *Figure 6.38* presents the dopant concentration with respect to depth. As previously mentioned, this calibration is only valid for the silicon region.
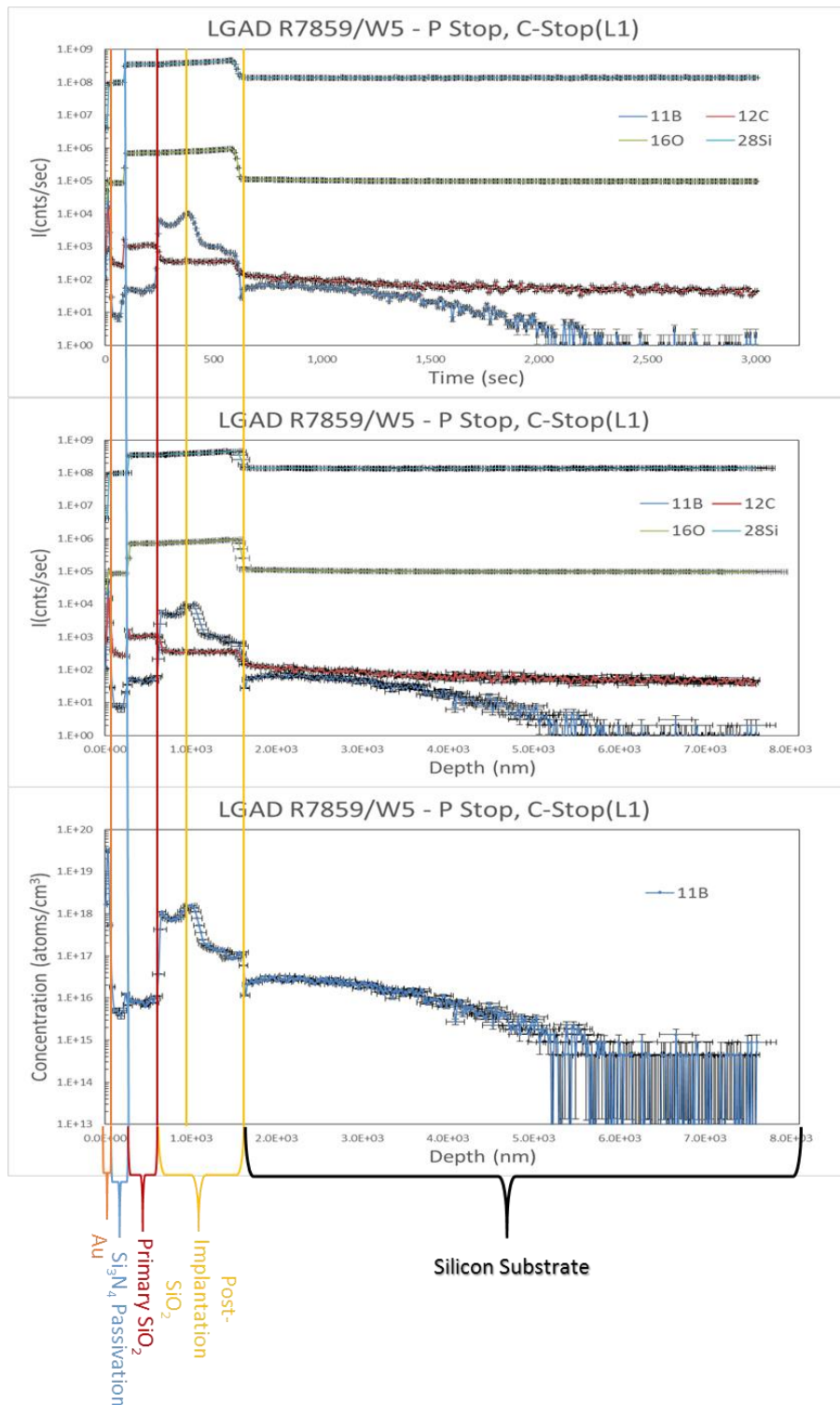

Figure 6.38: *SIMS measurement of the first region of the combined test structure. Secondary ion intensities with respect to measuring time are presented in the top plot. A depth calibration has been performed for the middle part while a dopant profile is presented for boron at the bottom plot.*

Layer	Thickness (nm)	Velocity (nm/sec)	Uncertainties
Au	55 ± 6	2.8 ± 1.0	Current: δI = 1 cts/sec
Si3N4 Passivation	223 ± 7	3.1 ± 0.6	(cts = counts per second)
Primary SiO2	382 ± 9	2.4 ± 0.4	Time : δt = 4.64 sec
Post implantation SiO2	929 ± 7	2.6 ± 0.3	
Silicon	6014 ±13	2.5 ± 0.1	

Table 6-11: *Different layers, thicknesses and corresponding ion velocities in each region for the first part of the test structure (L1) corresponding to the p$^+$ backside and guard ring implant.*

The same procedure is repeated for all subsequent test regions and subsequent dopant profile distributions are extracted. Uncertainty evaluation is performed through the procedure described in sections 6.6.2.2 and 6.6.2.3. A relative 5 % uncertainty is established concerning depth definition for the first and third measured profiles (*Figures 6.38 and 6.39*). However, for the four remaining profiles (*Figures 6.40 0 6.43*), uncertainties where not directly derived but rather calculated using the assumption that the relative density of equivalent layers is similar. Although this is a valid approximation, since all structures were at the same wafer, a subsequent rescaling is required since beam intensities between different profiles vary. As a results uncertainties scale up to 20 % in depth determination. An additional depth measurement of the oxide layers would solve the issue, but due to insufficient machine allocation, this was not possible for the current series of measurements. Concentration uncertainties remain under control at all cases, with a relative uncertainty less than 1%.
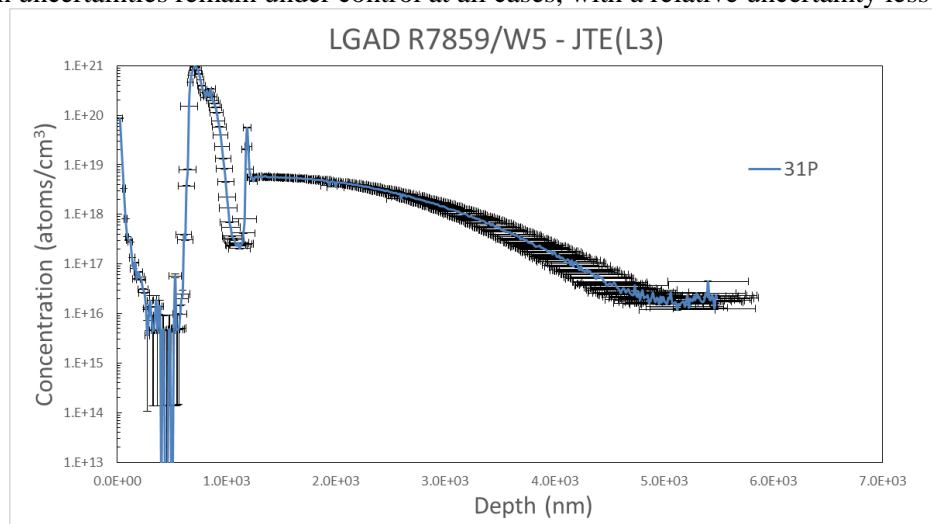
Figure 6.39: *Dopant profile of the JTE n implant, implemented at the edge of the LGAD sensor.*

By evaluating the initial part of all dopant profile distributions it can be concluded that the number and thickness of surface layers differ for each test region (*Table 6-12*). Distributions corresponding to deeply diffused regions are preceded by thicker oxide layers (*Figures 6.38, 6.39 and 6.40*) while the n$^+$ central region is only preceded by a screen oxide layer with no thermally grown oxidation (*Figure 6.41*). To compare the final dopant diffusion depth, one needs to infer all depth measurements with respect to the silicon interface. With respect to *Figure 6.42,* where the shallow n$^+$ central implant is represented over the p-type multiplication region (a combination of measurements presented in *figures 6.40 and 6.41*), it is apparent that the diffusion depth differs by a factor of 2 between the two species. In addition, the concentration of the phosphorus region is several order of magnitude higher of that of the multiplication implant below. The latter, presents a slowly decreasing profile, reaching 1 % of its peak value at 1.8 μm depth. For comparison, the shallow n implant can be seen found at the same value just after 0.4 μm.

175
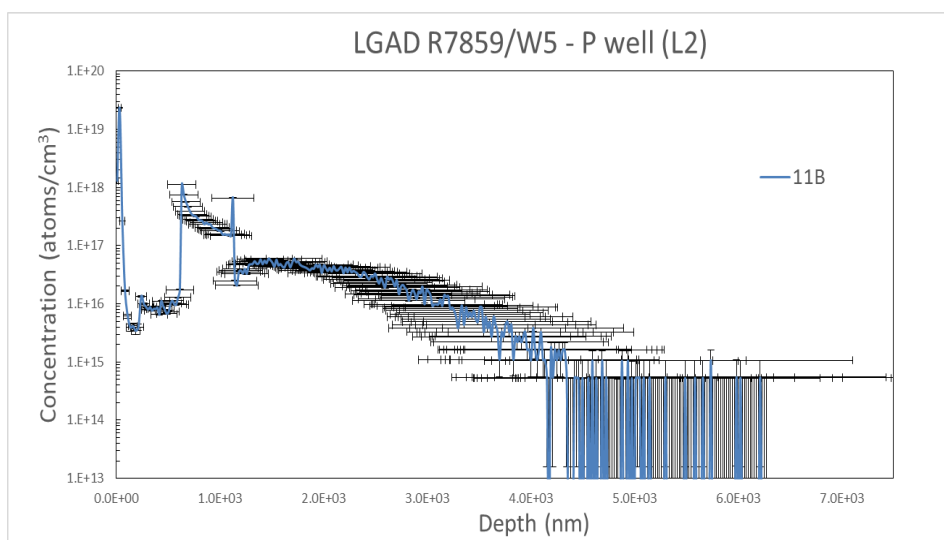
**Figure 6.40:** *Dopant profile of p⁺ multiplication region situated at the center of the sensor.*
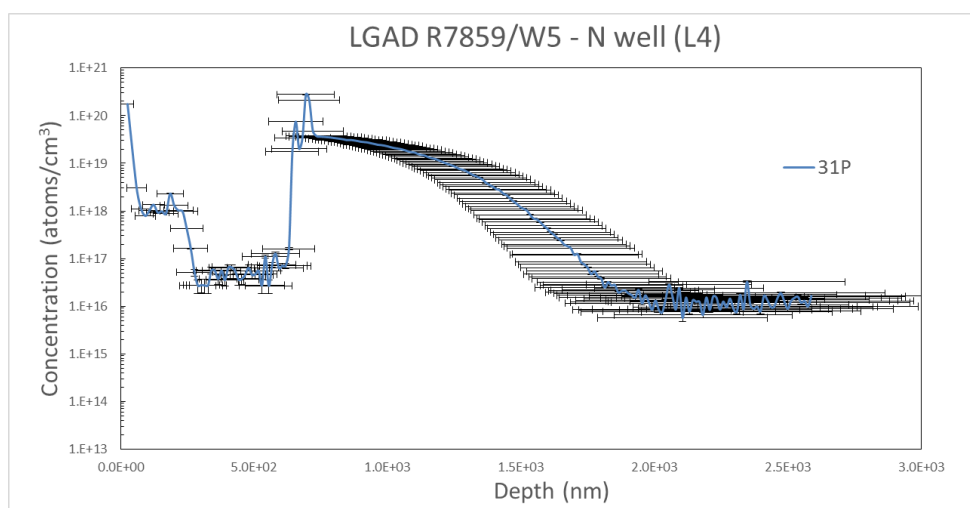
Figure 6.41: *Dopant profile of the shallow n implant of the center region.*
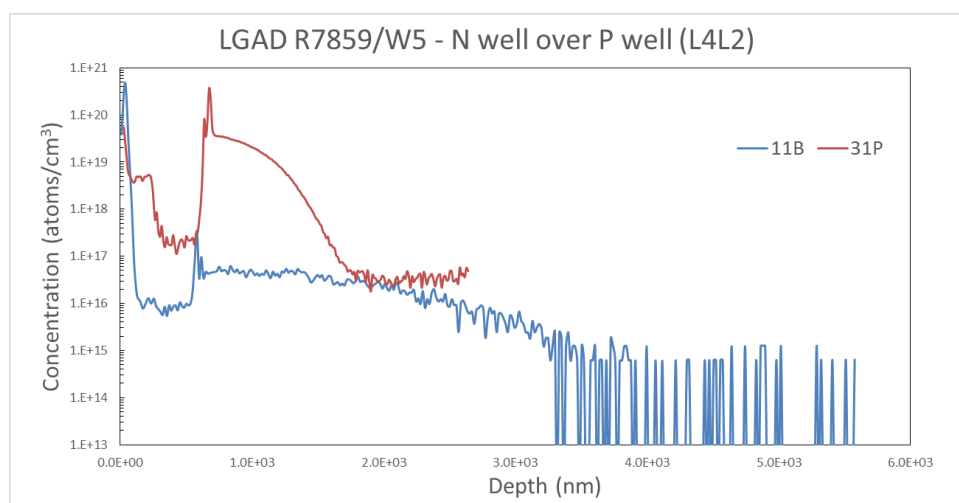
Figure 6.42: *Combined dopant profile of the shallow n⁺ implant and the p multiplication region in a single structure. This plot represents the combination of the two previously measured profiles presented in figures 6.40 and 6.41.*

Layer	L1	L2	L3	L4	L4+L2	L4+L3
Pd / Au	55 ± 6 μm	58 ± 29 μm	55 ± 6 μm	54 ± 34 μm	55 ± 38 μm	48 ± 48 μm
Si₃N₄	223 ± 7 μm	228 ± 55 μm	206 ± 11 μm	212 ± 56 μm	228 ± 57 μm	201 ± 51 μm
1ˢᵗ SiO₂	382 ± 9 μm	337 ± 117 μm	399 ± 10 μm	431 ± 89 μm	628 ± 251 μm	433 ± 176 μm
2ⁿᵈ SiO₂	929 ± 7 μm	503 ± 157 μm	521 ± 10 μm			

Table 6-12: *Layer thicknesses for the different test regions. The increased uncertainties visible for regions L2, L4, L4+L2 and L4+L3 are the result of the indirect measurement of the layer thickness through secondary ion velocity extrapolation*
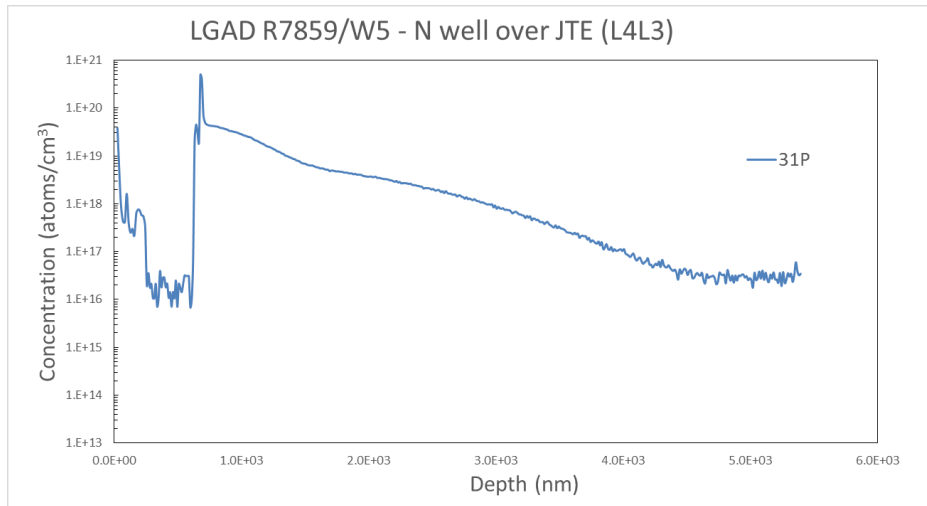
Figure 6.43: *Dopant profile of the JTE over the shallow n⁺ implant region.*

Finally, for the JTE over n⁺ shallow region, a particular distribution is observed. The profile remains fairly stable at the initial stages and steadily decreases towards 3 μm (*Figure 6.43*). Such a behavior is the result of the combination of a very high concentration shallow implantation for the n+ region and a highly diffused n implant of the JTE region.

To conclude, measurements performed on the LGAD test structures prove a good understanding of the technology with a high production yield. The diffusion depth of the shallow implant is larger than expected, while the multiplication region concentration in the section under the contact electrode can be adjusted to a slightly higher value for a better gain ratio.

6.6.4.5   *The Gallium Multiplication Region Test Run*

In several studies (see section 6.10) a dopant removal process has been recorded for boron implanted sensors. In an effort to increase radiation hardness and treat this effect, a special production run was introduced where the boron implant of the multiplication region was replaced by gallium. Being the third element of the boron group, it has an atomic number of 31 and presents 3 electrons on its outer shell, making it an effective acceptor type dopant. In contrast, its high atomic mass in comparison to boron (69 vs 11), make gallium a much more difficult element for deep implantation. Several uses have already been demonstrated in semi-conductive photon detectors, where it plays the role of the main dopant [65].

In the implemented production, an implantation energy of 60 KeV with a dose of 1.4×10^{13} atm/cm² was used in an effort to reproduce the multiplication region dopant profile distribution, as established in *Figure 6.40*. This first trial run was delivered for testing and evaluation using the same method and test structures as defined for the previous production. Given the innovative nature of the production, a simulation was also carried out to further evaluate obtained measurements.
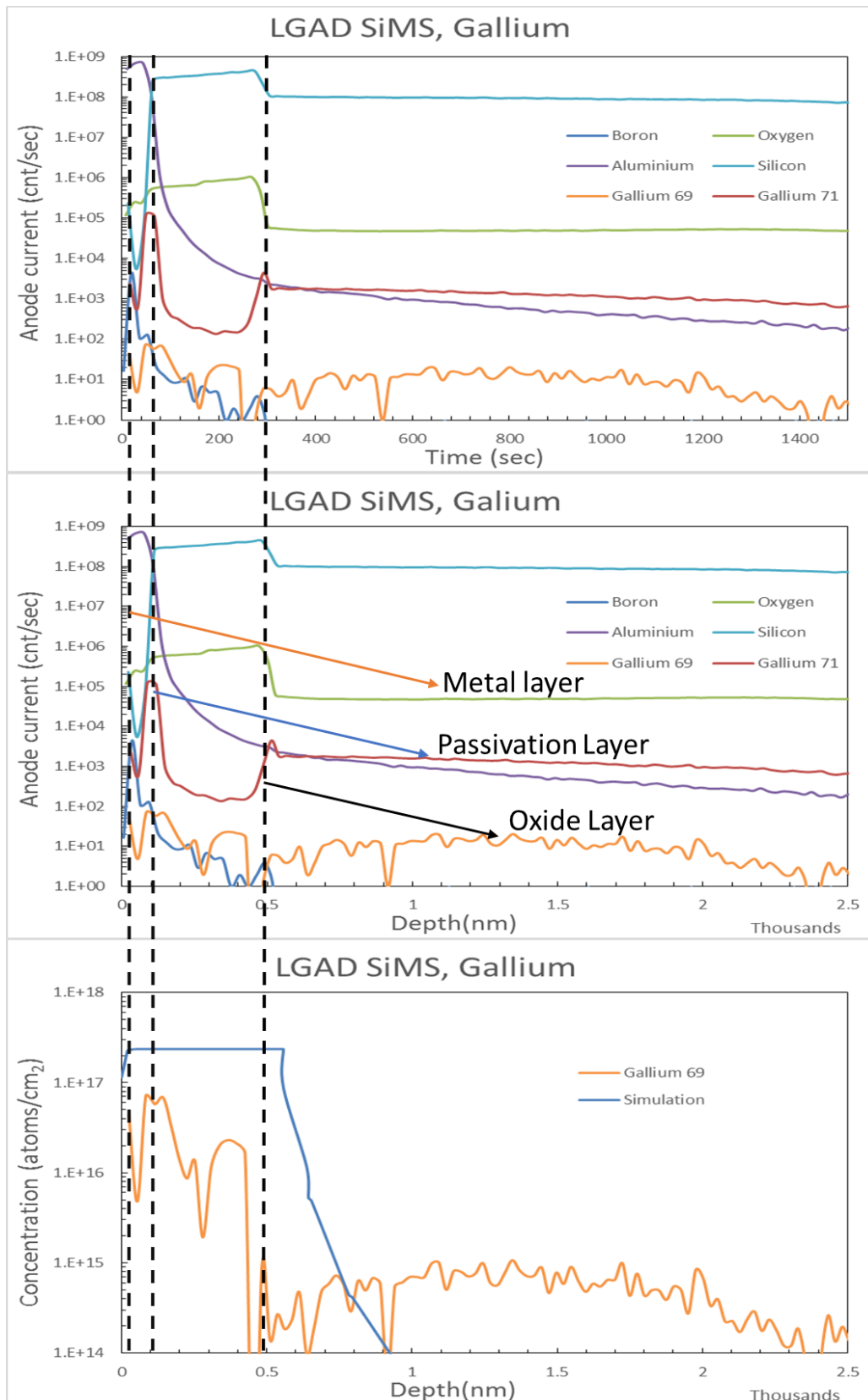
Figure 6.44: *SIMS measurements and simulations for a gallium multiplication implant. On the top plot the initial secondary ion intensities with respect to measuring time are presented. A depth calibration has been applied to the middle plot while, at the bottom, the simulated and measured dopant profile distributions are presented. Transition regions between different layers are marked with vertical lines. .*

The combined result is presented in *Figure 6.44*. Using the same approach as in the investigation of the boron production, at the upper part of the figure secondary ion intensities of monitored elements are presented with respect to measuring time. Oxygen and silicon serve as markers to define transition region from any silicon dioxide to the substrate while, as usual a metal layer was deposited at the surface of the sample before measurement. Both gallium isotopes are monitored in an effort to increase precision. However, it becomes clear that no sufficient amount of dopant can be found within the silicon substrate. Comparison with the simulated dopant profile (bottom plot of *Figure 6.44*) confirms that most of the implanted gallium is actually situated in the oxide layer on top of the silicon. In this region, because of the lack of calibration targets, SIMS cannot provide an accurate concentration estimation.

To understand the effect one need to examine closely the fabrication process. At first, the increased mass of the gallium atom with respect to boron, requires a higher implantation energy in order to achieve same penetration depth. Since gallium diffuses more in silicon than boron (9×10^{-12} cm²/sec vs 2×10^{-13} at 1100 ^{0}C), a compensation effect is possible. Because of the nature of the diffusion process, such an effect cannot occur. As demonstrated in the previous section, in LGAD standard production, activation is performed through thermal oxidation. In such a case the first layers of the silicon substrate will be transformed to SiO_2 and implant in this region will, to an certain level, be carried out to the final developed oxide. The positive elements of this process are an enhanced diffusion under the oxidizing region and a possible move of implant from the final oxidized region back to the substrate, depending on the segregation[h] value. For gallium, the positive segregation value ensures this last effect [55].

In spite of all these compensation mechanisms, in this case, the initial penetration depth is so shallow than none of the three effects (higher gallium diffusion speed, enhanced diffusion under oxidation, positive segregation) can transfer or diffuse fast enough the implant. As a result, all implanted gallium is found outside of the final active region and no multiplication can be observed.

6.7   Sensor Electrical Characterization

After production and process quality evaluation, electrical characterization is the final phase of sensor testing before interconnection with a readout electronics ASIC. In this section, the designs implemented in the common active edge pixel run presented in section 6.5 are being tested. Through the multitude of delivered sensors, a representative sample is selected to estimate design viability and define possible improvements or technology drawbacks.

Electrical characterization can reduce to two essential measurements. A bias voltage vs current measurement allows to define the depletion voltage, the level of leakage current and the break down voltage. In a general manner, one would require the smallest depletion voltage, to have a large possible operation range and also limit the dissipation power from high voltage power lines. The leakage current is the amount of charges per second generated by a fully depleted detector when no external excitation is provided. Since for silicon detectors the interest is to increase sensitivity, leakage current is always required to be the smallest possible. Since this corresponds to the number of electron-hole pairs intrinsically produced by the detector, if it is significant it will introduces noise to readout electronics. As a result, distinguishing signal induced by low energetic particles from the background is rendered more difficult. Finally, the breakdown voltage corresponds to the potential value for which the electrical field within the detector becomes so high that the structure operates in avalanche mode. In such a regime no energy linearity can be achieved and if the filed increases, the sensor will adapt a resistive behavior.

---

[h] The segregation coefficient k is defined as the ratio of an impurity within a crystal in the solid phase to that in the liquid phase

As a general trend, breakdown voltage is also required to be as high as possible. In an irradiated sensors defects are introduced and the performance decreases. To recover efficiency, an increase is needed to operating voltage. Therefore, it has to be assured that even after heavy irradiation with an increased biasing voltage, the breakdown value is sufficiently higher to allow stable operation.

Measurements are conducted in a clean room environment with the use of a probe station (*Figure 6.45*). Sensor biasing is performed using a low impendence probe while current is measured thought the copper conductive base chuck.
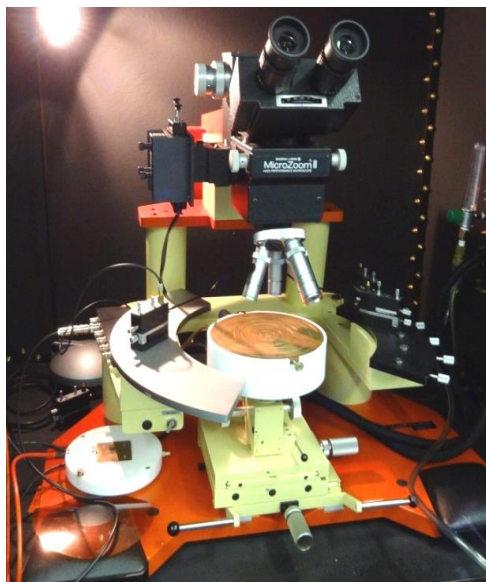
Figure 6.45: *Measuring probe station with an attached optical microscope and a conductive copper chuck. The needle probe and high precision mechanical base is also visible at the left side of the picture.*

To evaluate the influence of the design variations, all implemented variants were measured for thicknesses of 100 μm and 150 μm (*Figures 6.46 and 6.47*). All structures present leakage current in the order of 10^{-8}A with very low biasing voltages (< 10V). For both thicknesses, the most stable implementation is the design including only a bias rail. The breakdown voltage in both cases exceeds 100V, with the 100 μm thick structure being somehow more stable. The implementation with no edge structures behaves surprisingly stable, with breakdown voltages of 120 V and 70 V for the 100 μm and 150 μm production respectively. Finally, the structure including a guard ring, either in the guard ring plus bias rail implementation or in the guard ring only design, are the least stable structures. In particular, the design with the more elaborate edge structures seems to behave the worst in both cases, with increased leakage current and very low breakdown voltage.

A possible explanation for this erratic behavior can reached by considering the particularities of the corresponding production flow. The initial conclusion demonstrated is that completely active edge sensors with no edge structures are possible. Sidewall implantation implemented in this process can successfully contain the electrical field in the sensor interior and avoid breakdown. The more stable behavior of the bias rail structure is somehow expected since local inhomogeneities are evenly distributed through the bias grid while, its presence at the sensor edge further contributes to sustain lower field values at the edge region. On the same logic, one would also expect for structures with a floating guard ring as well as those with bias rail and guard ring, to present an equivalent behavior but this is not the case.

The effect can be explained when considering the minimum distance between different edge structures in all cases. In the case of a bias rail only implementation, minimum distance between consecutive structures is at 16 μm. For the design with no edge structures, this distance becomes

45μm, corresponding to the distance of the last pixel from the detector edge. However, for the designs with a bias rail and a guard ring or with the one with only a guard ring, minimum distance drops to 5 μm and 6 μm respectively. This distance corresponds to the region between the floating guard ring and the bias rail in the design with both edge structures whereas, for the guard ring only design it represents the distance between the last pixel and the guard ring. A 5 – 6 μm distance between successive implantation is small enough to allow for charge propagation between the structures when the field increases. If the p-spray implantation is not high enough in the interpixel region, there is no effective barrier to avoid charge propagation between different structures. An inconsistency at one point of the periphery will quickly create a high electric field that will propagate to the guard ring or bias rail and through them, to the entire sensor.
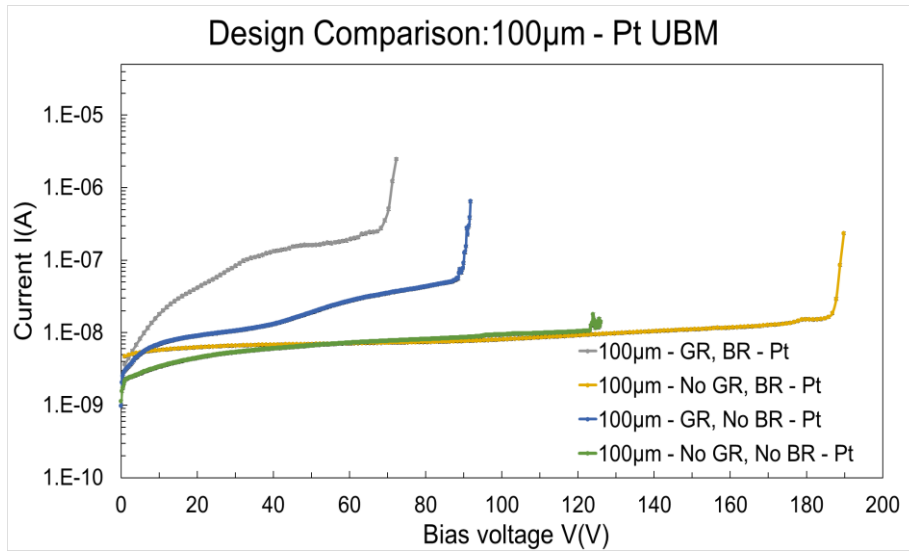
Figure 6.46: *Leakage current vs bias voltage for all implemented design variations at a 100 μm wafer thickness*
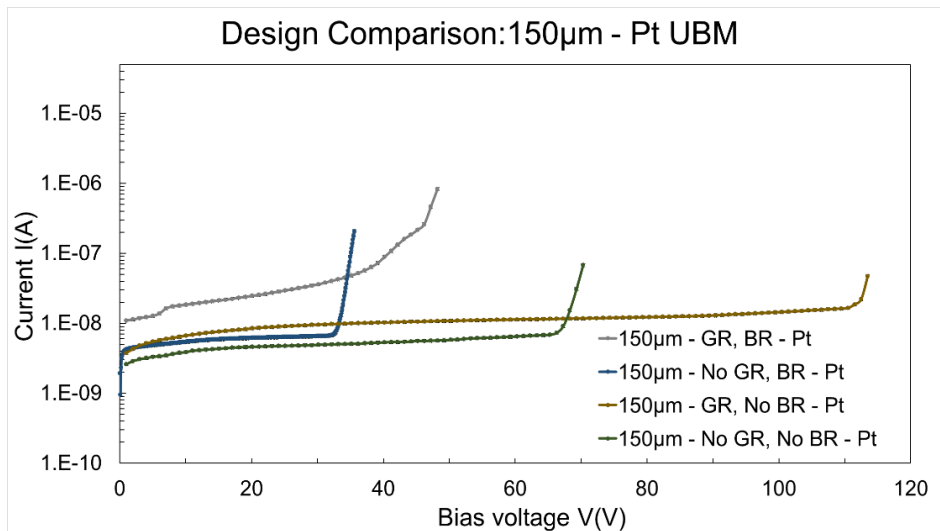
Figure 6.47: *Leakage current vs bias voltage for all implemented design variations at a 150 μm wafer thickness*

Concerning the more stable behavior of the 100 μm thick wafers, this is attributed to the specific edge implantation technique. Since sidewall doping is performed through ion bombardment in quadrants, if the incidence angle is kept the same in the two thicknesses, the sidewall dopant distribution is not equal. At a 100 μm, the ions can penetrate until the end of the trench and implant the total

length of the sidewall. When passing to 150 μm thickness, either an incidence angle recalibration is necessary or the sidewall is not uniformly implanted. Even after this recalibration, it is still possible that portions of the edge region towards the end of the trench present inconsistences.

6.8   Under Bump Metallization (UBM) Influence on the sensor behavior

6.8.1   Introduction

To interconnect the sensor to the read-out ASIC, an array of connections need to be made, one for each individual pixel. These vertical connections need to ensure electrical conductivity, to extract the signal as well as mechanical stability and oxidation resistance. The sensor and read-out ASIC are aligned and placed the one on top of the other with their front sides faced. Depending on the connection technology chosen, the chips are then fused together either by pressure or by a combination of pressure (0.5-1 Pa) and temperature (~250 °C) exposure. Most commonly, small solder balls are deposited in each pixel, at the interconnection point. Subsequently, the sensor and ASIC are brought together and through high temperature exposure, the solder fuses the two dices together.

The interconnection point needs to have a good electrical conductivity, resistance to oxidation and provide an adhesion surface for the soldering pad to be placed upon. Unfortunately, aluminum which is the last layer of most current sensor production, does not provide these properties. It can immediately oxidize when exposed to normal atmosphere, forming an insulating oxide that need to be scrubbed. Furthermore, it does not provide the proper solder adhesion and it is not suitable for chemical processing. The problem is treated by developing a special pad at the interconnection point, called the UBM (Under Bump Metallization) through lithographic processes and sputtering *(Figure 6.48)*.

The UBM must provide a low resistivity connection to the aluminum layer below as well as to the solder bump that will be placed on top. It needs to hermetically shield the aluminum layer from the environment to prevent any oxidation and to establish a good adhesion both to the metal layer and the surrounding passivation. Finally, it serves as a barrier, stopping diffusion of other metals or foreign elements to the substrate and as a chemical seed for the soldering process [66]. To achieve all these properties, several layers of different metals are used in the UBM formation. Earlier deposition techniques used lead-copper [67] combinations. This is a proven technology, also used for all interconnections of the current ATLAS pixel detector. Since UBM deposition accounts for a large portion of the cost of a sensor wafer, efforts are under way to develop more cost effective solutions, while new environmental standards prohibit the use of lead in electronics manufacture.
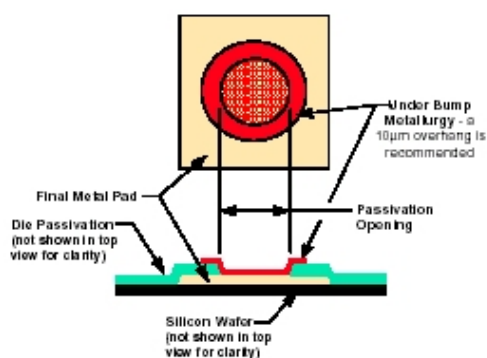
Figure 6.48: *Structure and placement of the UBM on a silicon wafer [66].*
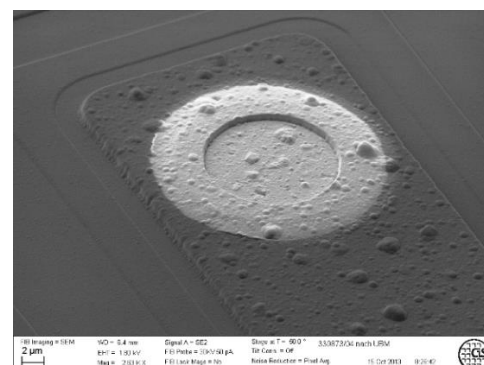
Figure 6.49: *STM photo of a NIAu UBM deposited on a pixel cell. The edge of the actuve region is visible while the metal layer protrudes from the wafer surface [68].*

A new technique is currently applied for UBM deposition, using a succession of Titanium, Nickel and Gold layers. Typical layer composition consists of 40 nm of Titanium, used as adhesion layer, 200 nm of nickel as the solder adhesive and finally 40 nm of gold to prevent oxidation. Typical structure height is approximately 300 nm, while it overshoots the open metal pad by 3-4μm extending over the passivation layer (*Figure 6.49*). Although a photolithographic process is generally required, a variation of this technique has also been developed in order to bypass this step. In this approach, nickel, deposited after the titanium layer, can be processed through an electroless technique, requiring neither vacuum nor photosensitive masks. Using an auto-catalytic chemical reaction, nickel alloy bonds directly to the metal substrate without requiring and electrical current or mask like electroplating and sputtering techniques [69].

6.8.2   The Discontinuity Effect

Although the use of this technique is already in place for current sensor production, it has been observed that post-UBM- deposition I-V curves demonstrate discontinuities close to the sensor depletion voltage value. This effect, presenting in the form of a step on the I-V curve, results to an instantaneous 40 % increase of the sensor leakage current (*Figure 6.50*). Nevertheless, such behavior was never demonstrated with the classic Pt deposition technology.

Segment	Initial Temp. (ºC)	Final Temp (ºC)	Rate (ºC/min)	Rate (ºC/hour)	Time (min.)
Gas out	20	20	0	0	60
Ramp-Up	20	180	5	300	32
Anneal	180	180	0	0	varies
Ramp-down	180	20	-5	-300	32

Table 6-13: *Specifications of the thermal cycle involved in each annealing step.*

To treat the effect, a series of thermal treatment steps have been applied and electrical measurements were conducted after each process. Using a closed tube furnace, consecutive temperature exposure steps were applied at 180⁰C for three different time intervals. The temperature point is chosen at a regime where it would could not pose any threat to the integrity of the final sensor aluminum metallization layer. Thermal treatment takes place in an Argon atmosphere to avoid any oxidation with ambient oxygen or humidity. Furnace interior is composed of silicon carbide in order to prevent gas releases from molecules trapped within any metal or ceramic lattice. Actual thermal cycle with corresponding ramping steps is presented in the following table and is kept close to actual production parameters (*Table 6-13*). Test structure is an IBL standard FE-I4 [70] compatible pixel matrix of n-in-n type, treated with NiAu UBMs at the final step.
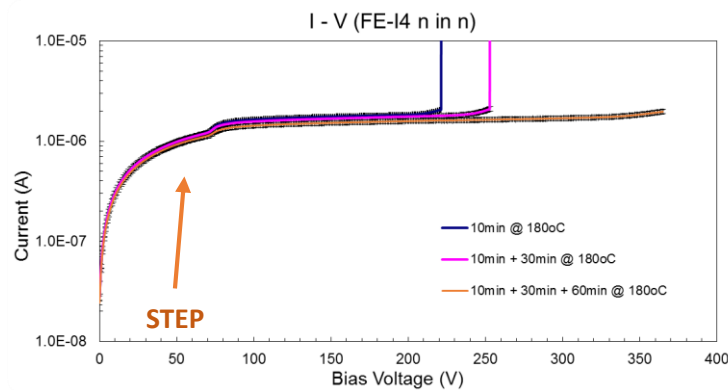
Figure 6.50: *Voltage-current curve of the tested structure after different thermal annealing. An abrupt discontinuity is apparent at the edge of depletion, while the curve turns smoother with every treatment step.*

6.8.3   Measurements and Results

I-V and C-V measurements are performed on the sensor after each thermal annealing steps and the basic quantities (depletion voltage, breakdown voltage and leakage current) are evaluated. To quantify the discontinuity effect in the I-V curve, the first derivative of the current with respect to bias voltage is computed (*Figure 6.50*). A clear peak is apparent at the exact voltage value were the discontinuity in the I-V curve is present. Given the delta-like form of the peak, a narrow width Gaussian approximation was applied and through a parametric fit the width, the maxima and the position are evaluated (*Table 6-14*). Depletion voltage is evaluated by capacitance measurements in the three basic measuring frequencies (*Figure 6.51*) of 10kHz, 50kHz and 100kHz and final depletion voltage value is extracted as a combination of these there individual measurements.

Treatment	*dV/dI* (V/A)	*Step Voltage* (V)	*Depletion Voltage* (V)	*Breakdown Voltage* (V)
10min 180oC	29.32 ± 0.88	73.58 ± 0.88	87.61 ± 4.73	221 ± 1
10min + 30min 180ºC	25.23 ± 0.95	73.65 ± 0.09	84.45 ± 4.87	252 ± 1
10min +30min + 60min 180ºC	13.95 ± 0.49	74.09 ± 0.10	87.39 ± 4.71	364 ± 1

Table 6-14: *Evolution of the sensors characteristics with respect to the thermal cycle.*

Although thought the consecutive thermal steps, the maxima of the derivative is reduced, the width as well as the mean position are not affected. Furthermore, its presence exactly before the structure's depletion point, suggest a charge accumulation under the UBM surface. The intrinsic characteristics of the structure (depletion voltage and leakage current) are unaffected while the breakdown voltage evolves towards higher values. In *Figure 6.52*, the evolution of these quantities is presented as a function of the total thermal exposure time. A clear decrease can be seen in the peak value of the first order current derivative with respect to annealing time increase, suggesting a beneficial effect. This work is subject to publication.
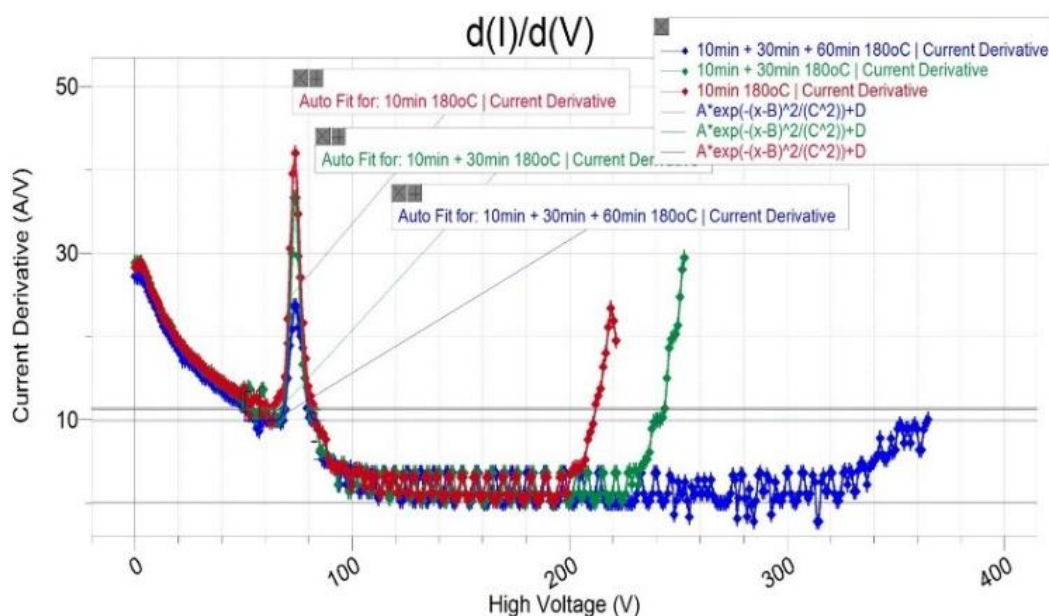
Figure 6.51: *dV/dI curve after various thermal treatment steps. The discontinuity effect is present at the same voltage value whereas the intensity decreases after each thermal step. A narrow width Gaussian approximation is followed to describe a delta-like potential corresponding to the chemical potential barrier hypothesis. The parameters extracted by the fit indicate the presence of the barrier at the point of depletion, while the width, peak position and width remain uniform among all fits*
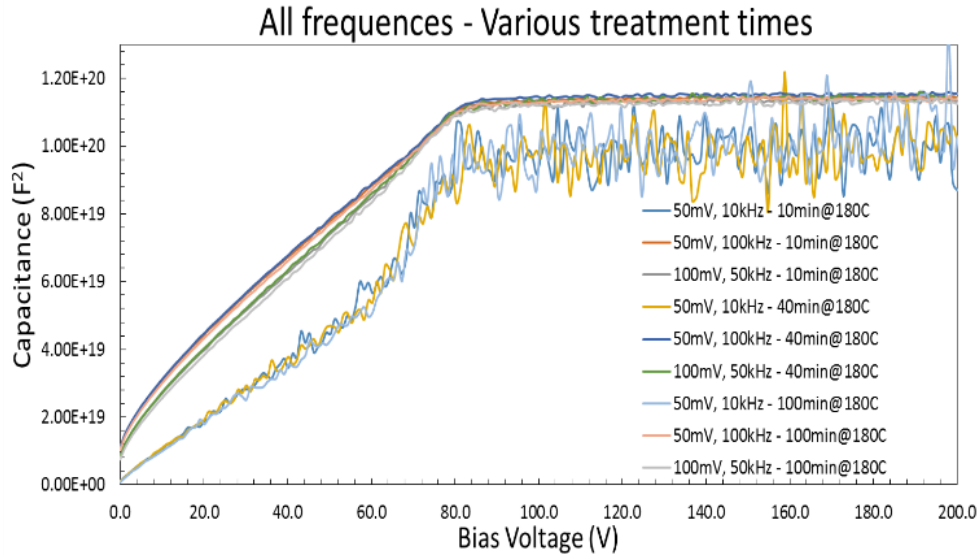
Figure 6.52: *Capacitance measurement for the three standard frequencies and voltages in the probed sensor. The curves do not present any alteration with respect to different annealing times. The inverse square of capacitance is represented as a function of the bias voltage. Depletion corresponds to the point of slope change. In a completely depleted structure the capacitance becomes minimal and the slope becomes stable.*

6.8.4   Conclusions

In general, thermal treatment annealing improves the behavior of the structure by diminishing the effect. After a 100 minutes cumulative exposure at 180 C, the leakage current increase rate evolves from 2.9 µA/V to 1.4 µA/V, representing 20 % increase with comparison to the normal ramping region. The nature of this abnormality, presenting itself at the same voltage value regardless of the number of thermal steps, at the boarder-line of depletion, suggests the presence of a potential barrier. Charges are accumulated until the critical value is reached to overcome the potential, most possibly due to chemical potential differences between the conductive layers comprising the UBM column. A thermal exposure in this sense rearranges the atomic layers introducing a smoother cross-over. Further investigation and studies are needed for a comprehensive explanation.

Figure 6.53: Evolution of the depletion voltage, peak value and step voltage with respect to thermal exposure time. The depletion voltage and step voltage are unaffected but the peak values significantly decreases.

6.9   Irradiated doping profiles

6.9.1   Introduction

In order to understand evolution of the sensors characteristics in a radiation hard environment, irradiation experiments are conducted under various conditions. Selected samples are exposed to neutron and proton radiation in collaborating facilities and their behavior is studied with respect to received dose. Since protons and neutrons induce different damage effects on silicon, experiments with both kinds of radiations are conducted. Exposure to thermal neutrons can be performed at the research reactor of the Jozef Stefan Institute in Ljubljana (JIS), while for proton radiation, the Karlsruhe Institute of Technology (KIT) in Germany is used, where protons are provided at the exit of a synchrotron accelerator.

Damage effects to any bulk material are proportional to the displacement Damage cross-section D. A more convenient equivalent quantity is the Non Ionizing Energy Loss factor (NIEL), which in its term, is also equivalent to material damage. Damage cross-section and NIEL factor values depend on particle composition and energy of incoming radiation. As a standard, one can consider the displacement damage caused by 1MeV proton radiation and any NIEL factors for other radiation type and energy can be expressed with respect to it. The hardness factor, or k, is the ratio between damage induced by other particle radiation with respect to the 1MeV neutron equivalent. In order to calculate exposure and dose values, fluences can be expressed in unites of neutron equivalent per unit of surface or n_{eq}/cm^2, while appropriate rescaling has to be applied in case of bombardment with other types and energies of particles [71].

In a first approximation, ionization radiation damage is not expected to change total dopant concentration within the detector nor its distribution, but rather affect the electrical characteristics of the device. Crystal lattice damage introduces interstitials and electron traps affecting charge propagation through the substrate. Furthermore, radiation damage can affect the way the dopant is integrated within the silicon matrix, rendering it electrically inactive. Complex defects can capture drifting electrons towards the anode, reducing charge collection efficiency. In an extreme condition, a high defect concentration in the substrate can result in a device that is no longer functional or cannot be depleted. Although defects may be of different nature (interstitials or vacancies), they can mostly be considered as p-type and in extreme conditions a type inversion for n-type substrates is observed.

Production	Imp. Energy	Imp. Dose	Resistivity	Thickness (µm)
n-in-n	130keV (100nm oxide) 240keV (100nm oxide)	$10^{15}cm^{-2}$	0.25kΩ·cm - Cz	380µm
p-spray	90keV (300nm oxide) 90keV (300nm oxide)	$3\times10^{12}cm^{-2}$	2Ω·cm - Cz	380µm

Table 6-15: *Irradiated doping profile samples from the n-in-n and p-spray productions.*

To investigate active and total dopant concentration after irradiation, selected samples from the n-in-n, n-in-p and p-spray test productions where irradiated with 25.3MeV protons to expected HL-LHC fluences. In particular, selected diced SIMS samples, implanted with parameters close to those used in actual pixel production (*Table 6-15*), were exposed to 25.3MeV protons at the Karlsruhe Irradiation Facility (KIT) to a total fluence of $10^{16}n_{eq}/cm^2$. A stable flux of 2.5×10^{13} p/(s·cm²) was applied, while temperature was kept at a range between -28°C to -34°C through N_2 gas foam flushing. Given the fact that for 25MeV protons, the calculated NEIL is 2.5 times higher (*Figure 6.54*) than the 1MeV neutron standard, actual delivered fluence was 5×10^{15} protons/cm². A low temperature is essential not only for proper sample cooling to avoid any dopant diffusion, but also to control annealing processes of any formed defects. Since in HL-LHC conditions detectors will always remain at a stable temperature of -25 ^{0}C during their lifetime, it is imperative to simulate the same

conditions in order to assess correctly radiation damage effects. Dose evaluation was performed through nickel foil dosimetry. After irradiation all samples were stored to -25C until any radioactive activity was dissipated.
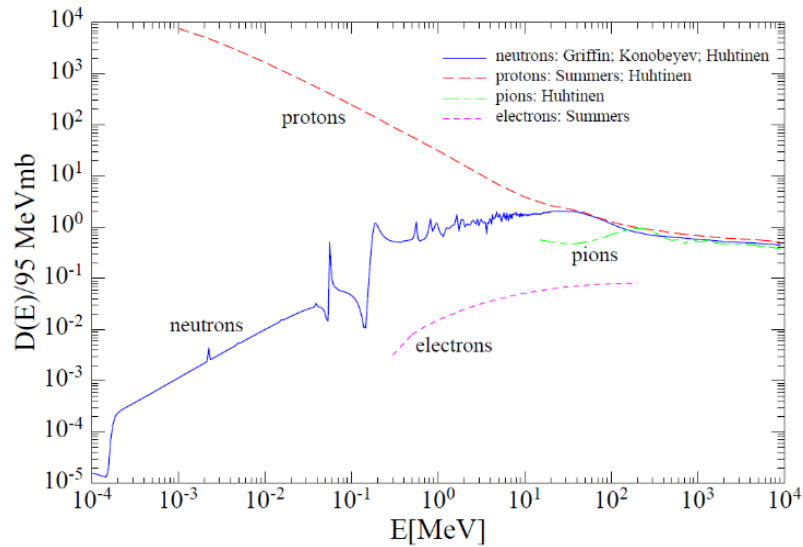
Figure 6.54: *Total Non-Ionizing Energy Loss for protons, neutrons electrons and pions. The ratio of 25MeV protons to the standard 1Mev neutrons is 1/2.5 [72].*

Because of the low temperature during irradiation, humidity condensation can appear on the samples surface. Oxygen in the conduced water is exposed to the proton flux and receives the same dose as the sample itself and becomes activated. In particular, through proton capture, it can transform to radioactive beryllium 7 through the following reaction (*equation 6-30*):

$$^6O + p \rightarrow \ ^7B \qquad (6\text{-}30\ )$$

Since half-life time for ^7B is 53.22 days, samples were kept in a sub-zero storage for a period of eight weeks for radiation levels to drop. Recurrent radio-protection controls resulted in an accumulation of room temperature exposure detailed in the following table (*Table 6-16*):

Date	Annealing time
24/10/14	17 min
29/10/14	1 h
10/12/14	15 min
17/12/14	1 h
18/12/14	15 min

Table 6-16: *Annealing time accumulation at room temperature*

To validate the hypothesis that no alteration is to be seen in the dopant profile, SIMS measurements where performed in the irradiated samples after complete deactivation of any radioactive residue. Results are compared with the ones obtained before irradiation and notably the dose integrals and the curve forms are being examined. To minimize treatment time and avoid any contamination, no oxide removal was performed and all measurements were done through the oxide layer.

6.9.2   n-in-n Irradiated Doping Profiles

The two irradiated n-in-n samples were measured and acquired data are superimposed to the profiles obtained before irradiation (*Figure 6.55*). The two series of measurements were conducted under different primary beam and calibration conditions. As a results, since there is no calibration

available for the silicon oxide region of the samples, only the silicon regions of the profiles are plotted. In an initial evaluation, no significant difference can be observed to the form of the distributions or to the total amount of phosphorous within the samples before and after irradiation. The systematic deviation of the non-irradiated profiles towards slightly higher concentration with respect to the irradiated ones is of systematic nature and uniform along the total distribution. This uniformity rather suggest a slight change of the calculated RSF than an actual profile modification and in any case is within the foreseen uncertainties in the concentration computation.
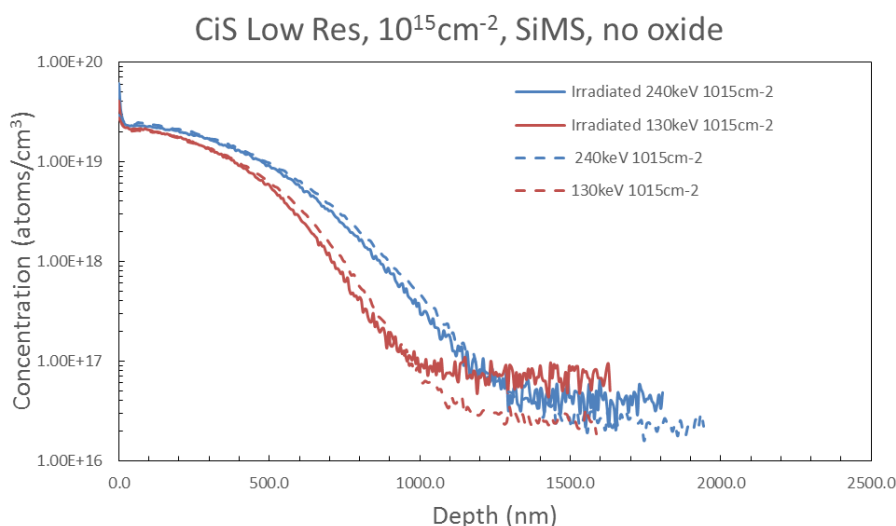
Figure 6.55: *Total dopant profile in the silicon substrate before and after irradiation. No visible alteration is observed.*

To better quantify any differences, dose integrals are calculated prior and after irradiation (*Table 6-17*). Since measurements do not always stop at the same depth, appropriate rescaling is applied. Given the 1 % quoted uncertainty in the most optimal conditions, no alteration of the total implant is visible. To conclude, total n-implant distribution is not affected by radiation exposure and SIMS dopant profiles remain identical.

Sample	Before Irradiation	After Irradiation
10^{15}cm^{-2} @ 130keV	8.39E+14 atoms/cm^2	8.38E+14 atoms/cm^2
10^{15}cm^{-2} @ 240keV	1.13E+15 atoms/cm^2	1.08E+15 atoms/cm^2

Table 6-17: *Calculated doses from SIMS measurements before and after irradiation. No difference within 1 % uncertainties is visible.*

6.9.3   p-Spray Irradiated Doping Profiles

Since no difference was observed with respect to phosphorous implanted wafers, the same hypothesis was tested in the second implant spices used in pixel production, boron. For the selected set of p-spray wafers, SIMS measurements were performed after irradiation and results are compared with ones obtained before irradiation (*Figure 6.56 and 6.57*). Although in both profiles no alteration on the form can be observed, there is an apparent slight fall in the concentration of the dopant inside the silicon substrate. This decrease is more prominent at the higher implanted dose where the difference between the two curves is outside estimated uncertainties in several regions. Any differences between the two profiles at the initial part of the curves cannot be taken into consideration since this region corresponds to the silicon oxide layer where no calibration is available. Actual profile comparison is performed after the first 500nm, immediately after the final implant peak marking the interface between silicon and SiO$_2$.
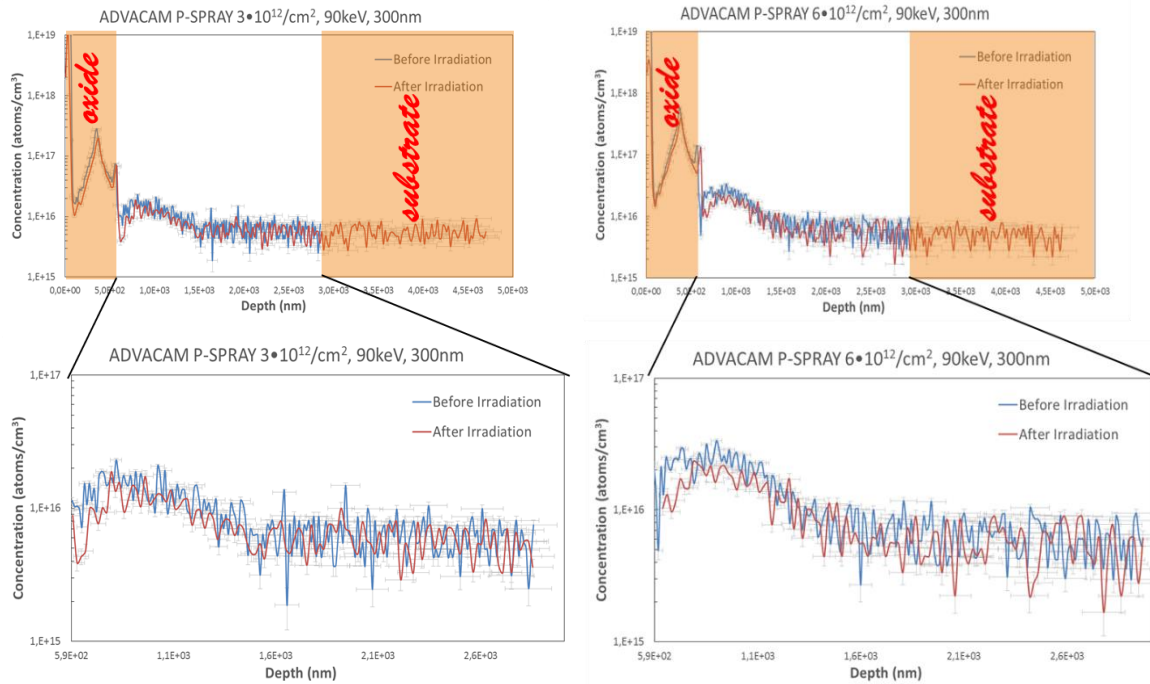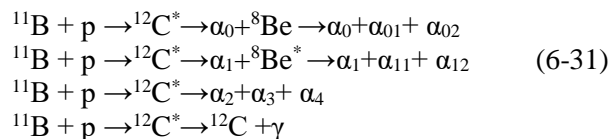
Figures 6.56 and 6.57: *Total measured dopant profile before (red) and after irradiation (blue) for the two p-sprat samples. A slight decrease is observed in the irradiated profile within the silicon region that for the highest dose is not compatible within uncertainties. Since SIMS calibration is not valid for the silicon oxide region, only the silicon region is compared between the two measurements. Measuring depth is normalized to the shallower measurement for dose integration*

By calculating the total implanted dose before and after irradiation, the profile difference becomes apparent (*Table 6-18*). Only silicon region is considered in this calculation while, appropriate rescaling is applied since measurements before and after irradiation did not extend to the same depth. An overall reduction of 15 % - 20 % in the total implant is observed in both samples. Nevertheless, uncertainties are quite high for the irradiated samples because of the coarse time step between consecutive measurements while resolution is degraded since the substrate is of the same type as the probed implant.

Sample	Before Irradiation	After Irradiation	% reduction
3×10^{12} atoms/cm^2 @ 90keV	$(1.95\pm0.97)\times10^{12}$ atoms/cm^2	$(1.66\pm0.65)\times10^{12}$ atoms/cm^2	15 %
6×10^{12} atoms/cm^2 @ 90keV	$(2.58\pm0.11)\times10^{12}$ atoms/cm^2	$(2.05\pm0.85)\times10^{12}$ atoms/cm^2	21 %

Table 6-18: *Calculated doses from SIMS measurements before and after irradiation for the p-spray samples. A 15 % - 20 % difference is visible while dominant uncertainties are introduced because of the coarse measuring time steps in post-irradiation measurements.*

An initial explanation of this decrease can be given by considering a boron nuclear reaction through proton capture. Available interaction channels are detailed in *equation 6-31*, with all passing through an exited ^{12}C nucleus. This intermediate nucleus will either further decay directly or through Beryllium, to a final product of three alpha particles, or can fall back to Carbon stable state by gamma radiation emission [73]. Independently of the interaction channel, at the final state, a boron decrease is expected accompanied by an increase in the carbon content and an increased helium concentration.

$$^{11}B + p \rightarrow ^{12}C^* \rightarrow \alpha_0 + ^8Be \rightarrow \alpha_0 + \alpha_{01} + \alpha_{02}$$
$$^{11}B + p \rightarrow ^{12}C^* \rightarrow \alpha_1 + ^8Be^* \rightarrow \alpha_1 + \alpha_{11} + \alpha_{12} \qquad (6\text{-}31)$$
$$^{11}B + p \rightarrow ^{12}C^* \rightarrow \alpha_2 + \alpha_3 + \alpha_4$$
$$^{11}B + p \rightarrow ^{12}C^* \rightarrow ^{12}C + \gamma$$

189

Reaction cross-section values diverge for each channel and heavily depend on the incoming proton energy. By approximating the sample as a uniform silicon target (the 500 nm oxide layer is sufficiently small with respect to the 360μm total thickness or the irradiated piece), for the incoming 25,3MeV protons, a stopping power of 10.85keV/μm is calculated at the initial part of the Bragg curve [74]. This translates to practically no energy loss of colliding protons until they reach the 600nm depth where the boron implant in the substrate is situated. Furthermore, their energy can be considered relatively constant within the first 5μm inside the target, which is the depth probed by SIMS measurements. Although no inclusive boron-proton fusion reaction cross-section information exist for projectile energies up to 25MeV, calculations are available up to the 10MeV scale (*Figure 6.58*. By extrapolating the tenancy observed in the 1-10MeV region up to 25MeV, we can assume a total cross-section of 7×10^{-2} b $\approx$ 70 mb [75, 76]. Although a complete dataset for all channels is not available, this estimation seems to be consistent when considering the available cross-sections for individual channels measures to 25MeV (*Table 6-19*).

Reaction	Cross-section	
	σ (mb)	δσ (mb)
$^{11}B \rightarrow {}^{7}Be$	20	3
$^{10}B \rightarrow {}^{11}C$	45	5
$^{10}B \rightarrow {}^{7}Be$	22	5
$^{10}B \rightarrow {}^{10}C$	0.1	estimated
$^{11}B \rightarrow {}^{11}C$	38	

Table 6-19: *Cross-sections of different proton capture reactions by boron measured and extrapolated from experimental data of the Landolt - Börnstein I/13 database.*
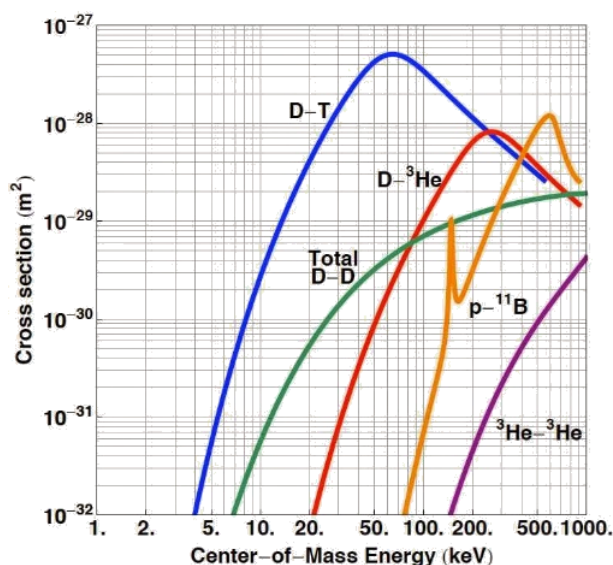
Figure 6.58: *Total cross-section of several fusion reaction as a function of the system kinetic energy at the center of mass. Considering the silicon target immobile and using the approximation that incident protons do not lose any significant amount of energy in the first few μm of silicon, the cross-section for 25MeV can be extrapolated at around 70 mb [77].*

Considering a total integrated proton dose of 5×10^{15}/cm^2, the total cross-section of 70 mb and the initial surface concentration of boron in the silicon bulk of 2.53×10^{12} atoms/cm^3, the surface concentration of reacted atoms can be calculated to 3.54×10^{13} atoms/cm^2. This is severely lower than the observed implant reduction and cannot account for the difference between the irradiated and non-irradiated profiles.

6.9.4   Conclusion

To conclude, a reduction of the total implant has been observed for the p-spray case in the order of 15 % within the silicon region. Although the possibility of a boron neutron capture nuclear reaction was considered, the corresponding cross-section cannot account for any significant dopant reduction. Uncertainties in the measured profiles can account for any differences while the poor resolution of the measurement because of the reduced initial concentration and the substrate type further degrades the result. A more accurate study with a higher implantation dose should be carried out to reach a final conclusion.

6.10   Development of a Data Acquisition System for Pixel Detectors

6.10.1   Introduction

In this section, work on the development of an innovative data acquisition system is presented, based on an open architecture. This project, initiated by the need for a new adaptable platform to test the in-house developed ASIC Omegapix, consist a contribution to the ATLAS pixel collaboration. The system is conceived to be compatible with a wide variety of sensor technologies and ASICs, ranging from the ATLAS standard Front-End integrated planar pixel readout circuit (FE-i4) to CMOS applications and LGAD sensors.

The difficulty of acquiring additional read-out systems for standard sensors (the current USB-PIX 2.0 system [78] is no longer available with the 3.0 version in development stage) and the high cost of commercially available solutions, have forced the pixel group in the recent years to increase efforts for an innovative data acquisition system development. Implementations already taking advantage of commercially available components have been presented [79], focusing on the FEI4 development. In that context, and using readily available components, a generic approach was selected to allow for easy and fast implementation with maximum compatibility.

6.10.2   System Base Board – SPEC

In every data acquisition system a direct communication bus in needed with the custom read-out ASIC, issuing the necessary operation commands and ensuring a direct memory access for analysis algorithms and data storage. This function, widely implemented through the FPGA technology, allows fast and easy adaptability to any electronic environment [80]. As a system base, a CERN developed, PCI Xpress board was used, equipped with a Xilinx Spartan 6 FPGA and 2Gbit of DDR3 random access memory. The card incorporates a 4 lane PCIe 2.0 interface to communicate with a standardized personal computer with no additional hardware requirements.

The so-called SPEC card [81] (*Figure 6.59*) was developed as an open hardware project, coupled with an internal FMC connector, controlled by the FPGA circuitry. Connectivity is assured by the 34 available differential pairs, allowing a wide range of application via additional daughter boards. The board also provides a 12V power output supporting up to 2A for development flexibility. FPGA input signals are fixed at 2.5 V with no alteration possible. A JTAG, USB and SATA interface is provided while the maximum communication bandwidth is at 4Gbit/sec.

Communication with a specific read-out ASIC is nevertheless not possible out-of-the-box, because of the different signal levels and protocols used by each technology. In addition, although with a customized firmware one would be able to manage and record data, the FPGA would also have to accept external triggers or additional commands to imitate data tasking. Finally, several ASIC designs couple power lines to the data bus. Such lines need to be isolated to avoid damage to the processing FPGA.

Figure 6.59: *The Simple FMC carrier (SPEC) card with the PCI press interconnection and the Xilinx FPGA [81].*

6.10.3   The Multi-Level Interconnection Board (MLIB)

An interconnection board had to be designed, assuring the maximum compatibility. Taking advantage of the full communication potential, it was decide to design a board with the maximum amount of I/O lines available, with individual line interrupts and direction assignement. In terms of mechanical specifications, it should not exceed the predefined space on the card for a daughter board, facilitating mechanical connections. Electrical requirements were defined in a manner that no external powering would be necessary while, the board would be adjustable and reprogrammable during operation, not requiring any kind of manual interventions. Finally, all connectors and other components needed to be as generic and easy to find as possible.
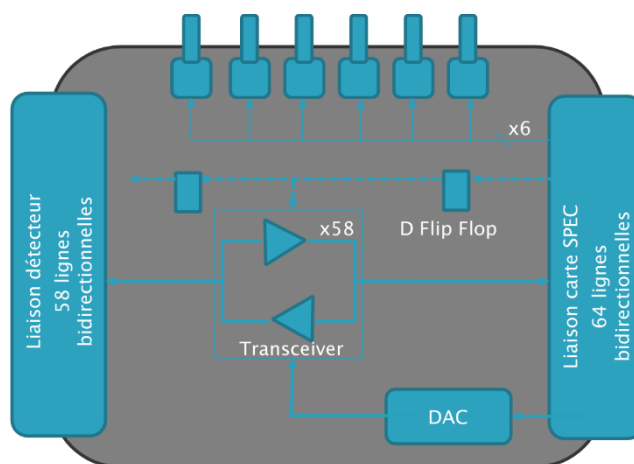
Figure 6.60: *Logic diagram of the MLIB card.*

With this set of requirements, a card was designed using 58 of the available communication lines. Multi-level bi-directional programmable transceivers were placed in each line, assuring operations in a signal level varying from 0.2 to 5.5 V. They also provide isolation capability to treat the issue of power return present in several technologies. An autosense function is integrated to allow automatic determination of the communication direction.

To adjust signal level in a continuous manner, an analog to digital converter was used, issuing relevant signals to the transceivers. Additional on-board powering for amplification and filtering was also added. Sacrificing the minimum number of available lines for internal programming, a serial interface was introduced though the use of consecutive D-type edge Flip-Flops. Six trigger

inputs were also foreseen, compatible with the NIM and TTL standard through software selection. Passive FPGA protection was added as well as adequate signal filtering. Flat-band HE10 standardized connectors were installed for ASIC communication and standard coaxial inputs for the trigger channels. A logical diagram of the design is presented in *Figure 6.60*.

Given the small available footprint, only surface mount components were used while, a thirteen level printed circuit board was necessary to accommodate all required routing. Production was completed at CERN with the first samples showing good performances (*Figure 6.61*)

Figure 6.61: *Front and back view of the completed MLIB daughter card.*

Although the use of the high –end silicon polymer capacitors was initially foreseen, due to spatial constraints, they were replaced with ceramic technology surface mount capacitors. However, due to their small size, the corresponding equivalent series resistance is increasingly high (>25 Ohm), inducing oscillations to the amplifier circuitry. Replacement of the filtering capacitors treated the issue but a technology improvement is foreseen in a next iteration.

6.10.4   Conclusion

A new, adaptable system has been designed and produced, compatible with a wide range of readout technologies and implementations. Based on commercially available products, it includes the minimum amount of custom made parts. Initial results demonstrate good functionality while fabrication issues are addressed and a new revision is planned.

6.11   Conclusions on Pixel Development

In this chapter, a complete and comprehensive approach in silicon pixel sensor development has been presented. Treated issues cover the hole extend of the conception process, from simulation and design to quality and production testing, electrical characterization and interconnections, radiation damage effects and data acquisition systems.

On the simulation domain, a complete 3D process simulation of the IBL design was implemented. A 0.4 μm lateral diffusion overshooting the metalized electrode was observed, resulting to possible field non-uniformities and distorted dynamic lines. This result was implemented to the four design variant introduced in the multi-project, active edge sensor production. Four edge geometries were introduced in the sensor production, with thinned dead regions varying from 100 μm to 47 μm, including a variant with no edge structures.

An evaluation of the production was performed through Secondary Ion Spectroscopy Measurements and simulations while, a reference library to be used in defining fabrication process parameters was developed for the most common pixel implantation procedures:

For the n-in-n production, a good comparison of simulation versus SIMS measurement is performed for low and intermediate doses, whereas at high doses (10^{16} atoms/cm^2) implant diffusion model needs modifications to correctly describe binary interactions. For the 10^{13}@240keV sample, a possible implantation instability could account for the observed deviations. No difference in the final acquired doping profile is observed between high and low resistivity substrates, while an accurate oxidation simulation is needed for better precision, to account for the density and quality differences between wet and dry developed silicon dioxide.

For the n-in p production, a very good agreement between SIMS measurements and simulations was observed for the n-in-p production. The post implantation activation via oxide development improves the uniformity in the first silicon layers and the agreement with the simulations. A systematic deviation for doses of 10^{15}atoms/cm^2 was observed and can be attributed to instabilities during implantation process. Model validity extends up to 10^{16}atoms/cm^2, where a deeper profile than predicted is observed for the highest energy. In the n-in-p production, this systematic model disagreement appears in slightly higher concentrations because of the nature of the substrate that compensates partially the effect.

The p-spray implantation is of low energy and as a result, quite shallow. The major part of the dopant is situated under few μm of the silicon layer. This is the result of an active choice, since most of the charge propagation to neighboring pixels takes place at surface layers. In addition, a quite low dose is selected in order not to disturb the effective pixel diode. As such, it has to be several orders of magnitude less than the pixel implant itself. From a production process side of view, it is observed that a very large portion of the implant is within the secondary oxide. Because of the low energy and the thick screening layers, most of the original implant stays at the first layers of the substrate. Subsequent oxidation transforms these layers to silicon dioxide and transfers the majority of the dopant outside the substrate. This technique constitutes an engineering choice, one allowing only the smooth tail part of the profile distribution to remain within the final silicon region, in order to avoid abrupt changes of the electrical field within the sensor.

A new innovative detector technology was studied, the Low Gain Avalanche Diodes and a production evaluation was performed using the acquired experience in doping profile analysis. Measurements performed in the test structures prove the technology to be particularly robust. Nevertheless, the diffusion depth of the shallow implant is larger than expected, while the multiplication region concentration in the section under the contact electrode can be adjusted to a slightly higher value for a better gain ratio.

Separate attention given to the possibility of replacing boron implant by gallium for increased radiation tolerance LGAD productions. In the initial test run, no gallium implant was introduced within the active silicone region. In spite of compensation mechanisms, the initial gallium penetration depth is so shallow than none of the three effects (higher gallium diffusion speed, enhanced diffusion under oxidation, positive segregation) can transfer or diffuse fast enough the implant. As a result, all implanted gallium is found outside of the final active region and no multiplication can be observed.

Active edge sensors were characterized and designs with no edge structures or lower thicknesses were more stable. The depressed distance between edges structures present in certain designs is introducing instabilities due to crosstalk and charge sharing. In addition, the trench doping technique with the use of quadrant angles, behaves better at thinner substrates as it assures a more uniform doping of the trench wall.

A study of the Under Bump Metallization effect on the leakage current was conducted. Thermal treatment was found to improve the behavior of the structure by diminishing the effect. After a 100 minutes cumulative exposure at 180 C, the leakage current increase rate evolves from 2.9 μA/V to 1.4 μA/V, representing 20 % increase with comparison to the normal ramping region. The nature

of this abnormality, presenting itself at the same voltage value regardless of the number of thermal steps, at the boarder-line of depletion, suggests the presence of a potential barrier. Charges are accumulated until the critical value is reached to overcome the potential, most possibly due to chemical potential differences between the conductive layers comprising the UBM column. A thermal exposure in this sense rearranges the atomic layers introducing a smoother cross-over. Further investigation and studies are needed for a comprehensive explanation.

Irradiated n-in-n and p-spray dopant profiles were examined. A reduction of the total implant has been observed for the p-spray case in the order of 15 % within the silicon region. Although the possibility of a boron neutron capture nuclear reaction was considered, the corresponding cross-section cannot account for any significant dopant reduction. Uncertainties in the measured profiles can account for any differences while the poor resolution of the measurement because of the reduced initial concentration and the substrate type further degrades the result. A more accurate study with a higher implantation dose should be carried out to reach a final conclusion.

Finally, a new adaptable read-out system has been designed and produced, compatible with a wide range of technologies and read-out ASICs . Based on commercially available products, it includes the minimum amount of custom made parts. Initial results demonstrate good functionality while, fabrication issues are addressed and a new revision is planned.

6.12 References

[1]   L. Rossi, O. Brüning, "High Luminosity Large Hadron Collider; a description of the European strategy preparatory group", Technical Report ATS-2012-236, Geneva, August 2012

[2]   The ATLAS Collaboration, "Letter of Intent for the Phase-II Upgrade of the ATLAS Experiment", CERN-2012-022, LHCC-I-023, January, 2013

[3]   G. Kramberger et al., "Effective trapping time of electrons and holes in different silicon materials irradiated with neutrons, protons and pions", Nucl. Instrum. Meth. A481 (2002) 297-305

[4]   H.L. Malm, D. Litchinsky, C. Canali, "Single carrier charge collection in semiconductor nuclear detectors", Revue de Physique Appliquee, 1977, 12 (2), pp.303-310

[5]   The Atlas Collaboration, "The ITK Initial Design Review", October 2014, http://atlas.web.cern.ch/Atlas/GROUPS/PHYSICS/UPGRADE/PLOT-UPGRADE-2014-001

[6]   P.A Markowich, C.A Ringhofer, C Schmeiser, "Semiconductor Equations", Springer-Verlag, Wien/New York (1990)

[7]   H. M. Heijne, "The Use Of Semiconductor Imagers In High Energy Particle Physics", Proc. SPIE 0591, Solid-State Imagers and their Applications, 1986, doi:10.1117/12.952071

[8]   Stanford University, "Silicon Technology Simulation", http://www-tcad.stanford.edu/~prophet/display/tech.html

[9]   B. Streetman, "Solid-State Electronic Devices", 4th Edition., Prentice-Hall, 1995

[10] Optique pour l'ingénieur, "Fundamentals of Semiconductor physics - Energy Bands", http://www.optique-ingenieur.org/en/courses/OPI_ang_M05_C02/co/Contenu.html

[11] Wikimedia Commons, PN Junction Diffusion and Drift, April 24 2010, https://upload.wikimedia.org/wikipedia/commons/3/3e/Pn_Junction_Diffusion_and_Drift.svg

[12] Wikimedia Commons, Forward Biased PN Junction, September 17 2015, https://upload.wikimedia.org/wikipedia/commons/thumb/a/a1/Forward-Biased_pn_Junction.svg/1280px-Forward-Biased_pn_Junction.svg.png

[13] Wikimedia Commons, (September 27, 2009), Reverse-Biased pn Junction [Online]. Available: https://upload.wikimedia.org/wikipedia/commons/f/ff/Reverse-Biased_pn_Junction.svg

[14] OpenWetWare. (September 10, 2006), Real Diode [Online].Available: http://openwetware.org/wiki/Image:Realidiode.jpg

[15] R.U.Ayres, P. Frankl, H. Lee, N. Wolfgang, "Silicon & Semiconductors", January 25, 1995

[16] S. A. Nelson, "Axial Ratios, Parameters, Miller Indices", Tulane University, September 2011

[17] M. Benoit, "Étude des détecteurs planaires pixels durcis aux radiations pour la mise à jour du détecteur de vertex d'ATLAS", PhD Thesis, Université Paris Sud, 2011

[18] L.Rossi, P. Fischer, T. Rohe, N. Wermes, "Pixel Detectors", Springer, ISBN 1611-1052

[19] D. Pitzl, N. Cartiglia, B. Hubbard, D. Hutchinson, J. Leslie, K. O'Shaughnessy, W. Rowe, H.F.-W. Sadrozinski, A. Seiden, E. spencer, H.J. Ziock, P. Ferguson, K. Holzscheiter, W.F. Sommer, "Type inversion in silicon", Nuclear Instruments and Methods A, 311:98–104, 1992

[20] G. Davies et al, "A model for radiation damage effects in carbon-doped crystalline silicon", Semiconductor Science Technology, 1987

[21] B. Mac Evoy, G. Hall, K. Gill, "Defect evolution in irradiated silicon detector material", IC/HEP Imperial College, 8, 1995

[22] H. Feick, "Radiation Tolerance of Silicon Particle Detectors for High Energy Physics Experiments", PhD thesis, University of Hamburg, 1997

[23] H.J. Ziock, et al., "Temperature dependence of the radiation induced change of depletion voltage in silicon pin detectors", Nuclear Instruments and Methods A, 342:96–104, 1994

[24] E. Fretwurs et al., "Reverse annealing of the effective impurity concentration and long term operational scenario for silicon detectors in future collider experiments", Nuclear Instruments and Methods A, 342:119–125, 1994

[25] M. Moll, "Radiation Damage in Silicon Particle Detectors - Microscopic Defects and Macroscopic Properties", PhD thesis, DESY-THESIS-1999-040, December 1999, ISSN 1435-8085

[26] W. Shockley, "Currents to Conductors Induced by a Moving Point Charge", Journal of Applied Physics 9 (10): 635 (1938), doi:10.1063/1.1710367

[27] S.Ramo, "Currents Induced by Electron Motion", Proceedings of the IRE 27 (9): 584–585, (1939), doi:10.1109/JRPROC.1939.228757

[28] H. Spieler, "Semiconductor Detectors, SLUO Lectures on Detector Techniques", LBNL, October 1998

[29] P. D. Yoder, K. Gartner, W. Fichtner, "A generalized Ramo–Shockley theorem for classical to quantum transport at arbitrary frequencies", J. Appl. Phys., Vol. 79, 1998

[30] DECTRIS, "Hybrid Pixel", https://www.dectris.com/Hybrid-Pixel_Details.html#main_head_navigation

[31] SYNOPSYS® Inc., 690 East Middlefield Road, Mountain View, CA 94043, http://www.synopsys.com/tools/tcad/Pages/default.aspx

[32] SILVACO® Inc., 55, Blaise Pascal, 38330 Montbonnot, St. Martin, France, http://www.silvaco.com/products/tcad.html

[33] P.E. Cottrell, E.M. Buturla, "Two-dimensional static and transient simulation of mobile carrier transport in a semiconductor," Proceedings NASECODE I (Numerical Analysis of Semiconductor Devices), pp. 31-64, Boole Press, 1979

[34] K.M. Cham, S.-Y. Oh, D. Chin, J. L. Moll, "Computer-Aided Design and VLSI Device Development", Kluwer Academic Publishers (KAP), 1986. ISBN 978-0-89838-204-4

[35] Wikimedia Commons, Linear interpolation of J0 (basis set),June 2015,https://commons.wikimedia.org/wiki/File:Linear_interpolation_of_J0_%28basis_set%29.svg

[36] SYNOPSYS®, "Sentaurus Process User Guide", Version E-2010.12, December 2010L

[37] J. P. Biersack, L. G. Haggmark, "A Monte Carlo computer program for the transport of energetic ions in amorphous targets", Nucl. Instr. Meth., 174:257, 1980

[38] A. Fick, "On liquid diffusion", Poggendorffs Annalen. 94, 59 (1855) - reprinted in Journal of Membrane Science, vol. 100 pp. 33-38 (1995)

[39] B. El-Kareh., "Fundamentals of Semiconductor Processing Technologies", Kluwer Academic Publishers, 1995.

[40] F. Boucard, "Dopant diffusion modelling in silicon for shallow junctions processing", Phd. thesis, Louis Pasteur University, September 2003

[41] SILVACO Athena user's guide, http://ridl.cfd.rit.edu/products/manuals/Silvaco/athena_users1.pdf

[42] S. Eranen, J. Kalliopuska, R. Orava, N. van Remortel, T. Virolainen, "3D processing on 6in. high resistive SOI wafers: Fabrication of edgeless strip and pixel detectors", Nucl. Instrum. Meth. A 607 (2009) 85

[43] L. Zheng et al., "Electrical and transient current characterization of edgeless Si detectors diced with different methods", IEEE Tran. Nucl. Sci. 46 (2002) 1040

[44] B.K. Daas, M.M. Islam, I. A. Chowdhury, F. Zhao, T.S. Sudarshan, M.V.S. Chandrashekhar, "Doping Dependence of Thermal Oxidation on n type 4H SiC", Department of Electrical Engineering, University of South Carolina, 301 S. Main St, Columbia, SC 29208

[45] X. Wu, J. Kalliopuska, S. Eränen and T. Virolainen, "Recent advances in processing and characterization of edgeless detectors", Journal of Instrumentation, Volume 7, February 2012, http://stacks.iop.org/1748-0221/7/i=02/a=C0200

[46] M. Povoli et al., "Development of planar detectors with active edge", Nucl. Instrum. Meth.A 658(2011) 103

[47] A. Lounis, C. De La Taille, N. Seguin-Moreau, G. Martin-Chassard, D. Thienpont, et al., "OMEGAPIX: 3D integrated circuit prototype dedicated to the ATLAS upgrade Super LHCpixel project", Topical Workshop on Electronics for Particle Physics (TWEPP-09), Sep2009, Paris, France. pp.443-447, 2009

[48] R. F. K. Herzog, F. Viehboeck, "Ion source for mass spectrography", Phys. Rev. 76 (6): 855–856, 1949, doi:10.1103/PhysRev.76.855

[49] G. Stingeder, U. Traxlmayr, E. Guerrero, M. Grasserbauer, H. Pötzl, "Quantitative Distribution Analysis of Phosphorus with Sims in the Layer System SiO2/Si", 1986 MRS Spring Meeting

[50] Washington State University St. Louis, WUSTL Secondary Ion Mass Spectrometer, http://pages.wustl.edu/sims

[51] J.W. McDonald, A.V. Hamza, M.W. Newman, J.P. Holder, D.H.G. Schneider, T. Schenkel, "Surface charge compensation for a highly charged ion emission microscope", Ultramicroscopy 101 (2004) 225–229

[52] CAMECA SAS., IMS 7F Sewcondary Ion Mass Spectrometer, http://www.cameca.jp/product/ims7f.html

[53] C. W. Magee, W. L. Harrington, R. E. Honig, "Secondary ion quadrupole mass spectrometer for depth profiling design and performance evaluation", Rev. Scient. Instrum. 49 (4): 477–485, 1978, doi:10.1063/1.1135438. PMID 18699129

[54] The ROSE collaboration, "RD48 status report", CERN/LHCC, 39, 1997

[55] S. W. Jones, "Diffusion in Silicon", IC Knowledge LLC, 2000

[56] T. Aoyama, H. Tashiro, K. Suzuki, "Diffusion of Boron, Phosphorus, Arsenic, and Antimony in Thermally Grown Silicon Dioxide", Journal of The Electrochemical Society, 146 (5) 1879-1883 (1999)

[57] G. Fisicaro et al., "Dopant dynamics and defects evolution in implanted silicon under laser irradiations: a coupled continuum and Kinetic Monte Carlo approach", 2013, http://in4.iue.tuwien.ac.at/pdfs/sispad2013/4-1.pdf

[58] W. Treberspurg, T. Bergauer, M. Dragicevic, M. Krammer, M. Valentan, "Backside doping profiles of irradiated silicon detectors", 2013 JINST 8 P04019

[59] A. Vasilescu, G. Lindstroem, "Displacement damage in silicon, on-line compilation", http://rd50.web.cern.ch/RD50/NIEL/default.html

[60] N. Cartiglia, M. Baselga, G. Dellacasa, S.Ely, V. Fadeyev, Z. Galloway, S. Garbolino, F. Marchetto, S. Martoiu, G. Mazza, J. Ngo, M. Obertino, C. Parker, A. Rivetti, D. Shumacher, H.F-W.Sadrozinski, A. Seiden, A. Zatserklyaniy, "Performance of Ultra-Fast Silicon Detectors", 2013, ArXiv:1312.1080v2 [physics.ins-det]

[61] V. Greco, P. Fernández - Martínez, D. Flores, S. Hidalgo, G. Pellegrini, D. Quirion, M. Baselga, N. Cartiglia, G. Kramberger et al., "Silicon Devices Optimised for Avalanche Multiplication", 23 International Workshop on Vertex Detectors, PoS(Vertex2014)031

[62] G. Pellegrini, P. Fernández-Martínez, M. Baselga, C. Fleta, D. Flores, V. Greco, S. Hidalgo, I. Mandic, G. Kramberger, D. Quirion and M. Ullan, "Technology developments and first measurements of Low Gain Avalanche Detectors (LGAD) for high energy physics applications", Nuclear Instruments and Methods in Physics Research, vol. A765, pp. 12-16, 2014

[63] P. Fernandez-Martinez, D. Flores, V. Greco, S. Hidalgo, G. Pellegrini, D. Quirion, M. Fernandez-Garcia, I. Vila, G. Kramberger, "Low Gain Avalanche Detectors for high energy physics ", 10th Spanish Conference in Electron Devices (CDE), February. 2015

[64] G. Kramberger, M. Baselga, V. Cindro, P. Fernandez-Martinez, D. Flores, Z. Galloway, A. Gorisek, V. Greco, S. Hidalgo, V. Fadeyev, I. Mandic, M. Mikuz, D. Quirion, G. Pellegrini, H.F-W. Sadrozinski, A. Studen, M. Zavrtani, "Radiation effects in Low Gain Avalanche Detectors after hadron irradiations", 2015 JINST 10 P07006

[65] E. Golla, "Crystal Growth and Evaluation of Silicon for VLSI and ULSI", CRC Press, 2015, ISBN: 13:978-1-4822-3282-0

[66] flipchipsDOTCOM, "Under Bump Metallization (UBM)", Tutorial 11, http://flipchips.com/tutorial/process/under-bump-metallization-ubm/

[67] Internationales Wissenschaftliches Kolloquium, "International Scientific Colloquium Proceedings", September 2006

[68] CiS Forschungsinstitut für Mikrosensorik GmbH, Konrad-Zuse-Straße 14, 99099 Erfurt, Allemagne, http://www.cismst.org/

[69] R. Parkinson, "Properties and applications of electroless nickel", Nickel Development Institute, http://nickelinstitute.org/~/Media/Files/TechnicalLiterature/PropertiesAndApplicationsOfElectrolessNickel_10081_.pdf

[70] The ATLAS IBL Collaboration, "Prototype ATLAS IBL Modules using the FE-I4A Front-End Readout Chip", arXiv:1209.1906v1 [physics.ins-det] 10 Sep 2012

[71] H. Vernon Wong, B. N. Breizman, J. W. Van Dam, "Proton-Boron (p−B11) colliding beam fusion reactor", Institute for Fusion Studies, The University of Texas at Austin, Austin, Texas 7871

[72] A. Vasilescu, Fluence normalization based on the NIEL scaling hypothesis, 3rd ROSE Workshop on Radiation Hardening of Silicon Detectors, DESY Hamburg 12 – 14, February 1998, DESY-PROCEEDINGS-1998-02

[73] A. G. Ruggiero, "Nuclear Fusion of Protons with Ions of Boron", IEEE 0-7803.1203-l/93, 1993

[74] C. Labaune et Al., "Fusion reactions initiated by laser-accelerated particle beams in a laser-produced plasma", Nature Communications 4:2506 doi:10.1038/ncomms3506 (2013), http://arxiv.org/pdf/1310.2002.pdf

[75] S. Atzeni, J. Meyer-ter-Vehn, "The Physics of Inertial Fusion", International Series of Monographs on Physics, Oxford university Press

[76] S. Dubovichenko, A. Dzhazairov - Kakhramanov, "Study of the neutron and proton capture reactions $^{10,11}B(n,\gamma)$, $^{11}B(p,\gamma)$, $^{14}C(p,\gamma)$, and $^{15}N(p,\gamma)$ at thermal and astrophysical energies", http://arxiv.org/ftp/arxiv/papers/1405/1405.6295.pdf

[77] H.-S. Bosch and G.M. Hale, Improved formulas for fusion cross-sections and thermal reactivities, Nuclear Fusion, Volume 33, Number 12, http://iopscience.iop.org/article/10.1088/0029-5515/33/12/513/pdf

[78] SiLab, "The USB Pix readout system", http://icwiki.physik.uni-bonn.de/twiki/bin/view/Systems/UsbPix

[79] T. Heim, "A PCIe BASED Pixel Readout System", 2014

[80] C. Maxfield, "Programmable Logic Design Line, Xilinx unveil revolutionary 65nm FPGA architecture: the Virtex-5 family", May 2006

[81] CERN Open Hardware Repository, "FMC Projects, Simple PCIe FMC carrier (SPEC)", http://www.ohwr.org/projects/spec/wiki#Simple-PCIe-FMC-carrier-SPEC

7 Conclusions

In this thesis, the work performed on two domains, analysis of ATLAS data and development of silicon sensors for high energy physics, is presented.

The H→ZZ*→4l mode analysis of Run 1 data was detailed. Along Run 1, several methods aiming to the background estimation were developed, evolving with the accumulated statistics. These have been extensively discussed with a particular emphasis in the "Truth to Reco" unfolding method for electron background estimation. Although this was not the default method selected for the final result, derived background estimation was used in systematic uncertainty evaluation. Results are compatible with the nominal 3l+X method, with 10.36 expected background events in the 125±5 GeV mass region. For sub-channels with a sub-leading electron-pair (4e and 2mu2e), 14 events are observed with 4.08 expected from background. The fraction of the reducible background is estimated at 27%. Final analysis result, based on 4.8 fb^{-1} of √s=7 TeV (2011) and 20.3 fb^{-1} of √s=8 TeV (2012) LHC data demonstrated an excess of events with a significance of 8.6 standard deviations is observed, corresponding to a mass of m$_H$ = 124.3 GeV.

An observability analysis the bbH(→2γ) mode with ATLAS detector in HL-LHC conditions was presented. The analysis was performed for two distinct cases of instantaneous luminosity, corresponding to μ = 200 and μ = 140 values, assuming a total integrated luminosity of 3000 fb^{-1}. Using extrapolated performances for Phase II conditions and available truth level simulated samples, the sensitivity to this mode was proven to be weak: a significance of 0.22 (0.11) for μ = 200 and 0.24 (.13) for μ = 140 with TMVA (cut-based) selection was found, reflecting to a μ limit of ~ 4 (9) for a no diphoton mass- cut analysis approach. PU contamination, poor jet tagging implementation and fake jet→photon objects where primary sources of background contamination. Improvements in this area, combined with increased MC statistics and adapted event treatment would allow in the future to achieve a more precise and consolidated result.

Finally, work is presented towards the development of a highly granular and radiation hard pixel detector, capable of coping with the harsh Phase II conditions. An integrated approach is adopted, with contributions to all design and evaluation steps towards a completed sensor. An initial 3D simulation of the current ATLAS pixel sensor is performed and conclusions are applied to the design of active edge pixel sensors. Several different design variants are included, in an effort to further optimize geometrical efficiency, with inactive regions ranging for 100 μm to 47 μm form the sensor edge. To evaluate production quality, a reference library is subsequently created, combining test production wafers and simulations. Through comparison of SIMS results with simulated dopant profiles, the simulation tool is validates and production process characteristic features are identified. This experience is applied in the development of the innovative LGAD technology, including a Gallium doped test production. Sensor evaluation is competed with electrical characterization of the active edge designs, with implementation featuring no protective edge structures performing very well up to 150 V and leakage current in the order of 10^{-8} A. Towards a complete sensor assembly, UBM induced surface effects are studies and a thermal treatment process is proposed to correct the issue. Finally, radiation studies are performed in n and p dopant distributions and a universal data acquisition system is developed.

8 Annexes

8.1 bbH Analysis Variables Discriminating Power and Distributions

Reference		Middle		Low	
Variable	**Discrimination Power**	**Variable**	**Discrimination Power**	**Variable**	**Discrimination Power**
$m_{\gamma\gamma}$	0.13	$m_{\gamma\gamma}$	0.13	$m_{\gamma\gamma}$	0.12
$\eta_{\gamma2}$	0.11	$\eta_{\gamma2}$	0.12	$\eta_{\gamma2}$	0.11
$\eta_{\gamma1}$	0.11	$\eta_{\gamma1}$	0.11	$\eta_{\gamma1}$	0.11
η_{j2}	0.10	η_{j2}	0.10	η_{j2}	0.11
$\Delta R_{\gamma\gamma}$	0.10	η_{j1}	0.10	$\Delta R_{\gamma1j1}$	0.10
$\Delta R_{\gamma1j1}$	0.10	$\Delta R_{\gamma1j1}$	0.10	$\Delta R_{\gamma\gamma}$	0.10
η_{j1}	0.10	$\Delta R_{\gamma\gamma}$	0.10	η_{j1}	0.10
ΔR_{bb}	0.09	ΔR_{bb}	0.10	ΔR_{bb}	0.10
$P_T^{Quadrouplet}$	0.07	$P_T^{Quadrouplet}$	0.08	$P_T^{Quadrouplet}$	0.08
$P_T(\gamma_2)$	0.06	$P_T(\gamma_2)$	0.05	$P_T(\gamma_2)$	0.05
$Nb._{jets}$	0.02	$Nb._{jets}$	0.02	$Nb._{jets}$	0.02

Table 8-1: *Discriminating power across three scoping scenarios. Small variation can be noticed but the behavior remains stable across scenarios with noticeably very low discriminating power even for the most prominent $m_{\gamma\gamma}$ variable*
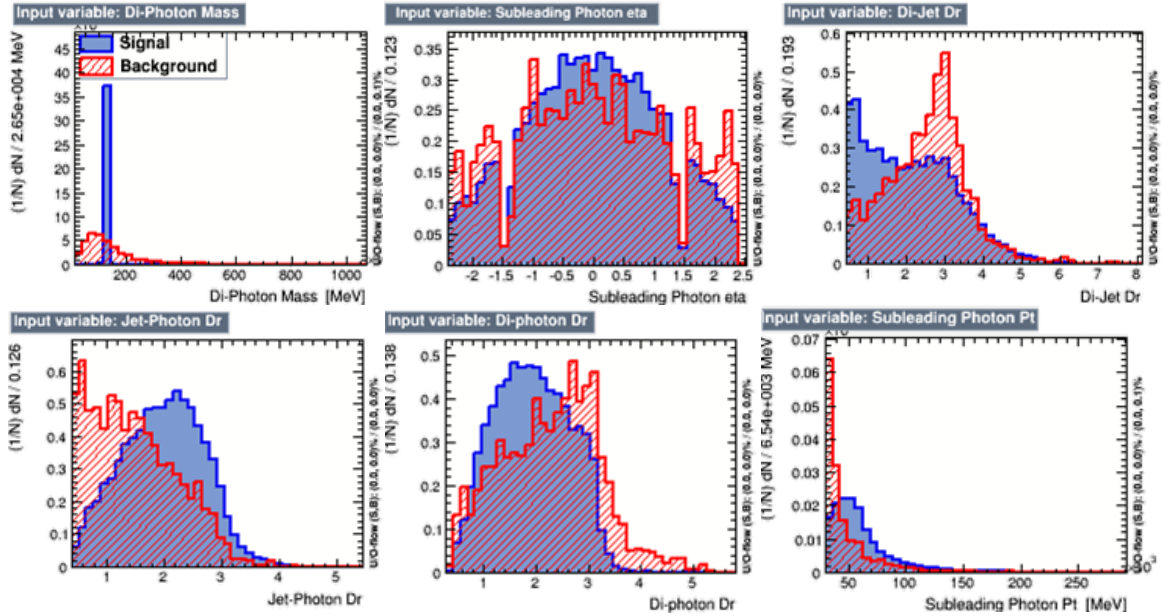
Figure 8.1: *Input variable distribution of the $\eta_{\gamma2}$, ΔR_{bb}, $m_{\gamma\gamma}$, $\Delta R_{\gamma\gamma}$, $P_T(\gamma_2)$, $\Delta R_{\gamma1j1}$ for the reference scenario at $\mu=140$. Blue area represent single region while red represents combined background. Plots are normalized to unity.*
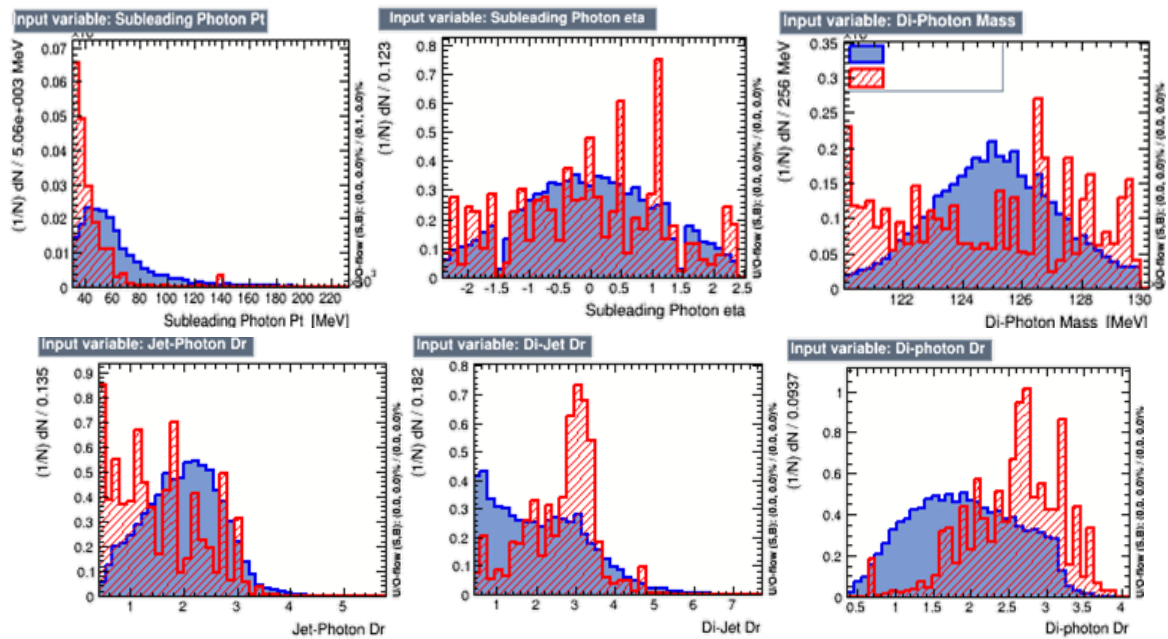
Figure 8.2: *Input variable distribution for di-photon mass cut preselection TMVA case of the $\eta_{\gamma 2}$, ΔR_{bb}, $\Delta R_{\gamma\gamma}$, $P_T(\gamma_2)$, $\Delta R_{\gamma 1 j1}$, $m_{\gamma\gamma}$ for the reference scenario at $\mu=140$.. Blue area represents the single region while the red is represents combined background. Plots are normalized to unity.*

8.2 The H(→bb)H(→γγ) mode

Given the bbH(→γγ) and H(→bb)H(→γγ) channel similarities in the final object pre-selection as well as the common physical backgrounds involved, an analysis consistency and benchmark test was performed for the HH case. Pre-selection process and applied frameworks were kept unaltered between the two channels since no difference is expected in the nature of the final quadruplet. A shift between signal and background definitions for bbH and HH samples in the TMVA input, in order to adjust the training for the di-jet resonant signal expected from thee Higgs decay, and a by default application of the 120 GeV < $m_{\gamma\gamma}$ < 130 GeV pre-selection cut where implemented. For the HH case, only the μ = 200 interactions per crossing was treated while input training variables were not specially optimized by probing all available quantities. Instead, same 11 most discriminant variables used in the bbH channel where introduced with the addition of the di-jet mass to allow discrimination in the resonance mass.
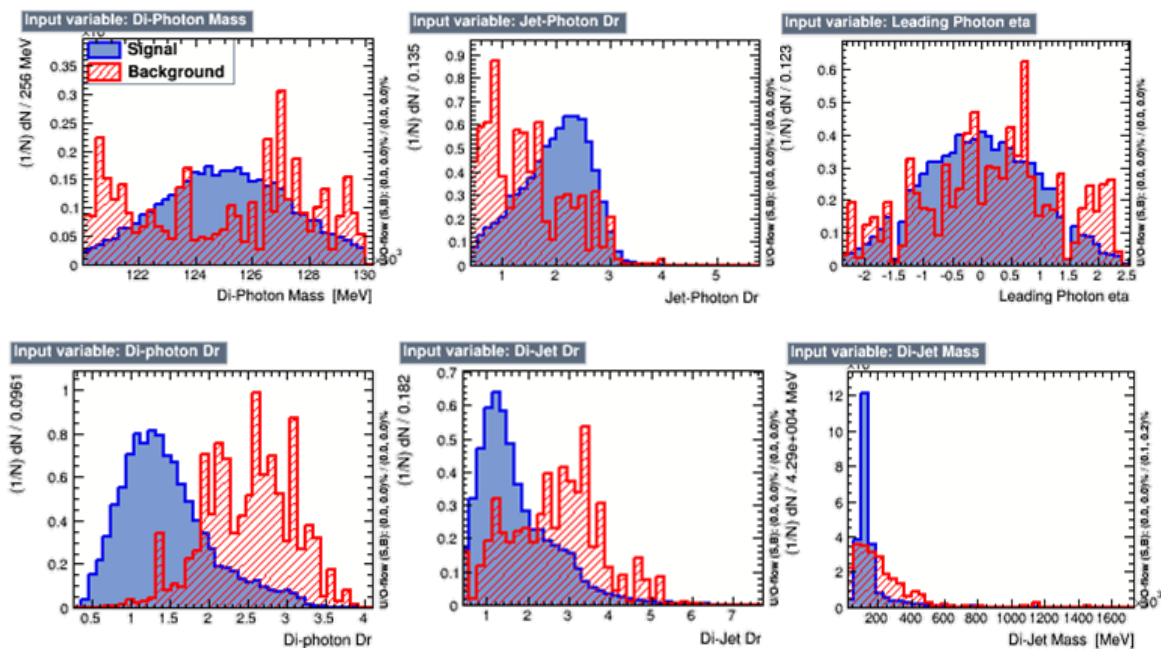
Figure 8.3: Input variable distribution of the $\Delta R_{\gamma\gamma}$, $\Delta R_{\gamma 1 j1}$, ΔR_{bb}, $\eta_{\gamma 1}$, m_{bb}, $m_{\gamma\gamma}$ for the reference scenario at μ=200. Blue area represent the single while with red represents combined background for HH case. Plots are normalized to unity.

In spite of the input variables been kept mostly identical as in the bbH case, discrimination power and ranking differs significantly with the ΔRs between photons, jets and leading photon-leading jet having the highest separation power (*Figure 8.3*). Di-photon mass and di-jet masses are well below the first three prominent ranking positions with the $m_{\gamma\gamma}$ pre-selection cut already rejecting the majority of the background. The effect here is much more dominant than in the bbH case, because of the higher signal statistics and the resonant nature of the di-jet pair allowing a more effective BDT training. Small ranking variations exist between scenarios with the six variables demonstrating the highest separation value changing ranking order.

Signal and backgrounds PDFs (*Figure 8.4*) demonstrate stronger separation than in the bbH case. Signal remains in the positive end of the classifier values while most of the non-resonant background sitting at the lower negative end has been removed by the di-photon mass pre-selection. The additional di-jet resonance allows a better separation moving the signal further to the right with respect to the bbH case and allowing for a better signal discrimination. Reduced background statistics result in significant uncertainties and fluctuating shape of the corresponding PDF, while for the signal the situation quite improved.
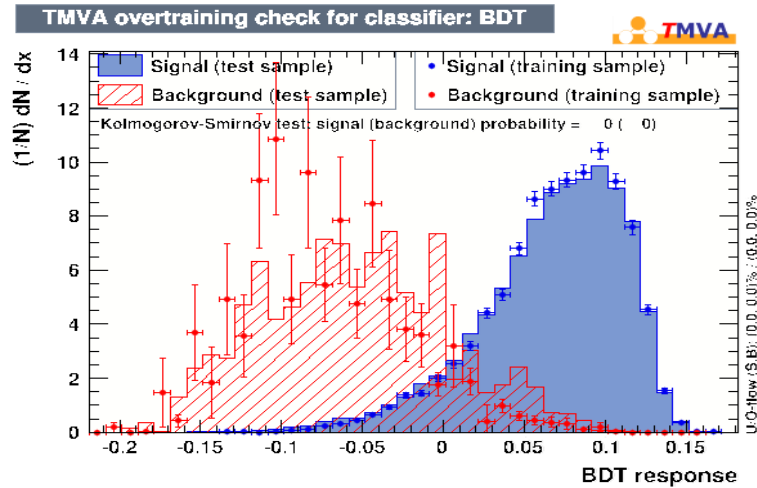
Figure 8.4: BDT response and output PDFs for the signal in blue and the background in red for the reference scenario at μ = 140. Training and testing samples are plotted together, with testing data represented as points.
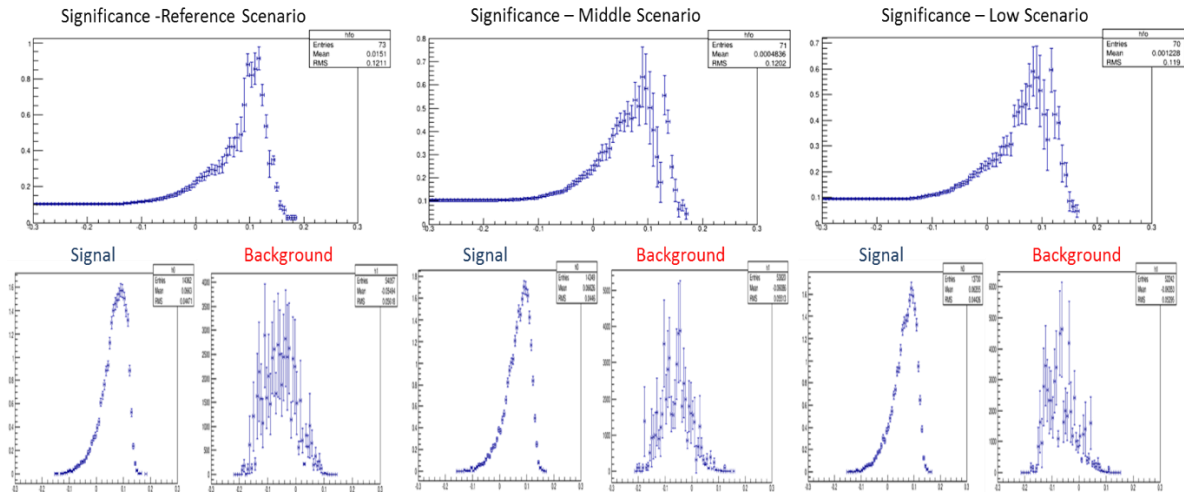
Figure 8.5: Significance distributions and signal and background PDFs for all three scenarios when for the HH channel at μ = 200. Fluctuations on the higher end of the significance curves are due to lack of background statistics in the increased weight samples.

Significance is calculated in each possible BDT value, maintaining the same binning and uncertainties definitions as in all previous cases. Instabilities at the higher end of the distributions (*Figure 8.5*) are still present but with a lower intensity than in the bbH mass cut analysis. One interesting observation is that the lack of statistical fluctuations for the distribution associated to the nominal scenario, being the one yielding most single events. This effect may be attributed to higher signal statistics at the top end of the distribution, compensating for the decrease of high weight events in the background samples towards large BDT values that induce abrupt significance variations. In contrast, instabilities are still present at the middle and low scenario. As usual, separate training was applied for each case whereas optimal BDT cut point is selected at a stable region for the nominal scenario and applied to the other two.

While in the nominal scenario fluctuation at the highest significance point are important (*Figure 8.5*) and a more coarse binning would give a clearer picture, preference of the scenario with respect to the other two can be inferred in terms of expected significance (*Table 8-2*). No conclusion can be drawn for any separation between the middle and low scenario since results are compatible within limits imposed by uncertainties. An explanation can be extracted by studying background

composition table for each scenario and its variation with respect to the optimal point. For the nominal scenario, main background contribution is the jjγγ presenting an identical final state as the signal with non-resonant distributions. The middle and low scenarios nevertheless are affected more by the fake photon identification efficiency, rendering the bbjγ the dominant background component. Foreseen acceptance extension for the nominal scenario results in an increase of jjγγ events, essentially because of the high eta contributions. This effect compensates the fake photon background that dominates the other two scenarios whereas statistical uncertainties in the bbjγ sample do not allow for a definite conclusion. With an event weight of 43, the 86 expected events for the middle and low scenario correspond to only 2 real events in the bbjγ sample (*Table 5-3*), which can be included or excluded by slight variations of the cut value.

	Reference	Middle	Low
Significance	0.92 ± 0.10	0.60 ± 0.22	0.53 ± 0.21
Signal	7.56 ± 0.12	7.61 ± 0.13	6.55 ± 0.12
Background	67 ± 10	163 ± 87	155 ± 87

Table 8-2: Significance value and expected signal and background events for all three scenarios for HH TMVA analysis assuming μ = 200.

Stream	Reference		Middle		Low	
	Events	Yield %	Events	Yield %	Events	Yield %
$b\bar{b}H(\to \gamma\gamma)$	0.92 ± 0.04	(1.38 ± 1.4) %	0.89 ± 0.03	(0.55 ± 0.6) %	0.87 ± 0.03	(0.56 ± 0.7) %
$b\bar{b}\gamma\gamma$	8.01 ± 2.00	(12.00 ± 4.4) %	9.83 ± 2.40	(6.04 ± 3.7) %	7.86 ± 1.97	(5.06 ± 3.3) %
$b\bar{b}j\gamma$	0 ± 0	(0 ± 0.0) %	86.42 ± 86.42	(53.13 ± 28.8) %	86.42 ± 86.42	(55.67 ± 31.5) %
$jj\gamma\gamma$	27.95 ± 9.56	(41.90 ± 8.9) %	45.97 ± 11.81	(28.26 ± 15.6) %	34.38 ± 10.13	(22.15 ± 12.9) %
$t\bar{t}\gamma$	2.19 ± 1.73	(3.28 ± 2.2) %	0 ± 0 %	(0 ± 0.0) %	5.47 ± 2.89	(3.52 ± 2.5) %
$t\bar{t}H(\to \gamma\gamma)$	13.1 ± 0.89	(19.62 ± 5.7) %	12.64 ± 0.88	(7.77 ± 4.7) %	12.68 ± 0.89	(8.17 ± 5.1) %
$t\bar{t}l$	0 ± 0	(0 ± 0.0) %	0 ± 0	(0 ± 0.0) %	0 ± 0	(0 ± 0.0) %
$Z(\to b\bar{b})H(\to \gamma\gamma)$	1.52 ± 0.05	(2.28 ± 1.9) %	1.58 ± 0.05	(0.97 ± 0.9) %	1.32 ± 0.05	(0.85 ± 0.9) %
$c\bar{c}\gamma\gamma$	13.03 ± 2.81	(19.53 ± 5.7) %	5.33 ± 1.48	(3.28 ± 2.2) %	6.24 ± 1.76	(4.02 ± 2.8) %
$c\bar{c}j\gamma$	0 ± 0	(0 ± 0.0) %	0 ± 0	(0 ± 0.0) %	0 ± 0	(0 ± 0.0) %

Table 8-3: Background composition for all three scenarios for the HH analysis case.

Overall, the analysis performs well in the HH channel yielding compatible results with cut based estimations [1] at Phase II luminosity, but suffers from lack of background statistics which cannot dive to a safe conclusion. An improvement is observed for the nominal scenario in the order of 25 % with respect to the other two while two most dominant background contributions can be traced to the jjγγ final state emulating the single and the bbγj, due to the jet to photon misidentification probabilities. With respect to bbH channel, more efficient BDT raining as well as the resonant nature of the di-jet pair significantly reduces background and doubles expected significance.

8.3 Doping Profile Reference Library

8.3.1 CiS n-in-n Test Wafers Simulation Parameters

Substrate properties		
	High Resistivity	Low Resistivity
Orientation	*100*	
Material	*Silicon*	
Type	*n-type (phosphorus)*	
Resistivity	*4000 Ω×cm*	*0.25 Ω×cm*
Dopant Concentration	*$1.1×10^{12}$ atoms/cm³*	*$3×10^{16}$ atoms/cm³*
Thickness	*525 µm*	*380 µm*

Table 8-4: Wafer substrate properties implemented into the simulation.

Simulators	
Process Simulation	*sprocess*
Differential equation solver	*parallel direct solver PARDISO*

Table 8-5: Process flow simulator and equation solving algorithm.

Geometrical parameters	
Coordinates System	*Unified Coordinate System*
Region	*1-Dimensional simulation*
Side	*Front*
Allow multiple annealing and diffusion steps using same grid	*Relaxed mechanical stress calculation*
Silicon Native Oxide thickness	*1.9 nm*

Table 8-6: Parameters related to geometry definition and structure treatment.

Implantation Parameters	
Implantation simulation	*Monte Carlo Simulation*
Monte Carlo Implantation Model	*CrystalTrim*
Implantation damage simulation	*Full Cascade model*
Parallel processes	*4*
Number of simulated pseudo-particles	*1000*
Monte Carlo Randomization Seed	*System Clock*
Increase number of trajectories in segments with low trajectory density	*Trajectory Splitting*
Maximum phosphorus trajectory splits in silicon	*4*
Maximum phosphorus trajectory splits per element in silicon	*2*
Trajectory replication	*Active*
Periodicity (Reflective boundaries)	*in X and Y directions*
Use Advanced Calibration Library	*Active*
Advanced Calibration library version	*2013.12*
Dopant diffusion model	*Constant*
	Charged Fermi
	Charged Pair
	Charged React
Dopant activation model	*BIC*

Table 8-7: Implantation parameters and used models. Parameters not included in this table are used in their default value as defined within Sentaurus database.

Fixed Mesh element lines Placemat

Region	Cell Size
0 μm – 3 μm	0.5 nm– 5 nm
3 μm – 7 μm	5 nm – 100 nm
7 μm – 10 μm	100 nm - 1 μm
10 μm – 100 μm	1 μm – 50 μm
100 μm – backside	50 μm

Table 8-8: Fixed lines and spacing parameters for meshing element control

Mesh refinements	
Meshing algorithm	*MGOALS*
Minimum grid element side size	*0.6 nm*
Adaptive meshing	*off*
Phosphorus absolute error	10^{14} *atoms/cm³*
Boron absolute error	10^{14} *atoms/cm³*

Table 8-9: Meshing parameters and refinements.

Simulated Process Flow:

1. Oxidation (for the 100 nm screen oxide layer)
    a. 5 minutes thermal diffusion step simulation at 1000 ^{0}C with O_2 presence
    b. 95 minutes thermal diffusion step simulation at 1000 ^{0}C with O_2 and HCl presence
    c. 20 minutes thermal diffusion step simulation at 1000 ºC with N_2 presence

- or -

1. Oxidation (for the 200 nm screen oxide layer)
    a. 1 minute thermal diffusion step simulation at 1000 ^{0}C with O_2 presence
    b. 10 minutes thermal diffusion step simulation at 1000 ^{0}C with O_2 and HCl presence
    c. 10 minutes thermal diffusion step simulation at 1000 ^{0}C with O_2 presence
    d. 22.75 minutes thermal diffusion step simulation at 1000 ^{0}C with O_2 and H_2 presence
    e. 5 minutes thermal diffusion step simulation at 1000 ºC with N_2 presence
2. Implantation
    a. Tilt angle: 7 degrees
    b. Rotation angle: -30 degrees
    c. Side: front
    d. Quadrant implantation: 1
    e. Energy and dose: varies depending on specification
3. Thermal annealing step
    a. 240 minutes exposure to 975 ^{0}C under N_2 atmosphere
4. Oxide etching step (optional)
    a. Type: Strip
    b. Material: Oxide
    c. Over etch: 1%
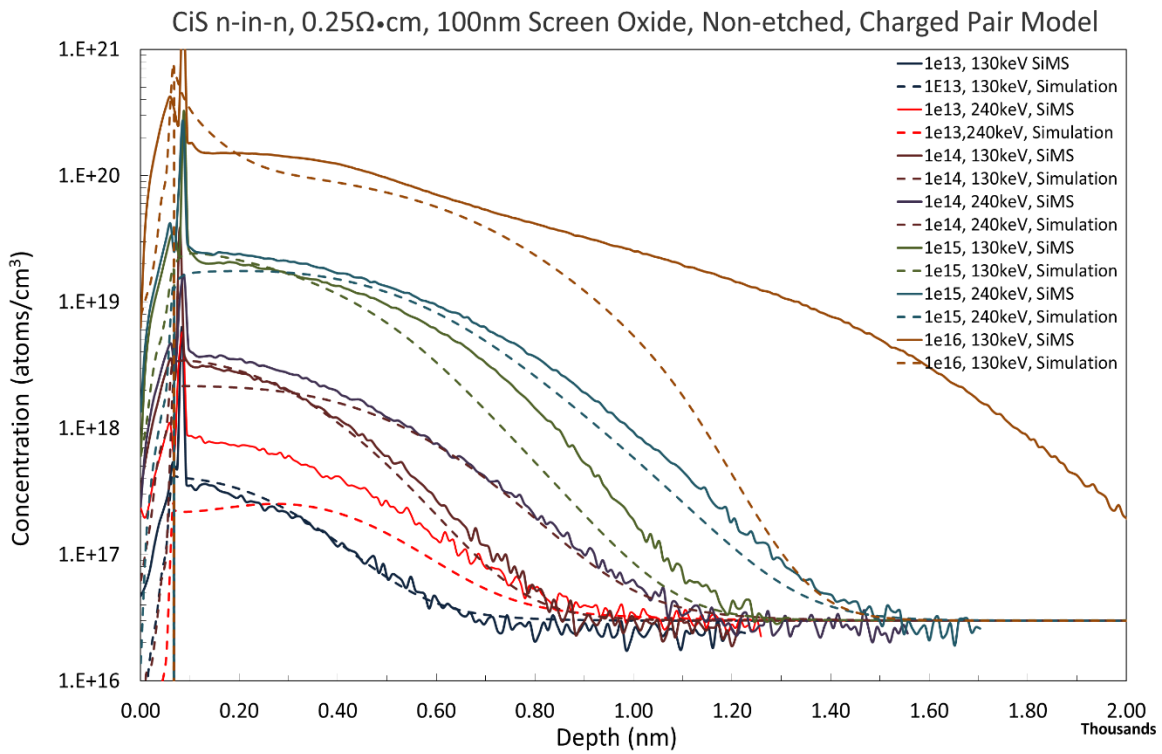   d. Etch stop material: Silicon
    e. Side: Front
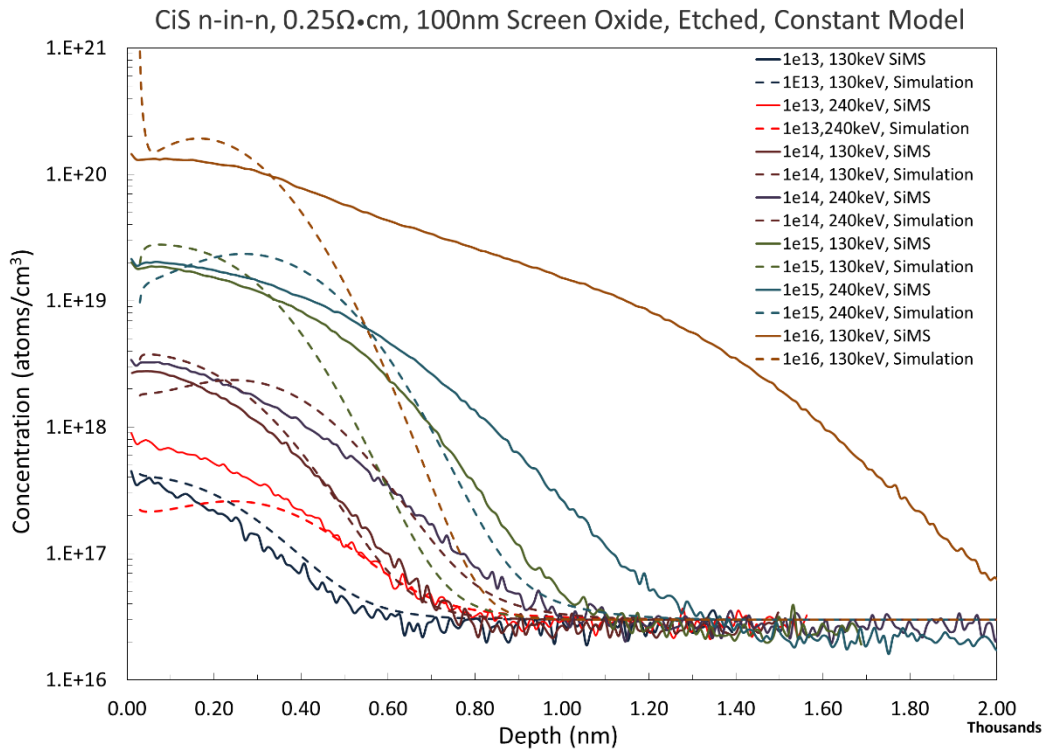
Figure 8.6: SIMS – Simulation comparison for the CiS n-in-n samples using the constant diffusion model for the low resistivity substrate. Additional silicon dioxide has been etched off the surface of the samples and an equivalent process is simulated.
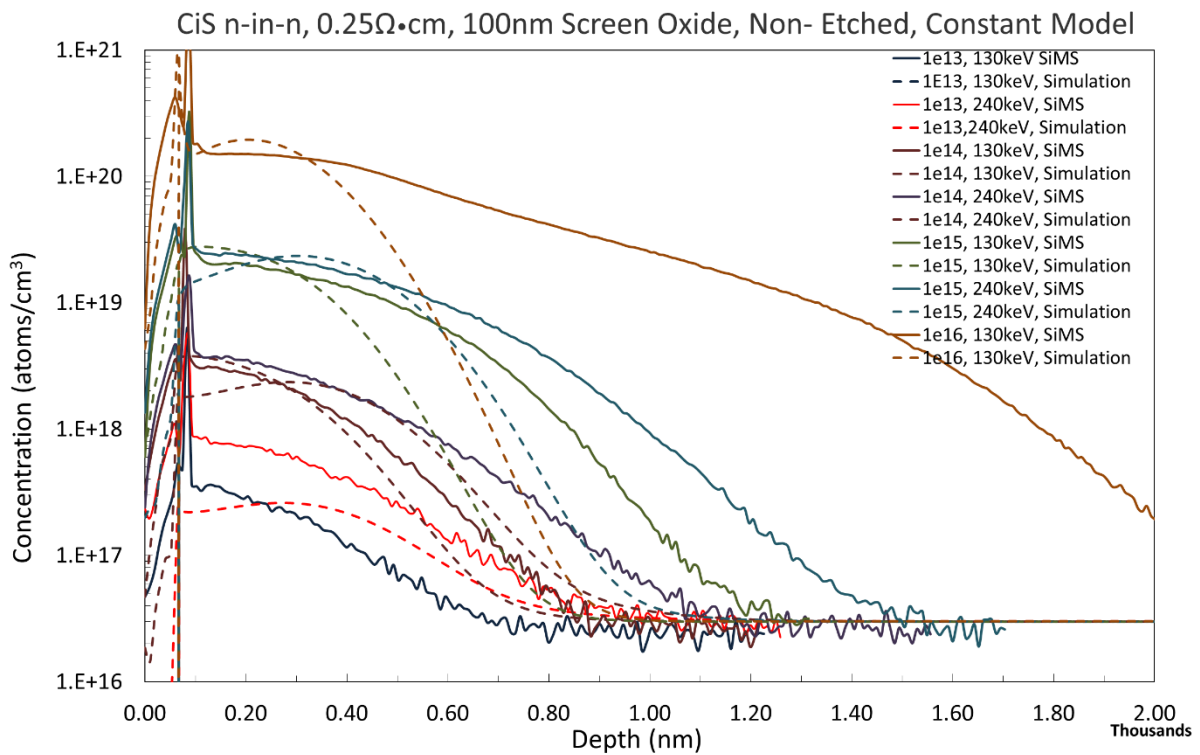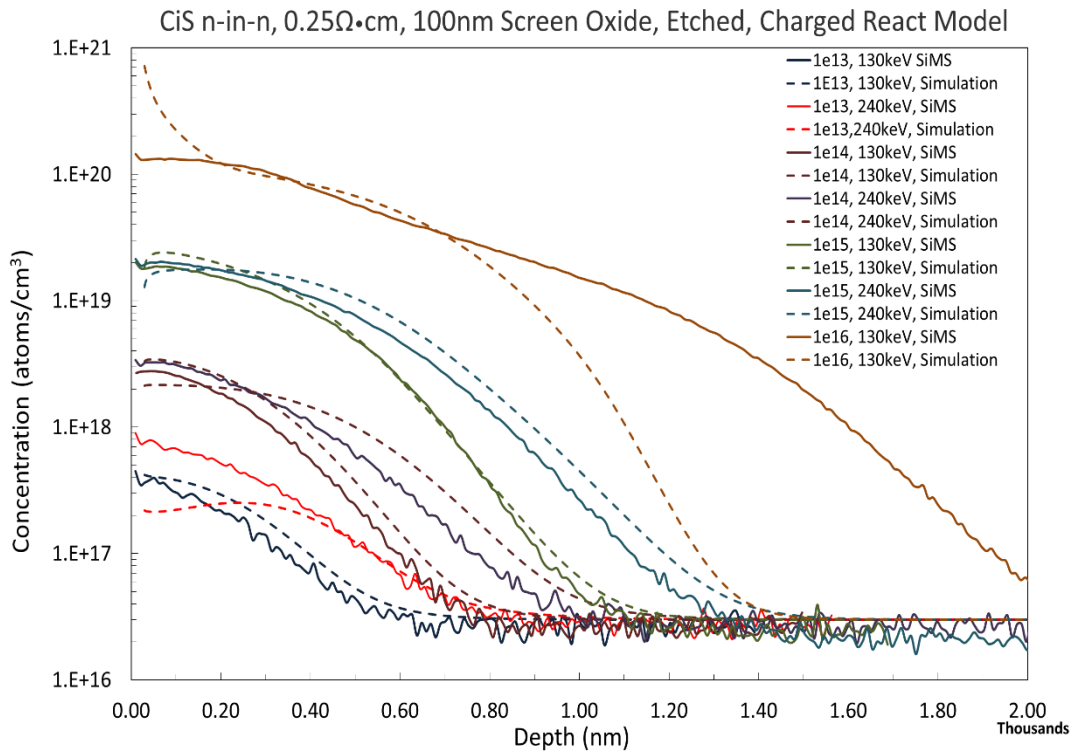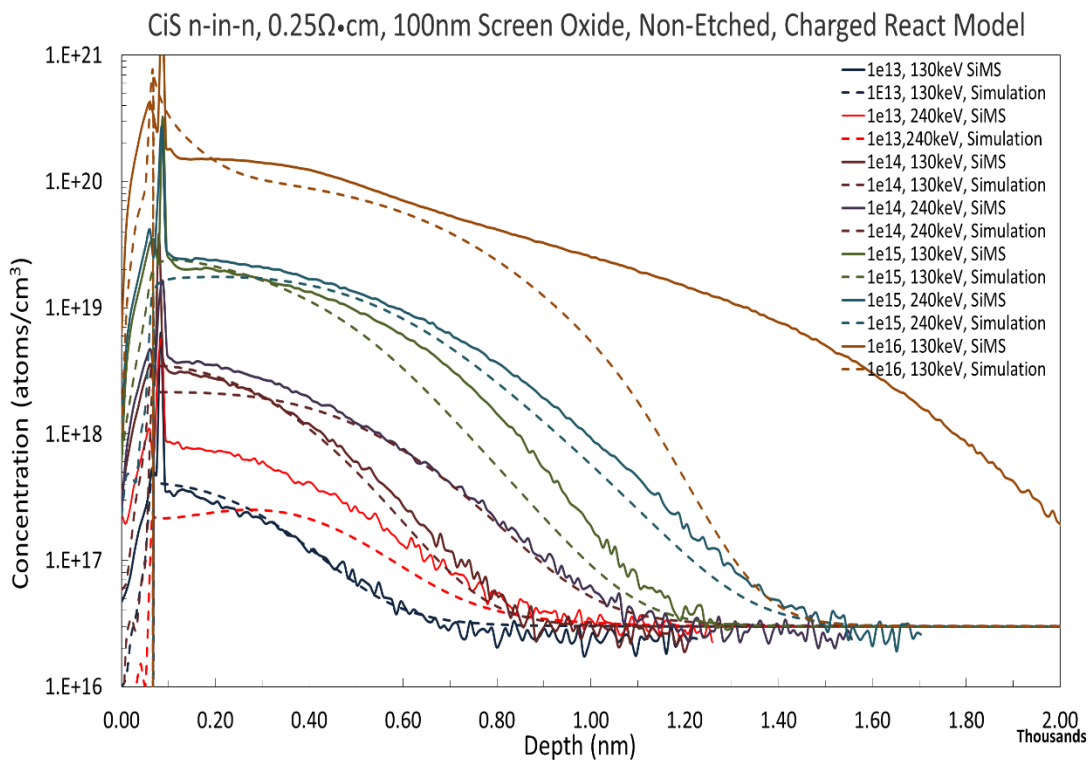

Figure 8.7: SIMS – Simulation comparison for the CiS n-in-n samples using the constant diffusion model for the low resistivity substrate. Measurements are performed through the silicon dioxide layer and the sharp peak marks the transition boundary between oxide and silicon.
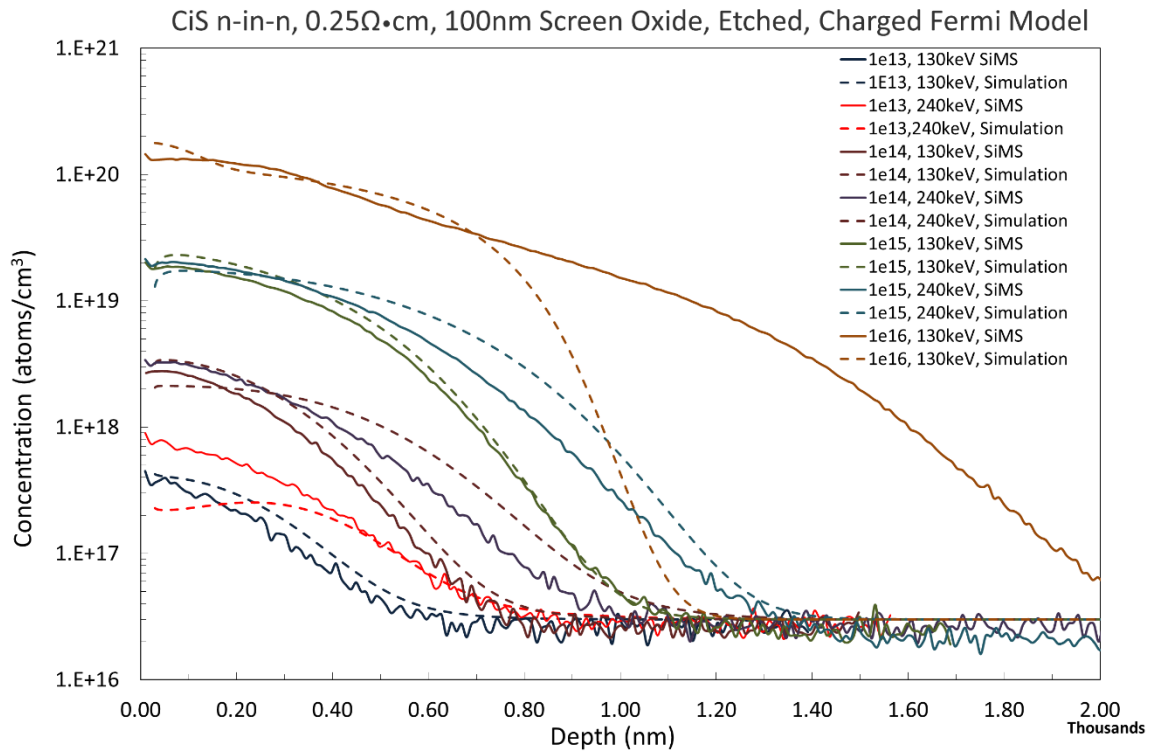
Figure 8.8: SIMS – Simulation comparison for the CiS n-in-n samples using the charged Fermi diffusion model for the low resistivity substrate. Additional silicon dioxide has been etched off the surface of the samples and an equivalent process is simulated.
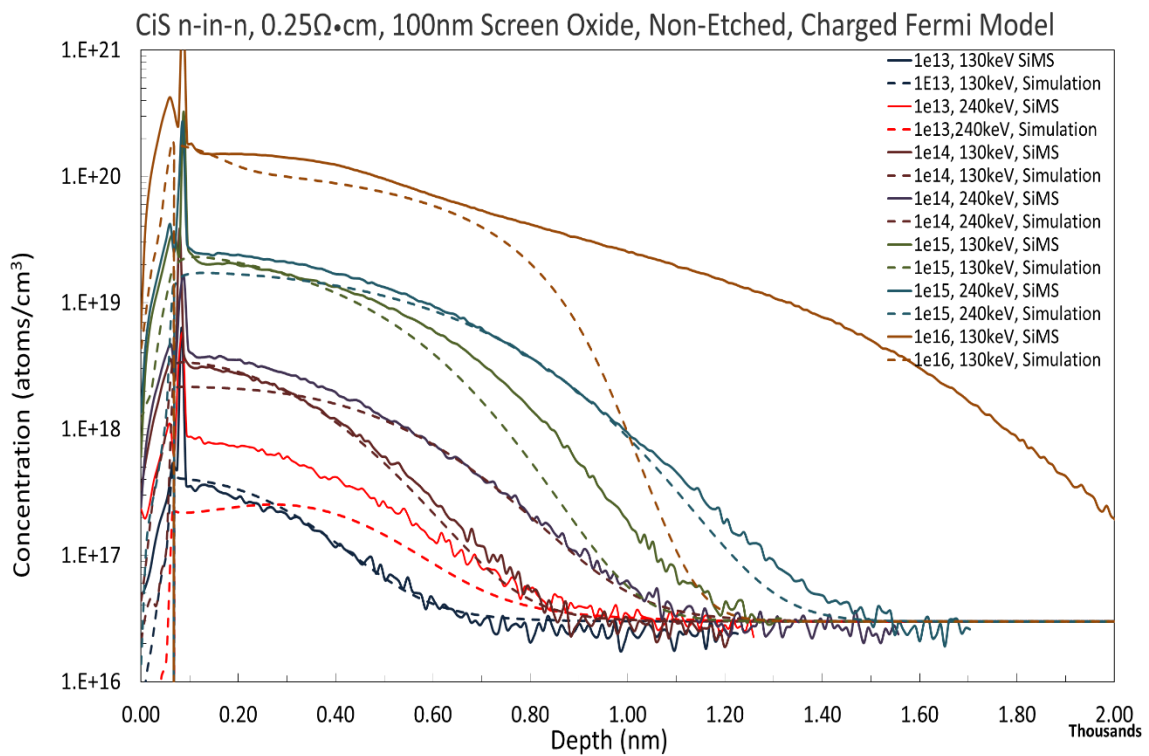
Figure 8.9: SIMS – Simulation comparison for the CiS n-in-n samples using the charged Fermi diffusion model for the low resistivity substrate. Measurements are performed through the silicon dioxide layer and the sharp peak marks the transition boundary between oxide and silicon.
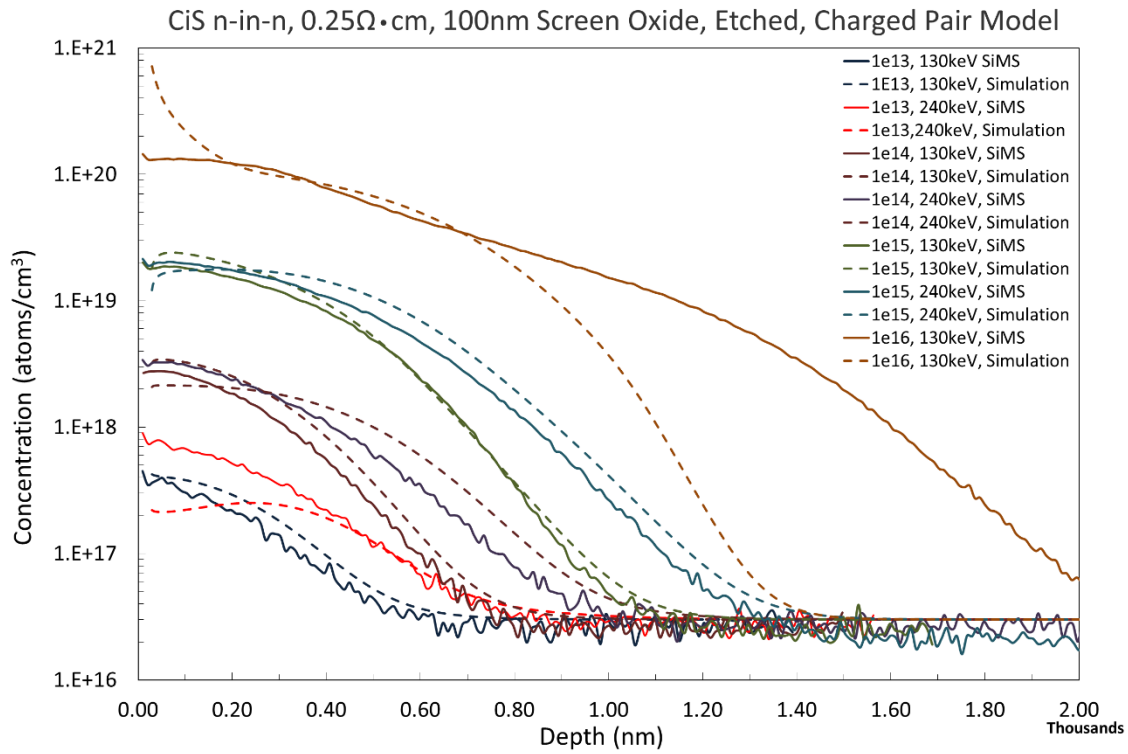
Figure 8.10: SIMS – Simulation comparison for the CiS n-in-n samples using the charged Pair diffusion model for the low resistivity substrate. Additional silicon dioxide has been etched off the surface of the samples and an equivalent process is simulated.

Figure 8.11: SIMS – Simulation comparison for the CiS n-in-n samples using the charged Pair diffusion model for the low resistivity substrate. Measurements are performed through the silicon dioxide layer and the sharp peak marks the transition boundary between oxide and silicon.

Figure 8.12: SIMS – Simulation comparison for the CiS n-in-n samples using the charged React diffusion model for the low resistivity substrate. Additional silicon dioxide has been etched off the surface of the samples and an equivalent process is simulated.

Figure 8.13: SIMS – Simulation comparison for the CiS n-in-n samples using the charged React diffusion model for the low resistivity substrate. Measurements are performed through the silicon dioxide layer and the sharp peak marks the transition boundary between oxide and silicon.

8.3.2 VTT n-in-p Test Wafers Simulation Parameters

Substrate properties		
	High Resistivity	Low Resistivity
Orientation	*100*	
Material	*Silicon*	
Type	*p-type (boron)*	
Resistivity	*10000 Ω×cm*	*2 Ω×cm*
Dopant Concentration	*1.3×10^{12} atoms/cm³*	*7×10^{15} atoms/cm³*
Thickness	*525 μm*	*675 μm*

Table 8-10: Wafer substrate properties implemented into the simulation.

Simulators	
Process Simulation	*sprocess*
Differential equation solver	*parallel direct solver PARDISO*

Table 8-11: Process flow simulator and equation solving algorithm.

Geometrical parameters	
Coordinates System	*Unified Coordinate System*
Region	*1-Dimensional simulation*
Side	*Front*
Allow multiple annealing and diffusion steps using same grid	*Relaxed mechanical stress calculation*
Silicon Native Oxide thickness	*1.9 nm*

Table 8-12: Parameters related to geometry definition and structure treatment.

Implantation Parameters	
Implantation simulation	*Monte Carlo Simulation*
Monte Carlo Implantation Model	*CrystalTrim*
Implantation damage simulation	*Full Cascade model*
Parallel processes	*4*
Number of simulated pseudo-particles	*1000*
Monte Carlo Randomization Seed	*System Clock*
Increase number of trajectories in segments with low trajectory density	*Trajectory Splitting*
Maximum phosphorus trajectory splits in silicon	*4*
Maximum phosphorus trajectory splits per element in silicon	*2*
Trajectory replication	*Active*
Periodicity (Reflective boundaries)	*in X and Y directions*
Use Advanced Calibration Library	*Active*
Advanced Calibration library version	*2013.12*
Dopant diffusion model	*Constant*
	Charged Fermi
	Charged Pair
	Charged React
Dopant activation model	*BIC*

Table 8-13: Implantation parameters and used models. Parameters not included in this table are used in their default value as defined within Sentaurus database.

Fixed Mesh element lines Placemat

| Region	Cell Size
0 μm – 3 μm	0.5 nm– 5 nm
3 μm – 7 μm	5 nm – 100 nm
7 μm – 10 μm	100 nm - 1 μm
10 μm – 100 μm	1 μm – 50 μm
100 μm – backside	50 μm

Table 8-14: Fixed lines and spacing parameters for meshing element control

Mesh refinements	
Meshing algorithm	*MGOALS*
Minimum grid element side size	*0.6 nm*
Adaptive meshing	*off*
Phosphorus absolute error	10^{14} *atoms/cm^3*
Boron absolute error	10^{14} *atoms/cm^3*

Table 8-15: Meshing parameters and refinements.

Simulated Process Flow:

1. Oxide Deposition (no full oxidation simulation at this stage)
   a. Material: Oxide
   b. Thickness: 100 nm or 200 nm
   c. Dopant: None
   d. Side: Front
   e. Deposition type: Isotropic
2. Thermal Annealing (to simulate oxidation thermal stresses)
   a. Temperature: 1000 ^{0}C
   b. Time: 10 minutes (for 100 nm) or 24 minutes (for 200 nm)
   c. Correspondence to oxidation: wet oxidation assuming native oxide
3. Implantation
   d. Tilt angle: 7 degrees
   e. Rotation angle: -30 degrees
   f. Side: front
   g. Quadrant implantation: 1
4. Post-Implantation Oxidation
   a. Dopant dependent occupation: Active
   b. 60 minutes thermal diffusion step simulation at 1000 ^{0}C with N_2 presence
   c. 60 minutes thermal diffusion step simulation at 1000 ^{0}C with O_2 presence
   d. 60 minutes thermal diffusion step simulation at 1000 ^{o}C with H_2O presence
5. Oxide etching step (optional)
   a. Type: Strip
   b. Material: Oxide
   c. Over etch: 1%
   d. Etch stop material: Silicon
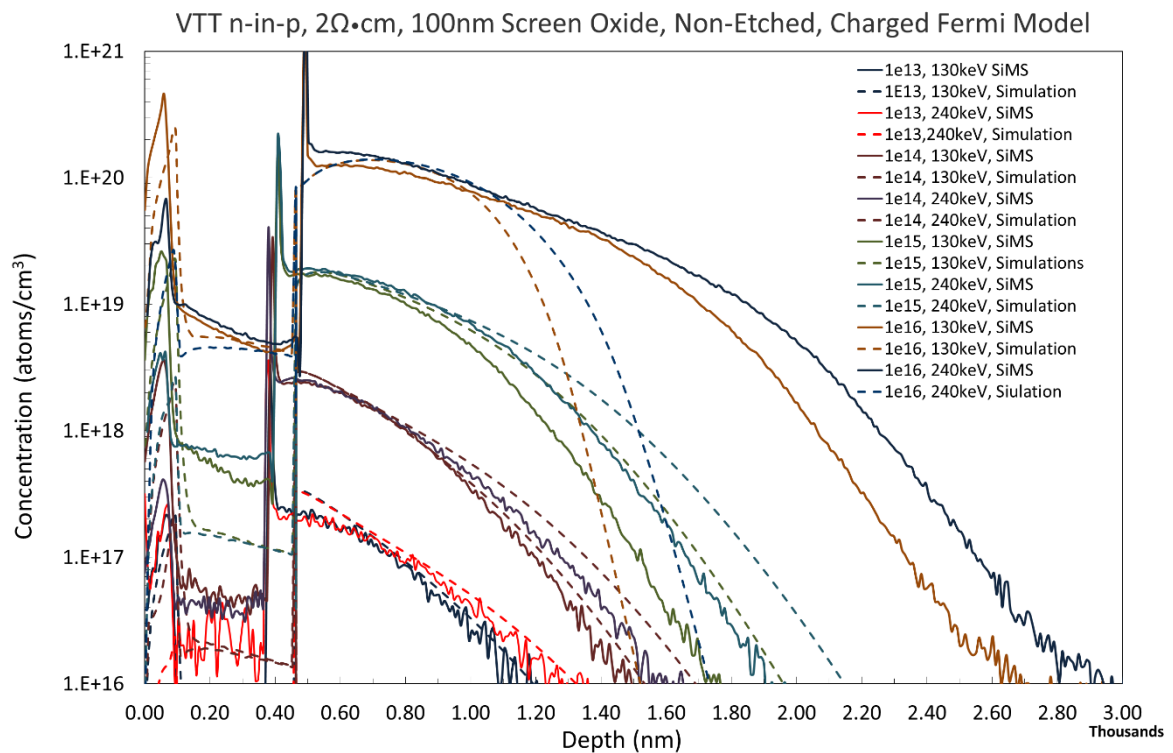   e. Side: Front
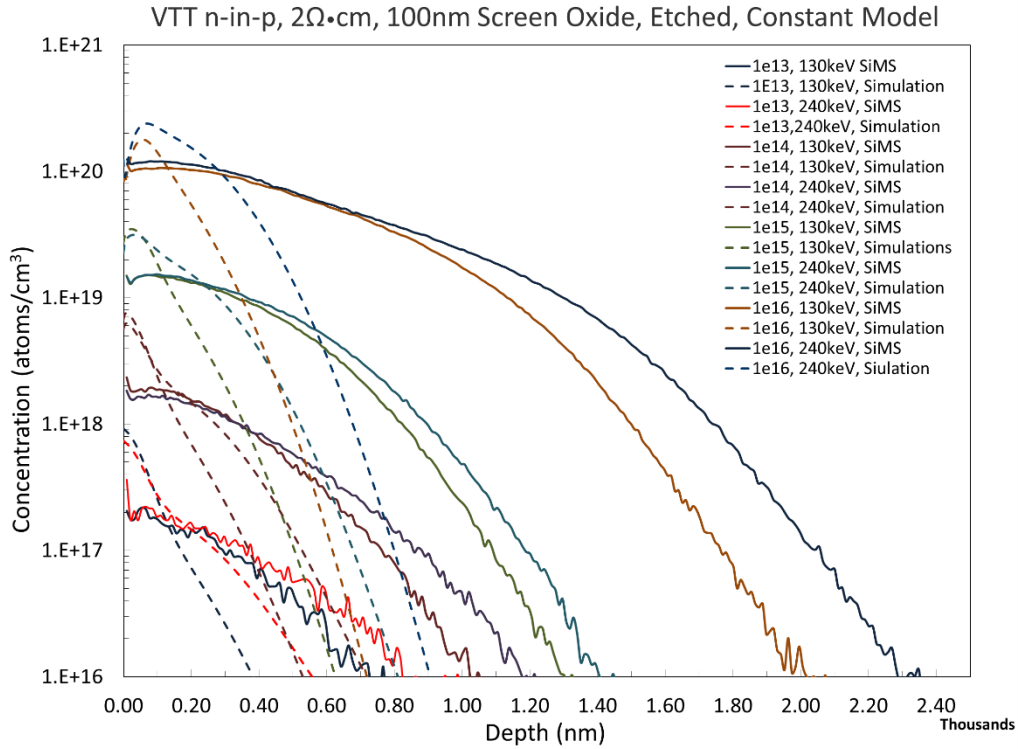
Figure 8.14: SIMS – Simulation comparison for the VTT n-in-p samples using the constant diffusion model for the low resistivity substrate. Additional silicon dioxide has been etched off the surface of the samples and an equivalent process is simulated.
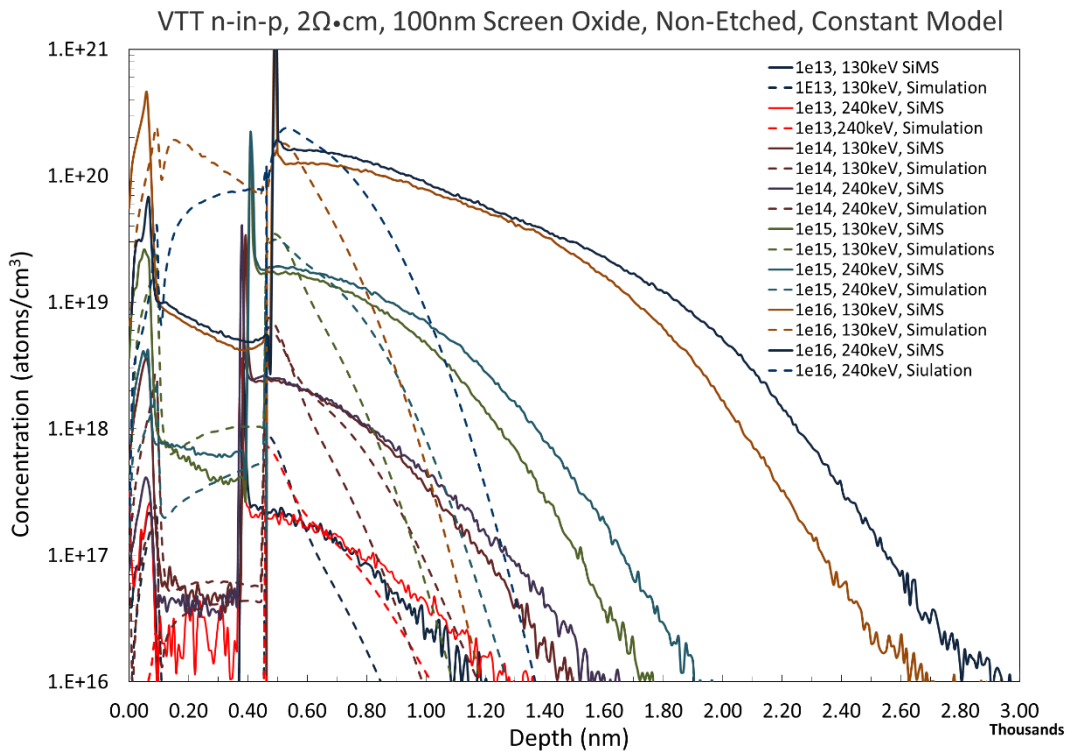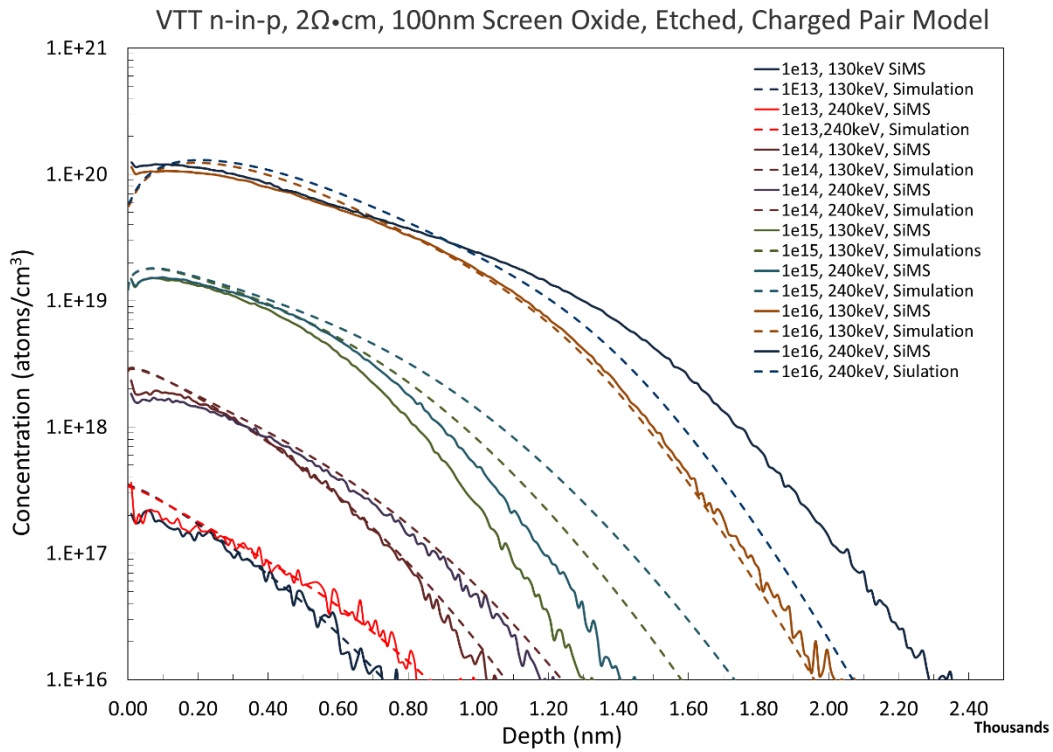

Figure 8.15: SIMS – Simulation comparison for the VTT n-in-p samples using the constant diffusion model for the low resistivity substrate. Measurements are performed through the silicon dioxide layer and the sharp peak marks the transition boundary between oxide and silicon.
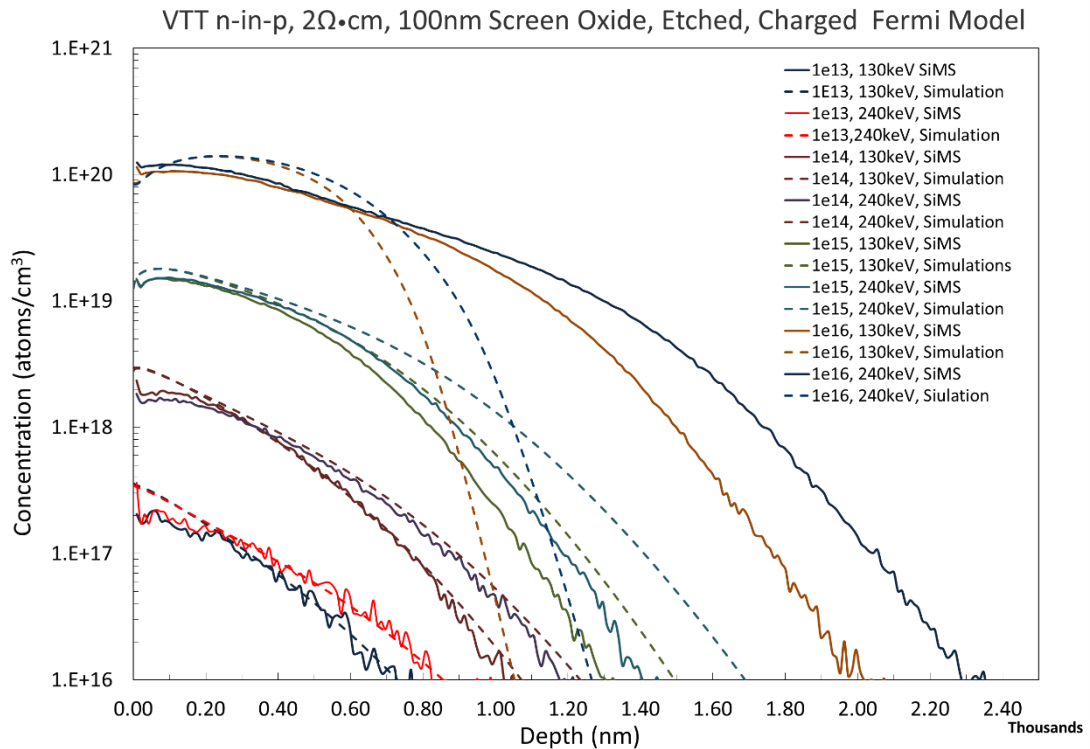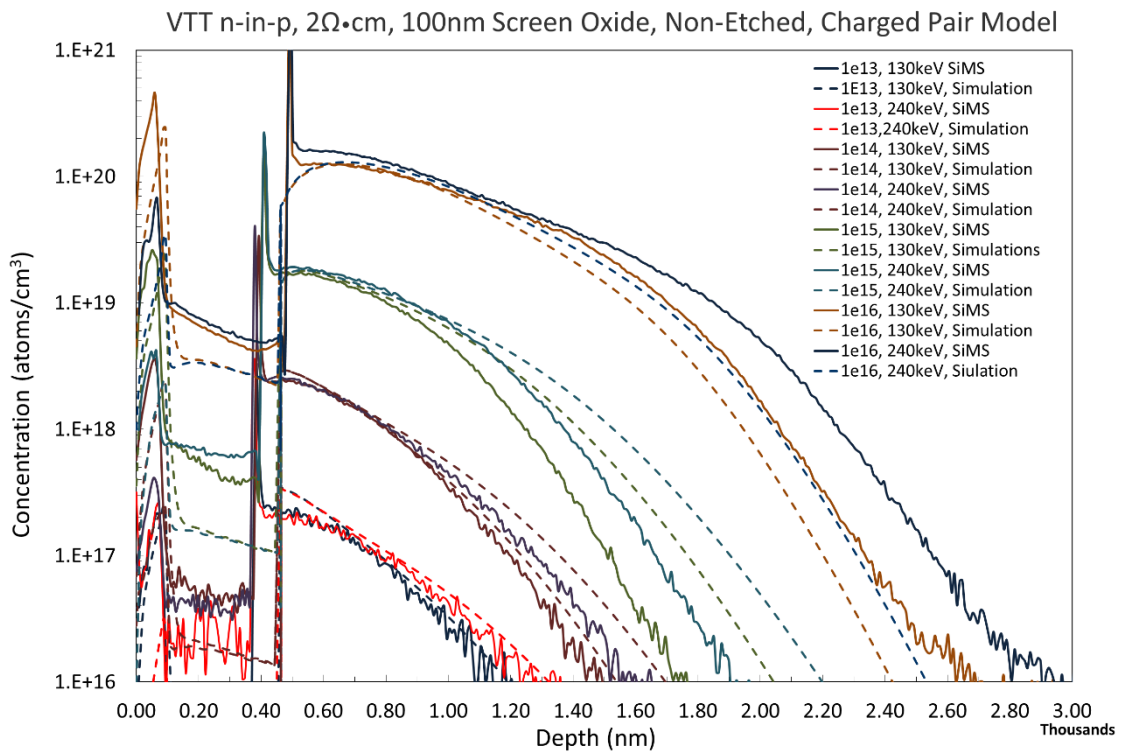
Figure 8.16: SIMS – Simulation comparison for the VTT n-in-p samples using the charged Fermi model for the low resistivity substrate. Additional silicon dioxide has been etched off the surface of the samples and an equivalent process is simulated.
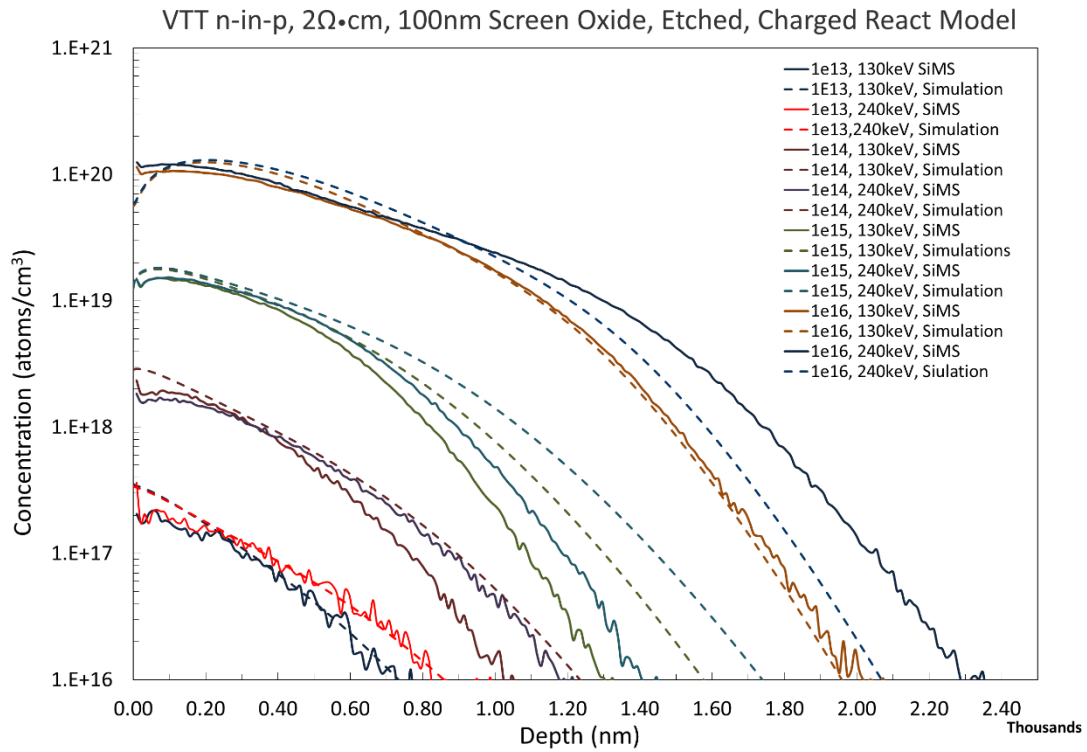

Figure 8.17: SIMS – Simulation comparison for the VTT n-in-p samples using the charged Fermi model for the low resistivity substrate. Measurements are performed through the silicon dioxide layer and the sharp peak marks the transition boundary between oxide and silicon.
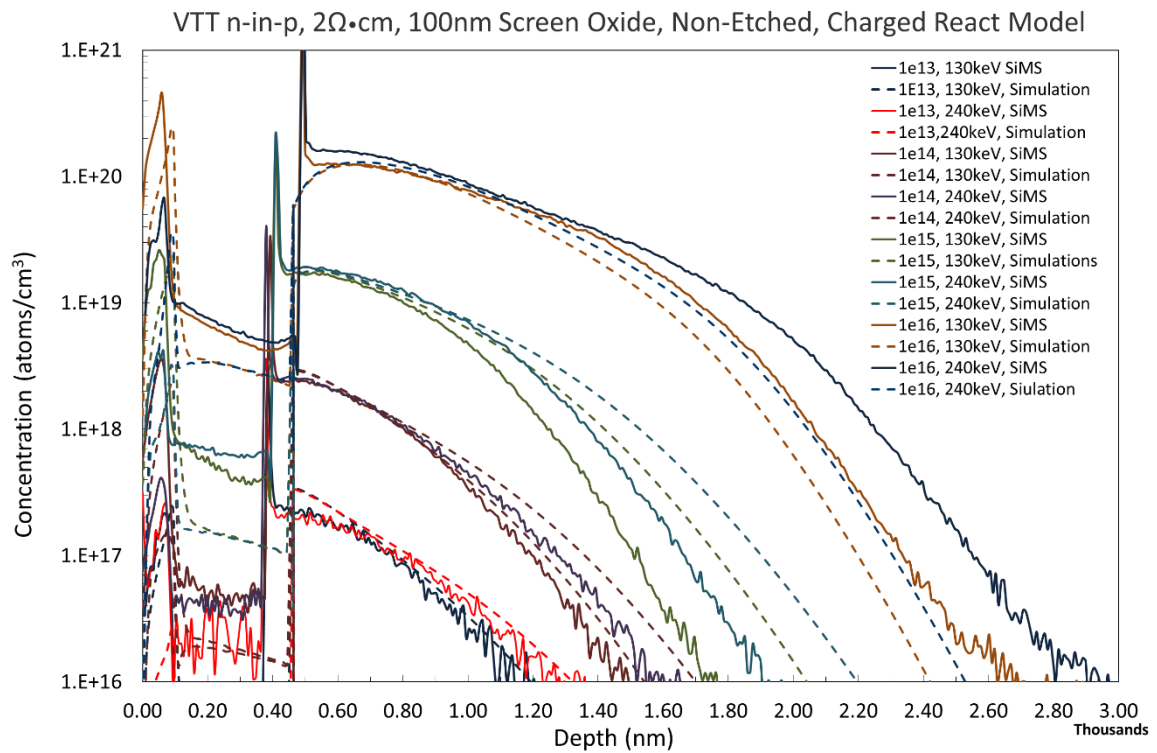
Figure 8.18: SIMS – Simulation comparison for the VTT n-in-p samples using the charged Pair model for the low resistivity substrate. Additional silicon dioxide has been etched off the surface of the samples and an equivalent process is simulated.

Figure 8.19: SIMS – Simulation comparison for the VTT n-in-p samples using the charged Pair model for the low resistivity substrate. Measurements are performed through the silicon dioxide layer and the sharp peak marks the transition boundary between oxide and silicon.

Figure 8.20: SIMS – Simulation comparison for the VTT n-in-p samples using the charged React model for the low resistivity substrate. Measurements are performed through the silicon dioxide layer and the sharp peak marks the transition boundary between oxide and silicon.

Figure 8.21: SIMS – Simulation comparison for the VTT n-in-p samples using the charged React model for the low resistivity substrate. Measurements are performed through the silicon dioxide layer and the sharp peak marks the transition boundary between oxide and silicon.

8.4 References

[1] Weiming Yao (LBNL), "Studies of measuring Higgs self-coupling with HH→bbγγ at the future hadron colliders", Sep 2013,http://arxiv.org/abs/1308.6302v2